Light Harvesting Strategies for Large Area, Stable and Efficient Organic Solar Cells

A Thesis Submitted in Partial Fulfillment of

The Requirements of the Degree of

Doctor of Philosophy

By

Anshuman Jyothi Das

Chemistry and Physics of Materials Unit

Jawaharlal Nehru Centre for Advanced Scientific Research Bangalore,

Karnataka – 560064, INDIA

April 2013

DECLARATION

I hereby declare that the matter embodied in this thesis is the result of the work carried out by me under the supervision of Prof. K. S. Narayan, at Molecular Electronics Laboratory, in Chemistry and Physics of Materials Unit, Jawaharlal Nehru Centre for Advanced Scientific Research, Bangalore, India. It has not been submitted for the award of any degree or diploma or associateship of any other university or institute.

In keeping with the general practice in reporting scientific observations, due acknowledgment has been made whenever the work described is based on the findings of other investigators.

(Anshuman J. Das)

Candidate

JAWAHARLAL NEHRU CENTRE FOR ADVANCED SCIENTIFIC RESEARCH

Jakkur, Bangalore − 560064, India

K. S. NARAYAN
Professor
Dean (Research and Development)
PHONE: +91 80 2208 2822/2548
E-mail: narayan@jncasr.ac.in
Fax: +91 80 2208 2766

April 24th, 2013

CERTIFICATE

I hereby certify that the matter embodied in this thesis entitled "*Light Harvesting Strategies for Large Area, Stable and Efficient Organic Solar Cells*" has been carried out by Mr. Anshuman Jyothi Das at the Molecular Electronics Laboratory, Jawaharlal Nehru Centre for Advanced Scientific Research, Bangalore, India, under my supervision and it has not been submitted elsewhere for the award of any degree or diploma.

Prof. K. S. Narayan

(Research Supervisor)

The most beautiful experience we can have is the mysterious – the fundamental emotion which stands at the cradle of true art and true science. –Albert Einstein

Dedicated to my grandparents

Aja, Aai, Jejebapa and Jejemaa

Acknowledgment

"It takes two flints to make a fire."— Louisa May Alcott

An acknowledgement is not a formality, but only a very small way of saying that nothing is achieved alone! This work has seen the light of the day because of the efforts of many wonderful people. I thank all the people- critics, friends, musicians, technicians, scientists and my family for assisting me in developing the right approach to science, for the temperament, for better clarity, for support and for a host of other things that may be better left unsaid.

I would like to express my sincere thanks to my research supervisor, Prof. K. S. Narayan, for providing a wonderful, warm and a challenging atmosphere at the Molecular Electronics Laboratory. The freedom to explore, the zeal to pursue, and the enthusiasm to succeed were things I learnt here. This will surely hold me in good stead in my future endeavours.

I would like to extend my special thanks to Prof. C. N. R. Rao for the Sheikh Saqr fellowship and his zeal and the energy that he inspires.

I thank the Chairman of Chemistry and Physics of Materials Unit, Prof. Balasubramanian Sundaram for his professionalism and leadership that has inspired me along with his sense of humor.

I would like to express my gratitude to my course instructors Prof. Chandrabhas Narayana, Prof. Umesh Waghmare, Prof. G. U. Kulkarni for the wonderful things I learnt.

I was also inspired by my interactions with young faculty members, Dr. Vidyadhiraja, Dr. Sridhar Rajaram and Dr. Subi George. I am thankful to the other entire CPMU faculty for the making this place a lovely place to do research.

I would like to express my heartfelt gratitude to Prof. Joseph Zyss, Dr. Melanie Lebental and Mr. Clement Lafargue for their wonderful hospitality during my stay Cachan, Paris. The city of Paris mesmerized me as much as their research and warmth.

I am thankful to the staff at JNC office, library, academic section, computer lab, dining hall and purchase section.

I would like to acknowledge the Department of Science and Technology, Govt. of INDIA for two travel grants to visit Paris and Boston. I remain indebted to them for this opportunity that allowed me to explore science as much as these wonderful cities.

I thank NCBS, for their confocal microscopy facilities and IISc for the electron microscopy at Nanoscience Center.

I acknowledge the support from a very skillful and enterprising person, Mr. Arokianathan, at the CPMU workshop for shaping metals, plastics and almost anything.

My seniors have taught me a lot. I was very new to the field of organic electronics and virtually learnt everything here. Had it not been the knowledge they passed on, things would have been very difficult. I thank to my past and present lab members, Drs. Dinesh, Dhritiman, Arun, Manohar, Balraju, Srinidhi, Monojit, Kishore, Poonam. Going-to-be-Drs Shruti, Arun, Vini, Satyaprasad, Ravichandran, Prashant, Ashar, Vijay, Nishit, Madhu, Raaghesh and Swathi. Special thanks to my good friends Monojit and Sachi, with whom I had a lot of fun inside and outside the lab.

I also acknowledge support from other friends at JNC Drs. Shrini, Saiki, Dinesh, Vishwas. Our music team here at JNC was one of the highlights of my stay here. Not only did I get to share some music, I got to learn a lot. Surbhi, Jithesh, Monojit, Piyush, Soumik and Vijay were a great team of drummers, singers, keyboardists and guitarists. Music brought a lot of balance to my life here.

My teachers from school and graduation have shaped, inspired and mentored me. A special thanks to the wonderful physicists Dr. Ramesh Sharma, Dr. Shailesh Srivastava, Dr. Raj Kumar Jain and Dr. O. S. K. S. Sastri.

They say that a single friend can be your world. I have one such friend who makes me a better person, takes pride in my achievements, and takes joy in my joy. I cannot thank you enough, Surbhi, for making a friend out of me.

I was fortunate to have stayed at home during this time. I have had hardly stayed with my parents all my life and it was much needed. It feels very awkward to thank my parents as words limit my feelings. I know that my mom and dad will be there for me like they have been though this time. I couldn't have asked for more in life as I have the most wonderful parents ever! Apart from delicious home-cooked food, I was also able work on my music and culinary skills staying at home.

My brother Anupam, is the best friend I have had since we were kids. His creativity, talent and passion inspire me. We could build a professional music studio with his enthusiasm and also do the music for a commercial film! My dog, Roamy was my personal stress-buster during this time. The mischief and unconditional love she brings to my life is irreplaceable.

Finally, I salute the one who is the source of infinite wisdom, enlightenment and intellectual excellence, Sai…

April 24th, 2013

JNCASR, Bangalore Anshuman J. Das

List of Publications

In this thesis:

1. **Anshuman J Das** and K. S. Narayan, "Retention of efficiency in organic solar cells: from small to large area polymer solar cells", Advanced Materials, 25, 2193 (2013). Selected as frontispiece.

2. Sabyasachi Mukhopadyay, **Anshuman J Das** and K. S. Narayan, "High-resolution photocurrent imaging of bulk heterojunction solar cells", Invited Perspective. The Journal of Physical Chemistry Letters, 4, 161 (2013).

3. **Anshuman J Das**, Clement Lafargue, Melanie Lebental, Joseph Zyss and K. S. Narayan, "Three-dimensional microlasers based on polymer fibres fabricated by electrospinning", Applied Physics Letters, 99, 263303 (2011).

4. **Anshuman J Das**, Sabyasachi Mukhopadhyay and K. S. Narayan, "Characteristic noise features in light transmission across membrane protein undergoing photocycle", Journal of Chemical Physics, 134, 175101 (2011).

5. **Anshuman J. Das** and K. S. Narayan, "Observation of Bessel beams from electric field induced patterns on polymer surfaces", Optics Letters, 34, 3391 - 3393 (2009).

Posters presented at Conferences

1. **Anshuman J. Das** and K. S. Narayan, Low Temperature and Vacuum-free Processing of Large Area Organic Solar Cells, IWAM 2013, Ras Al Khaimah, UAE.

2. **Anshuman J. Das** and K. S. Narayan, Low Temperature, Vacuum-free Processing for Fabrication of Large Area Organic Solar-cell Device Structure, MRS Fall Meeting 2012, Boston.

3. Sabyasachi Mukhopadhyay, **Anshuman J. Das**, S. Ravichandran and K. S. Narayan. High Resolution Photocurrent Imaging of Bulk Heterostructure Blends. **Nominated for best poster** in MRS Fall Meeting 2012, Boston.

4. Monojit Bag, **Anshuman J. Das** and K. S. Narayan, Dynamics, NIR response and Improved device lifetime of organic solar cells by melt-phase vacuum-free fabrication utilizing alloy based cathode materials. INDO-UK APEX Meeting, January 2012, Bangalore.

5. **Anshuman J. Das** and K. S. Narayan. Observation of Bessel Beams from Electric-Field Induced Patterns on Polymer Surfaces. Fifth JNCASR Research Conference on Chemistry of Materials. October 2009. Alleppey, Kerala.

News related to our research:

Enhancement of efficiencies in large area organic solar cells,
By Anshuman J. Das, and K. S. Narayan, Appeared in *Printed Electronics World.*

What if Umbrellas Could Generate Solar Power? Appeared in *Forbes India*.

Synopsis

Organic photovoltaics constitute an important research topic that is being pursued by several research groups aiming to achieve a cost-effective energy solution. In order to attain performances comparable to that of silicon based solar cells, several issues need to be addressed both from device physics and processing perspective. The thesis addresses two major themes in organic solar cells research, namely, the area-scaling and stability. The device architecture and design of organic solar cells (OSC) permits incorporation of light management strategies that improve device performance to overcome certain drawbacks of active materials.

The first part of the thesis addresses the *area-scaling* issue which has been a major hurdle in OSCs due to the finite sheet resistances of the transparent and metal electrodes. Loss of voltage due to these resistances causes a drop in critical device parameters like the short-circuit current density and fill factor. Designs are proposed that retain efficiency of OSC as the area is scaled up. The concept of fabricating several small area devices that are electrically connected seems to be a solution. In this regard a novel fabrication protocol is established which utilizes low melting alloys as electrode materials in organic solar cells. These alloys can be manipulated or printed in small dimensions and the entire process along with the alloy is cost-effective. Studies were carried out to optimize the shape, size and spacing of the electrodes. The spacing between the electrodes was dictated by the decay length of the polymer blend (~ 50 μm). The decay length represents the region in the vicinity of an electrode at which there is a substantial lateral photocurrent collection. The size or area of the pixels was optimized at $1mm^2$. From an optical trapping perspective, the optimum shape of the electrodes is determined. For the same area, considering simple geometric shapes, triangular pixels have the largest perimeter as compared to squares or circles. Designs that incorporated patterns in accordance with the above considerations minimized series resistance losses and lead to efficient devices over large areas.

The next part of the thesis addresses light management strategies for efficiency enhancement. Even though patterning minimizes series resistance it leaves gaps in the device structure resulting in lower currents. Additionally, most donor-acceptor polymers exhibit low

absorption regions in the blue-green regions of the solar spectrum. This feature is partially compensated by the incorporating acceptor molecules. Nevertheless, a region of low absorption exists in the external quantum efficiency. In this regard, we demonstrate that introducing a suitable dye in the spaces between the patterned electrodes can enhance the device efficiency. The dye is chosen such that it absorbs in the low-absorption regions of the polymer and emits in the high-absorption region of the polymer. This process of down-conversion ensured that unabsorbed light was efficiently converted to useful light and also channeled back to the active material, resulting in enhanced efficiency.

Another light harvesting strategy is the utilization of microlenses to concentrate light. Microlens arrays were fabricated in a facile manner over large areas by soft lithography methods. An applied electric field was utilized to bring about an electro-hydro-dynamic instability in visco-elastic films of polydimethyl siloxane (PDMS). A thin film of PDMS has been observed to self organize in columnar structures under the influence of an electric field. We probed the columnar structures for uniformity of cross-section and found that they possessed non-cylindrical profiles akin to that of pedestals. This fact was utilized to fabricate microlenses during the formation of the instabilities and freeze the shape and size of the microlenses using thermal treatment. Lenses with non-spherical profiles were observed which had the ability to transform an incoming Gaussian beam to a Bessel beam. These beams had large depth-of-focus and hence can be utilized in concentrating solar energy with larger tolerances in alignment.

In the next part, optical characteristics of three-dimensional microlasers were studied. Organic fibre lasers were fabricated with non-cylindrical cross-sections. These cavities were investigated for size-dependent lasing and the nature of optical modes. From guiding and polarization dependent lasing studies it was concluded that the lasing modes had a three-dimensional quantized path. The lasers had low lasing thresholds and moderately high Q-factors.

The final section of the thesis addresses the *stability* issue in OSC. Device aging was studied by monitoring changes in the current, voltage and fill factor as a function of time. The polymer blend was found to be stable in the time frame of the measurements. The polymer-electrode interface turned out to be the limiting factor due to the highest rate of degradation. Alloy electrodes, in this regard, improve device lifetimes considerably. It was

observed that devices with solvent additives exhibited higher efficiency but their lifetimes were lower as compared to devices without the additive. Capacitance-voltage measurements revealed that an excess concentration of the acceptor molecules on the surface modified the metal-semiconductor interface. This modification is in the form of a reaction that begins at the edge of the electrode and permeates inward. This process eventually slowed down and is reflected as a saturation of the efficiency along with disappearance of a pseudo-inductive or a negative capacitance effect. Noise measurements were also carried out to probe the formation of defects as the device degraded. Photocurrent noise was amplified and Fourier transform was carried out on the data after suppressing the DC component. The noise spectrum had a characteristic $1/f^{\delta}$ feature at low frequencies and a log-normal high frequency distribution. The exponent δ was found to oscillate until the efficiency of the device reached saturation. We propose that edge-sealing, non-fullerene acceptors and metal alloys with superior thermal properties can enhance the stability of OSCs.

Table of Contents

List of Figures

Notations/Abbreviations

Abbreviations	Details
2D	Two dimensional
3D	Three dimensional
BHJ	Bulk-heterojunction
C-V	Capacitance-voltage
D-A	Donor-Acceptor
EQE	External quantum efficiency
FF	Fill factor
HOMO	Highest occupied molecular orbital
I-V	Current-voltage
LUMO	Lowest unoccupied molecular orbital
NC	Negative capacitance
OSC	Organic solar cell
OSC	Organic solar sell
PCE	Power conversion efficiency

Chapter1
Introduction

"I have no doubt that we will be successful in harnessing the sun's energy. If sunbeams were weapons of war, we would have had solar energy centuries ago."

-George Porter, Nobel Prize winner in Chemistry, 1967

In the present times when energy needs have multiplied, it is essential to explore alternative sources of energy. Non-renewable energy sources like natural gas, petroleum and coal account for a major share in the total energy consumption. But a sustainable energy solution cannot be achieved from such sources. Renewable sources like the wind and sun need to become the answers to the energy needs. The energy emitted from sun in a single year is several exajuoles (10^{18} Joules), which can sufficiently bridge this energy deficit. Unfortunately, a majority of this energy goes unutilized. Hence there is a need to investigate this imbalance so as to facilitate efficient utilization and storage of this form of energy. In this regard solar cells have increasingly become a feasible option to tackle the energy crisis.

At the heart of a solar cell is a material that absorbs solar light and gives out electrons that can lead to a current. The most commonly used material for solar cells is silicon which is generally doped with n-type or p-type impurities. Even though silicon solar cells are a matured technology today, they are expensive and hence inaccessible to a large fraction of the society. The processes involved in growing crystals of silicon and manufacturing modules is sophisticated, time and energy consuming. Nevertheless, high efficiencies have been observed for silicon solar cells which make them attractive materials for energy applications. It would be worthwhile mentioning the power conversion limits of solar cells in this context. The widely accepted theoretical limit was proposed by William Shockley and Hans J. Queisser in 1961, a fundamental theoretical work which is considered to be one of the most important contributions to solar energy production. They showed on the basis of the second law of thermodynamics, the existence of a theoretical limit for a single p-n junction solar cell, known as Shockley-

Queisser (S-Q) limit or the detailed balance limit [1]. This theory was modified by C. Henry in 1980 along the following directions a) a graphical analysis method was proposed to show the magnitudes of the intrinsic losses, b) both single and multiple energy gap cells were considered, c) an actual terrestrial solar spectrum (AM 1.5) was considered instead of a blackbody radiation spectrum, d) effect of concentrated sunlight was also taken into account, and e) it was discussed why the efficiency of ideal cells falls below this limit [2]. It was estimated that the maximum efficiency of a single junction p-n solar cell is 31% under 1 sun illumination.

1.1 Shockley-Queisser Limit and Detailed balance

A photovoltaic device is a device that absorbs some fraction of the incident solar radiation and converts it to electrical power. Absorption of a photon creates an electron-hole pair which can either separate to give free charges or recombine. The electron-hole pair can recombine either radiatively emitting another photon or non-radiatively as heat. Radiative recombination leads to photon emission which can either be reabsorbed or exit the cell. This is a loss process and is an unavoidable consequence of detailed balance. On the other hand, non-radiative recombination can be reduced by using high quality trap-free materials.

Radiative recombination turns out to be an unavoidable consequence of this theory and it can be understood by the following explanation. Considering the total current generated by the solar cell under the assumption that there are no non-radiative processes or other losses, $I_{tot}=q$(absorbed photons-emitted photons), where q is the electronic charge. At the open circuit, the net current in the circuit is zero. Since the cell is under continuous illumination, the rate of absorption must equal the emission rate. This implies that the cell must emit radiation.

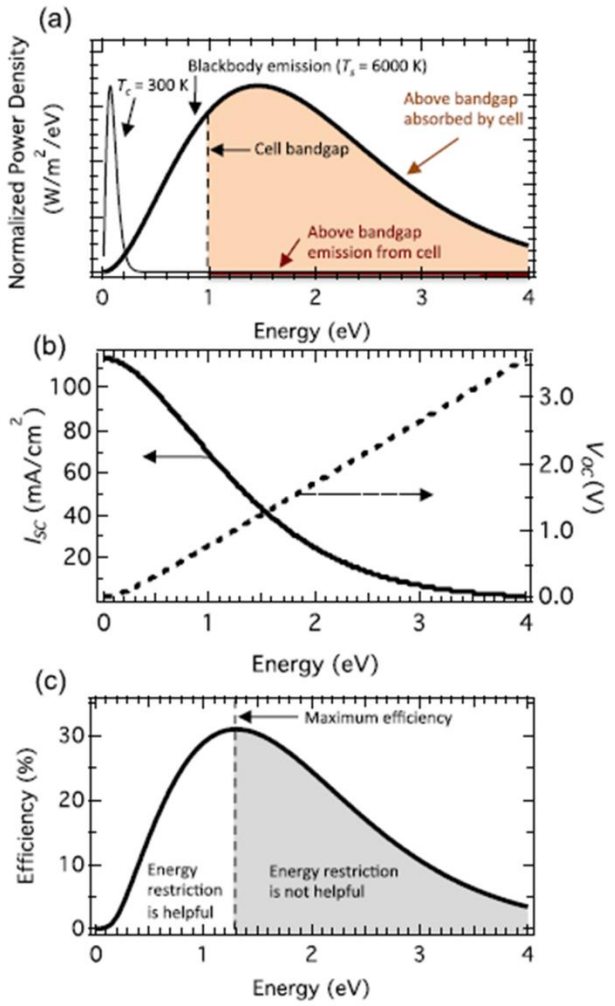

Figure 1.1: *(a) Spectral power density showing absorption above the band-gap and emission from a solar cell at T_c=300 K. (b) Variation of short circuit current and open circuit voltage with semiconductor band-gap energy. (c) As a result of tradeoff between current and voltage, the maximum theoretical efficiency occurs at about 1.3 eV. (Reprinted with permission from J. N. Munday, The effect of photonic bandgap materials on the Shockley-Queisser limit. Journal of Applied Physics 2012, 112. ©2012, American Institute of Physics).*

If the illumination is treated as a blackbody, the spectral photon flux is given by Planck's law in the form,

$$F_s = \frac{2n^2}{h^3c^2}\frac{E^2}{e^{E/K_bT_s}-1} \quad \text{..... (1.1)}$$

where, h is the Planck constant, k_B is the Boltzmann constant, c is the speed of light, n is the refractive index surrounding material and T_s is the source temperature. Normalized power density of a blackbody emitter is shown in Figure 1.1(a) where the temperature T_s = 6000 K (black line).

The shaded region in Figure 1.1(a) represents the above band-gap absorption of the cell which can lead to photocurrent generation. When the cell is maintained at dark conditions (non-illuminated), it remains in thermodynamic equilibrium with its surroundings. In other words, it behaves like a blackbody at the ambient cell temperature $T = T_c$ with resembling absorption and emission profiles. Dominant contribution to emission can be assumed to arise from excited carrier recombination, which occurs for wavelengths above the semiconductor band-gap energy, as shown in Figure 1.1(a).

When the cell is illuminated it deviates from thermal equilibrium condition with respect to its surroundings. The Fermi level splits by qV due to the presence of additional charge carrier separation. This splitting results in an increased photon flux out of the cell given by the expression,

$$F_c = \frac{2n^2}{h^3c^2}\frac{E^2}{e^{(E-qV)/K_bT_c}-1} \quad \text{.....(1.2)}$$

The total emission rate is then given by the integral,

$$\int_{E,\Omega,A} e(E)F_c(V)cos\theta dE d\Omega dA \text{.....(1.3)}$$

where, e(E) is the emissivity (probability of a photon emission of energy E), A is the area, Ω is the solid angle.

The total current in the device is given by difference between the current generated due to absorption of photons and the emission loss (Eq. 1.3) at a given voltage,

$$I_{tot} = I_L - I_0 \left[exp\left(-\frac{qV}{k_B T_c}\right) - 1\right] \quad \text{.....(1.4)}$$

The efficiency (η) is proportional to the product of the current and voltage, $\eta \alpha I_{sc} V_{oc}$, where I_{sc} is the short-circuit current and V_{oc} is the open-circuit voltage. The current voltage relationship from the device can be evaluated from Eq. (1.4) by imposing conditions like V=0 and $V=V_{oc}$. It turns out that $V_{oc} \alpha E_g$ (band gap) and $I_{sc} \alpha 1/E_g$ leading to a tradeoff between the current and the open circuit voltage. Lower band-gaps lead to larger currents but the open circuit voltage decreases due to increased emission as shown in Figure 1.1(b). Considering a single junction with impedance matching, the theoretical limit for maximum efficiency turns out to be 30% for a band-gap of 1.28 eV at T_c=300 K as shown in Figure 1.1(c). Hence, there is a need to implement strategies like tandem or multi-junction cells, multiple excitonic systems and photonic crystal based solar cells to beat the 30% limit [3].

1.2 Generations of Solar Cells

From a historical point of view, considering the progress in solar cells, there has been a classification based on the type of materials, the process of charge generation and the various device geometries. Earlier generations of solar cells have matured to a commercial technology today whereas the newer generations are on the verge of commercialization.

1.2.1 First Generation Solar Cells

Solar cells are traditionally made from silicon which comprises about 80% of the total commercial panels all over the world. Though other solar cells made out of competing materials like GaAs have shown higher efficiencies, silicon solar cells remain the most popular solar cells available for residential use. These devices have superior stability and are long lasting than most other non-silicon based cells. The classification of

first generation solar cells is based on the type of silicon that is used to make the modules.

1.2.1.1 Mono-crystalline Silicon Cells

This is the oldest and most popular solar cell technology today fabricated from thin wafers of silicon. As the name suggests, they are mono-crystalline and the cells are sliced from large single crystals [4-8]. The process of growing single crystals over large area is extremely complicated and requires the process to be carried out in controlled conditions. Typically, the cells dimensions are a few inches, and multiple cells are connected to create a grid or a panel. Even though the efficiency is high, growing large crystals of pure silicon is a very energy-intensive process, which makes the production cost the highest among other silicon solar cell technologies.

1.2.1.2 Polycrystalline Silicon Cells

These solar cells are made from polycrystalline silicon which is easier to grow and hence reduces the cost [9-11]. The growth conditions can be relaxed as compared to the mono-crystalline devices. In this technology, a number of silicon crystals grow together and can assume multiple crystalline properties. Panels made out of polycrystalline silicon turn out to be cheaper than single crystal silicon but the efficiency is not as high as mono-crystalline solar cells.

1.2.1.3 Amorphous Silicon Cells

Amorphous silicon need not be grown like crystalline silicon; it can instead be deposited as a very thin layer on to a substrate like metal, glass or plastic [12-13]. Though the production methods are complex, they are less energy intensive than crystalline technologies and the costs have reduced as the mass production has gone up. These devices can be coated on conformal substrates and can be made flexible too [14]. They are much less efficient as compared to their crystalline counterparts and are generally suitable for small electronic devices such as mobile phones and calculators.

Their flexibility makes them an excellent choice in building integration and for use on curved surfaces.

1.2.1.4 Hybrid Silicon Cells

In the recent years, a new technology that combines the advantages of the various silicon solar cell technologies has emerged [15]. Several researchers as well as companies have begun exploring techniques to combine different materials to improve solar cell characteristics like efficiency, life time, and at the same time reduce costs. In 2011, Sanyo announced a hybrid HIT Power® 225A solar module with single cell conversion efficiencies of 20.2% and module efficiencies of 17.8%. Highly efficient monocrystalline silicon was sandwiched between the amorphous-Si leading to superior conversion efficiency as well as excellent temperature stability.

1.2.2 Second Generation Solar Cells

Thin-film solar cells constitute this category of photovoltaic technology. These devices are made of semiconductor layer ranging from several hundreds of nanometers to a few microns thick in contrast to crystalline silicon based cells which can be several hundred microns thick. Since the usage of active material is drastically reduced it is envisioned that the cost of panels could be lowered as compared to silicon technologies. Three types of solar cells fall into this category -amorphous silicon that overlaps with the first generation solar cells, and two non-silicon based solar cells namely cadmium telluride (CdTe) [16-21], and copper indium gallium selenide ($CuIn_{1-x}Ga_xSe_2$ or CIGS) [22-23]. These solar cells are an appealing alternative as they are inexpensive with production costs aimed at under $0.7/watt. Even though efficiencies of above 20% have been demonstrated, it turns out to be difficult to produce CIGS solar cells in large quantities at prices competitive with silicon solar cells for similar efficiencies.

1.2.3 Third Generation Solar Cells

Third-generation solar cells constitute a large fraction of the current solar cell research around the world. This generation is the recent most generation of solar cells and is based on new materials like nano-materials, quantum-dots [24-25], organic dyes sensitized solar cells [26-29], and conductive plastics [30-31]. Research in this generation is aimed at improving the current technology by utilizing novel materials that absorb efficiently over a wider band of solar energy as compared to silicon. Materials can be designed to absorb in the infrared to harvest additional light, their processing methods are

generally inexpensive and hence can be made into a less expensive technology. However, most of the research on third generation solar cells is limited to the laboratory, with a few companies attempting commercial modules with reasonable success.

Figure 1.2 presents a complete chart of efficiencies of different photovoltaic systems in a chronological manner. As can be seen the third generation solar cells are at the bottom but steadily climbing to pose a serious competition to the second generation counterparts.

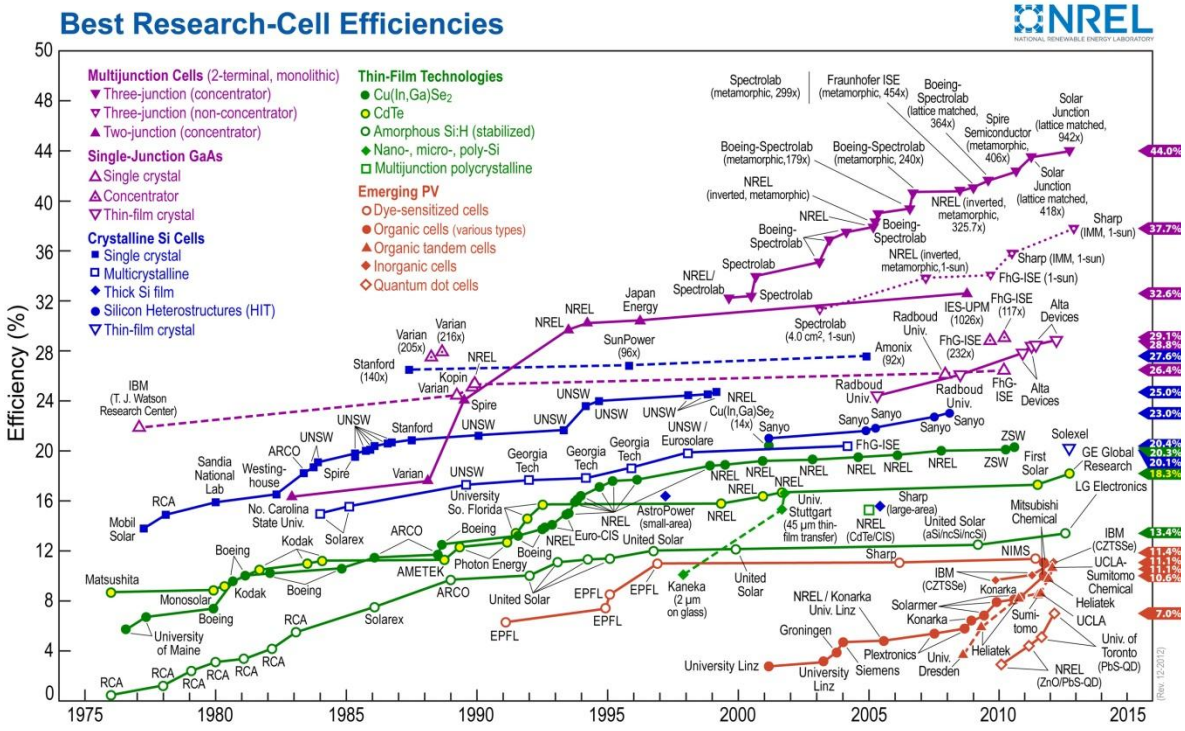

Figure 1.2: *Chart depicting record efficiencies of different types of solar cells. (Courtesy NREL)*

1.3 Overcoming the S-Q Limit

Currently tandem solar cells hold the record for the highest efficiency in a photovoltaic technology scaling over the 44% mark. Even though the theoretical limit is posed at around 30%, it holds good for a single junction. Multi-junction or tandem solar cells incorporate two or more cells that have complementary absorption spectra and can absorb light in the complete solar spectrum. There have been successful attempts by many companies and laboratories that surpassed the 40% mark [32]. But there is another research theme that has emerged in the recent times aiming at overcoming the S-Q limit either by engineering materials or implementing photonic designs that assist in surpassing the theoretical limit for a single junction device. Some of the strategies are mentioned in the following section.

1.3.1 Multiple exciton generation

The concept of multiple exciton generation (MEG) has been extensively studied by several research groups over the last few years. Semiconductor nanocrystals or quantum dots (QDs) possess tunable optical properties and serve as ideal platforms for MEG [33-38]. The mechanism of MEG is shown in Figure 1.3, where the absorption of a photon of sufficiently high energy by a QD, leads to the formation of an electron-hole (e-h) pair or an exciton. Excitons are confined in these semiconductors and differ from excitons in bulk semiconductors. Excitons in confined regions of space interact with the coulomb potential, in contrast to bulk semiconductors, where excitons exist only if k_BT is lower than the exciton binding energy. If the incident photon has an energy greater than the band-gap (E_g) of the material, it can be absorbed by higher energy states to produce a "hot exciton" with an excess energy, $\Delta E_{ex} = hv\text{-}E_g$. Under the condition $\Delta E_{ex} > E_g$ $(hv > 2E_g)$, this excess energy can be converted into kinetic energy leading to the generation of additional e-h pairs for a single incident photon.

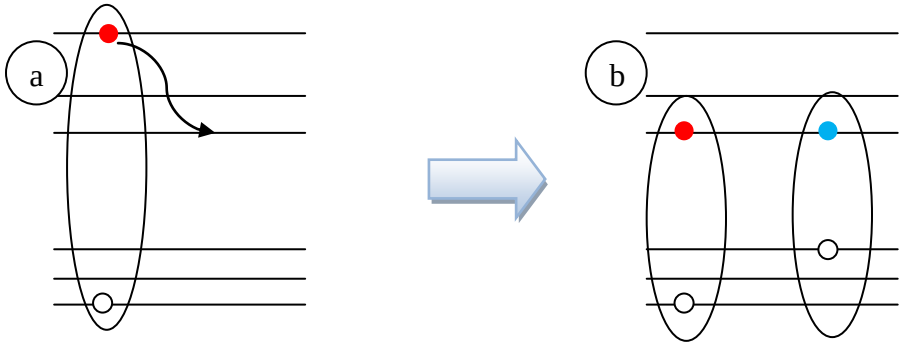

Figure 1.3: *Mechanism of multiple exciton generation. (a)Generation of a singlet exciton with hot carriers. The hot electron loses energy and approached the band edge. (b) The excess energy is used to excite another exciton.*

This process is called impact ionization, where additional energy of the photon can excite another e-h pair. In bulk semiconductors, the likelihood of that hot carriers undergoing impact ionization is reduced due to a) limited density of final states and b) rapid hot carrier cooling via phonon emission. Hence, impact ionization does not produce multiple e-h pairs even for $hv >$ (4-5) E_g. In QDs, fundamental limits are set by energy conservation alone long-range repeating atomic potentials are absent. Hot-carrier relaxation can be controlled in QDs to make MEG process efficient. Recent reports demonstrated that external quantum efficiencies of over 100% leading to the realization of MEG in these systems [39].

1.3.2 Singlet exciton fission

Singlet fission is another process to realize MEG where a singlet exciton leads to the formation two triplet excitons, which can be further dissociated to produce charge carriers [34, 38, 40-41]. This process is analogous to internal conversion or a radiation-less transition between two electronic states of equal multiplicity. This transition can be a very fast process and if the coupling is favorable, it can occur on a picosecond time scale, and can out-compete fluorescence.

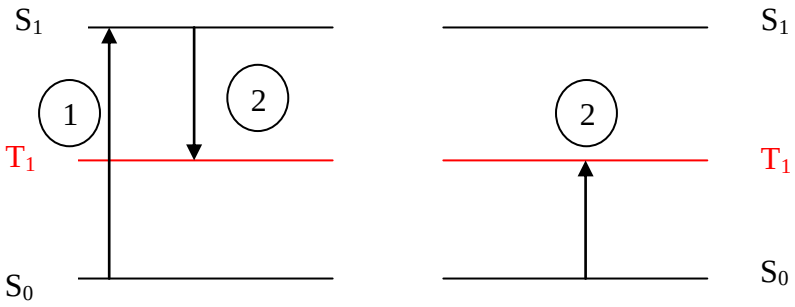

Figure 1.4: *Mechanism of singlet fission.*

The implications of such a process are useful in the field of photovoltaic technology. Quantitative analysis for incorporating singlet fission sensitizer results in a theoretical limit of 50% as compared to the Shockley- Queisser limit of about 33%. Hence the process of generation of two triplets resulting from the absorption of a sufficiently energetic single photon can improve device performance drastically. As shown in Figure 1.4, the absorption of a single photon creates a singlet exciton, depicted by the S_0-S_1 transition. The energy of this singlet can be transferred to a triplet via S_1-T_1 provided there is sufficient coupling. The remaining energy of the singlet exciton can excite another triplet giving rise to two triplets for one photon. Singlet fission has been observed in materials like tetracene and copper phthalocyanine. Tetracene absorbs wavelengths lower than 550 nm and generates two triplets at an energy of 1.2 eV. These triplets can diffuse through a CuPC layer which has a triplet level at 1.1 eV and can be subsequently dissociated at an appropriate interface. Hence, a photocurrent conversion efficiency of about 200% can be achieved at certain wavelengths in the absorption spectrum [38].

1.3.3 Photonic crystals

Another method to overcome the S-Q limit is by using photonic crystals to capture emitted light and re-direct it back to cause further excitations [3]. Placing a photonic crystal (PC) on top of the solar cell modifies the absorption and emission (Figure 1.5 (a-b)). If the photonic crystal is selected with a band-gap that extends from the semiconductor band-gap energy E_g to the photonic band-gap E_{pc}, photons in this range of energies will be reflected and cannot reach the cell. Similarly, photons are emitted as a result of radiative recombination with energy greater than E_g. Furthermore, only photons with energy greater than E_{pc} can escape the cell. Photons with intermediate energies in between E_g and E_{pc}, will be reflected by the PC and will be absorbed and re-emitted continuously –a process called photon recycling at the open circuit. This process leads to a high concentration of separated charge carriers and an increased open circuit voltage. Increased carrier concentrations can lead to an increase in the quasi-Fermi level splitting within the cell. In the case of a typical solar cell, the quasi-Fermi level for the electrons lies within E_g (Figure. 1.6(a)).

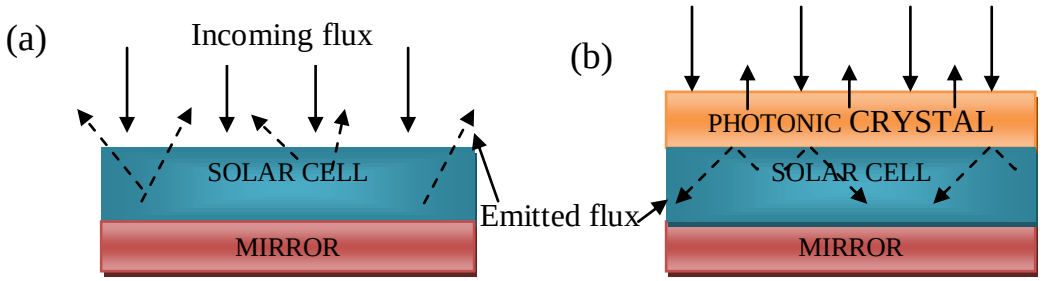

Figure 1.5: *Emission profiles for a) conventional solar cell and b) solar cell with a photonic crystal.*

If the cell is sandwiched in between a mirror and a suitable photonic crystal, the emitted photons cannot escape the device (Figure 1.6 (b-c)). This leads to a high photon flux within the cell, which leads to increased carrier concentration. Though for an ideal photonic crystal the quasi-Fermi level can shift into the conduction band due to the excess carrier concentration, for the non-ideal case there is light leakage and loss in the open circuit voltage.

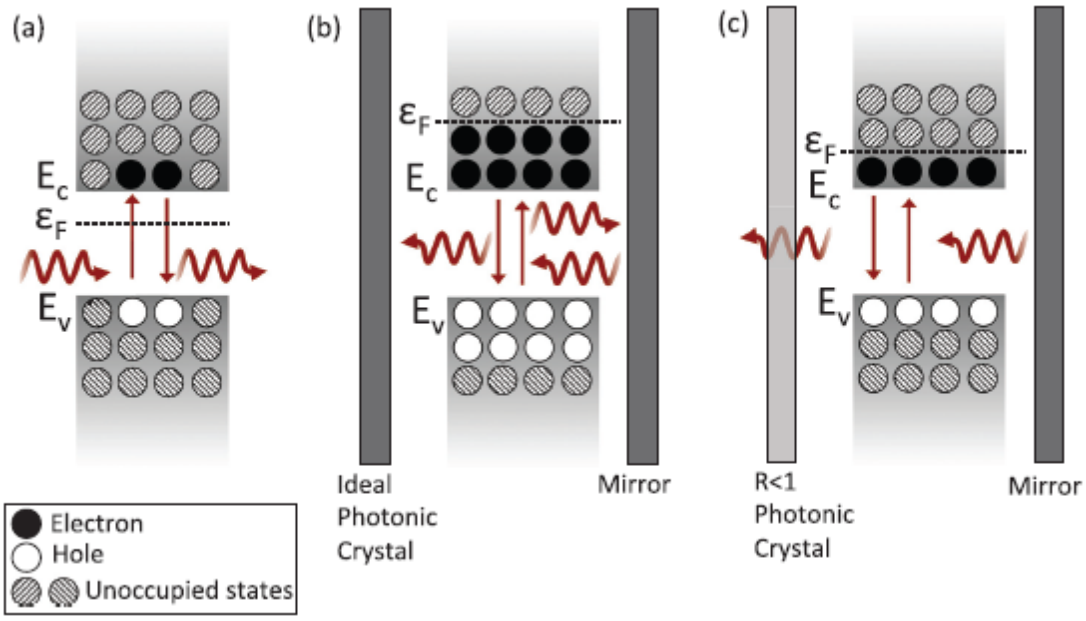

Figure 1.6: *Mechanism to overcome S-Q limit by incorporating a photonic crystal and a reflective mirror. Occupancy of conduction and valence bands for (a)conventional solar cell, (b) solar cell sandwiched in between and mirror and an ideal photonic crystal and (c) solar cell with a non-ideal photonic crystal and a mirror (Reprinted with permission from J. N. Munday, The effect of photonic bandgap materials on the Shockley-Queisser limit. Journal of Applied Physics 2012, 112. ©2012, American Institute of Physics).*

1.4 Solar Concentrators

The key driving factor in solar cell research and development today is to increase efficiency while maintaining the minimal cost of production. Third Generation PVs aim at a better utilization of the complete solar spectrum in order to get the maximum efficiency for a particular system. Some examples include intermediate band-gap cells [42], quantum dot based concentrators [43-46] and up/down-converters [47-48]. Conversion of the incident solar spectrum into a precisely matched spectrum of the absorber can significantly increase the efficiency of solar cells. One such example is down conversion and the technology is referred to as luminescent solar concentrators (LSC) [49-54]. A LSC essentially consists of a highly transparent plastic matrix, in which luminescent materials like organic dye molecules are dispersed, as shown in Figure 1.7. Upon illumination, these dyes absorb and re-emit at a red-shifted wavelength, often with very high quantum efficiency. Since the refractive index of the plastic is higher than its surroundings, total internal reflection ensures that much of this light reaches the solar cell placed at the sides of the plastic matrix. LSCs can capture light that is direct or diffuse and concentrate them sufficiently, eliminating the need for solar tracking, thereby minimizing costs. Furthermore, they can be applied to any solar cell technology-from silicon to organic materials.

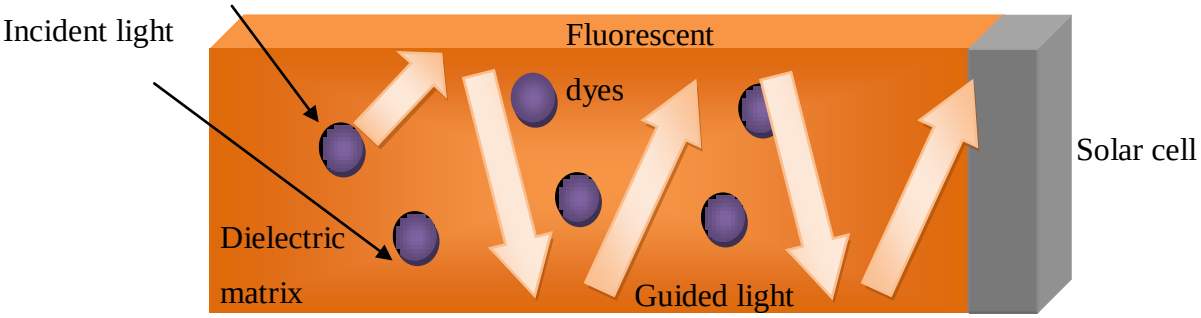

Figure 1.7: *Schematic of functioning of a luminescent solar concentrator.*

Fluorescent materials in the LSC need not be limited by organic dyes alone. Many organic dyes are prone to oxidation and other degradation mechanisms that limit their lifetime. Quantum dots have been a promising alternative with superior stability and comparable optical properties. QDs offer a wide range of tunability and can be easily embedded in plastics.

1.5 Losses in solar cells

In general, solar cells do not operate at the theoretical limits of the efficiency. This is due to the presence of several losses of photons and charge carriers [55-58]. There are five intrinsic loss mechanisms apart from a host of other extrinsic losses like Fresnel reflection and non-ideal back reflectors [57]. Intrinsic losses cause a reduction in current or voltage, modifying current–voltage characteristics. These losses are i) Carnot loss- there is always an energy penalty incurred when thermal energy from the Sun is converted to electrical work leading to a voltage drop. ii) Boltzmann loss- caused by increased entropy as a result of a mismatch between absorption and emission angles. This loss mechanism can be described by Boltzmann's equation and can be minimized for devices with restricted emission angles. iii) Thermalization loss- causes as a result of strong interaction of excited charge carriers and lattice phonons. This loss can be minimized in multi-junction or hot carrier solar cells. iv) Emission loss-caused by charge recombination leading to emission. Emission of light from the cell is an indication that the excited charges were not collected at electrodes leading to the lowering of current; v) Band-gap loss- caused by the limited band-gap of the device. Photons with energies lower than the band-gap are not absorbed leading to a loss in current. Major loss mechanisms in solar cells are summarized in Figure 1.8.

Below E_g	$\int_0^{E_g} E \cdot n(E, T_S, 0, \Omega_{abs})\, dE \approx \Omega_{abs}\left(\chi(0, T_S) - \exp\left(-\frac{E_g}{kT_S}\right)\chi(E_g, T_S)\right)$
Thermalisation loss	$\int_{E_g}^{\infty} E \cdot n(E, T_S, 0, \Omega_{abs})\, dE - E_g \int_{E_g}^{\infty} n(E, T_S, 0, \Omega_{abs})\, dE \approx \Omega_{abs} \exp\left(-\frac{E_g}{kT_S}\right)\left(\chi(E_g, T_S) - E_g \cdot \gamma(E_g, T_S)\right)$
Emission loss	$E_g \int_{E_g}^{\infty} n(E, T_A, eV_{opt}, \Omega_{emit})\, dE \approx \Omega_{emit} E_g \gamma(E_g, T_A) \exp\left(\frac{eV_{opt} - E_g}{kT_A}\right)$
Boltzmann loss	$kT_A \ln\left(\frac{\Omega_{emit}}{\Omega_{abs}}\right) J_{opt}$
Carnot loss	$E_g\left(\frac{T_A}{T_S}\right) J_{opt}$
Power out	$J_{opt} V_{opt}$

Figure 1.8: *Expressions for different losses in solar cells (Reprinted with permission from L. C. Hirst, N. J. Ekins-Daukes, Fundamental losses in solar cells. Progress in Photovoltaics 2011, 19, 286. ©2011, John Wiley and Sons).*

Hence, these intrinsic loss mechanisms appear as a cumulative effect leading to fundamental limits in efficiency. These losses need to be quantified and their contribution to the limit needs to be addressed. Better materials with the appropriate band-gaps and absorption matching with that of the solar spectrum along with photonic designs can be envisaged to overcome these losses.

1.6 Modules

A single solar cell, even if very efficient, is not capable generating sufficient power to drive anything useful. Hence many such cells need to be electrically connected so that their voltages or currents add up to provide useful power. Such an arrangement is called a module as shown in Figure 1.9. A PV module consists of an array of individual solar cells connected in series in order to deliver a certain power or voltage [59-62]. Commonly, the voltage of a PV module is chosen so as to be compatible with a 12 V DC battery. Typically, solar cells generate a photo-voltage of 0.6-0.8 V under 1 sun AM1.5 illumination. Hence at least 18-36 cells need to be connected in series to generate 6-12 V considering that the operating voltage is always lower than the open circuit voltage.

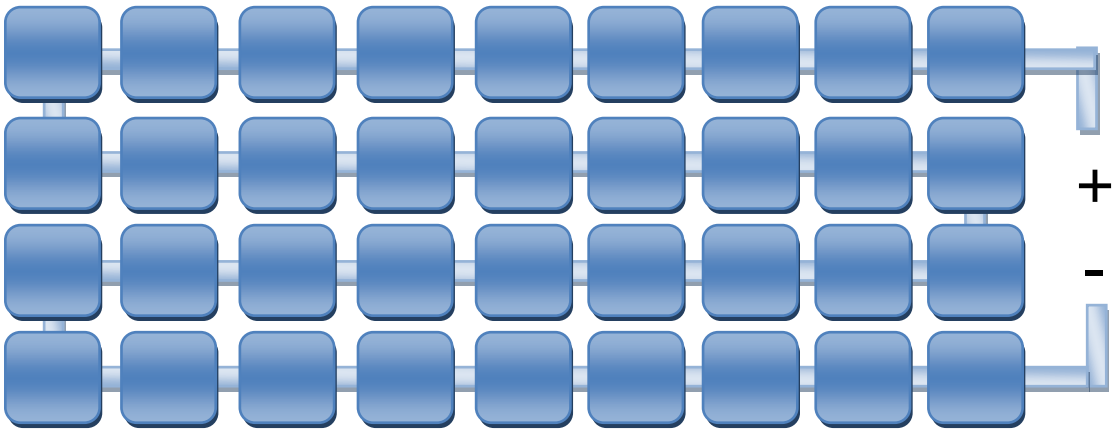

Figure 1.9: *Typical 36-cell module architecture that delivers a voltage of 12 V and currents ranging from 3-4 A.*

While the number of cells in series determines the voltage of the PV module, the current is dependent on the area or size of the solar cells and efficiency of each cell. e.g. at AM1.5 illumination, a commercial solar cell delivers a current density of about 36 mA/cm^2. Hence they can deliver the short-circuit current in the range of 3-4 A.

1.6.1 Module optimization

A single cell needs to be optimally connected to construct a module and several modules need to be connected to give rise to a grid or a system [63-64]. Hence there are optimizations and computer aided designs (CAD) necessary to minimize losses and maximize power delivery to the load.

Cell Level: Design criteria

- Maximizing efficiency
- Optimizing contacts, junctions, anti-reflective coatings

Module Level: Design criteria

- Interconnect optimization

System Level: Design criteria

- Optimize performance taking into account tilt of sun etc.
- Maximize delivered power to the grid, inverter system impedance matching etc.

1.7 Organic solar cells

Organic solar cells (OSC) are classified in to the third generation solar cells as mentioned earlier. Even though moderate efficiencies have been achieved, advantages like solution processing and ability to be printed on large, flexible substrates make them an attractive cost-effective approach [65-71]. Active materials can be synthesized using synthetic chemistry methods in contrast to growing crystals in the case of silicon solar cells. As a result, the energy required to fabricate these cells is very low as compared to crystalline solar cell technologies. Low input energy implies low fabrication and processing cost. Hence, organic solar cells can be printed over large areas to create low cost modules for a range of applications.

Electrical transport in organic semiconductors is very different from other inorganic semiconductors. Charge carrier mobilities are limited due to presence of traps and inherent disorder. Conductivity in organic materials arises due to an extended π-conjugation of the carbon backbone leading to a delocalized electron cloud [72]. It turns out that a one-dimensional polymer chain with non-bonding electrons at each site is unstable referred to as the Peierls instability. Hence an alternating single and double bonded chain is favoured and found in most conjugated polymeric semi-conductors. This distortion leads to the opening up of gaps in the energy referred to as the highest occupied molecular orbital (HOMO) and lowest unoccupied molecular orbital (LUMO). These levels are analogous to the valence and conduction band in inorganic crystalline semiconductors. These energy states can be modified by controlling the extent of conjugation or addition of electron withdrawing or donating groups to the backbone. In most cases it can be done with ease with a variety of synthetic procedures. Recent breakthroughs in materials like donor-acceptor (D-A) polymers have enabled low-band gap, high efficiency solar cells [73-74]. The ease with which optical properties can be

tuned along with solution processing and advantages of roll-to-roll processing makes these materials a promising alternative for photovoltaic technology [68, 75-77].

OSCs are further classified based on the device geometry. First generation OSC were fabricated by sandwiching a semiconducting organic layer in between two metal electrodes of suitable work functions as shown in Figure 1.10 (a) [78]. These devices were very inefficient and the power conversion efficiencies were in the range of 10^{-3} to 10^{-1} with low open-circuit voltage. Second generation OSC were bi-layer devices consisting of a donor and acceptor layer in contact as shown in Figure 1.10 (b). These devices are generally fabricated by vacuum deposition of the donor and acceptor layers sequentially. Thought the efficiencies were low initially, currently devices have been demonstrated with higher conversion efficiency.

The third generation and by far the most popular geometry is the bulk heterojunction polymer solar cell (BHJ). In this geometry a certain suitable ratio of the donor and acceptor was mixed in a common solvent and spin cast on the substrate resulting in an intermixed network as shown in Figure 1.10 (b) [31, 74]. Under optimum processing conditions, BHJ devices are capable of PCE approaching 10%. Fine mixing of the donor and acceptor materials leads to a phase separated morphology with percolation pathways. This enables the photo-excited charge carriers to be collected at their respective electrodes. Morphology of the heterojunction plays a very crucial role in determining the efficiency of the device. Processing parameters like the choice of solvent, thermal annealing and the usage of additives have been useful in arriving at the optimum morphology and also better performance of the solar cells. Optimum morphology ensures that dissociation of bound electron–hole pairs or excitons is efficient at interfaces leading to better charge collection [31, 79]. In this regard there have been numerous attempts to control the morphology via templating using block co-polymer, self assembly, porous materials and self organization of nano-particles. Efficiency of 9.2% has been achieved with the use of additives in BHJ solar cells [80]. Hence it is imperative to understand and explore the basis of charge transport and opto-electronic properties of the individual materials and mixtures and their impact on the BHJ device performance.

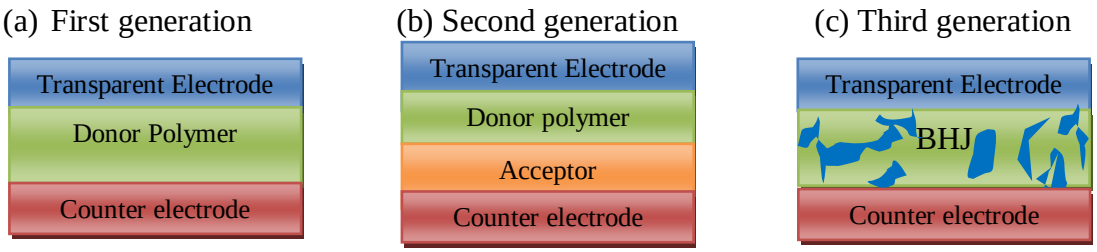

Figure 1.10: *Generations of organic solar cells.*

1.7.1 Semiconducting polymers

Conjugated polymers are anisotropic, quasi-one-dimensional materials where a resonant interaction π electrons results in a delocalization of the electronic states. As a result of conjugation, *p* orbitals split in energy into two levels (or bands in molecular materials): bonding orbital (π), and anti-bonding orbital (π*), with low and high energy, respectively. In the absence of an excitation, the π orbitals are occupied as they are low energy states. Hence the π orbital is termed as the highest occupied molecular orbital (HOMO) and the π* orbitals is termed as lowest unoccupied molecular orbital (LUMO). In materials with larger extent of conjugation, these levels are broadened into bands. Since the HOMO and the LUMO constitute a band-gap like feature they are analogous to valence band and the conduction band, in inorganic semiconductors. Upon photo-excitation several excitations occur in the polymer chains like solitons, polarons, or bipolarons, depending on the degeneracy of the ground-state [81-82]. If the ground state is degenerate, like in the case of trans- polyacetylene, solitons are the primary excitations. In the case of non-degenerate systems, like polypyrrole and polythiophene, polarons and bipolarons are responsible for charge transport. Such non-linear excitations form the basis of photo-physics in these materials. Depending on the strength of the electron-electron interactions and the electron-phonon interactions, these elementary excitations manifest as mobile charge carriers (charged polarons) or bound electron-hole pairs such as excitons.

1.7.2 Theory of transport in organic materials

In amorphous semiconducting polymers charge transport is governed by inherent structural and energetic disorders. Positional disorders and fluctuations in local conjugation length are the major source of energetic disorder [29]. Unlike crystalline semiconductors the transport in amorphous polymers is via a hopping mechanism. Charges carriers hop from site to site of different energy determined by a probability that minimizes the total energy. The density of state (DOS) is distributed about the HOMO and LUMO levels in organic semiconductors and can be represented by a Gaussian distribution [83-85]. The DOS is given by:

$$DOS(E) = \frac{N_V}{\sqrt{2\pi}.\sigma} exp\left[-\left(\frac{E-E_0}{\sqrt{2\pi}.\sigma}\right)^2\right] \qquad \text{.....(1.5)}$$

where, E is energy, E_0 the centre of the distribution, N_V is the DOS and σ is the width of the Gaussian. Localized states hinder charge transport as the charges can be captured or trapped. Trapped carriers may be released after a specific time period but may recombine with the oppositely charged carriers resulting in the formation of a recombination centre. Trap states can originate from various sources like impurities, structural defects and geminate pairs. The understanding of transport in these media is well explained by the temperature-dependent transport energy (E_t) that was introduced by Monro et al. [86]. According to this model, a charge carrier in deep tail states has a high probability to escape to states of energy E_t. Hence, states that lie below the E_t are trap states, while the states above are regular transport sites. Thermal excitations can release charge carriers from the trap states to the transport states [87]. The Gaussian disorder model for charge transport is based on a cubic arrangement of charge transport sites [88]. Whereas the Marcus model [89], proposes that hopping transport between two sites depends on –i) transfer integral of wave functions and ii) thermally activated processes that describe the local charge transport.

The probability (ν_{ij}) that a charge at a point *i* will hop to a point *j*, considering spatial disorder and thermal activation is given by Miller-Abrahams expression [90]

$$\nu_{ij} = \nu_o exp(-\gamma r_{ij}) \begin{cases} exp\left(-\frac{\Delta E_{ij}}{kT}\right), \Delta E_{ij} > 0 \ (up\ hop) \\ 1, \Delta E_{ij} \leq 0 \ (down\ hop) \end{cases} \quad \ldots\ldots\ldots\ldots\ldots\ldots \quad (1.6)$$

where ν_{ij} the hopping rate, ν_o is the frequency pre-factor, γ is the inverse localization radius (proportional to the transfer integral) and r_{ij} is the distance between the sites *i* and *j*. A kinetic Monte-Carlo algorithm was employed to compute the motion of charges across the lattice leading to the expression for carrier mobility with temperature. Calculations are carried out over a range of lattices, temperatures and electrical fields *E*, leading to an empirical expression for measured mobility (μ).

1.7.3 Bulk heterojunction solar cells and geometries

In the case of OSCs, the entire process of the conversion of sunlight into an electric current can be classified in to five processes that occur sequentially:

(i) Absorption of a photon by the polymer leading to the formation of electron-hole pair called an exciton

(ii) Diffusion of the exciton to the D-A interface region,

(iii) Formation of a charge transfer complex (C-T) at the interface

(iv) Dissociation of the C-T complex

(v) Transport and collection of free carriers to the anode (hole) and cathode (electron)

If the unabsorbed and reflected light is excluded, the internal quantum efficiency (IQE) of photovoltaic devices (η_{int}) is determined by i) the fraction of photons absorbed (η_A), ii) the fraction of dissociated excitons (η_{ED}), iii) fraction of separated charge carriers that reach the electrodes (η_{CT}) and iv) the fraction of charges collected at their respective electrodes (η_{CC}) [91]. Hence the IQE is a product of all these fractions given by,

$$\eta = \eta_A \eta_{ED} \eta_{CT} \eta_{CC} \quad \ldots\ldots\ldots\ldots\ldots\ldots\ldots\ldots\ldots\ldots \quad (1.7)$$

These individual fractions can be determined independently to arrive at the net IQE. Since the absorption coefficient (α) and the thickness of the films (*t*) are known, η_A can

be determined from the Beer-Lambert law considering multiple reflections from two metal electrodes (*R*),

$$\eta_A = (1-R)(1-e^{-\alpha t}) \quad \text{(1.8)}$$

η_{ED} is depends on the probability of exciton diffusion to the regions where the charge separation occurs and the charge separation probability. η_{CT} is dependent on the film morphology and a better network of percolation pathways ensures better the carrier transport. A charge collecting electrode with suitable work-function is required to maximize η_{CC}. These processes lead to the formation of concentration gradients at the interface resulting in diffusion currents and a field- induced drift currents that drive the carriers to the electrodes. Even though the IQE can approach 100% in efficient materials with the optimum morphology and the right choice of electrodes, the external quantum efficiency often is considered more useful as it takes in to account reflection and other losses. EQE is analogous to the incident photon to current conversion efficiency (IPCE) and gives an estimate regarding number of charges collected for a certain input photon flux,

$$IPCE(\lambda) = EQE(\lambda) = \frac{n_{electron}}{n_{photon}} = \frac{J/e}{P/h\upsilon} = \frac{J}{P}\frac{hc}{e\lambda} = \frac{J}{P}\frac{1240}{\lambda(nm)} \quad \text{(1.9)}$$

where, *J* is short circuit current density (A/m^2) and *P* is incident light power (W/cm^2). EQE essentially is a measure of the photocurrent conversion efficiency at each absorbing wavelength. It is generally obtained by measuring the photocurrent at different wavelengths (λ) of light and determining the conversion efficiency. In many of the OSCs today, EQE of the order of 80% have been demonstrated. The current-voltage (I-V) or current density-voltage (J-V) characteristics are often sufficient to calculate the efficiency (η) of OSCs. The J-V curve of a typical polymer solar cell is shown in the Figure 1.11 under illumination of 1 sun (100 mW/cm^2). Under illumination, charges are generated, separated and under the influence of the electric field, they drift to their respective electrodes.

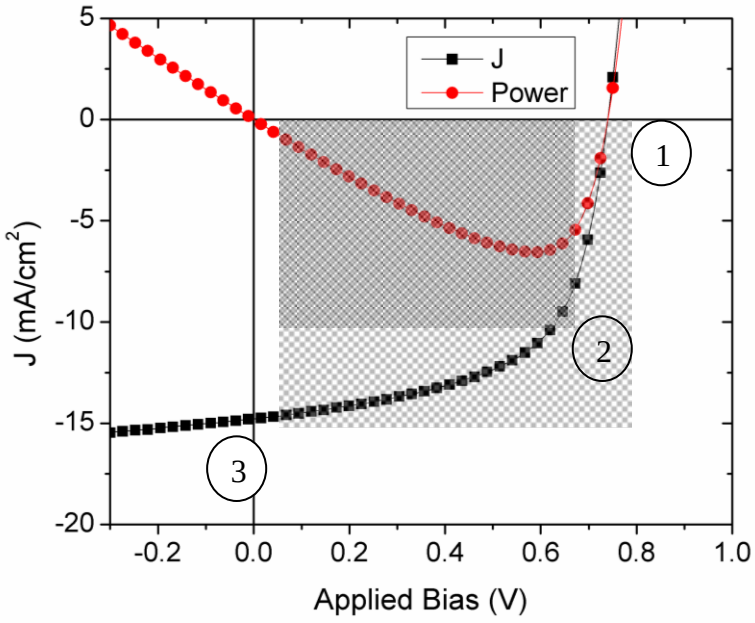

Figure 1.11: *Typical J-V characteristics of an OSC along with the power (J x V) curve showing the maximum power point.*

At a particular voltage, termed as the open-circuit voltage (V_{oc}) the applied field balances the built-in field leading to zero current flowing through the external circuit. Ideally a large V_{oc} is desirable, which also indicates a large built-in voltage that would be essential for better charge collection at the short circuit conditions. When the solar cell is illuminated, electrons flow towards the cathode and the holes towards the anode. But under forward bias, the current direction is reversed. These two currents are balanced out at point (1) in Figure 1.11, in other words, the drift balances the diffusion leading to zero current. At the short circuit condition there is no applied external field or opposing current and hence, the current is maximum at point (3) in Figure 1.11. But points (1) and (3) are cannot be operating points for practical device and hence power generated by the device is a more useful quantity. There exists a maximum power point (MPP), at point (2) in *J*-V response shown in Figure 1.11, where the *J*×V product or the power delivered by the device is maximum. Hence the PCE can be represented by the open circuit voltage V_{oc}, short circuit current density J_{sc} (J_{sc} = I_{sc} */active area)* and fill factor *FF*. The fill factor can be determined as $FF = V_{MPP} \times J_{MPP}/(V_{oc} \times J_{sc})$ which is a ratio of the maximum

obtainable power to the product of V_{oc} and J_{sc}. PCE of a solar cell can be expressed by the following expression,

$$\eta_{Power} = \frac{P_{out}}{P_{in}} = \frac{I_{MPP}.V_{MPP}}{P_{in}} = \frac{FF.I_{SC}.V_{OC}}{P_{in}} \quad \cdots\cdots\cdots\cdots\cdots\cdots\cdots\cdots \quad (1.10)$$

Certain standards need to be implemented so that efficiencies that are reported by different groups can be compared without discrepancies. The efficiency of OSC is temperature dependent and the incident light intensity and spectrum should be strongly matched to the sun. Standard protocols for reporting efficiency are [92];

Light Intensity	100 mW/cm^2 or 1000 W/m^2
Sun Spectrum	AM 1.5 Global (IEC 904-3)
Sample Temperature	25° C
Device area	Using an optical mask

Attempts are made to match the spectrum of the source (sun simulator or solar simulator) to match the spectrum of the sun at a particular favourable angle. A reference cell is needed to calibrate the source and arrive at a spectral mismatch factor M,

$$M = \frac{\int E_{1.5G}(\lambda) S_R(\lambda) d\lambda}{\int E_S(\lambda) S_R(\lambda) d\lambda} \frac{\int E_S(\lambda) S_T(\lambda) d\lambda}{\int E_{1.5G}(\lambda) S_T(\lambda) d\lambda} \quad \cdots\cdots\cdots\cdots\cdots \quad (1.11)$$

where, E_S is the solar spectrum. $E_{1.5G}$ is the AM 1.5 global spectrum calibrated with a reference cell, (S_T) and (S_R) are the spectral response of test devices and the calibrated cell, respectively.

1.7.3.1 Circuit model for a solar cell

The *J-V* characteristics can provide quantitative information about the various parameters of interest like leakage current and recombination losses. The Shockley equation has been successful in describing the characteristics of organic solar cells [93]. A solar cell can be represented as an ideal diode along with two parasitic resistances (Figure 1.12)- i) series resistance R_S, which describes the contact resistances like injection barriers and sheet resistance of the transparent conductor and metals. ii) The parallel

resistance R_P which represents the effect of shunts between two electrodes. From the Shockley equation, the net current density consists of contribution from i) photoinduced short circuit current, ii) diode current and iii) the parallel current through R_P, and can be expressed as,

$$J(V) = J_{ph} + J_0\left[exp\left(\frac{q(V-JR_S)}{nkT}\right) - 1\right] - \frac{V-JR_S}{R_P} \quad \ldots\ldots\ldots\ldots\ldots \quad (1.12)$$

where, J_0 is the reverse-saturation current density and n represents the diode ideality factor [92]. For inefficient devices a strong field-dependent photocurrent behavior is observed in the current which increases linearly with increase in reverse bias. This is an indication of reduced FF and the solar cell efficiency. Such devices cannot be explained by the above equation accurately.

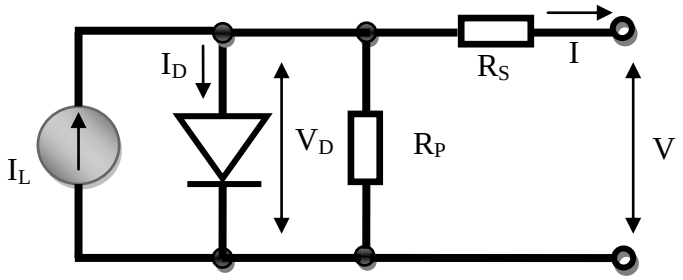

Figure 1.12: *Equivalent circuit model for a solar cell.*

In the case of an ideal diode, $R_S \rightarrow 0$ and $R_P \rightarrow \infty$. In order to arrive at the influence of these losses on the *J-V* curve, the equation can by differentiated with respect to bias (*V*). For the zero current and zero voltage modes of operation setting $V\,(j = 0) \Rightarrow V_{OC}$ and $V\,(j = j_{SC}) \Rightarrow 0$, under the assumption $R_S << R_P$,

$$\frac{\partial V}{\partial J}\Big|_{j=0} = R_S + \frac{R_P}{1+\frac{J_0 R_P}{nkT} exp\frac{V_{oc}}{nkT}} \approx R_S \quad \ldots\ldots\ldots\ldots\ldots \quad (1.13)$$

and

$$\frac{\partial V}{\partial J}\Big|_{V=0} = R_S + \frac{R_P}{1+\frac{J_0 R_P}{nkT} exp\left(-\frac{J_{sc} R_S}{nkT}\right)} \approx R_S + R_P \approx R_P \quad \ldots\ldots\ldots\ldots\ldots (1.14)$$

Hence the derivatives of the illuminated *J-V* curve at the V_{oc} and J_{sc} represent R_S and R_P, respectively.

1.7.3.2 Exciton generation, diffusion and charge-transfer states

Typically the donor material in an OSC absorbs the light as a result of very high absorption coefficients (~ 10^5 cm^{-1}). Absorbed photons generate excitons whose binding energies larger than the thermal energy leading to stable species at ambient temperature [94]. These excitons have a certain lifetime (~*ns*) within which they need to be dissociated in order to obtain free charges. Which means that their diffusion lengths are of the order of 10-20 nm and they must encounter the D-A interface or they will recombine. Hence, in polymer BHJ solar cells, the size of the individual domains in the phase separated morphology needs to be of the order of exciton diffusion length (L_{Diff}). The exciton dissociates efficiently at the interface due to the presence of an electron acceptor. Charge transfer is an extremely fast event, generally in order of tens of femtoseconds [95]. This process, in fact, is much faster other processes like photoluminescence or inter-system crossing [95-96]. In most D-A blends the acceptor also has a limited optical absorption and contributes to a smaller fraction of the total current. However, the exciton generation rate in small molecule acceptors is much lower as compared to the polymer [78]. Hence, an optimum morphology is a prerequisite for the working of an efficient BHJ solar cell.

1.7.3.3 Morphology of the blend

Studies on the morphology of the BHJ solar cell has been the subject of research for a large number of reports. The morphological structure has been elusive and only after a series of recent developments, a consensus seems to be a possibility. It was proposed and also accepted for a while that a bi-continuous network existed in the D-A blend [95]. There were several parallel theories suggesting that the driving factor for phase separation was spinodal decomposition, polymer crystallization or acceptor agglomeration. *Flory-Huggins* (F-H) *model* was used to compute the temperature-composition phase diagram for D-A in a solvent mixture. It was concluded that acceptor

solubility is an important thermodynamic parameter to control morphology in a blend film. In polymer-fullerene blends, the solubility limit of fullerene acceptor is in the range 10 to 47 mg/ml [97]. Rapid solvent evaporation during thermal annealing, the fullerene concentration in the liquid phase exceeds the equilibrium limit, leading to nucleation and growth of fullerene crystals [98]. At higher fullerene concentrations, island formation was observed in heterojunction films [99]. The fullerene diffusion and formation of crystalline domains can be partially explained by Fick's diffusion process

$$\frac{\partial \Phi}{\partial t} = -D \frac{\partial^2 \Phi}{\partial x^2} \qquad \text{.....(1.15)}$$

where Φ and *D* are the fullerene concentration and diffusion coefficient respectively.

1.7.3.4 Mixed phases

The diffusion model only partially explains the origin of phase separation and finally achieved morphology. There is a strong evidence of mixed phases i.e. absence of well defined interfaces in BHJ blends [100-101]. It turns out that there is an intermixing of the two components of the blend at the interface depending upon the miscibility of the two materials. X-ray and neutron scattering techniques along with electron microscopy techniques like the energy-filtered transmission electron microscopy have provided evidence that there are pure phases of the components along with mixed phases at the interface. New imaging methods that are more sensitive and compatible with soft materials have assisted in a more accurate reconstruction of the BHJ morphology [102]. Recent studies on efficient donor polymers like PCPDTBT have shown to form crystalline fibrils along with amorphous chains mixed with PCBM agglomerates. Resonant-soft X-ray Scattering (R-SoXS) has enabled to probe PTB7 blend films to arrive at a better morphological description [101, 103].

1.7.3.5 Normal and inverted solar cells

OSCs have been demonstrated in two geometries depending on the position of the hole and electron collecting electrodes (Figure 1.13). In the normal geometry the transparent conductor collects holes and the metal electrode collects electrons. It turns out that device fabricated in this manner are unstable due to the oxidation of the low work-

function metal electrode along with the acidic PEDOT:PSS film on ITO as shown in Figure 1.13 (a). It was demonstrated that sol-gel derived films of metal oxides like ZnO and TiO_2 can easily be deposited to collect electrons and a MoO_3 layer on the polymer blend can collect holes in combination with a high work-function metal electrode as shown in Figure 1.13 (b) [80, 104-106]. The advantages of this structure are that high work-function metals are more stable and the ZnO film is not acidic. An added advantage is that the ZnO and TiO_2 are wide band-gap materials and absorb UV radiation and filter it before it can reach the polymer layer which is susceptible to photo-oxidation.

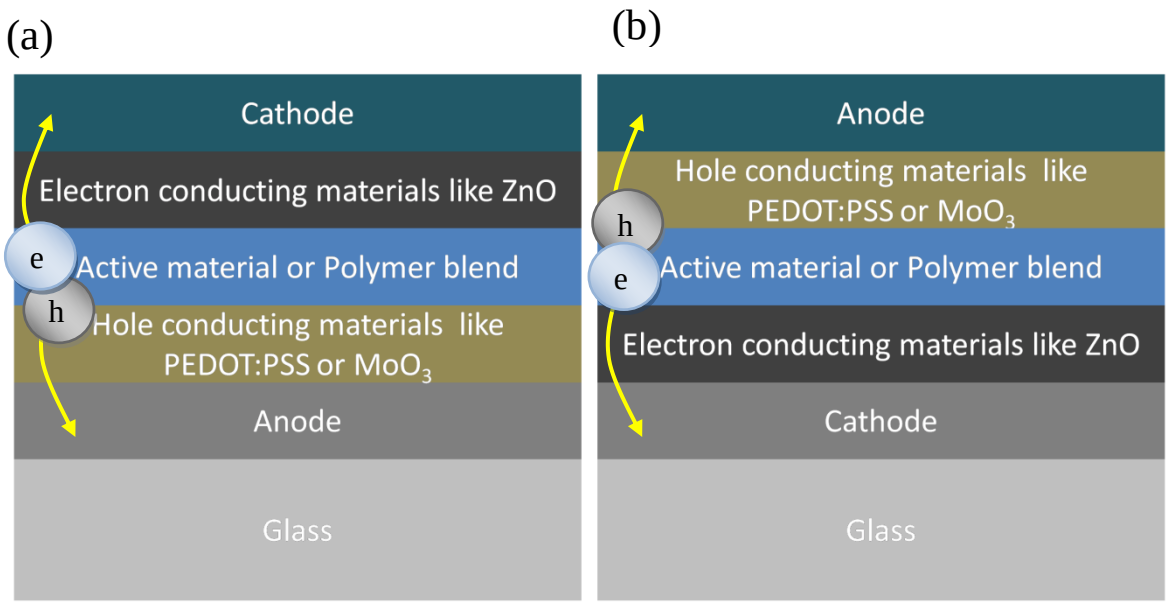

Figure 1.13: *Geometries for organic solar cells (a) Normal architecture and (b) inverted architecture.*

The inverted devices not only show superior stabilities, additionally as a result of incorporating hole and electron buffer layers their efficiency is higher than the normal device [106-113]. In fact, the highest reported efficiency of organic solar cell to date is for an inverted device of PTB7 polymer with an efficiency of 9.2% [80].

1.8 Challenges in commercialization of organic solar cells

Organic solar cells are maturing to a technology but certain issues need to be addressed so as to present a realistic picture. Research related to OSCs is directed three-fold, namely- i) development of new materials, ii) scaling device area or roll-to-roll processing ability and iii) stability.

1.8.1 Area scaling issue

New materials have been synthesized with excellent photovoltaic properties yielding high efficiency [80]. But retention of this efficiency over large areas and long time frames has been an area of concern. Most solar cells that have been reported to be efficient are only small area devices as shown in Figure 1.14 [114] and Table 1.1 [115]. In order to make a device that can be useful to power small applications like cell-phones or larger grid like applications, the area needs to be several square inches up to square meters. Figure 1.14 shows the dependence of short circuit current density on device area. As the area is increased from 1 mm^2 to 0.5 cm^2, the short circuit current density falls by a factor of two.

In spite of the area scaling being a major issue, there have been few studies on the area dependence of efficiency and the causes of such an observation. There have been even fewer reports suggesting or implementing solutions that can overcome this problem. It turns out that the resistance of the transparent conductor sets a limit on the area of the device. e.g. the sheet resistance of a popular transparent conductor Indium Tin Oxide (ITO) can range from a 7-20 Ω/□. In large devices with areas in the range of 1 cm^2 to 1 sq. in., this becomes a limit factor as there is a voltage drop across this series resistance [114].

Photoactive layer	Cell area, [cm^2]	I_{SC} (mA cm^2)	V_{OC} (V)	FF	PCE (%)
P3HT/PCBM	0.148	9.5	0.63	0.68	5
P3HT/PCBM	0.148	11.1	0.61	0.66	5
P3HT/PCBM	Not mentioned	11.3	0.64	0.69	5.2
P3HT/PCBM	0.19	11.1	0.65	0.54	4.9
PSBTBT/PCBM	0.12	12.7	0.68	0.55	5.1
PCPDTBT:C_{70}-PCBM	0.17	16.2	0.62	0.55	5.5
PTB4/PCBM	0.095	13.0	0.74	0.61	6.1
PCDTB: $PC_{70}BM$	0.127	10.593	0.88	0.64	6.0[a]
—[b]	0.043	10.321	0.81	0.72	6.0[a]
tandem PCDTB:PCBM/P3HT:$PC_{70}BM$ BHJ	0.045	7.8	1.24	0.67	6.5
Low band gap polymer[c]/PCBM	0.047	13.3	0.76	0.66	6.8[a]
Low band gap polymer[c]/PCBM	0.047			0.71	7.6[a]
Low band gap polymer[c]/PCBM	Not mentioned				8.13[a]

***Table 1.1**: Table of high efficiency OSC along with the area and other electrical parameters. The oval depicts the small areas over which high efficiency has been achieved. (Reprinted with permission from A. Manor, E. A. Katz, T. Tromholt, B. Hirsch, F. C. Krebs, Origin of size effect on efficiency of organic photovoltaics. Journal of Applied Physics **2011**, 109.©2011, American Institute of Physics).*

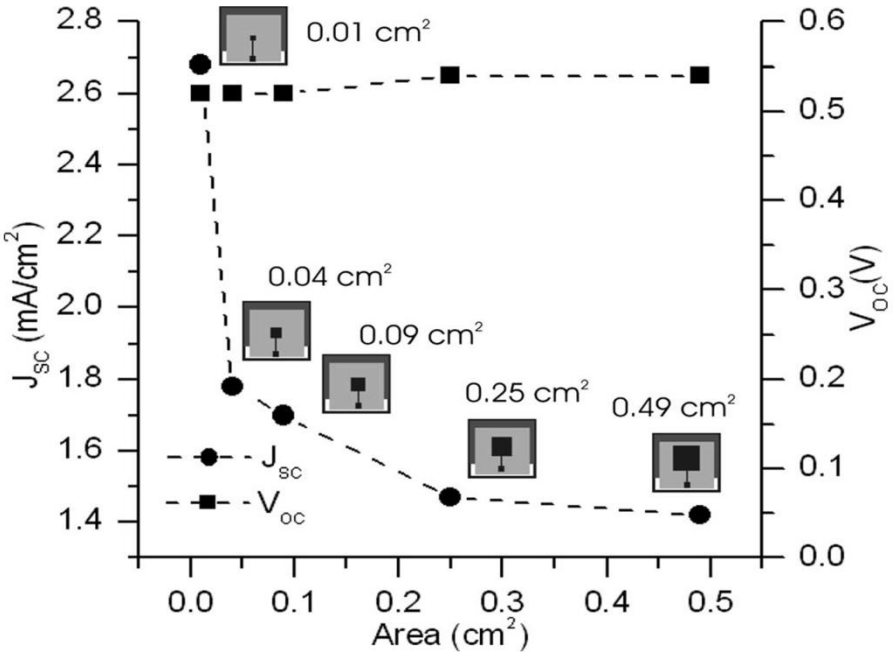

***Figure 1.14:** Area dependence of efficiency of organic solar cells. (Reprinted with permission from D. Gupta, M. Bag, K. S. Narayan, Area dependent efficiency of organic solar cells. Applied Physics Letters **2008**, 93.©2008, American Institute of Physics).*

This results in a loss of the built-in voltage and the FF along with a drop in J_{sc} as summarized in Table 1.2 [116]. While an obvious solution is to replace ITO by other materials with better conductivity, there have not been many successful demonstrations. Highly conducting forms of PEDOT:PSS have been used in conjunction with silver grids with limited success. The acidic nature of PEDOT:PSS films results in low stability of such devices. Thin films (5 nm) of silver and gold also have been used as replacements for ITO but their transmittance is low. Hence there is a conflict between the thickness of the transparent conductor which leads to lower resistances but at the same time lower transmittance.

In this regard, certain designs have been proposed that can utilize the existing ITO films and improve charge collection. Multiple collection pads can be deposited around the device that can improve the fill factor as the device area is scaled up. The collection pads can be deposited as a single strip or multiple strips around the device on the ITO film. These strips can consist of metal films which have a lower resistance as compared to ITO and thereby reduce the series resistance of the device.

Parameters	Values						
Area [cm^2]	0.09	0.38	0.5	1.02	4.0	9.0	16.0
PCE [%]	3.38	3.44 ± 0.07	3.43 ± 0.18	3.35 ± 0.12	2.81 ± 0.15	2.04	1.13
J_{sc} [mA/cm^2]	9.12	9.25 ± 0.46	9.51 ± 0.23	8.92 ± 0.21	9.18 ± 0.6	8.45	6.69
V_{oc} [V]	0.57	0.57 ± 0.001	0.57 ± 0.01	0.58 ± 0.01	0.55 ± 0.01	0.56	0.59
FF	0.65	0.65 ± 0.02	0.65 ± 0.007	0.64 ± 0.01	0.56 ± 0.06	0.43	0.29
R_s [Ωcm^2]	1.8	3.0 ± 0.15	2.2 ± 1.1	4.4 ± 1.4	12.1 ± 0.24	22.9	44.7
R_p [$k\Omega cm^2$]	5.9	1900	22	28	88	10	24
J_s [$\mu A/cm^2$]	0.002	0.001	0.001	0.002	0.01	0.009	0.002
n	1.57	1.55	1.56	1.56	1.55	1.56	1.56

Table 1.2: *Variation of solar cell parameters as a function of device area. (Reprinted with permission from W.-I. Jeong, J. Lee, S.-Y. Park, J.-W. Kang, J.-J. Kim, Reduction of Collection Efficiency of Charge Carriers with Increasing Cell Size in Polymer Bulk Heterojunction Solar Cells. Advanced Functional Materials* ***2011****, 21, 343. ©2011, John Wiley and Sons).*

However, there have not been scalable solutions to the area problem. Most of the above mentioned approaches need additional metal deposition steps increasing the manufacturing costs. PEDOT:PSS based approaches lead to unstable devices due to the acidic nature of PEDOT:PSS. Hence there is a need for alternative transparent materials along with novel electrode architectures and designs that can minimize losses due to high resistances.

1.8.2 Stability of organic solar cells

Commercialization and implementation of OSCs as a technology has been hampered also due to the short device lifetimes. In comparison to the first and second generation PVs which promise 10-25 yr device lifetimes, OSCs with the best stability have shown reasonable performance over several months. For this concept to be incorporated to industry, such lifetimes are unacceptable. Hence, one of the important thrusts of this research field is to overcome this drawback by investigating the causes, developing new materials and designs that are resistant to degradation.

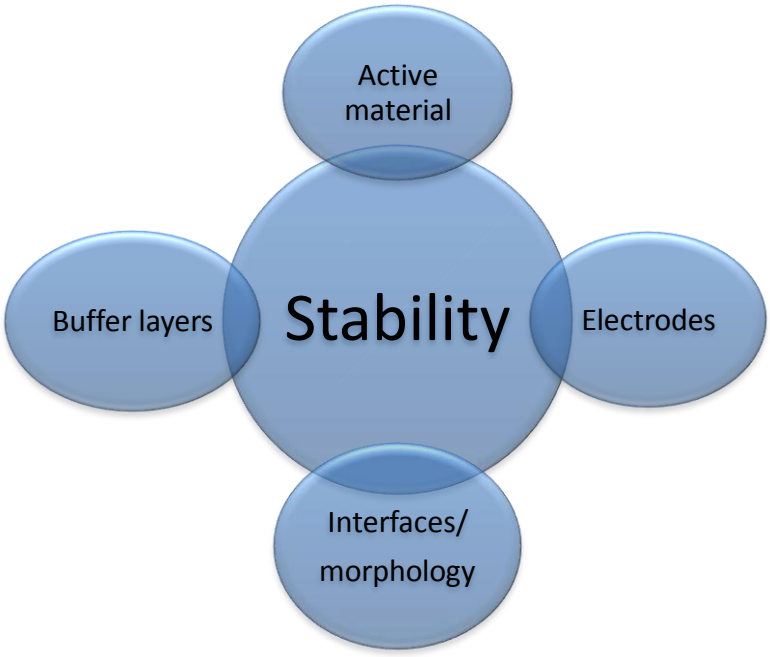

Figure 1.15: *Various factors affecting the stability of organic solar cells.*

Fundamentally, soft materials are not as stable as crystalline materials due to weak bonds that hold together their constituent molecules. But they are easily processible and can be fabricated or manipulated at low temperatures. Hence there is a tradeoff between cost and stability. There have been numerous attempts to approach the problem of stability in OSC [75, 107, 117-119]. The problem can be broken up into the study of the stability of different materials that are involved in an OSC. Broadly, they can be classified as active materials, electrode materials, buffer materials and interfaces between these materials as shown in Figure 1.15.

1.8.2.1 Organic material stability

The active layer in the organic solar cell is prone to degradation and which results in lowering of the power conversion efficiency as a function of time. Photo-degradation or light-induced degradation is the major reaction that lowers efficiency. Due to persistent research in this direction, stability of devices has been extended from a few minutes to several months to years. Most organic molecules and polymers like poly-phenylenevinylene (PPV) undergo photo-oxidation. Causes of degradation were shown to involve side chain degradation as well as vinylene moieties [120]. But a popular polymer poly(3-hexyl-thiophene) (P3HT) was found to be much stable [121] and hence could be utilized in realistic devices.

Films of P3HT were found to completely photo-oxidize resulting in complete bleaching after few hundreds of hours. Addition of the acceptor PCBM slows this process by quenching the reactive excited state of P3HT [122] by forming a charge transfer complex. Also the oxidation of PCBM [123] can create traps for the electron transport resulting in decreased electron mobility.

Active layer burn-in

Even though the active layer is susceptible to photo-oxidation, it is somewhat protected by the other buffer layers in the device. Since each material like oxides, behaves like a barrier for water and oxygen, the photo-oxidation of the active layer is impeded as compared to the case when it directly exposed to the ambient atmosphere. But there is still a finite rate of photo-oxidation at the early stages of the device. The

efficiency falls rather rapidly in the 24-48 hr period after exposure and then stabilizes to a certain lower value at extended time intervals (Figure 1.16). This process is called burn-in and is present even when the devices are sufficiently encapsulated and isolated from water and oxygen [124]. This effect is present irrespective of the active material. The origin of this loss of efficiency seems to be a photo-induced reaction in the active material leading to the formation of sub-band-gap states. As a result trap-mediated recombination increases leading to reduced hole mobility along with build-up of space-charge. This lowers the open circuit voltage and the short circuit current as the electric field that drives charge separation is diminished.

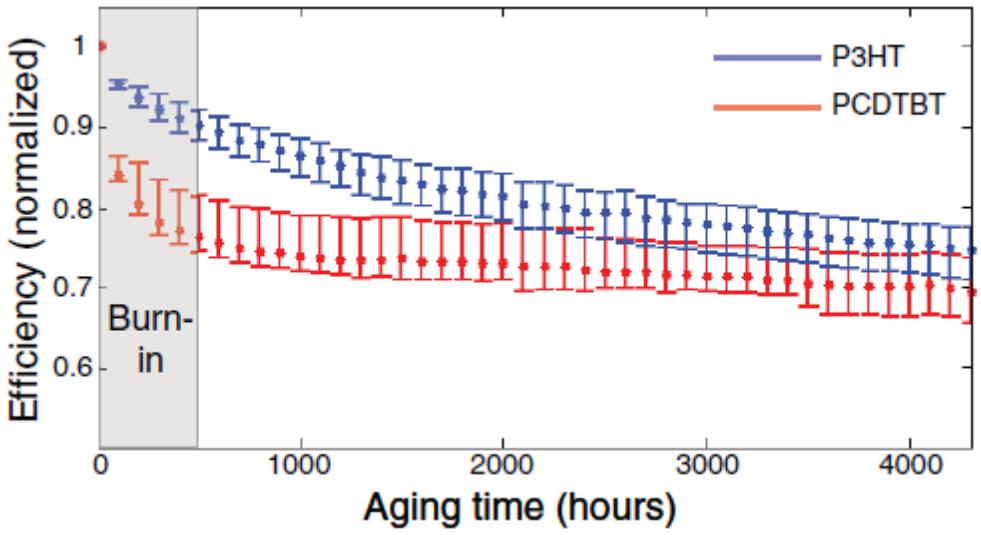

Figure 1.16: *Burn-in effect in organic solar cells (Reprinted with permission from C. H. Peters, I. T. Sachs-Quintana, W. R. Mateker, T. Heumueller, J. Rivnay, R. Noriega, Z. M. Beiley, E. T. Hoke, A. Salleo, M. D. McGehee, The Mechanism of Burn-in Loss in a High Efficiency Polymer Solar Cell. Advanced Materials 2012, 24, 663. ©2012, John Wiley and Sons).*

1.8.2.2 The Metal Electrode

Most popular electrode materials in normal solar cell geometry are aluminium and calcium or a sequential deposition of both. Calcium has a low work-function and improves charge collection in combination with aluminium. The need for low work-function materials brings the disadvantage of reactivity to atmosphere. But both aluminium and calcium films are highly reactive but do not pose a problem when stored under inert conditions. In a realistic application the effect of moisture and oxygen eventually leads to degradation of the device. Even though the rate of transmission can be controlled to a certain extent by encapsulating the device, in most cases it is not sufficient for long time operation. Low work function of these metals makes them act as reducing agents in the presence of water and alcohols. As a result, water diffuses through pores in the metal leading to the formation metal oxides at the metal-polymer interface. These metal oxides are insulating and create electrical transport barriers leading to decrease in fill factor, short circuit current and lowering the efficiency. There were a series of reports that showed that the formation of Al_2O_3 gives rise to increased capacitance leading to S-shaped I-V curve with low fill factors [125-126].

Inverted devices are more stable as the metal electrode used to collect holes and can have a higher work function. Metals like silver and gold are less reactive and more tolerant ot degradation by oxygen or water. But metal deposition in vacuum is not a cost effective process and cannot be used for large area devices. A promising alternative is emulsions or inks with a high content of metal particles that can be printed over large areas. However many of these emulsions were not designed for organic solar cells and hence show a variation in efficiency due the incorporation of various binders [127-128].

1.8.2.3 The Hole Transport Layer

The most widely used hole transport layer is the commercially available PEDOT:PSS. This ionic polymer is water based suspension that can spin coated or printed in solar cell devices [75]. Most formulations of PEDOT:PSS are acidic with a pH in the range of 1-3. The acidic nature of PEDOT:PSS has been shown to cause degradation of the ITO electrode [129]. Recent reports show that hygroscopic nature of

PEDOT:PSS results in cathode oxidation in polymer solar cells [130-131]. Vacuum deposited MoO_3 turns out to be a stable replacement as the hole conducting layer.

1.8.2.4 Organic/Metal Electrode Interface

Along with individual material layers in the solar cell, interfaces do play a significant role in deciding the stability. Studies have shown that the organic-metal electrode interface is susceptible to degradation when contacted by oxygen and water. The following photo-degradation mechanisms can occur: i) formation of barriers due to oxidation of low work function electrodes such as aluminium and calcium, ii) photo-oxidation of the active organic material that decreases mobility of charge carriers leading to poor photovoltaic performance, and iii) formation of adducts with the organic material that are reactive to atmospheric conditions. Photo-oxidation of the organic layer in the organic-metal interface has been studied for various types of organic solar cells [132-134]. The mechanism of diffusion of water and oxygen through the evaporated aluminium electrode turns out to be very different. Water diffuses through the interface via spaces in the aluminium grains where as oxygen diffuses through microscopic pinholes in a preferential manner [134]. Hence, water results in a homogeneous oxidation of the organic material at the interface whereas oxygen results in an inhomogeneous oxidation that is centered around microscopic pinholes. Such features caused due to photo-oxidation can be viewed and analyzed by interference microscopy and AFM [133].

1.8.3 Encapsulation

OSCs are sensitive to prolonged exposure to UV light, oxygen and moisture. An obvious approach is to encapsulate them and cut-off any supply of oxygen or environmental effects by incorporating barriers. Barrier coatings can also be used to improve the mechanical stability, scratch resistance and as filters for removing UV components of the solar spectrum. The most popular and perhaps a crude method involves sealing devices in between glass cover slips in an inert atmosphere. This would require gluing the device to a sheet of glass and sealing the edges. Devices are no longer flexible, but they minimize the transmission rate of oxygen and moisture. It is important to note that barriers used in food packaging and other industrial packaging are not suitable for devices. In fact, much superior barrier coatings are essential. In the past PET

foils have been used as barrier but it was not sufficient [135]. Other feasible solutions include lamination of plastic barrier films on top of the devices. PEG barriers [136], cytop barriers [137], multilayer stacks [138] and many other strategies have been utilized but with limited success. Any high temperature processing cannot be used with soft materials as they are susceptible to damage. Barrier coating on top of thin metal films sometimes lower the integrity of the film leading to current loss. Hence, the challenge of finding the right material and encapsulation technique still remains a challenge.

1.9 Overview and Scope of thesis

Though organic solar cells are on the verge of maturing to a commercial technology, several critical issues need to be addressed. Area scalability and device stability are certainly few of the most important challenges that are being addressed. This thesis attempts to provide feasible solutions to the above mentioned issues along with enhancements that can be brought about by exploiting light harvesting strategies.

In this thesis, Chapter 2 presents an overview of materials used for device fabrication. It also presents information regarding device fabrication methods along with instrumentation setups utilized to carry out various experiments.

Chapter 3 deals with the issue of area scaling and strategies to overcome this problem. A novel, cost-effective, scalable and printable method is proposed that utilizes unconventional electrodes like low-melting metal alloys. Not only does this geometry minimize series resistance losses, it also significantly improves device stability. This chapter also presents design guidelines for the shape and size of pixelated solar cells.

Light harvesting strategies for organic solar cells are discussed Chapter 4. Two novel, cost-effective strategies are proposed that maximize light capture and power conversion efficiency in large area devices. The first strategy involves the utilization of fluorescent dyes in the solar cell encapsulation that are capable of down-conversion and redirecting unabsorbed light back to the active material. The second strategy involves the utilization of microlens arrays as light concentrators for solar cells.

Chapter 5 discusses the degradation processes in organic solar cells. Data gathered over large time intervals were analyzed by capacitance-voltage, current-voltage measurements. Noise in organic solar cells has also been monitored as a function of device aging and insights are provided that can assist in better device performance over extended intervals of time.

Fabrication and characterization of novel three-dimensional microlasers are presented in Chapter 6. Lasing characteristics, mode analysis, polarization dependence and evidence of three-dimensional lasing is discussed in this chapter.

References

[1] W. Shockley, H. J. Queisser, Detailed Balance Limit of Efficiency of p-n Junction Solar Cells. *Journal of Applied Physics* **1961**, *32*, 510.

[2] C. H. Henry, Limiting efficiencies of ideal single and multiple energy gap terrestrial solar cells. *Journal of Applied Physics* **1980**, *51*, 4494.

[3] J. N. Munday, The effect of photonic bandgap materials on the Shockley-Queisser limit. *Journal of Applied Physics* **2012**, *112*.

[4] K. Roy, Monocrystalline and Multicrystalline Silicon Solar-Cells - Recent Developments and Future Perspectives. *Proceedings of the Workshop on Materials Science and Physics of Non-Conventional Energy Sources* **1991**, 236.

[5] T. M. Bruton, Current Status - Production of High-Efficiency Monocrystalline Silicon Solar-Cells. *Renewable Energy* **1995**, *6*, 299.

[6] R. Brendel, H. Artmann, S. Oelting, W. Frey, J. H. Werner, H. J. Queisser, Monocrystalline Si waffles for thin solar cells fabricated by the novel perforated-silicon process. *Applied Physics a-Materials Science & Processing* **1998**, *67*, 151.

[7] J. H. Zhao, A. H. Wang, M. A. Green, F. Ferrazza, 19.8% efficient "honeycomb" textured multicrystalline and 24.4% monocrystalline silicon solar cells. *Applied Physics Letters* **1998**, *73*, 1991.

[8] K. A. Munzer, K. T. Holdermann, R. E. Schlosser, S. Sterk, Thin monocrystalline silicon solar cells. *Ieee Transactions on Electron Devices* **1999**, *46*, 2055.

[9] J. K. Rath, Micro-/poly-crystalline silicon materials for then film photovoltaic devices: Application in solar cells. *Photovoltaic and Photoactive Materials - Properties, Technology and Applications* **2002**, *80*, 183.

[10] J. K. Rath, H. Meiling, R. E. I. Schropp, Purely intrinsic poly-silicon films for n-i-p solar cells. *Japanese Journal of Applied Physics Part 1-Regular Papers Short Notes & Review Papers* **1997**, *36*, 5436.

[11] Y. W. Zhao, X. N. Jiang, W. J. Wang, Z. M. Li, Y. Yu, X. B. Liao, Poly-silicon thin films and solar cells prepared by rapid thermal CVD. *Conference Record of the Twenty Sixth Ieee Photovoltaic Specialists Conference - 1997* **1997**, 731.

[12] D. E. Carlson, Multijunction Amorphous-Silicon Solar-Cells. *Philosophical Magazine B-Physics of Condensed Matter Statistical Mechanics Electronic Optical and Magnetic Properties* **1991**, *63*, 305.

[13] D. E. Carlson, Amorphous-Silicon Solar-Cells. *Ieee Transactions on Electron Devices* **1989**, *36*, 2775.

[14] Y. R. Chen, Z. Q. Li, X. H. Chen, C. Liu, X. J. Ye, Z. B. Wang, Z. Sun, S. M. Huang, Improved performance of flexible amorphous silicon solar cells with silver nanowires. *Journal of Applied Physics* **2012**, *112*.

[15] P. Nubile, P. Torres, C. Hof, D. Fischer, Analysis of the inner collection efficiency in hybrid silicon solar cells. *Solid-State Electronics* **1997**, *41*, 1202.

[16] A. Rios-Flores, O. Ares, J. M. Camacho, V. Rejon, J. L. Pena, Procedure to obtain higher than 14% efficient thin film CdS/CdTe solar cells activated with HCF2Cl gas. *Solar Energy* **2012**, *86*, 780.

[17] X. Wu, J. Zhou, A. Duda, J. C. Keane, T. A. Gessert, Y. Yan, R. Noufi, 13.9%-efficient CdTe polycrystalline thin-film solar cells with an infrared transmission of similar to 50%. *Progress in Photovoltaics* **2006**, *14*, 471.

[18] N. Amin, T. Isaka, A. Yamada, M. Konagai, Highly efficient 1 mu m thick CdTe solar cells with textured TCOs. *Solar Energy Materials and Solar Cells* **2001**, *67*, 195.

[19] T. Aramoto, S. Kumazawa, H. Higuchi, T. Arita, S. Shibutani, T. Nishio, J. Nakajima, M. Tsuji, A. Hanafusa, T. Hibino, K. Omura, H. Ohyama, M. Murozono, 16.0% efficient thin-film CdS/CdTe solar cells. *Japanese Journal of Applied Physics Part 1-Regular Papers Short Notes & Review Papers* **1997**, *36*, 6304.

[20] H. Ohyama, T. Aramoto, S. Kumazawa, H. Higuchi, T. Arita, S. Shibutani, T. Nishio, J. Nakajima, M. Tsuji, A. Hanafusa, T. Hibino, K. Omura, M. Murozono, 16.0% efficient thin-film CdS/CdTe solar cells. *Conference Record of the Twenty Sixth Ieee Photovoltaic Specialists Conference - 1997* **1997**, 343.

[21] T. L. Chu, S. S. Chu, C. Ferekides, C. Q. Wu, J. Britt, C. Wang, 13.4-Percent Efficient Thin-Film Cds/Cdte Solar-Cells. *Journal of Applied Physics* **1991**, *70*, 7608.

[22] D. Guimard, N. Bodereau, J. Kurdi, J. F. Guillemoles, D. Lincot, P. P. Grand, M. BenFarrah, S. Taunier, O. Kerrec, P. Mogensen, Efficient CIGS solar cells prepared by electrodeposition. *Proceedings of 3rd World Conference on Photovoltaic Energy Conversion, Vols a-C* **2003**, 515.

[23] A. Bosio, N. Romeo, A. Podesta, S. Mazzamuto, V. Canevari, Why CuInGaSe2 and CdTe polycrystalline thin film solar cells are more efficient than the corresponding single crystal? *Crystal Research and Technology* **2005**, *40*, 1048.

[24] S. Q. Ren, L. Y. Chang, S. K. Lim, J. Zhao, M. Smith, N. Zhao, V. Bulovic, M. Bawendi, S. Gradecak, Inorganic-Organic Hybrid Solar Cell: Bridging Quantum Dots to Conjugated Polymer Nanowires. *Nano Letters* **2011**, *11*, 3998.

[25] M. Wright, A. Uddin, Organic-inorganic hybrid solar cells: A comparative review. *Solar Energy Materials and Solar Cells* **2012**, *107*, 87.

[26] S. Kim, J. K. Lee, S. O. Kang, J. Ko, J. H. Yum, S. Fantacci, F. De Angelis, D. Di Censo, M. K. Nazeeruddin, M. Gratzel, Molecular engineering of organic

sensitizers for solar cell applications. *Journal of the American Chemical Society* **2006**, *128*, 16701.

[27] P. R. Somani, S. P. Somani, M. Umeno, A. Sato, Concept and demonstration of all organic Gratzel solar cell (dye sensitized solar cell). *Applied Physics Letters* **2006**, *89*.

[28] D. Y. Chen, Y. Y. Hsu, H. C. Hsu, B. S. Chen, Y. T. Lee, H. Fu, M. W. Chung, S. H. Liu, H. C. Chen, Y. Chi, P. T. Chou, Organic dyes with remarkably high absorptivity; all solid-state dye sensitized solar cell and role of fluorine substitution. *Chemical Communications* **2010**, *46*, 5256.

[29] J. H. Delcamp, A. Yella, T. W. Holcombe, M. K. Nazeeruddin, M. Gratzel, The Molecular Engineering of Organic Sensitizers for Solar-Cell Applications. *Angewandte Chemie-International Edition* **2013**, *52*, 376.

[30] H. Neugebauer, C. Brabec, J. C. Hummelen, N. S. Sariciftci, Stability and photodegradation mechanisms of conjugated polymer/fullerene plastic solar cells. *Solar Energy Materials and Solar Cells* **2000**, *61*, 35.

[31] S. E. Shaheen, C. J. Brabec, N. S. Sariciftci, F. Padinger, T. Fromherz, J. C. Hummelen, 2.5% efficient organic plastic solar cells. *Applied Physics Letters* **2001**, *78*, 841.

[32] M. A. Green, K. Emery, Y. Hishikawa, W. Warta, Solar cell efficiency tables (version 36). *Progress in Photovoltaics* **2010**, *18*, 346.

[33] M. C. Beard, R. J. Ellingson, Multiple exciton generation in semiconductor nanocrystals: Toward efficient solar energy conversion. *Laser & Photonics Reviews* **2008**, *2*, 377.

[34] E. C. Greyson, B. R. Stepp, X. D. Chen, A. F. Schwerin, I. Paci, M. B. Smith, A. Akdag, J. C. Johnson, A. J. Nozik, J. Michl, M. A. Ratner, Singlet Exciton Fission for Solar Cell Applications Energy Aspects of Interchromophore Coupling. *Journal of Physical Chemistry B* **2010**, *114*, 14223.

[35] J. C. Johnson, Z. Havlas, A. Akdag, M. B. Smith, B. R. Stepp, J. Michl, Molecules for singlet fission. *Abstracts of Papers of the American Chemical Society* **2010**, *240*.

[36] M. B. Smith, J. Michl, Singlet Fission. *Chemical Reviews* **2010**, *110*, 6891.

[37] P. J. Jadhav, P. R. Brown, N. Thompson, B. Wunsch, A. Mohanty, S. R. Yost, E. Hontz, T. Van Voorhis, M. G. Bawendi, V. Bulovic, M. A. Baldo, Triplet Exciton Dissociation in Singlet Exciton Fission Photovoltaics. *Advanced Materials* **2012**, *24*, 6169.

[38] P. J. Jadhav, A. Mohanty, J. Sussman, J. Lee, M. A. Baldo, Singlet Exciton Fission in Nanostructured Organic Solar Cells. *Nano Letters* **2011**, *11*, 1495.

[39] O. E. Semonin, J. M. Luther, S. Choi, H. Y. Chen, J. B. Gao, A. J. Nozik, M. C. Beard, Peak External Photocurrent Quantum Efficiency Exceeding 100% via MEG in a Quantum Dot Solar Cell. *Science* **2011**, *334*, 1530.

[40] W. L. Chan, M. Ligges, A. Jailaubekov, L. Kaake, L. Miaja-Avila, X. Y. Zhu, Observing the Multiexciton State in Singlet Fission and Ensuing Ultrafast Multielectron Transfer. *Science* **2011**, *334*, 1541.

[41] B. Ehrler, M. W. B. Wilson, A. Rao, R. H. Friend, N. C. Greenham, Singlet Exciton Fission-Sensitized Infrared Quantum Dot Solar Cells. *Nano Letters* **2012**, *12*, 1053.

[42] A. Luque, A. Marti, Increasing the efficiency of ideal solar cells by photon induced transitions at intermediate levels. *Physical Review Letters* **1997**, *78*, 5014.
[43] K. Barnham, J. L. Marques, J. Hassard, P. O'Brien, Quantum-dot concentrator and thermodynamic model for the global redshift. *Applied Physics Letters* **2000**, *76*, 1197.
[44] V. Sholin, J. D. Olson, S. A. Carter, Semiconducting polymers and quantum dots in luminescent solar concentrators for solar energy harvesting. *Journal of Applied Physics* **2007**, *101*.
[45] S. M. Reda, Synthesis and optical properties of CdS quantum dots embedded in silica matrix thin films and their applications as luminescent solar concentrators. *Acta Materialia* **2008**, *56*, 259.
[46] M. G. Hyldahl, S. T. Bailey, B. P. Wittmershaus, Photo-stability and performance of CdSe/ZnS quantum dots in luminescent solar concentrators. *Solar Energy* **2009**, *83*, 566.
[47] T. Trupke, M. A. Green, P. Wurfel, Improving solar cell efficiencies by down-conversion of high-energy photons. *Journal of Applied Physics* **2002**, *92*, 1668.
[48] T. Trupke, M. A. Green, P. Wurfel, Improving solar cell efficiencies by up-conversion of sub-band-gap light. *Journal of Applied Physics* **2002**, *92*, 4117.
[49] M. J. Currie, J. K. Mapel, T. D. Heidel, S. Goffri, M. A. Baldo, High-efficiency organic solar concentrators for photovoltaics. *Science* **2008**, *321*, 226.
[50] C. L. Mulder, P. D. Reusswig, A. P. Beyler, H. Kim, C. Rotschild, M. A. Baldo, Dye alignment in luminescent solar concentrators: II. Horizontal alignment for energy harvesting in linear polarizers. *Optics Express* **2010**, *18*, A91.
[51] C. L. Mulder, L. Theogarajan, M. Currie, J. K. Mapel, M. A. Baldo, M. Vaughn, P. Willard, B. D. Bruce, M. W. Moss, C. E. McLain, J. P. Morseman, Luminescent Solar Concentrators Employing Phycobilisomes. *Advanced Materials* **2009**, *21*, 3181.
[52] R. Reisfeld, M. Eyal, V. Chernyak, R. Zusman, Luminescent Solar Concentrators Based on Thin-Films of Polymethylmethacrylate on a Polymethylmethacrylate Support. *Solar Energy Materials* **1988**, *17*, 439.
[53] R. Kondepudi, S. Srinivasan, Collection Parameters of Luminescent Solar Concentrators Using Mixed Dye Solutions. *Indian Journal of Pure & Applied Physics* **1991**, *29*, 438.
[54] M. A. ElShahawy, A. F. Mansour, Optical properties of some luminescent solar concentrators. *Journal of Materials Science-Materials in Electronics* **1996**, *7*, 171.
[55] L. H. Slooff, A. R. Burgers, M. G. Debije, Reduction of escape cone losses in luminescent solar concentrators with cholesteric mirrors. *High and Low Concentration for Solar Electric Applications Iii* **2008**, *7043*.
[56] F. Haase, S. Eidelloth, R. Horbelt, K. Bothe, E. G. Rojas, R. Brendel, Loss analysis of back-contact back-junction thin-film monocrystalline silicon solar cells. *Journal of Applied Physics* **2011**, *110*.
[57] L. C. Hirst, N. J. Ekins-Daukes, Fundamental losses in solar cells. *Progress in Photovoltaics* **2011**, *19*, 286.

[58] H. K. Lyu, S. H. Woo, S. Jeong, K. P. Kim, J. K. Shin, Investigation of power loss and device efficiency using a three-dimensional finite element simulation on organic solar cell geometry. *Solar Energy Materials and Solar Cells* **2012**, *96*, 66.

[59] P. E. Sims, A. E. Ingram, E. J. DelleDonne, J. P. Yaskoff, D. H. Ford, J. A. Rand, A. M. Barnett, Silicon-on-ceramic monolithically interconnected solar cell modules. *Proceedings of 3rd World Conference on Photovoltaic Energy Conversion, Vols a-C* **2003**, 1217.

[60] L. A. Verhoef, P. P. Michiels, R. J. C. Vanzolingen, H. H. C. Demoor, A. R. Burgers, R. A. Steeman, W. C. Sinke, Low-cost multicrystalline silicon solar modules with 16% encapsulated cell efficiency. *1994 Ieee First World Conference on Photovoltaic Energy Conversion/Conference Record of the Twenty Fourth Ieee Photovoltaic Specialists Conference-1994, Vols I and Ii* **1994**, 1547.

[61] J. Zhao, A. Wang, M. Taouk, F. Yun, A. Ebong, A. W. Stephens, S. R. Wenham, M. A. Green, 20-Percent Efficient Silicon Solar-Cell Modules. *Conference Record of the Twenty Third Ieee Photovoltaic Specialists Conference - 1993* **1993**, 1246.

[62] H. Saha, G. Bhattacharya, D. Mukherjee, Mismatch Losses in Series Combinations of Silicon Solar-Cell Modules. *Solar Cells* **1988**, *25*, 143.

[63] C. W. Kuo, S. H. Du, F. S. Juang, Y. Y. Ho, Solar Cell Module Installation Optimization and Evaluation of Power Conversion Simulation. *2009 International Conference on Power Electronics and Drive Systems, Vols 1 and 2* **2009**, 1069.

[64] V. Badescu, Simple optimization procedure for silicon-based solar cell interconnection in a series-parallel PV module. *Energy Conversion and Management* **2006**, *47*, 1146.

[65] M. Hiramoto, H. Fujiwara, M. Yokoyama, 3-Layered Organic Solar-Cell with a Photoactive Interlayer of Codeposited Pigments. *Applied Physics Letters* **1991**, *58*, 1062.

[66] J. K. Lee, W. L. Ma, C. J. Brabec, J. Yuen, J. S. Moon, J. Y. Kim, K. Lee, G. C. Bazan, A. J. Heeger, Processing additives for improved efficiency from bulk heterojunction solar cells. *Journal of the American Chemical Society* **2008**, *130*, 3619.

[67] S. I. Na, S. H. Oh, S. S. Kim, D. Y. Kim, Efficient organic solar cells with polyfluorene derivatives as a cathode interfacial layer. *Organic Electronics* **2009**, *10*, 496.

[68] F. Y. Chang, H. Y. Lin, W. L. Lai, C. J. Ting, J. H. Tsai, S. H. Chang, T. C. Wu, Roll to roll processing for flexible nanophotonics. *19th International Conference on Design Theory and Methodology/1st International Conference on Micro and Nano Systems, Vol 3, Part a and B* **2008**, 967.

[69] M. Niggemann, B. Zimmermann, J. Haschke, M. Glatthaar, A. Gombert, Organic solar cell modules for specific applications - From energy autonomous systems to large area photovoltaics. *Thin Solid Films* **2008**, *516*, 7181.

[70] B. Zimmermann, H. F. Schleiermacher, M. Niggemann, U. Wurfel, ITO-free flexible inverted organic solar cell modules with high fill factor prepared by slot die coating. *Solar Energy Materials and Solar Cells* **2011**, *95*, 1587.

[71] G. Dennler, C. Lungenschmied, H. Neugebauer, N. S. Sariciftci, A. Labouret, Flexible, conjugated polymer-fullerene-based bulk-heterojunction solar cells:

Basics, encapsulation, and integration. *Journal of Materials Research* **2005**, *20*, 3224.

[72] H. Shirakawa, E. J. Louis, A. G. MacDiarmid, C. K. Chiang, A. J. Heeger, Synthesis of electrically conducting organic polymers: halogen derivatives of polyacetylene, (CH). *Journal of the Chemical Society, Chemical Communications* **1977**, *0*, 578.

[73] Y. Numata, I. Ashraful, Y. Shirai, L. Y. Han, Preparation of donor-acceptor type organic dyes bearing various electron-withdrawing groups for dye-sensitized solar cell application. *Chemical Communications* **2011**, *47*, 6159.

[74] G. Yu, J. Gao, J. C. Hummelen, F. Wudl, A. J. Heeger, Polymer Photovoltaic Cells - Enhanced Efficiencies Via a Network of Internal Donor-Acceptor Heterojunctions. *Science* **1995**, *270*, 1789.

[75] F. C. Krebs, S. A. Gevorgyan, J. Alstrup, A roll-to-roll process to flexible polymer solar cells: model studies, manufacture and operational stability studies. *Journal of Materials Chemistry* **2009**, *19*, 5442.

[76] N. Espinosa, H. F. Dam, D. M. Tanenbaum, J. W. Andreasen, M. Jorgensen, F. C. Krebs, Roll-to-Roll Processing of Inverted Polymer Solar Cells using Hydrated Vanadium(V)Oxide as a PEDOT:PSS Replacement. *Materials* **2011**, *4*, 169.

[77] Y. G. Huang, J. K. Chen, Z. P. Yin, Y. L. Xiong, Roll-to-Roll Processing of Flexible Heterogeneous Electronics With Low Interfacial Residual Stress. *Ieee Transactions on Components Packaging and Manufacturing Technology* **2011**, *1*, 1368.

[78] G. A. Chamberlain, Organic solar cells: A review. *Solar Cells* **1983**, *8*, 47.

[79] J. G. Xue, B. P. Rand, S. Uchida, S. R. Forrest, Mixed donor-acceptor molecular heterojunctions for photovoltaic applications. II. Device performance. *Journal of Applied Physics* **2005**, *98*.

[80] Z. C. He, C. M. Zhong, S. J. Su, M. Xu, H. B. Wu, Y. Cao, Enhanced power-conversion efficiency in polymer solar cells using an inverted device structure. *Nature Photonics* **2012**, *6*, 591.

[81] Y. Furukawa, A. Sakamoto, H. Ohta, M. Tasumi, Raman Characterization of Polarons, Bipolarons and Solitons in Conducting Polymers. *Synthetic Metals* **1992**, *49*, 335.

[82] A. J. Heeger, S. Kivelson, J. R. Schrieffer, W. P. Su, Solitons in Conducting Polymers. *Reviews of Modern Physics* **1988**, *60*, 781.

[83] S. V. Novikov, D. H. Dunlap, V. M. Kenkre, P. E. Parris, A. V. Vannikov, Essential role of correlations in governing charge transport in disordered organic materials. *Physical Review Letters* **1998**, *81*, 4472.

[84] M. Vanderauweraer, F. C. Deschryver, P. M. Borsenberger, H. Bassler, Disorder in Charge-Transport in Doped Polymers. *Advanced Materials* **1994**, *6*, 199.

[85] P. M. Borsenberger, H. Bassler, Concerning the Role of Dipolar Disorder on Charge Transport in Molecularly Doped Polymers. *Journal of Chemical Physics* **1991**, *95*, 5327.

[86] M. Singh, Y. Tarutani, K. Takagi, Dynamics of Carrier Hopping in Exponential Band Tails of Quasi-One-Dimensional Systems in Electric-Field. *Physica Status Solidi B-Basic Research* **1995**, *189*, 499.

[87] T. Tiedje, A. Rose, A physical interpretation of dispersive transport in disordered semiconductors. *Solid State Communications* **1981**, *37*, 49.

[88] H. Bassler, Charge Transport in Disordered Organic Photoconductors - a Monte-Carlo Simulation Study. *Physica Status Solidi B-Basic Research* **1993**, *175*, 15.

[89] J. M. Lluch, Perspective on "On the theory of oxidation-reduction reactions involving electron transfer. I" - Marcus RA (1956) J Chem Phys 24 : 966-978. *Theoretical Chemistry Accounts* **2000**, *103*, 231.

[90] A. Miller, E. Abrahams, Impurity Conduction at Low Concentrations. *Phys. Rev.* **1960**, *120*, 745.

[91] S. Shaked, S. Tal, Y. Roichman, A. Razin, S. Xiao, Y. Eichen, N. Tessler, Charge density and film morphology dependence of charge mobility in polymer field-effect transistors. *Advanced Materials* **2003**, *15*, 913.

[92] A. J. Mozer, N. S. Sariciftci, Negative electric field dependence of charge carrier drift mobility in conjugated, semiconducting polymers. *Chemical Physics Letters* **2004**, *389*, 438.

[93] S. M. Tuladhar, M. Sims, J. Kirkpatrick, R. C. Maher, A. J. Chatten, D. D. C. Bradley, J. Nelson, P. G. Etchegoin, C. B. Nielsen, P. Massiot, W. N. George, J. H. G. Steinke, Influence of alkyl chain length on charge transport in symmetrically substituted poly(2,5-dialkoxy-p-phenylenevinylene) polymers. *Physical Review B* **2009**, *79*.

[94] Y. Roichman, N. Tessler, Generalized Einstein relation for disordered semiconductors - Implications for device performance. *Applied Physics Letters* **2002**, *80*, 1948.

[95] J. Bisquert, G. Garcia-Belmonte, A. Munar, M. Sessolo, A. Soriano, H. J. Bolink, Band unpinning and photovoltaic model for P3HT:PCBM organic bulk heterojunctions under illumination. *Chemical Physics Letters* **2008**, *465*, 57.

[96] C. H. Lei, A. Das, M. Elliott, J. E. Macdonald, M. L. Turner, Au-poly(3-hexylthiophene) contact behaviour at high resolution. *Synthetic Metals* **2004**, *145*, 217.

[97] S. Gunes, H. Neugebauer, N. S. Sariciftci, Conjugated polymer-based organic solar cells. *Chemical Reviews* **2007**, *107*, 1324.

[98] Y. A. Shang, Q. K. Li, L. Y. Meng, D. Wang, Z. G. Shuai, Device simulation of low-band gap polymer solar cells: Influence of electron-hole pair dissociation and decay rates on open-circuit voltage. *Applied Physics Letters* **2010**, *97*.

[99] I. Riedel, E. von Hauff, H. Parisi, N. Martin, F. Giacalone, V. Dyakonov, Diphenylmethanofullerenes: New and efficient acceptors in bulk-heterojunction solar cells. *Advanced Functional Materials* **2005**, *15*, 1979.

[100] B. A. Collins, J. R. Tumbleston, H. Ade, Miscibility, Crystallinity, and Phase Development in P3HT/PCBM Solar Cells: Toward an Enlightened Understanding of Device Morphology and Stability. *The Journal of Physical Chemistry Letters* **2011**, *2*, 3135.

[101] K. Vakhshouri, D. R. Kozub, C. Wang, A. Salleo, E. D. Gomez, Effect of Miscibility and Percolation on Electron Transport in Amorphous Poly(3-Hexylthiophene)/Phenyl-C_{61}-Butyric Acid Methyl Ester Blends. *Physical Review Letters* **2012**, *108*, 026601.

[102] S. Mukhopadhyay, A. J. Das, K. S. Narayan, High-Resolution Photocurrent Imaging of Bulk Heterojunction Solar Cells. *Journal of Physical Chemistry Letters* **2013**, *4*, 161.
[103] K. Vakhshouri, S. V. Kesava, D. R. Kozub, E. D. Gomez, Characterization of the mesoscopic structure in the photoactive layer of organic solar cells: A focused review. *Materials Letters* **2013**, *90*, 97.
[104] S. K. Hau, H. L. Yip, N. S. Baek, J. Y. Zou, K. O'Malley, A. K. Y. Jen, Air-stable inverted flexible polymer solar cells using zinc oxide nanoparticles as an electron selective layer. *Applied Physics Letters* **2008**, *92*.
[105] D. Angmo, M. Hosel, F. C. Krebs, All solution processing of ITO-free organic solar cell modules directly on barrier foil. *Solar Energy Materials and Solar Cells* **2012**, *107*, 329.
[106] B. Y. Yu, A. Tsai, S. P. Tsai, K. T. Wong, Y. Yang, C. W. Chu, J. J. Shyue, Efficient inverted solar cells using TiO(2) nanotube arrays. *Nanotechnology* **2008**, *19*.
[107] B. Zimmermann, U. Wurfel, M. Niggemann, Longterm stability of efficient inverted P3HT:PCBM solar cells. *Solar Energy Materials and Solar Cells* **2009**, *93*, 491.
[108] H. Cheun, C. Fuentes-Hernandez, Y. H. Zhou, W. J. Potscavage, S. J. Kim, J. Shim, A. Dindar, B. Kippelen, Electrical and Optical Properties of ZnO Processed by Atomic Layer Deposition in Inverted Polymer Solar Cells. *Journal of Physical Chemistry C* **2010**, *114*, 20713.
[109] C. H. Hsieh, Y. J. Cheng, P. J. Li, C. H. Chen, M. Dubosc, R. M. Liang, C. S. Hsu, Highly Efficient and Stable Inverted Polymer Solar Cells Integrated with a Cross-Linked Fullerene Material as an Interlayer. *Journal of the American Chemical Society* **2010**, *132*, 4887.
[110] H. S. Wang, S. Y. Chen, M. H. Su, Y. L. Wang, K. H. Wei, Inverted heterojunction solar cells incorporating fullerene/polythiophene composite core/shell nanorod arrays. *Nanotechnology* **2010**, *21*.
[111] J. Bandara, K. Shankar, C. A. Grimes, M. Thelakkat, Efficient and stable, structurally inverted poly(3-hexylthiopen): [6,6]-phenyl-C61-butyric acid methyl ester heterojunction solar cells with fibrous like poly(3-hexylthiopen). *Thin Solid Films* **2011**, *520*, 582.
[112] J. M. Sun, Y. X. Zhu, X. F. Xu, L. F. Lan, L. J. Zhang, P. Cai, J. W. Chen, J. B. Peng, Y. Cao, High Efficiency and High V-oc Inverted Polymer Solar Cells Based on a Low-Lying HOMO Polycarbazole Donor and a Hydrophilic Polycarbazole Inter layer on ITO Cathode. *Journal of Physical Chemistry C* **2012**, *116*, 14188.
[113] S. Wilken, T. Hoffmann, E. von Hauff, H. Borchert, J. Parisi, ITO-free inverted polymer/fullerene solar cells: Interface effects and comparison of different semi-transparent front contacts. *Solar Energy Materials and Solar Cells* **2012**, *96*, 141.
[114] D. Gupta, M. Bag, K. S. Narayan, Area dependent efficiency of organic solar cells. *Applied Physics Letters* **2008**, *93*.
[115] A. Manor, E. A. Katz, T. Tromholt, B. Hirsch, F. C. Krebs, Origin of size effect on efficiency of organic photovoltaics. *Journal of Applied Physics* **2011**, *109*.

[116] W.-I. Jeong, J. Lee, S.-Y. Park, J.-W. Kang, J.-J. Kim, Reduction of Collection Efficiency of Charge Carriers with Increasing Cell Size in Polymer Bulk Heterojunction Solar Cells. *Advanced Functional Materials* **2011**, *21*, 343.

[117] C. Lin, E. Y. Lin, F. Y. Tsai, Enhanced Thermal Stability and Efficiency of Polymer Bulk-Heterojunctioin Solar Cells by Low-Temperature Drying of the Active Layer. *Advanced Functional Materials* **2010**, *20*, 834.

[118] M. D. Wang, Q. Tang, J. An, F. Y. Xie, J. A. Chen, S. Z. Zheng, K. Y. Wong, Q. A. Miao, J. B. Xu, Performance and Stability Improvement of P3HT:PCBM-Based Solar Cells by Thermally Evaporated Chromium Oxide (CrO(x)) Interfacial Layer. *Acs Applied Materials & Interfaces* **2010**, *2*, 2699.

[119] H. C. Chen, C. W. Lai, I. C. Wu, H. R. Pan, I. W. P. Chen, Y. K. Peng, C. L. Liu, C. H. Chen, P. T. Chou, Enhanced Performance and Air Stability of 3.2% Hybrid Solar Cells: How the Functional Polymer and CdTe Nanostructure Boost the Solar Cell Efficiency. *Advanced Materials* **2011**, *23*, 5451.

[120] S. Chambon, A. Rivaton, J.-L. Gardette, M. Firon, L. Lutsen, Aging of a donor conjugated polymer: Photochemical studies of the degradation of poly[2-methoxy-5-(3′,7′-dimethyloctyloxy)-1,4-phenylenevinylene]. *Journal of Polymer Science Part A: Polymer Chemistry* **2007**, *45*, 317.

[121] M. Manceau, S. Chambon, A. Rivaton, J.-L. Gardette, S. Guillerez, N. Lemaître, Effects of long-term UV–visible light irradiation in the absence of oxygen on P3HT and P3HT:PCBM blend. *Solar Energy Materials and Solar Cells* **2010**, *94*, 1572.

[122] C. J. Brabec, G. Zerza, G. Cerullo, S. De Silvestri, S. Luzzati, J. C. Hummelen, S. Sariciftci, Tracing photoinduced electron transfer process in conjugated polymer/fullerene bulk heterojunctions in real time. *Chemical Physics Letters* **2001**, *340*, 232.

[123] M. O. Reese, A. M. Nardes, B. L. Rupert, R. E. Larsen, D. C. Olson, M. T. Lloyd, S. E. Shaheen, D. S. Ginley, G. Rumbles, N. Kopidakis, Photoinduced Degradation of Polymer and Polymer-Fullerene Active Layers: Experiment and Theory. *Advanced Functional Materials* **2010**, *20*, 3476.

[124] C. H. Peters, I. T. Sachs-Quintana, W. R. Mateker, T. Heumueller, J. Rivnay, R. Noriega, Z. M. Beiley, E. T. Hoke, A. Salleo, M. D. McGehee, The Mechanism of Burn-in Loss in a High Efficiency Polymer Solar Cell. *Advanced Materials* **2012**, *24*, 663.

[125] M. Glatthaar, M. Riede, N. Keegan, K. Sylvester-Hvid, B. Zimmermann, M. Niggemann, A. Hinsch, A. Gombert, Efficiency limiting factors of organic bulk heterojunction solar cells identified by electrical impedance spectroscopy. *Solar Energy Materials and Solar Cells* **2007**, *91*, 390.

[126] M. Glatthaar, N. Mingirulli, B. Zimmermann, T. Ziegler, R. Kern, M. Niggemann, A. Hinsch, A. Gombert, Impedance spectroscopy on organic bulk-heterojunction solar cells. *Physica Status Solidi a-Applications and Materials Science* **2005**, *202*, R125.

[127] F. C. Krebs, T. Tromholt, M. Jorgensen, Upscaling of polymer solar cell fabrication using full roll-to-roll processing. *Nanoscale* **2010**, *2*, 873.

[128] F. C. Krebs, R. Sondergaard, M. Jorgensen, Printed metal back electrodes for R2R fabricated polymer solar cells studied using the LBIC technique. *Solar Energy Materials and Solar Cells* **2011**, *95*, 1348.

[129] M. P. de Jong, L. J. van IJzendoorn, M. J. A. de Voigt, Stability of the interface between indium-tin-oxide and poly(3,4-ethylenedioxythiophene)/poly(styrenesulfonate) in polymer light-emitting diodes. *Applied Physics Letters* **2000**, *77*, 2255.

[130] E. Voroshazi, B. Verreet, A. Buri, R. Muller, D. Di Nuzzo, P. Heremans, Influence of cathode oxidation via the hole extraction layer in polymer:fullerene solar cells. *Organic Electronics* **2011**, *12*, 736.

[131] E. Voroshazi, B. Verreet, T. Aernouts, P. Heremans, Long-term operational lifetime and degradation analysis of P3HT: PCBM photovoltaic cells. *Solar Energy Materials and Solar Cells* **2011**, *95*, 1303.

[132] M. Hermenau, M. Riede, K. Leo, S. A. Gevorgyan, F. C. Krebs, K. Norrman, Water and oxygen induced degradation of small molecule organic solar cells. *Solar Energy Materials and Solar Cells* **2011**, *95*, 1268.

[133] K. Norrman, N. B. Larsen, F. C. Krebs, Lifetimes of organic photovoltaics: Combining chemical and physical characterisation techniques to study degradation mechanisms. *Solar Energy Materials and Solar Cells* **2006**, *90*, 2793.

[134] K. Norrman, S. A. Gevorgyan, F. C. Krebs, Water-Induced Degradation of Polymer Solar Cells Studied by (H2O)-O-18 Labeling. *Acs Applied Materials & Interfaces* **2009**, *1*, 102.

[135] F. C. Krebs, J. Alstrup, H. Spanggaard, K. Larsen, E. Kold, Production of large-area polymer solar cells by industrial silk screen printing, lifetime considerations and lamination with polyethyleneterephthalate. *Solar Energy Materials and Solar Cells* **2004**, *83*, 293.

[136] J. W. Jung, J. W. Jo, W. H. Jo, Enhanced Performance and Air Stability of Polymer Solar Cells by Formation of a Self-Assembled Buffer Layer from Fullerene-End-Capped Poly(ethylene glycol). *Advanced Materials* **2011**, *23*, 1782.

[137] J. Granstrom, J. S. Swensen, J. S. Moon, G. Rowell, J. Yuen, A. J. Heeger, Encapsulation of organic light-emitting devices using a perfluorinated polymer. *Applied Physics Letters* **2008**, *93*.

[138] Z. X. Wu, L. D. Wang, C. Chang, Y. Qiu, A hybrid encapsulation of organic light-emitting devices. *Journal of Physics D-Applied Physics* **2005**, *38*, 981.

Chapter2
Materials and Methods

"I'm trying to assemble materials for a different mode of life."- Henry Flynt

2.1 Introduction

The recipe for a good device involves the choice of the right set of materials and their optimal processing. Semiconducting polymers constitute the active material or the light absorbers in solar cells. Buffer materials improve hole and electron conductivity as well as charge collection. Electrodes of the right work function are essential for charge collection. The assembly of these materials in an optimal manner gives rise to highly efficient devices. Along with electronic materials, this chapter also introduces fluorescent dye materials utilized in the light harvesting experiments and elastomers for microlenses.

2.2 Solar cell related materials

Solar cell related materials include donor polymers, acceptor small molecules, electrode materials like Aluminium and alloys, buffer layers for hole and electron transport and dyes for down-conversion of transmitted light.

2.2.1 Donor polymers

Polymeric semiconductors can be designed to have suitable optical band-gap and high charge mobility leading to high power conversion efficiency. The structure of these materials plays an important role in deciding the electronic and optical properties of the solar cell. Low band-gap co-polymers have recently shown to be promising candidates in BHJ solar cells with power conversion efficiency of above 8% [1]. These co-polymers have alternating D-A units facilitating intra-chain coupling of electron donating and accepting units leading to lowering of the band-gap. Small band-gaps can absorb low energy infrared photons leading to high short circuit currents [2].

PCPDTBT:

(a)

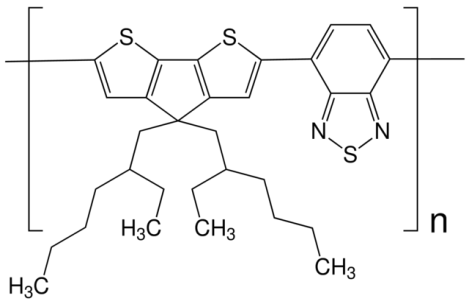

(b)

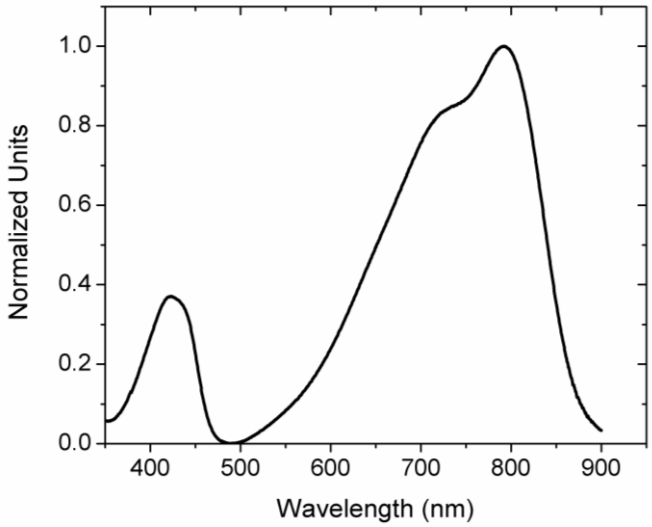

HOMO: 5.1 eV Bang-gap: 1.5 eV

LUMO: 3.6 ev

μ_{hole} : 3 x 10^{-3} cm^2 $V^{-1}s^{-1}$

Figure 2.1*: Electronic and optical properties of PCPDTBT. (a) Chemical structure. (b) Absorption spectrum*

PBDTTT-C-T:

(a)

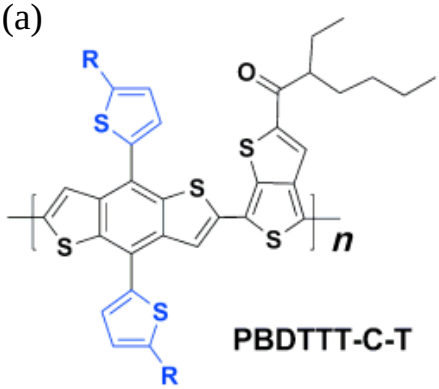

(b)

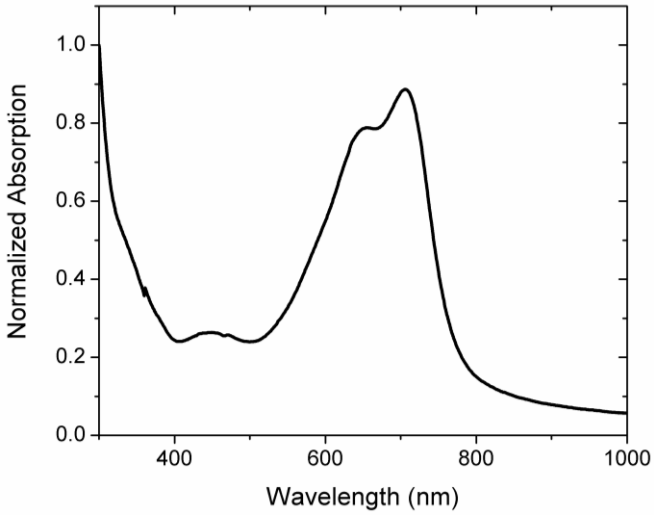

HOMO: 5.11 eV

LUMO: 3.25 eV

Band-gap: 1.58 eV

μ_{hole} :0.27 cm^2 $V^{-1}s^{-1}$

Figure 2.2*: Electronic and optical properties of PBDTTT-C-T. (a) Chemical structure. (b) Absorption spectrum*

An important class of low band gap polymers consist of electron deficient units like benzothiadiazole (BT) which are covalently attached to the electron rich units like thiophenes on both sides [1-4]. An example of such a co-polymer is Poly[2,1,3-benzothiadiazole-4,7-diyl[4,4-bis(2-ethylhexyl)-4H-cyclopenta[2,1-b:3,4-b']dithiophene-2,6-diyl]] (PCPDTBT) [4-7]. These polymers absorb up to 900 nm in the red-infrared red region of the spectrum (Figure 2.1) and provide larger currents but smaller open circuit voltage as predicted by Shockley-Queisser limit [8]. A major drawback of these polymers is the presence of low absorption region in the green part of spectrum. Hence they have shown efficiency of about 5% as compared to the newly synthesized class of polymer-poly{[4,8-bis-(2-ethyl-hexyl-thiophene-5-yl)-benzo[1,2-b:4,5-b′]dithiophene-2,6-diyl]-alt-[2-(2′-ethyl-hexanoyl)-thieno[3,4-b]thiophen-4,6 diyl]}(PBDTTT-C-T) (Figure 2.2), which show a PCE of above 8.8% [9].

2.2.2 Acceptors

PCBM:

Fullerenes have been the most popular n-type semiconductor molecules in BHJ solar cells so far [10]. They seem to work with most donor polymers, although in different concentrations. The most widely used to fullerene derivatives are phenyl-C61-butyric acid methyl ester or PCBM[60] and PCBM[70] which is a C70 derivative (Figure 2.3). Fullerenes haven't found any competing materials yet as they have excellent solubility in a host of organic solvents, high electron mobility, appropriate LUMO levels and good film morphology.

Ultra-fast spectroscopy of polymer-fullerene blends shows that the forward photo-induced electron transfer is a very fast process occurring in the sub-picosecond timescale [11]. The optimum morphology and the size of the domains are arrived at from exciton diffusion length of C60 which is of the order of 40 nm. Very high electron mobility up to 6 $cm^2V^{-1}s^{-1}$ have been reported [12-13]. Fullerene derivatives have suitable LUMO levels (-3.7 eV) which are ideal for most donors polymers for efficient photo-induced electron transfer. The HOMO levels (- 6.1 eV) are also positioned so as to avoid electron transfer back to the donor. PCBM[60] though popular, has limited absorption and modifications

of the fullerene lead to increased optical absorption and larger efficiency (C_{70} and C_{84}). PCBM[70] has shown efficiencies greater than 9% in combination with some low band-gap polymers like PTB7 [8, 14-15].

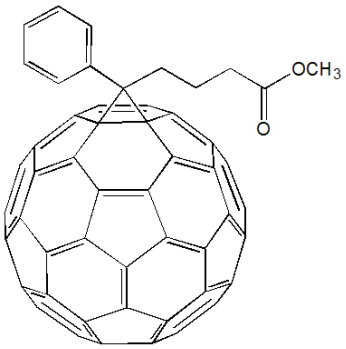

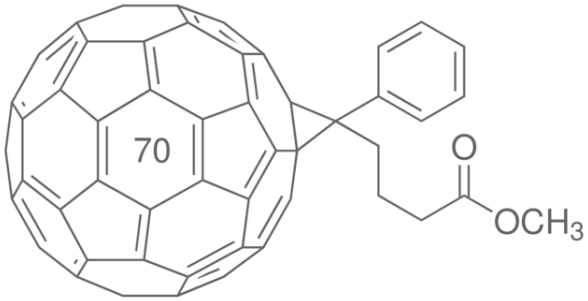

HOMO: 6.1 eV

LUMO: 4.3 eV

Band-gap: 1.8 eV $\mu_{electron} > 10^{-3}$ cm^2 V^{-1} s^{-1}

***Figure 2.3**: Electronic properties of PCBM[60] and PCBM[70].*

2.2.3 Conducting polymer buffer layers

PEDOT:PSS

Buffer conducting layers are essential in solar cells to increase charge collection and the fill factor. Typically, a thin buffer layer (40 nm) of conducting polymer poly(3,4-ethylenedioxythiophene) : poly(4-styrenesulfonic acid) (PEDOT:PSS) is spin-coated on the transparent conducting electrode in order to improve hole collection. PEDOT:PSS is commercially available as a water based dispersion of colloidal particles of PEDOT and PSS. PSS is introduced as a stabilizer during polymerization of PEDOT [16]. Conductivity of PEDOT:PSS is often improved upon annealing or addition of dopants.

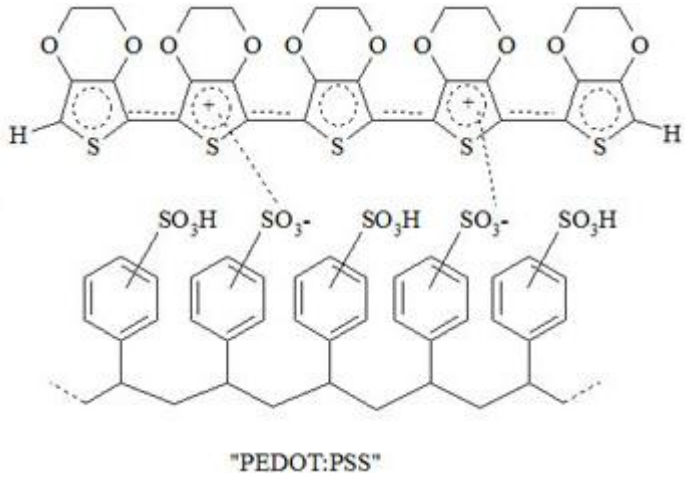

***Figure 2.4**: Electronic properties of PEDOT:PSS.*

2.2.4 Metal electrodes

Low work-function metals are essential to enhance charge collection without barriers. Typically metals like Al (W_F=4.3 eV), or Ca (W_F=2.9 eV) or a combination of both, have been used as electrodes. They are coated using a vacuum evaporator under a pressure of 10^{-6} torr. Thin films of 40-100 nm can be obtained. But these films are prone to oxidative processes limiting the lifetime of devices if not encapsulated immediately. Hence interfacial materials like LiF have been used to improve electron collection and also lifetime [17], [18].

2.2.5 Oxide buffer layers

Oxides like ZnO and TiO_2 are extensively used in inverted solar cell geometries. They are easily processed using sol-gel methods and can be spray coated over large substrates. They act as good hole blocking and electron conducting layers and also enhance the stability of the devices [19-20]. Similarly, films of molybdenum oxide (MoO_3) or vanadium pentoxide (V_2O_5) are coated on the polymer in inverted structures to improve hole collection at gold/silver electrode [21].

2.2.6 Alloys

In this work, low melting alloys of Indium, Tin, Bismuth and Lead and their combinations have been utilized as electrodes for electron or hole collection. These alloys can be easily processed without the need for thermal evaporation.

Table 2.1: List of alloys and their melting points

Approx Liquidus Temp (^{o}F) (Numbers in brackets are in ^{o}C)	Antimony	Bismuth	Cadmium	Lead	Tin	Indium
117 (47)	0 %	44.7%	5.3%	22.6%	8.3%	19.1%
136 (58)	**0 %**	**49%**	**0%**	**18%**	**12%**	**21%**
140 (60)	0 %	47.5%	9.5%	25.4%	12.6%	5%
144 (62)	0 %	32.5%	0 %	0 %	16.5 %	51 %
147 (64)	0 %	48%	9.6%	25.6%	12.8%	4%
158 (70)	0 %	50%	10%	26.7%	13.3%	0%
158-190 (70-88)	0 %	42.5%	8.5%	37.7%	11.3%	0%
203 (95)	**0%**	**52.5%**	**0%**	**32%**	**15.5%**	**0%**
212 (100)	**0%**	**39.4%**	**0%**	**29.8%**	**30.8%**	**0%**
217-440 (103-227)	**9%**	**48%**	**0%**	**28.5%**	**14.5%**	**0%**
255 (124)	**0%**	**55.5%**	**0%**	**44.5%**	**0%**	**0%**
281 (138)	**0%**	**58%**	**0%**	**0%**	**42%**	**0%**
Low 281-338 (138-170)	0%	40%	0%	0%	60%	0%

They can be laminated on to BHJ solar cells and other devices thereby allowing for printing and roll-to-roll processing. Alloys provide a low cost alternative towards BHJ solar cells [22-24]. Excellent efficiencies > 6% have been achieved in our work without

the use of buffer layers [25]. Details regarding the fabrication procedure are presented later in Chapter 3. The row in blue shows the properties of the alloy utilized in the current work. The rows highlighted in red in Table 1 are suggestions for alloys that can be used for fabrication of stable, high-temperature deposited solar cells.

2.2.7 Additive materials

Since morphology is a key issue in BHJ solar cells, there have been attempts to control morphology by thermal annealing, solvent annealing using co-solvents and ternary solvents. Thermal annealing is effective in the case of crystalline donor materials. But most D-A polymers are amorphous and thermal annealing has a negligible effect on the morphology. Solvent additives have been very successful in controlling morphology and improving the photovoltaic efficiency. Alkane-dithiols have shown to increase the morphology of P3HT:PCBM blends from 2.5% to 5.5% [26-27]. Di-iodooctane is another popular additive that has been used to improve the performance of PCPDTBT, PBDTTT-C-T, PTB7 blends. These processing additives are high boiling point solvents that preferentially dissolve PCBM as compared to the donor polymer. Selective dissolution leads to the formation of three phases during the liquid-liquid phase separation- fullerene-additive phase, polymer phase and polymer-fullerene phase. These phases can be viewed using high resolution TEM [28]. Additives have a higher boiling point as compared to the host solvent and tend to stay even after the host has dried. Removal of the additive is a slow process and enables more control on phase separation leading to optimized BHJ morphology. Eventually the additive dries and is completely removed leading to PCBM diffusion to the surface. The role of the additive in optimizing morphology has been established and after the drying there are no traces of the additive as ascertained by FTIR, XPS and Raman Spectroscopy [28-29]. There are a host of additives that have been used to improve efficiency of BHJ devices. DMSO, PDMS, PET amongst many other additives have shown better device performance [30-32].

2.2.8 Dyes for solar cell

LDS 759 (Exciton, Inc.) dye (Benzothiazolium, 2-[[2-[2-[4-(dimethylamino) phenyl] ethenyl]-6-methyl-4H-pyran-4-ylidene]methyl]-3-ethyl perchlorate) was selected for light harvesting applications in this work. This dye is suitable for PCPDTBT as it absorbs efficiently in the low absorption region of PCPDTBT (Figure2.5). It also emits in the red-infrared region which is the high absorption region of PCPDTBT (Figure 2.5). Hence it down converts radiation in to more useful radiation leading to enhanced photocurrent.

Host materials:

LDS 759 is soluble in most solvents and can be doped in Poly methyl methacrylate (PMMA) or Poly vinylene difluoride host matrices to yield intensely emissive films.

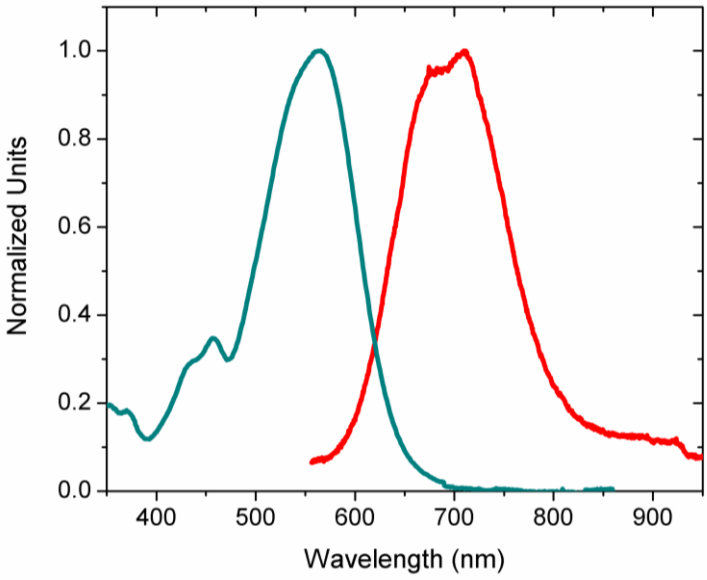

***Figure 2.5**: Absorption and emission spectrum (red) for LDS 759.*

2.3 Dyes for microlasers: DCM

DCM, 4-(Dicyanomethylene)-2-methyl-6-(4-dimethylaminostyryl)-4H-pyran, is a popular laser dye and has been widely utilized as a lasing material in a variety of laser geometries [33-34]. It can be excited or pumped efficiently at 532 nm, which is a popular green line second harmonic Nd:YAG laser. Emission of DCM is centered around 600-620 nm as shown in Figure 2.6.

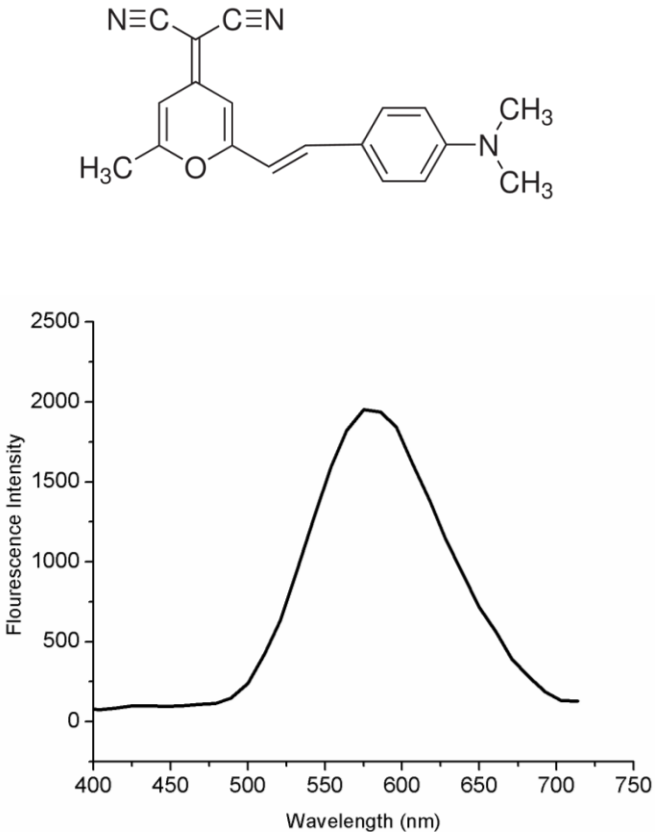

***Figure 2.6**: Chemical structure and emission spectrum of DCM.*

2.4 Microlens materials: PDMS

Poly dimethyl siloxane is a popular elastomeric material used in mircro-fluidics, lithography, soft molding among many other applications. PDMS is a clear viscous liquid, optically transparent and can be molded into various multi-dimensional shapes and

channels. PDMS is generally used with a curing agent (Sylgard 184) which is mixed in a ratio of 10 % (wt.). Under thermal treatment, the curing agent facilitates cross-linking of PDMS chains. This leads to the formation of a sufficiently cross-linked rubber-like PDMS film. These films are stretchable and can be used as substrates for a wide range of applications [35-38].

Poly dimethyl siloxane

Refractive Index: 1.43

Young's modulus: 360-870 KPa

Dielectric constant: 2.3-2.8

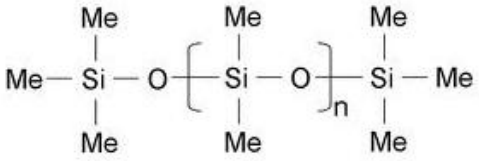

***Figure 2.7**: Chemical structure and properties of PDMS.*

In our experiments we exploit the excellent optical transmittance and the molding properties of PDMS to fabricate microlens arrays that are suitable for concentrating solar light in photovoltaic applications.

2.5 Device fabrication and characterization

The following section presents details about device fabrication procedures and the different characterization and testing methods.

2.5.1 Solar Cell Fabrication:

The device structures for normal geometry, typically consist of the following arrangement ITO/PEDOT:PSS/PCPDTBT:PCBM/Alloy or Al. Donor polymers are PCPDTBT (Konarka or Lumtec) or PBDTTT-C-T (Solarmer). Acceptors are PCBM[60] or PCBM[70] (Konarka or American Dye Source). PEDOT:PSS (Baytron P) is the hole transport layer, spun at about 2000 to 2500 rpm resulting in a 40 to 80 nm film. The alloy is a eutectic mixture of (In:Sn:Bi:Pb) with a melting point of 58^{o}C. PCPDTBT:PCBM blend is optimized in the ratio of 1:3.5, and spin cast at about 2200 rpm from a 30 mg/ml

solution in chlorobenzene with or without 1,8-Diiodooctance (DIO) as the additive. PBDTTT-C-T (Solarmer) is coated from a 10 mg/ml solution of 1,2-dichlorobenzene/DIO with PCBM[70] in the ratio 1:1.5.

The temperature of the molten alloy is maintained using a heating plate. A vertical translation stage is used to bring the ITO/Polymer-blend film in contact with the alloy film. The alloy is laminated and the temperature is gradually cooled to below the melting point of the alloy. Al is coated using a thermal evaporation unit (Hind HiVac) under 10^{-6} mbar pressure and a current of about 20 A.

Patterning solar cells

Patterned or pixelated solar cells have shown to exhibit better performances as compared to large un-pixelated devices. Patterning was carried out using commercially available polycarbonate sheets (LEXAN™) that were drilled (mechanically or laser assisted) or punched to create perforations ranging from 2 mm to 5 mm in diameter. The electrode was made to flow through these perforations giving rise to patterned solar cells.

Dye coating on Polycarbonate

LDS 759 (Exciton) is dissolved in a mixture of PVDF/DMA or PMMA/DMF in the weight ratio (0.01:0.20:4) and spin coated on to PC substrates before the patterning is carried out.

2.5.2 Solar Cell Characterization

Device are characterized using a Oriel Sol3A solar simulator (AM 1.5G, Class AAA, Newport) with a uniform illumination of 2 in. x 2 in or 5.1 cm x 5.1 cm. The test solar cell is connected to a sourcemeter (Keithley 2400) for I-V measurements. The data from the sourcemeter is collected vis a LabView program in to the computer. Device area is precisely measured using a calibrated optical microscope connected to a CCD camera. Optical masks are used in certain measurements to quantify the extent of peripheral contribution. Attempts are made to ensure that any overestimation of any overestimation of efficiency due to mask-less illumination would be minimized.

EQE measurements

A xenon lamp (Oriel) is used in combination with a monochromator (SPEX 500M, Jobin Yvon). Light from the spectrometer is split using a beam splitter and is incident on a calibrated Si-detector and the test cell. A multichannel multimeter (Keithley 2001) is used to simultaneously measure the current in the device and reference. Data is acquired using LabView™ software as shown in Figure 2.8. Further processing is carried out incorporating the responsivity of the reference detector to arrive at the EQE.

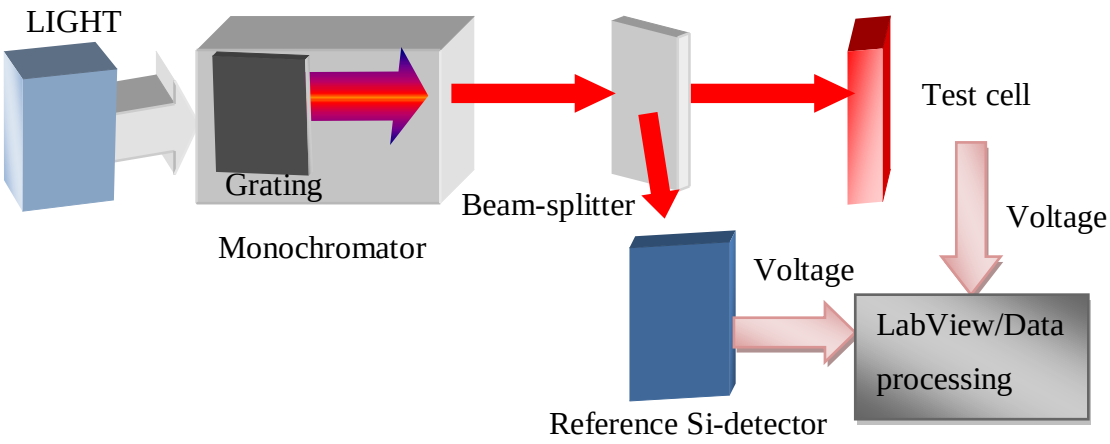

Figure 2.8: *Setup for EQE measurement.*

2.5.3 Optical Simulations:

Finite Difference Time Domain (FDTD) simulations are performed using the commercially available OptiFDTD™ 8.0 package. Time dependent Maxwell's equations are numerically solved using the FDTD approach. The device structure that is to be simulated is implemented in the designer module. The materials are then assigned appropriate parameters like the refractive index. Optical fields are then calculated by creating a suitable mesh depending upon the wavelength of excitation. In the present studies, optimized lateral and longitudinal mesh size is chosen as 40 nm along with anisotropic perfectly matched layer (APML) boundary conditions. Light sources in the simulation are modelled with transverse electric (TE) polarization. Additional parameters

are utilized to model light sources such as the pulse half-width in the case of Gaussian modulated sources and modal profiles.

Experimentally obtained absorption, transmission or reflection spectra or ellipsometric data like refractive index and extinction coefficient are utilized to construct a Lorentz-Drude (L-D) model for the material as shown below:

$$\varepsilon(\omega) = \varepsilon_{\infty} + \sum_{n=1}^{\infty} \left(\frac{\chi_o \, G_n \, \omega_{on}^2}{\omega_{on}^2 + i\Gamma_n \omega - \omega^2} \right) \quad \text{.....(2.1)}$$

where, ω_{0n} are the resonant frequencies, G_n are related to the oscillator strengths, Γ_n are the damping coefficients, ε_∞ is the permittivity at $\omega=\infty$, χ_0 is the permittivity at $\omega=0$. An open source software RefFIT is used to fit data to a L-D model with reasonable fitting parameters. L-D models for the polymer blends and LDS 759 is included in the Appendix B. Other buffer layers are treated as dielectrics as they do not exhibit appreciable dispersion in the visible range. The refractive indices for PEDOT:PSS is taken as 1.53, ITO as 1.8, PVDF as 1.4 and PMMA as 1.5.

2.6 Capacitance-Voltage measurement

Capacitance-voltage measurements are carried out with the Keithley parameter analyzer. Compensation procedures are carried out to eliminate any parasitic capacitances due to the cables at open and short circuit conditions. The voltage is swept from 0-2V in steps of 40-50 mV. Measurements are carried out at 10 kHz with a rms amplitude of 100 mV.

2.7 Noise measurement

Noise measurements are carried out by placing the device in a custom built Faraday cage. A 20W DC powered tungsten lamp is powered by a 6 V, 4 Ah, battery in order to eliminate 50 Hz line noise that may interfere with spectral information from the device (Figure 2.9). Data is collected using LeCroy (Waverunner 6100A) oscilloscope at

250 kHz and 2 MHz sampling rates in order to capture the low frequency and high frequency noise features, respectively.

Pre-amplifier

DLPCA-200 (FEMTO Msstechnik GmbH). NEP = 13 - 450 $fAHz^{-1/2}$ at High Speed 10^7 -10^9gain). Coupling (AC // 5 pF) resistance 50 Ω-1 kΩ. Maximum input current 1 nA-1μA. The gain-bandwidth plot is shown in Figure 2.10.

Noise data analysis

Algorithms are applied on the time series data to compute Fast Fourier Transform (FFT) (See Appendix for MATLAB code). The time series data is split in to several sub-windows and FFT (4096-8192 points) is carried out on each window. The data is averaged in order to maximize the signal-to-noise ratio. The resulting spectrum is referred to as the power spectral density.

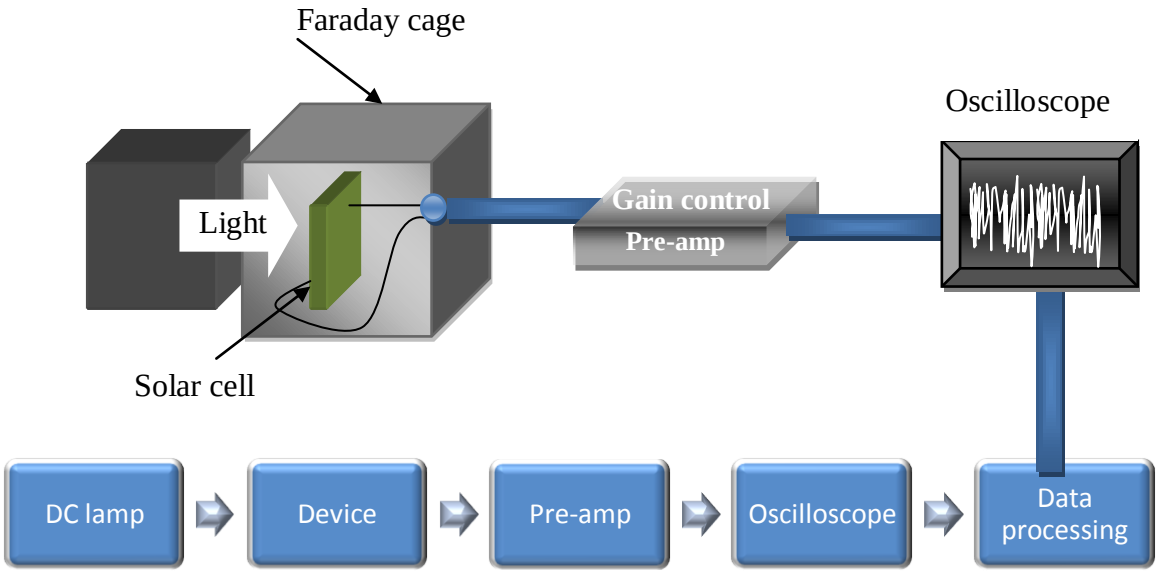

Figure 2.9: *Schematic of noise measurement in organic solar cells.*

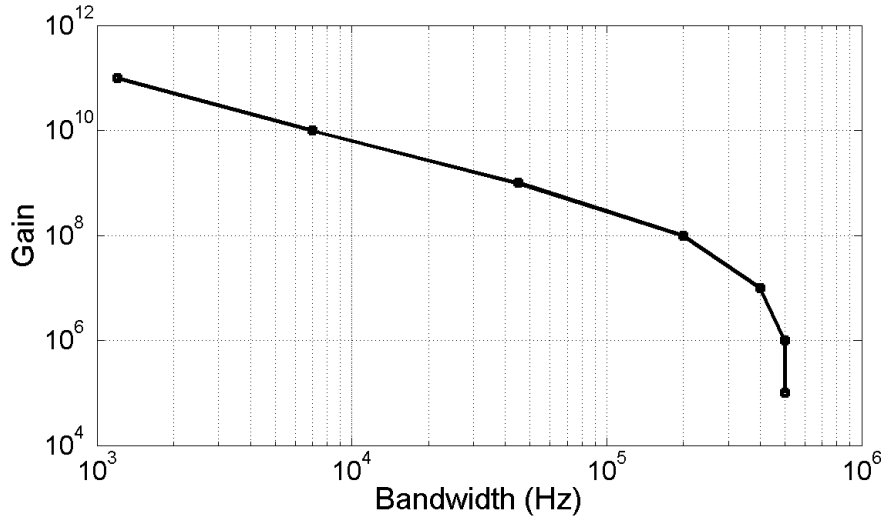

Figure 2.10: *Gain-bandwidth plot of the pre-amp.*

2.8 Optical microscopy

Confocal microscopy is carried out on dye doped polymer fibres in order to probe the uniformity of the dye distribution. FV1000 (Olympus) and LSM 700 (Zeiss) microscopes are utilized with laser lines of 543 nm or 540 nm corresponding to the absorption of the dye (DCM). The spectral scanning units provide the spatial emission profiles and the z-stack provides the 3D distribution of the dye in the fibre.

2.9 AFM and Kelvin probe microscopy

The surface of the alloy was characterized for roughness and electrical properties like work-function using AFM and KPM, respectively. A JPK AFM (Nanowizard 3) was used with an AFM tip with resolution of 2 nm. KPM measurements were performed in the AC mode with a voltage signal applied to the cantilever tip.

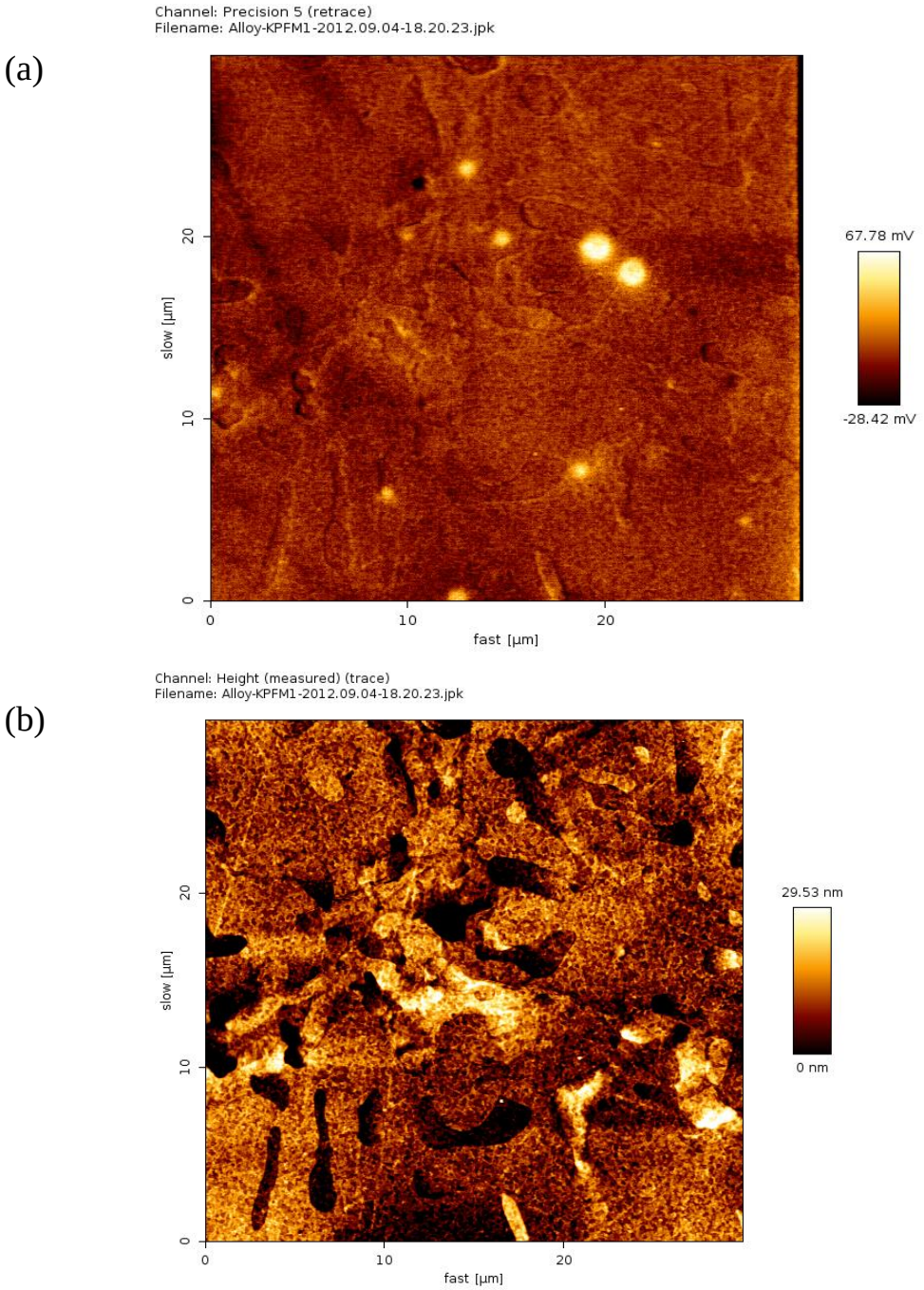

Figure 2.11: *(a) Kelvin probe force microscope image of alloy surface. (b) AFM image of the alloy surface cast from cover glass.*

The tip was coated with platinum/chrome with a known work-function. Prior to carrying out measurements on the alloy, gold and ITO films were utilized for calibration. The work function of the alloy was determined to be in the range of 4.3 to 4.4 eV.

2.10 Scanning electron microscopy

SEM is utilized to probe the distribution and shape of microlenses as well as polymer microfibres. Field Effect SEM is also utilized to image microfibres and to probe the cross-section as it does not require additional metal sputtering steps. Fibres are placed on substrates like silicon or ITO/glass and the samples are tilted from 0-40^{o} to observe the fibre cross-section.

2.11 Electrospinning of polymer fibres

Fibres are electrospun from a PS/THF (30 wt %) solution with 4-dicyanomethylene-2-methyl-6-p-dimethylaminostyryl-4H-pyran (DCM, Sigma Aldrich) dye (5 wt%) as the active molecular species. A voltage of 6 kV is applied across the metallic syringe and the substrate ground plane which are maintained at distance of about 2 cm (Figure 2.11). Fibres are either collected on a substrate and isolated using HF solution or scooped from the syringe with a glass slide. We choose the system parameters such that non-cylindrical fibres are favoured over the uniform cross-section fibres [17]. Some fibres are cleaved (one or two edges) with a razor blade to induce defects that provide additional reflections.

2.11.1 Characterization of fibres

Fibres are characterized by SEM and z-stack confocal microscopy in order to access the cross-sectional shape. A 543 nm He-Ne laser is used as the excitation source in the confocal measurements and the z step is taken as 1 μm. The deviation from a uniform cylindrical cross-section is evidenced from the SEM and confocal images. Spectral scans are also carried out using confocal microscopy.

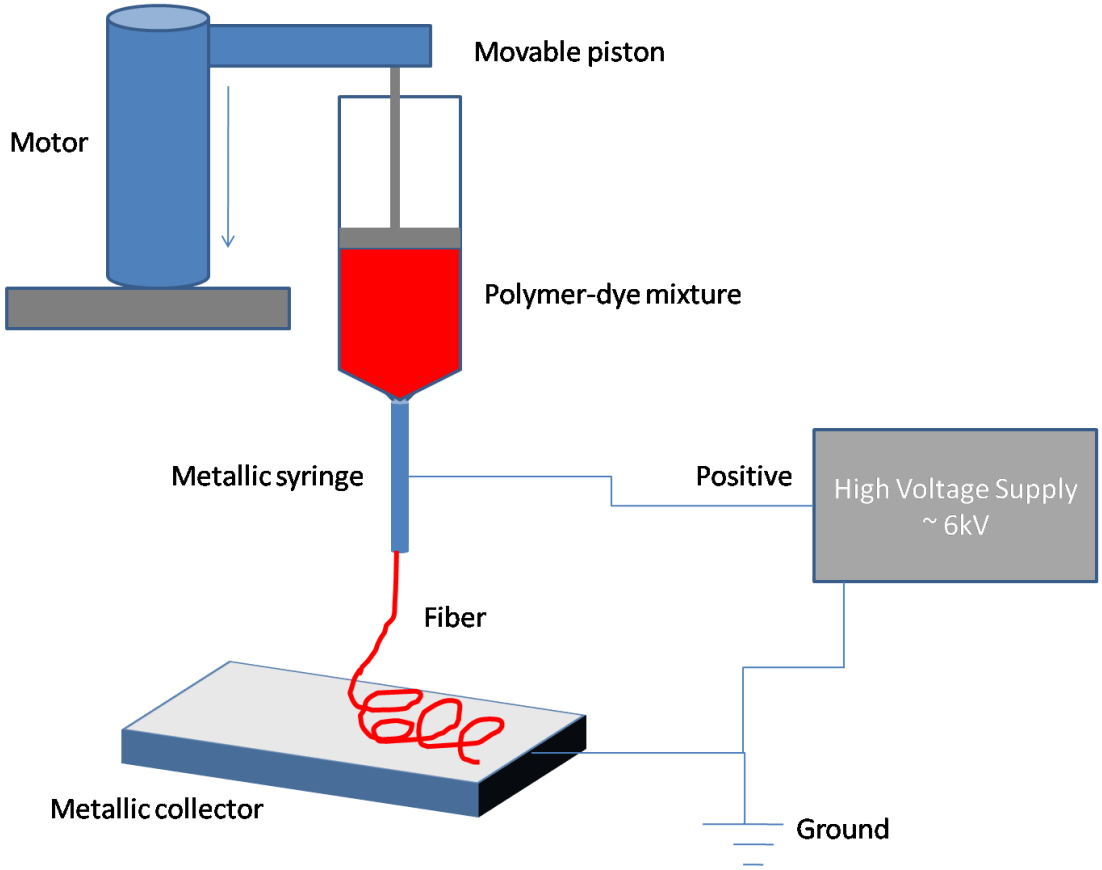

Figure 2.12: *Setup for electrospinning of fibres. A motorized stage pushes the piston in a metallic syringe containing the polymer-dye solution. As the solution emerges from the tip, the electric field deforms the drop into a cone. The cone elongates to form fibres. The fibres are collected on a glass slide placed on a metallic substrate.*

2.11.2 Substrate preparation

In 2D resonators based on dye-doped polymer films, the substrate plays a very important role in confining light in the active layer. However, in the present case where the fibre diameter is of the order of 10s of microns, the nature of the substrate ceases to be critical. Typically a low index substrate is required in order to achieve better confinement. The isolated fibres which have a refractive index in the range of 1.65 (at λ=600nm) were placed on top of a low refractive index (n=1.34) Cytop© coated glass

substrate. Cytop© films are coated at 3000 rpm with an acceleration of 2000 rpm/s for 30 s. They are annealed at 120 ^{o}C for 5 min on a hot plate and this procedure is repeated thrice to obtain 2 μm thick films. This step is followed by annealing the film at 180 ^{o}C for 2 hrs.

2.11.3 Optical setup for excitation of fibres

The fibres are pumped with a frequency doubled Nd-YAG laser (532 nm, 500 ps pulse width, 10 Hz repetition rate). The typical spot size of the pump is 200 μm. The direction of the pump beam is set normal to the substrate plane containing the fibre. The emitted light is collected along the substrate plane. Spectra are collected using a lens to fibre coupler which is in turn connected to a spectrometer and the spectra are integrated over 30 pump pulses. Pump intensity is controlled using a polarizer half wave plate combination, and the pump polarization is then controlled by another half wave plate. Optical microscopy of guiding in the fibres is carried out on an inverted microscope equipped with a digital camera (Moticam 480, Motic) and a pump blocking filter.

2.12 Review of printed organic solar cells

The motivation of research in OSC is driven by low cost materials along with cost effective fabrication and processing which will enable cheaper alternatives for energy in comparison to the silicon and other solar cell technologies. Demonstration of small area cells (few sq. mm) which have been fabricated by techniques such as spin coating and thermal evaporation are routine. But real devices capable of delivering useful power need to consider device area and long term stability. As discussed in Chapter 1, the unstable nature of semiconducting polymers under illumination combined with the reactive nature of low work-function metals has lead to devices fabrication in the inert atmosphere of a glove box. Such fabrication and processing techniques cannot, for obvious reasons, be used to scale the device area. Even though PCE >9% has been reported it is limited to an area of a few mm^2 to around 1 cm^2. Hence there is a need for a paradigm shift of manufacturing process that will enable this research to mature to a technology. Spin coating and high vacuum thermal evaporation are suitable for small demonstrations at the

laboratory level but do not support high throughput production. Utilizing the flexible nature of these devices roll-to-roll (R2R) processing is the solution to produce large area devices in a short time. It turns out that equipment needed to print devices is extremely expensive and complicated to operate, at the same time requiring to dispose a large amount of expensive polymeric semiconductors. And there is no guarantee that the efficiency will preserved when the area is scaled up. In fact as discussed in Chapter 1, the PCE is not retained in large area devices due to various losses. In light of these challenges, if this research has to be translated to a technology, a considerable effort is required in improving R2R processing and makes it feasible and accessible to minimize costs. Some of the different printing and coating techniques are presented in this section that support R2R processing and aim at large scale production of OSC in the future.

2.12.1 Types of printing

Various printing geometries are presented in this section, many of which have been adapted from existing printing technologies.

2.12.1.1 Gravure printing

A popular printing method that has been adapted to printing solar cells is gravure printing. This technique is widely used in printing of newspapers, magazines and other media where a high volume print is necessary. As shown in Fig. 2.13, the technique involves i) transfer of ink from small cavities forming the pattern on the gravure cylinder, ii) contacting of the print media with the gravure cylinder accompanied by pressure from the impression cylinder. The pattern and depth of the cavities define the shape and thickness of the final imprint. The process of filling the cavities on the gravure cylinder occurs in a continuous manner and the residual or excess ink is removed by a doctor blade technique. Even though gravure printing works reasonably well for low viscous inks, it requires optimization of the ink's surface tension. Hence optimization is cumbersome and many times it is based on trial and error. The quality of the print is dependent on ink rheology, speed of printing, and the pressure applied by the impression cylinder. Due to these factors the use of gravure printing for solar cell fabrication has been reported in very few cases [39-42].

2.12.1.2 Flexographic printing

Flexographic printing unlike gravure printing is based on transfer of the ink from reliefs and not small cavities (Figure 2.13). The printing plate is generally made of a photopolymer and the pattern stands out from this plate. Fountain rollers in the 'flexo' system continuously transfer ink to the ceramic roller allowing ink to be transferred to the relief on the printing cylinder. Roll-to-roll flexographic printing has been recently demonstrated for printing highly conductive PEDOT:PSS and metal grids on the hole and electron collecting electrodes [43-44].

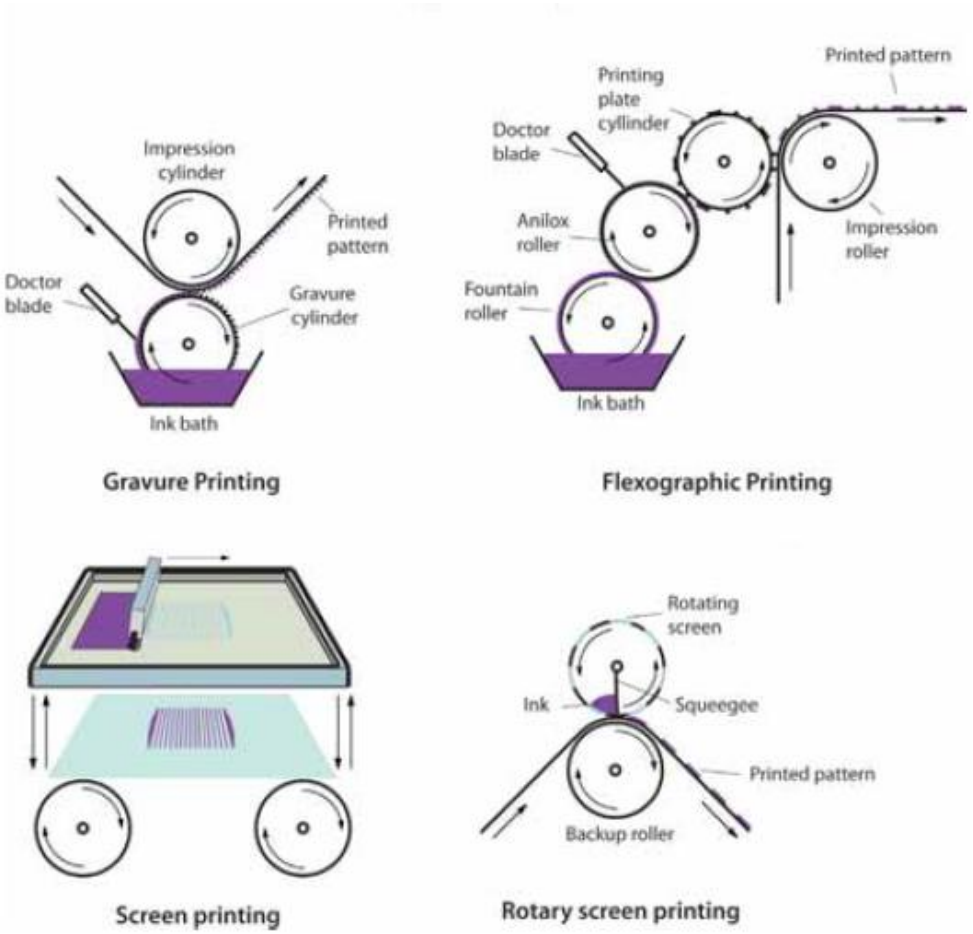

Figure 2.13: *Schematic of different printing methods. (Reprinted from R. Sondergaard, M. Hosel, D. Angmo, T. T. Larsen-Olsen, F. C. Krebs, Roll-to-roll fabrication of polymer solar cells. Materials Today* ***2012****, 15, 36. © 2012, with permission from Elsevier).*

Printing methods like flexographic, can be used to implement device geometries aiming at replacing ITO by alternative electrodes such as metal grids, which can be printed with an accuracy of 50 μm and lower [45]. However, it has not been used for printing the active polymeric blends [43].

2.12.1.3 Screen printing

In contrast to flexographic and gravure printing, screen printing is a method that allows for printing of thick wet layers and thick dry films. These films are ideal for printed electrodes that need to be thick in order to have highly conductive properties. One of the major drawbacks of thermal evaporation is the thickness of the deposited films being in the 50 to100 nm range. Such films are highly resistive and limit the current in the solar cells. With screen printing, typical layer thicknesses can be in the range of 10 to 500 μm. Screen printing geometries are of two types: i) flat-bed screen printing and ii) rotary screen printing. The basic principle of the two methods is the similar as shown in Figure 2.13. The ink formulation is forced through the mesh by a squeegee moving relative to the screen. This results in the printing of the required pattern on the substrate. There are also certain differences the operation of the two processes. The flat-bed printing method is inherently low cost and it is possible to make a single print at a time. It cannot be utilized to continuously print. However, for laboratory demonstration purposes and for initial development of inks it is sufficient. Rotary screen printing, on the other hand, utilizes a fixed internal squeegee with the ink contained inside the rotating cylinder. As compared to the flat-bed method, the mask is more expensive. But this method outscores the flat-bed method in terms of speed, edge resolution, achievable wet thickness ranges. Unlike the flat-bed technique, the rotary screen printing is a true roll-to-roll printing technique. It remains unpopular due to the expensive mask, but successful demonstrations have been reported for the printing of the front and back electrodes for polymer solar cells [46-47]. Additionally, it has also been utilized to print active layers unlike the flexographic printing technique [44, 48].

2.12.1.4 Knife coating and slot-die coating

Doctor blading is a very common laboratory technique to deposit films with reasonable precision and in a facile manner. Knife coating, in this regard is very similar to the doctor blading method. The coating process incorporated an ink reservoir that supplies ink to the meniscus before the knife can print the pattern (Figure 2.14). The knife gradually sweeps the ink resulting in a certain thickness of the film. Slot-die coating can only be used to coat stripes of a defined width along the web direction, inherently allowing for one-dimensional patterning. As the name suggest, a slot provides the ink using a pump and the wet thickness can be controlled by the speed of movement of the web or the supply rate of ink through the slot or both (Figure 2.14). Hence there are certain factors that finally define the limits of wet thicknesses that can be achieved with these methods. Properties of the ink are crucial along with the surface properties of the web. Wetting and compatibility of both are essential, so is the coating geometry.

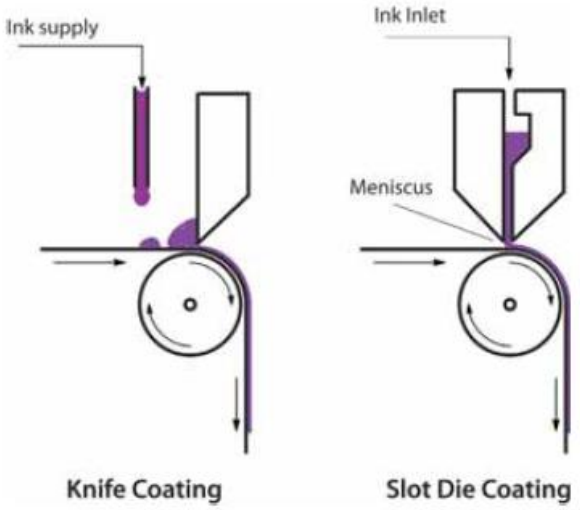

Figure 2.14:*Schematic of knife and slot-die coating (Reprinted from R. Sondergaard, M. Hosel, D. Angmo, T. T. Larsen-Olsen, F. C. Krebs, Roll-to-roll fabrication of polymer solar cells. Materials Today* ***2012****, 15, 36. © 2012, with permission from Elsevier).*

Several large area demonstrations of solar cells have been reported utilizing these techniques. Typically, several closely spaced stripes are coated at a few meters per minute, and the resulting solar cell module is capable of generating a current of several 100 mA and a voltage of 2-4 V [47, 49-51].

Summary

Electronic, optical and dielectric properties of various materials utilized in the thesis were presented in this chapter. Solar cell fabrication methods and several experimental setups utilized for characterization and probing the devices were introduced. Finally, a review of various printing and roll-to-roll technologies for solar cells was presented.

References

[1] J. Peet, J. Y. Kim, N. E. Coates, W. L. Ma, D. Moses, A. J. Heeger, G. C. Bazan, Efficiency enhancement in low-bandgap polymer solar cells by processing with alkane dithiols *Nature Materials* **2007**, *6*, 497.

[2] J. Y. Kim, Y. Qin, D. M. Stevens, V. Kalihari, M. A. Hillmyer, C. D. Frisbie, High Open-Circuit Voltage Photovoltaic Cells with a Low Bandgap Copolymer of Isothianaphthene, Thiophene, and Benzothiadiazole Units *J. Phys. Chem. C* **2009**, *113*, 21928.

[3] P. Boland, K. Lee, G. Namkoong, Device optimization in PCPDTBT:PCBM plastic solar cells *Solar Energy Materials and Solar Cells* **2010**, *94*, 915.

[4] J. Kettle, M. Horie, L. A. Majewski, B. R. Saunders, S. Tuladhar, J. Nelson, M. L. Turner, Optimisation of PCPDTBT solar cells using polymer synthesis with Suzuki coupling *Solar Energy Materials and Solar Cells* **2011**, *95*, 2186.

[5] P. Boland, K. Lee, G. Namkoong, Device optimization in PCPDTBT:PCBM plastic solar cells *Sol. Energy Mater. Sol. Cells* **2010**, *94*, 915.

[6] F. C. Jamieson, T. Agostinelli, H. Azimi, J. Nelson, J. R. Durrant, Field-Independent Charge Photogeneration in PCPDTBT/PC70BM Solar Cells *J. Phys. Chem. Lett.* **2010**, *1*, 3306.

[7] M. Koppe, H.-J. Egelhaaf, G. Dennler, M. C. Scharber, C. J. Brabec, P. Schilinsky, C. N. Hoth, Near IR Sensitization of Organic Bulk Heterojunction Solar Cells: Towards Optimization of the Spectral Response of Organic Solar Cells *Adv. Funct. Mater.* **2010**, *20*, 338.

[8] J. Y. Kim, K. Lee, N. E. Coates, D. Moses, T.-Q. Nguyen, M. Dante, A. J. Heeger, Efficient Tandem Polymer Solar Cells Fabricated by All-Solution Processing *Science* **2007**, *317*, 222.

[9] X. H. Li, W. C. H. Choy, L. J. Huo, F. X. Xie, W. E. I. Sha, B. F. Ding, X. Guo, Y. F. Li, J. H. Hou, J. B. You, Y. Yang, Dual Plasmonic Nanostructures for High Performance Inverted Organic Solar Cells *Advanced Materials* **2012**, *24*, 3046.

[10] J. Roncali, Linear pi-conjugated systems derivatized with C-60-fullerene as molecular heterojunctions for organic photovoltaics *Chemical Society Reviews* **2005**, *34*, 483.

[11] C. J. Brabec, G. Zerza, G. Cerullo, S. De Silvestri, S. Luzzati, J. C. Hummelen, S. Sariciftci, Tracing photoinduced electron transfer process in conjugated polymer/fullerene bulk heterojunctions in real time *Chemical Physics Letters* **2001**, *340*, 232.

[12] P. Peumans, A. Yakimov, S. R. Forrest, Small molecular weight organic thin-film photodetectors and solar cells *Journal of Applied Physics* **2003**, *93*, 3693.

[13] P. Peumans, A. Yakimov, S. R. Forrest, Small molecular weight organic thin-film photodetectors and solar cells (vol 93, pg 3693, 2003) *Journal of Applied Physics* **2004**, *95*, 2938.

[14] J. Peet, J. Y. Kim, N. E. Coates, W. L. Ma, D. Moses, A. J. Heeger, G. C. Bazan, Efficiency enhancement in low-bandgap polymer solar cells by processing with alkane dithiols *Nature Mater.* **2007**, *6*, 497.

[15] Z. C. He, C. M. Zhong, S. J. Su, M. Xu, H. B. Wu, Y. Cao, Enhanced power-conversion efficiency in polymer solar cells using an inverted device structure *Nature Photonics* **2012**, *6*, 591.

[16] J. Huang, P. F. Miller, J. S. Wilson, A. J. de Mello, J. C. de Mello, D. D. C. Bradley, Investigation of the Effects of Doping and Post-Deposition Treatments on the Conductivity, Morphology, and Work Function of Poly(3,4-ethylenedioxythiophene)/Poly(styrene sulfonate) Films *Adv. Funct. Mater.* **2005**, *15*, 290.

[17] M. Reyes-Reyes, K. Kim, D. L. Carroll, High-efficiency photovoltaic devices based on annealed poly(3-hexylthiophene) and 1-(3-methoxycarbonyl)-propyl-1-phenyl-(6,6)C[sub 61] blends *Appl. Phys. Lett.* **2005**, *87*, 083506.

[18] J.-H. Kim, S.-Y. Huh, T.-i. Kim, H. H. Lee, Thin pentacene interlayer for polymer bulk-heterojunction solar cell *Appl. Phys. Lett.* **2008**, *93*, 143305.

[19] M. Reinhard, J. Hanisch, Z. Zhang, E. Ahlswede, A. Colsmann, U. Lemmer, Inverted organic solar cells comprising a solution-processed cesium fluoride interlayer *Appl. Phys. Lett.* **2011**, *98*, 053303.

[20] S. Cho, K. Lee, A. J. Heeger, Extended Lifetime of Organic Field-Effect Transistors Encapsulated with Titanium Sub-Oxide as an 'Active' Passivation/Barrier Layer *Advanced Materials* **2009**, *21*, 1941.

[21] S. K. Hau, H.-L. Yip, A. K. Y. Jen, A Review on the Development of the Inverted Polymer Solar Cell Architecture *Polym. Rev.* **2010**, *50*, 474.

[22] M. Bag, D. Gupta, N. Arun, K. S. Narayan, Deformation of metallic liquid drop by electric field for contacts in molecular-organic electronics *Proceedings of the Royal Society a-Mathematical Physical and Engineering Sciences* **2009**, *465*, 1799.

[23] B. Omrane, C. K. Landrock, Y. Chuo, D. Hohertz, J. Aristizabal, B. Kaminska, K. L. Kavanagh, Long-lasting flexible organic solar cells stored and tested entirely in air *Applied Physics Letters* **2011**, *99*, 263305.

[24] J. F. Salinas, J. L. Maldonado, G. Ramos-Ortiz, M. Rodriguez, M. A. Meneses-Nava, O. Barbosa-Garcia, R. Santillan, N. Farfan, On the use of Woods metal for fabricating and testing polymeric organic solar cells: An easy and fast method *Solar Energy Materials and Solar Cells* **2011**, *95*, 595.

[25] A. J. Das, K. S. Narayan, Retention of Power Conversion Efficiency - from Small Area to Large Area Polymer Solar Cells *Advanced Materials* **2013**, *25*, 2193.

[26] J. K. Lee, W. L. Ma, C. J. Brabec, J. Yuen, J. S. Moon, J. Y. Kim, K. Lee, G. C. Bazan, A. J. Heeger, Processing Additives for Improved Efficiency from Bulk Heterojunction Solar Cells *J. Am. Chem. Soc.* **2008**, *130*, 3619.

[27] J. Peet, C. Soci, R. C. Coffin, T. Q. Nguyen, A. Mikhailovsky, D. Moses, G. C. Bazan, Method for increasing the photoconductive response in conjugated polymer/fullerene composites *Appl. Phys. Lett.* **2006**, *89*, 252105.

[28] J. T. Rogers, K. Schmidt, M. F. Toney, G. C. Bazan, E. J. Kramer, Time-Resolved Structural Evolution of Additive-Processed Bulk Heterojunction Solar Cells *J. Am. Chem. Soc.* **2010**, *134*, 2884.

[29] J. Peet, J. Y. Kim, N. E. Coates, W. L. Ma, D. Moses, A. J. Heeger, G. C. Bazan, Efficiency enhancement in low-bandgap polymer solar cells by processing with alkane dithiols *Nat Mater* **2007**, *6*, 497.

[30] K. R. Graham, J. G. Mei, R. Stalder, J. W. Shim, H. Cheun, F. Steffy, F. So, B. Kippelen, J. R. Reynolds, Polydimethylsiloxane as a Macromolecular Additive for Enhanced Performance of Molecular Bulk Heterojunction Organic Solar Cells *Acs Applied Materials & Interfaces* **2011**, *3*, 1210.

[31] B. Park, Y. H. Huh, M. Kim, Surfactant additives for improved photovoltaic effect of polymer solar cells *J. Mater. Chem.* **2010**, *20*.

[32] T. Y. Chu, S. Alem, S. W. Tsang, S. C. Tse, S. Wakim, J. P. Lu, G. Dennler, D. Waller, R. Gaudiana, Y. Tao, Morphology control in polycarbazole based bulk heterojunction solar cells and its impact on device performance *Applied Physics Letters* **2011**, *98*.

[33] D. Wright, E. Brasselet, J. Zyss, G. Langer, W. Kern, Dye-doped organic distributed-feedback lasers with index and surface gratings: the role of pump polarization and molecular orientation *Journal of the Optical Society of America B-Optical Physics* **2004**, *21*, 944.

[34] S. Lozenko, N. Djellali, I. Gozhyk, C. Delezoide, J. Lautru, C. Ulysse, J. Zyss, M. Lebental, Enhancing performance of polymer-based microlasers by a pedestal geometry *Journal of Applied Physics* **2012**, *111*.

[35] D. H. Wang, D. G. Choi, K. J. Lee, O. O. Park, J. H. Park, Active layer transfer by stamping technique for polymer solar cells: Synergistic effect of TiO(x) interlayer *Organic Electronics* **2010**, *11*, 599.

[36] H. B. Yu, G. Y. Zhou, F. S. Chau, F. W. Lee, Fabrication and characterization of PDMS microlenses based on elastomeric molding technology *Optics Letters* **2009**, *34*, 3454.

[37] H. S. Chuang, S. Wereley, Design, fabrication and characterization of a conducting PDMS for microheaters and temperature sensors *Journal of Micromechanics and Microengineering* **2009**, *19*.

[38] Y. C. Tung, K. Kurabayashi, A single-layer PDMS-on-silicon hybrid microactuator with multi-axis out-of-plane motion capabilities - Part II:

Fabrication and characterization *Journal of Microelectromechanical Systems* **2005**, *14*, 558.

[39] J. M. Ding, A. D. Vornbrock, C. Ting, V. Subramanian, Patternable polymer bulk heterojunction photovoltaic cells on plastic by rotogravure printing *Solar Energy Materials and Solar Cells* **2009**, *93*, 459.

[40] P. Kopola, T. Aernouts, S. Guillerez, H. Jin, M. Tuomikoski, A. Maaninen, J. Hast, High efficient plastic solar cells fabricated with a high-throughput gravure printing method *Solar Energy Materials and Solar Cells* **2010**, *94*, 1673.

[41] P. Kopola, T. Aernouts, R. Sliz, S. Guillerez, M. Ylikunnari, D. Cheyns, M. Valimaki, M. Tuomikoski, J. Hast, G. Jabbour, R. Myllyla, A. Maaninen, Gravure printed flexible organic photovoltaic modules *Solar Energy Materials and Solar Cells* **2011**, *95*, 1344.

[42] M. M. Voigt, R. C. I. Mackenzie, C. P. Yau, P. Atienzar, J. Dane, P. E. Keivanidis, D. D. C. Bradley, J. Nelson, Gravure printing for three subsequent solar cell layers of inverted structures on flexible substrates *Solar Energy Materials and Solar Cells* **2011**, *95*, 731.

[43] A. Hubler, B. Trnovec, T. Zillger, M. Ali, N. Wetzold, M. Mingebach, A. Wagenpfahl, C. Deibel, V. Dyakonov, Printed Paper Photovoltaic Cells *Advanced Energy Materials* **2011**, *1*, 1018.

[44] R. Sondergaard, M. Hosel, D. Angmo, T. T. Larsen-Olsen, F. C. Krebs, Roll-to-roll fabrication of polymer solar cells *Materials Today* **2012**, *15*, 36.

[45] F. C. Krebs, J. Fyenbo, M. Jorgensen, Product integration of compact roll-to-roll processed polymer solar cell modules: methods and manufacture using flexographic printing, slot-die coating and rotary screen printing *Journal of Materials Chemistry* **2010**, *20*, 8994.

[46] Y. Galagan, J. E. J. M. Rubingh, R. Andriessen, C. C. Fan, P. W. M. Blom, S. C. Veenstra, J. M. Kroon, ITO-free flexible organic solar cells with printed current collecting grids *Solar Energy Materials and Solar Cells* **2011**, *95*, 1339.

[47] F. C. Krebs, T. Tromholt, M. Jorgensen, Upscaling of polymer solar cell fabrication using full roll-to-roll processing *Nanoscale* **2010**, *2*, 873.

[48] F. C. Krebs, M. Jorgensen, K. Norrman, O. Hagemann, J. Alstrup, T. D. Nielsen, J. Fyenbo, K. Larsen, J. Kristensen, A complete process for production of flexible large area polymer solar cells entirely using screen printing-First public demonstration *Solar Energy Materials and Solar Cells* **2009**, *93*, 422.

[49] L. Blankenburg, K. Schultheis, H. Schache, S. Sensfuss, M. Schrodner, Reel-to-reel wet coating as an efficient up-scaling technique for the production of bulk-heterojunction polymer solar cells *Solar Energy Materials and Solar Cells* **2009**, *93*, 476.

[50] F. C. Krebs, S. A. Gevorgyan, J. Alstrup, A roll-to-roll process to flexible polymer solar cells: model studies, manufacture and operational stability studies *Journal of Materials Chemistry* **2009**, *19*, 5442.

[51] B. Zimmermann, H. F. Schleiermacher, M. Niggemann, U. Wurfel, ITO-free flexible inverted organic solar cell modules with high fill factor prepared by slot die coating *Solar Energy Materials and Solar Cells* **2011**, *95*, 1587.

Chapter3
Large Area Organic Solar Cell Design

"I'd put my money on the Sun and Solar Energy, what a source of Power! I hope we don't have to wait until oil and coal run out, before we tackle that."

-Thomas Edison

3.1 Introduction

For a solar cell to deliver useful power it needs to be of a certain minimum area. Since the solar flux per unit area is constant, larger the area, larger is the current. Several such cells connected in series can deliver the voltage and the required power. Hence, demonstrating the performance for large area devices rather than small-area pixels is necessary for polymer bulk heterojunction solar cells. However, it has been observed that the power conversion efficiency scales inversely with the active area [1-5]. Small area devices appear to be more efficient for a variety of reasons. Hence, it is of great interest to come up with strategies where the efficiency is retained as device area is scaled up. It would also be necessary then to minimize the dead-zone i.e. the non-active are region and to retain roll to roll processing capability [6-7].

There is a need to drastically reduce manufacturing costs if the bulk heterojunction [8-9] (BHJ) solar cells have to become a market reality. Other solar cell technologies are more efficient today and their production is cost effective due to industrial participation. Due stiff competition from other solar cell technologies, there has to be a paradigm shift in fabrication methods to reduce the manufacturing cost for organic solar cells [10-13]. Some examples of cost effective fabrication methods are printing based electrode deposition without vacuum evaporation. Indium is expensive and ITO-free transparent electrodes need to be explored for cost effective alternatives in large area roll-to-roll fabrication [14-17]. In this context, we implement a technique to fabricate efficient large area solar cells that consist of arrays of small area cells with roll-to-roll compatibility.

3.2 Area dependence of efficiency

Earlier reports from our laboratory have shown that small areas devices (< 1mm^2) are more efficient as compared to larger devices (~1cm^2) [3] (Figure 3.1). The reasons for such an observation is threefold reduction in electrical resistive losses [5], enhanced collection efficiency [4, 18] and a finite number of photo-generated carriers in the vicinity of the top electrode [3]. Analysis of detailed studies on different substrates of varying thickness and series resistance losses indicated that a substantial contribution from lateral transport factors existed [19]. This improvement was correlated to the fact that regions in the vicinity of the cathode contribute to the overall current [19-23]. This result implied that it would be sufficient to coat the cathode into small area patterns separated by an optimum gap and not a single large area cathode. This approach has also been pursued by other research groups [4].

Fabricating patterned devices in accordance with the above requirement is challenging as pixelation demands an additional common interconnect for shorting the individual pixels. Another important factor to be considered is the pixel to gap coverage ratio which can comprise of about 15-20% of the total module for inter-cathode gaps in the 50-100 µm scale. Conventional thermal evaporation processes would need to employ several coating cycles with complex masks to achieve an air-stable device with an encapsulation layer. In this context, we implement a strategy for realizing an organic photovoltaic module with two key features:

(a) Utilizing low temperature meltable alloys as cathode materials; ensuring patterned devices and scalability with enhanced stability.

(b) Light harvesting by introducing suitable fluorescent dye-molecules in the gap zone of the pixelated device.

The first aspect assists in minimizing series resistance losses utilizing the efficacy of small area solar cells in a collective-optimized manner. The second aspect not only ensures minimal loss of radiation in a pixelated device, but also bridges the low-absorption regions in the absorption of the donor polymer by down conversion and re-directing the transmitted light in to the dead region between the pixels.

This approach handles these shortcomings of area-scaling and dead-zones by combining the stability and roll-to-roll processing ability of low temperature meltable alloys and a dye-dispersed dielectric-matrix for light harvesting. The electrode thickness can be controlled in a facile manner to provide an effective barrier for

moisture and oxygen diffusion enabling stable solar cells. The fluorescent dye matrix introduced in the electrode gaps is selected to absorb in the low-yield region of the solar cell and re-emit it into a spectral range suitable for the donor polymer absorption. Hence this device geometry combines the advantages of small-area-patterning and luminescent solar concentrators (LSC) [24-27] to efficiently harness and convert solar energy. A detailed description of light management strategies is presented in Chapter 4.

3.3 Mechanism of loss in large area devices

The major source of loss in large area devices is the sheet resistance of the electrodes. Typical sheet resistance values of commercial ITO range from 7-20 Ω/□. This loss is not very significant for small area devices as charges are generated and collected at points without much of a spatial offset. In large area devices, as shown in Figure 3.1, charges that are generated at electrode extremes need to traverse high resistance paths in order to be collected at the collection contacts.

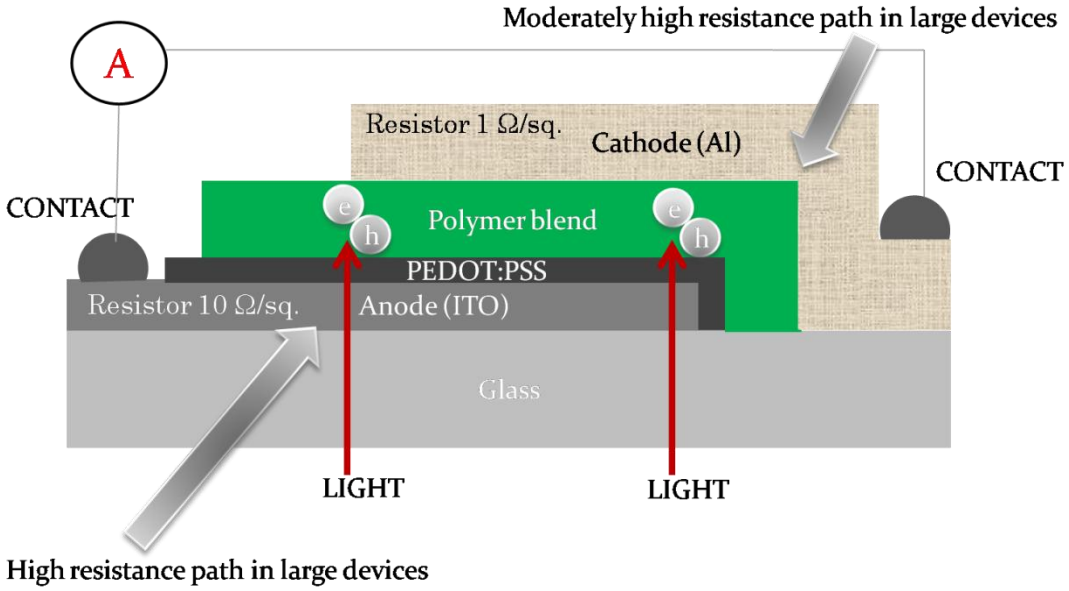

Figure 3.1: *Loss mechanism in large area devices.*

Effectively, the charges generated in the large area devices encounter the sheet resistance of the electrodes. Thin metal electrodes that are utilized as electrodes have sheet resistances ranging from 0.1-1 Ω/□. This is lower as compared to ITO but also contributes to the losses in large area devices. One strategy to minimize this collection

loss is by depositing multiple contact points or strips forcing the charges to traverse short lengths [28]. This improvement comes at the cost of loss in active area. We implement another strategy where the electrodes are patterned and the charges are vertically collected. The advantage here is that the sheet resistance need not limit the device performance. But patterning causes spaces in the device geometry which could lead loss of charge collection regions. We circumvent this problem by optimizing the spacing between sub-electrodes in a way that causes minimal loss of charges.

3.4 Overcoming losses in large area devices

Earlier reports from our laboratory had shown that the regions in the vicinity of the electrode had finite charge collection ability (Figure 3.2 (a)). There is evidence of a lateral field that assists in charge collection over several tens of micrometers. Pure diffusive processes cannot have effects over such large lengths. The current from the electrode edge diminishes in an exponential manner and the decay length (L_d) is dependent on the mobility of charge carriers and the morphology of the blend. Hence, spatial dimensions of the electrode gaps need to be of the order of L_d so as to assist collection of photogenerated charges. These length scales can be independently ascertained using local photocurrent (I_{ph}) profile scans. For . in the case of blend of PCPDTBT and PCBM, this length for the electron is ≈ 60-80 μm (Figure 3.2(a)). This observation can be further supported by the fact that introducing an optical mask around the electrode leads to a current density drop by about 8% [29] (Figure 3.2 (b)). Given the electrode dimensions, the contribution of peripheral current can be estimated by integrating the current from the electrode edge to infinity (see Appendix A). The expression for the percentage gain in photocurrent turns out to be $G = 200/(aR+2)$, where R is the radius of the electrode and $a= 1/L_d$. Hence for $L_d= 80\mu m$, R=1.5 mm, G=9.6%. This implies that 10% of the current contribution originates from the vicinity for a circular electrode of radius 1.5 mm.

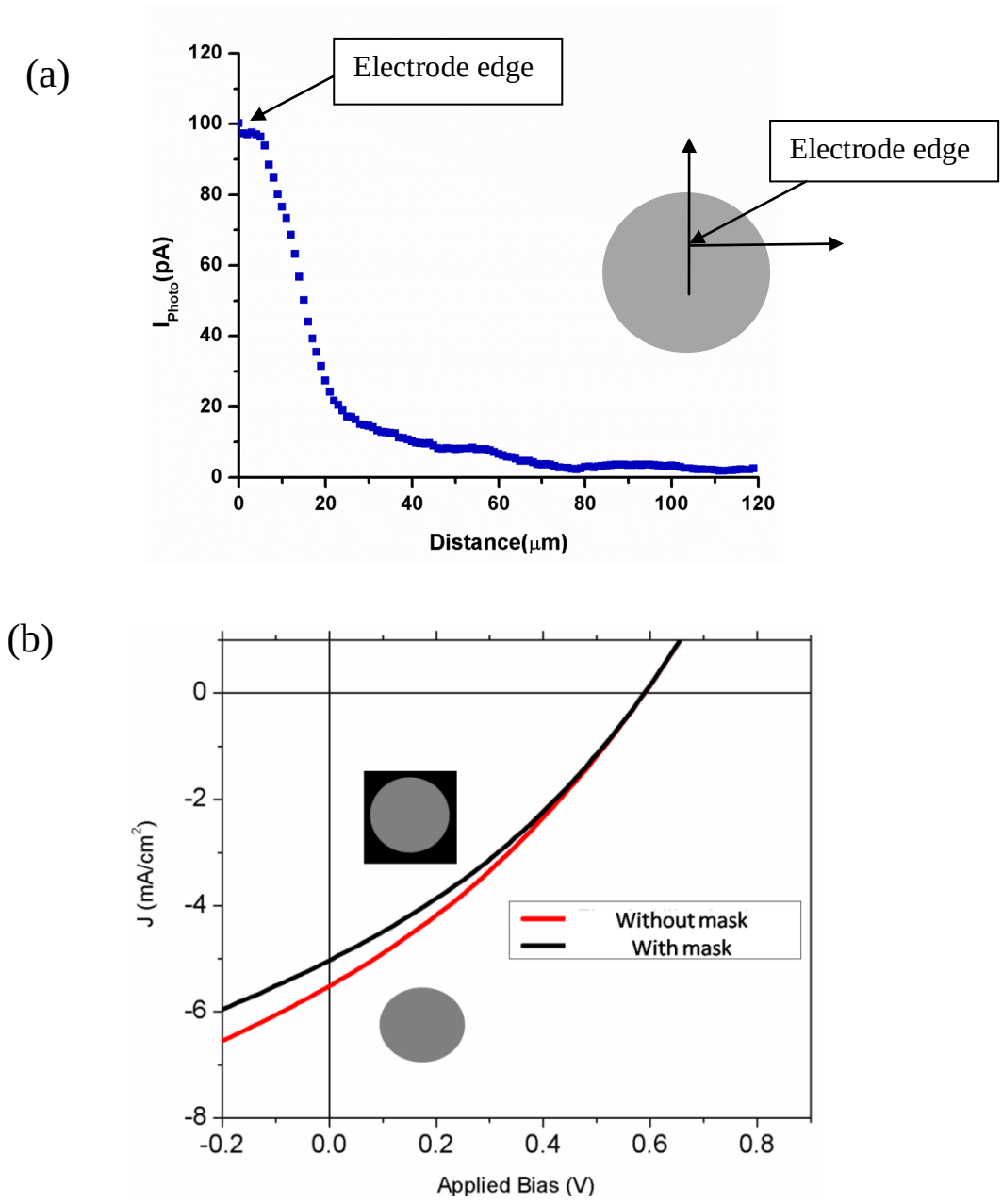

Figure 3.2: *(a) Typical decay length profile for PCPDTBT:PCBM BHJ blend. (b) J-V curve for a device with and without an optical mask.*

Optimum electrode spacing can minimize losses due to loss of electrodes in the inter-electrode regions. We propose a device structure that incorporates vertical collection of charges through patterned electrodes with the optimum spacing (~L_d) as shown in Figure 3.3. The next section presents details about the device fabrication procedure that yields patterned devices with optimal spacing, shape and size.

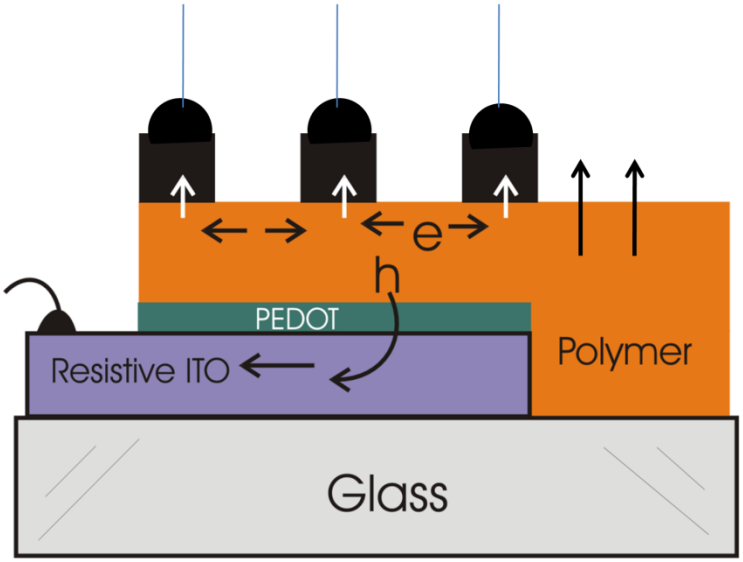

Figure 3.3: *Device design to minimize series resistance loss by vertical collection of charges.*

3.5 Device fabrication using alloy electrodes

Alloy based organic solar cells (alloy-OSC) were fabricated by melting eutectic alloys and making them flow through a perforated polycarbonate (PC) sheet. This process resulted in *patterned* and *interconnected* electrodes without the need of additional shorting contacts. The low melting eutectic alloy chosen in this work is a ternary alloy (Indium: Tin: Bismuth: Lead, melting point, 58^{o}C) which exhibited reasonable device performance in BHJ based solar cells [30]. Figure 3.4 (j) shows the energy level diagram of the solar cell along with work function of the alloy derived from Kelvin probe microscopy (earlier described in chapter 2). Fabrication process involves with cleaning and processing ITO substrates and coating PEDOT:PSS and the polymer blend in a sequential manner. Once the devices were ready to be coated, a molten film of the alloy was deposited on an aluminium foil which acts like a scaffold (Figure 3.4(a)). Due to the large surface energy of the alloy, wetting had to be induced on the scaffold so that it could form a film. A patterned PC sheet was brought into contact with the liquid alloy film such that the alloy emerged from the perforations (Figure 3.4(b,c)). The ITO/PEDOT:PSS/blend substrate was mounted on to a vertical translation stage with the blend facing down (Figure 3.4 (d, f)). The vertical stage was moved till it made contact with the alloy. Since the surface energy of the alloy film was lowered, application of pressure caused the alloy to flow through the

perforations and make contacts with the polymer blend. The contact was allowed to equilibrate for 10 min followed by gradual reduction in the temperature to 40-50^{o}C (below the melting point of the alloy). The device was then cooled to room temperature to freeze the patterned solar cell (Figure 3.4(e,g)).

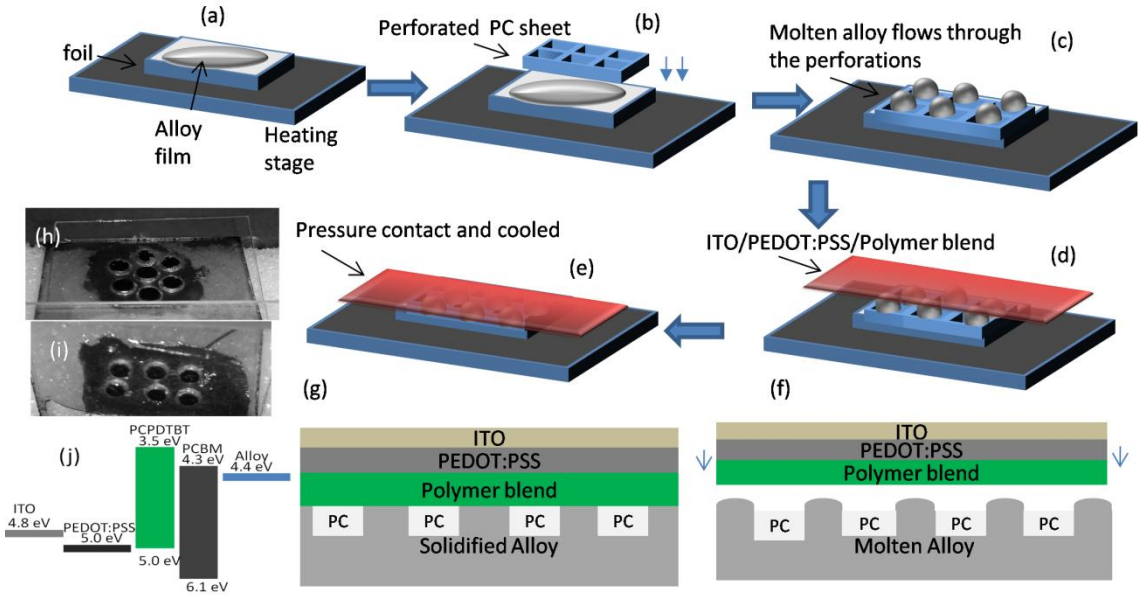

Figure 3.4: *Scheme of fabrication of alloy based organic solar cells. (a-c) Patterning of the molten alloy film, (d-g) integrating and lamniating with the polymer blend, (h-i) photographs of working patterned alloy solar cells. (j) Energy level diagram of PCPDTBT:PCBM alloy based solar cell. For details, see text. (Reprinted with permission from A. J. Das, K. S. Narayan, Retention of Power Conversion Efficiency - from Small Area to Large Area Polymer Solar Cells. Advanced Materials 2013, 25, 2193. © 2013 John Wiley and Sons and Patent Application Appl. No. PCT/IB2012/056338)*

Representative images of the alloy-organic solar cell (alloy-OSC) are shown in Figure 3.4 (i,j), with different electrode patterns. Low melting alloys can be processed at low temperatures thereby reducing the cost of fabrication. Depending on the alloy composition, a wide choice of alloy mixtures is available which can meet the requirements for solar cells in extreme conditions [31-32]. The alloy thickness can be controlled by the thickness of the PC film, which can be several hundred micrometers thick (~125-400 μm).

This electrode geometry reduces the sheet resistance and at the same time is impermeable for oxygen and water thereby imparting air stability to the device without the need for any additional encapsulation.

For the PCPDTBT system, typical device characteristics with alloy electrodes were V_{oc}= 0.6 V, J_{sc}= 10 mA/cm^2 and η= 2.5-3% as shown in Figure 3.5. For the device system with poly{[4,8-bis-(2-ethyl-hexyl-thiophene-5-yl)-benzo[1,2-b:4,5-b′]dithiophene-2,6-diyl]-alt-[2-(2′-ethyl-hexanoyl)-thieno[3,4-b]thiophen-4,6 diyl]}(PBDTTT-C-T), the solar cell characteristics were V_{oc}= 0.74 V, J_{sc}= 14.7 mA/cm^2 and η= 6% under 100 mW/cm^2 AM 1.5G illumination, as shown in Figure 3.6. Hence, the capability of the alloy as an electrode could be validated [33-34].

This method was also assessed for scalability by fabricating patterned devices with 6-30 sub-cells of 1 mm^2 area connected in a parallel combination. As can be seen in Figure 3.7, η and J_{sc} of (1 mm^2 x 18 pixels) and (1 mm^2 x 25 pixel) devices are comparable to that of an un-patterned, small-area device. In contrast, an un-patterned large area device (1 cm^2) exhibits a drastic reduction in J_{sc} and fill factor (FF) in expected lines due to various loss mechanisms [3-4]. Series (R_s) resistance extracted from the I-V plots of patterned devices also indicate that the efficiency is retained while the area is scaled up. Table 1 summarizes the size dependence of efficiency, where an un-patterned small area device exhibited R_s of 9 Ω cm^2 which was similar to a patterned device (17.4 Ω cm^2), whereas an un-patterned large area device showed R_s of 44.9 Ω cm^2 which is higher than the small area device.

Lower R_s values are reflected in the higher FF for patterned large area devices as summarized in Table 1. A single-pixel small area device showed a FF= 57.4% as which is similar to a 16-pixel patterned device (=50.6%) with an area 5 times that of the small device. In contrast, a large area unpatterned device showed a FF of 42.8% due to higher resistive losses. Since the voltage drop across the electrodes is lowered in patterned devices with thick electrodes, the built in potential remains high. This results in enhanced collection efficiency over larger areas in patterned devices.

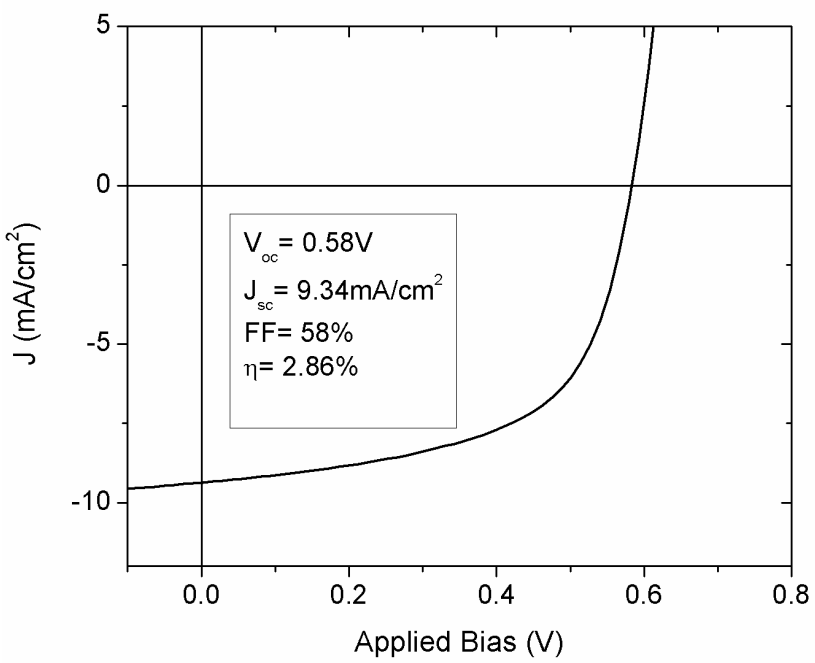

Figure 3.5: *J-V characteristics of PCPDTBT:PCBM solar cell with alloy electrode*

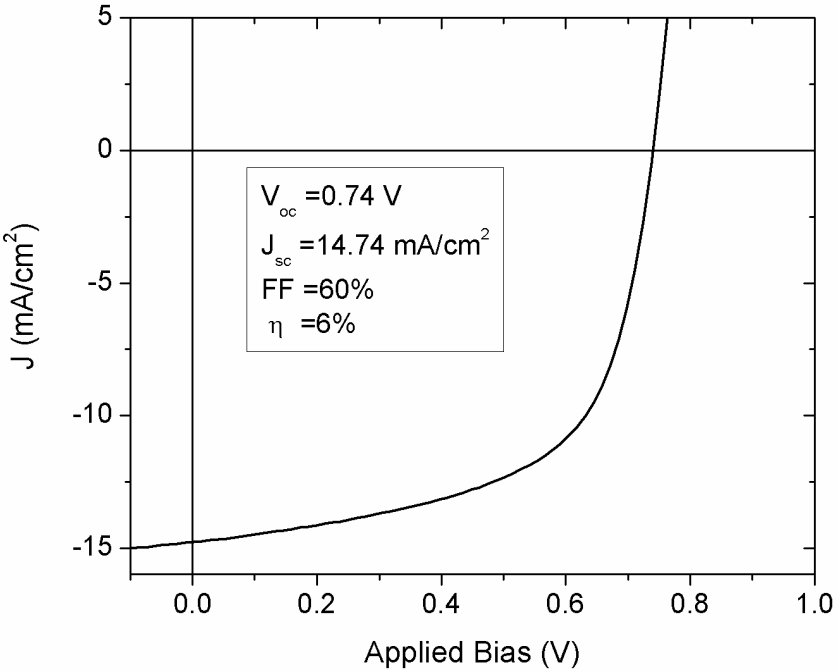

Figure 3.6: *J-V characteristics of PBDTTT-C-T:PCBM solar cell with alloy electrode. (Reprinted with permission from A. J. Das, K. S. Narayan, Retention of Power Conversion Efficiency - from Small Area to Large Area Polymer Solar Cells. Advanced Materials* ***2013****, 25, 2193. © 2013 John Wiley and Sons)*

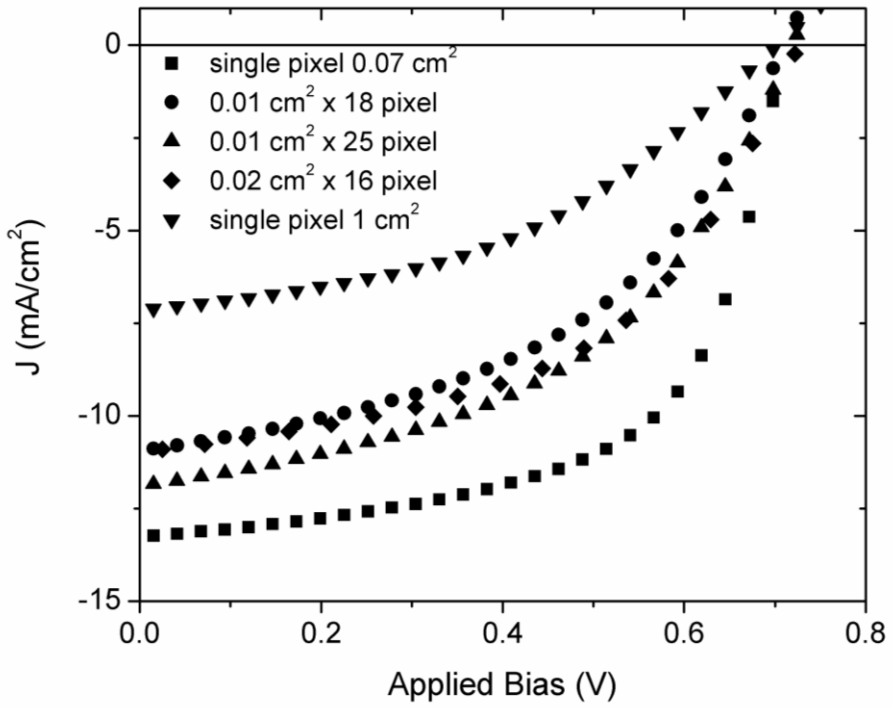

Figure 3.7: *J-V characteristics of patterned and un-patterned PBDTTT-C-T:PCBM solar cells with alloy electrode. (Reprinted with permission from A. J. Das, K. S. Narayan, Retention of Power Conversion Efficiency - from Small Area to Large Area Polymer Solar Cells. Advanced Materials* ***2013****, 25, 2193. © 2013 John Wiley and Sons)*

This device structure incorporates light management effectively as most of the emitted light from the dye encounters alloy reflectors. Hence it is reflected back to the blend periphery efficiently. Recent reports have shown that patterning the dye film limits re-absorption and improves efficiency [26] in LSC based solar cells, a fact that is inherently incorporated in our design. An important design criterion that arises from patterning is the optimum shape and size of the sub-electrode/pixel. Considering that a single exponential function can be used to fit the decay from the electrode edge, we calculated that effective area gained due to diffusion at the electrode periphery is $2\pi RL_d$ for a circular electrode of radius R (see Appendix A). Estimated peripheral contribution for PCPDTBT:PCBM can be as high as 14% for a 1 mm pixel radius. Hence, pixel dimensions of 1 mm or smaller is ideal for large area devices. Circular pixels do not effectively fill a 2-D space unlike triangular or square pixels. In addition, higher pixel perimeter is advantageous as the peripheral contribution can be maximized. It turns out that triangular pixels have the largest perimeter for the same

area. Hence triangular pixels with individual pixel area < 1 mm^2 and a spacing of L_d can retain efficiency while the device dimensions are scaled up.

Additional factors like edge effects and electric field fringing may also be beneficial in improving charge carrier generation and collection at the periphery of the electrode. Triangular electrodes can be designed to have sharp edges that can concentrate the field and lead to higher charge carrier generation. Since the dimensions of the electrodes are in several 100 μm, plasmonic effects are insignificant. Nevertheless, electrode designs with plasmonic nano-particles can be envisaged that harness the large electric fields at edges as well as in the inter-electrode gaps.

Table 3.1: Comparison of performance for un-patterned and patterned devices

Device geometry	J_{sc} (mA/cm^2)	FF(%)	V_{oc} (V)	η(%)	R_s(Ω cm^2)
Single pixel (0.07 cm^2)	13.55	57.4	0.682	4.74	9.0
18 pixel x 0.01 cm^2	10.91	46.7	0.709	3.22	19.3
25 pixel x 0.01 cm^2	11.86	47.9	0.718	3.65	17.4
16 pixel x 0.02 cm^2	10.94	50.6	0.726	3.59	16.6
Single pixel (1 cm^2)	7.12	42.8	0.702	1.91	44.9

*(Reprinted with permission from A. J. Das, K. S. Narayan, Retention of Power Conversion Efficiency - from Small Area to Large Area Polymer Solar Cells. Advanced Materials **2013**, 25, 2193. © 2013 John Wiley and Sons)*

3.6 Optimum Pixel Shape

From electrical considerations, triangular pixels seem to possess the largest perimeter for the same area as compared to other basic shapes such as squares and circles[35]. Large perimeters indicate larger collection of charges carriers at the electrode vicinity. FDTD simulations have also been carried out in order to arrive at the optimum shape from an optical point of view. The device structure was simulated using the OptiFDTD package as discussed in Chapter 2. Time dependent Maxwell's equations were solved in order to arrive at the electric field distribution in the inter-electrode gaps. All the simulations use plane waves of green wavelengths (λ=532 nm)

incident from both lateral directions on to a set of two pixels of different shapes but similar area. TE polarization of light was used and the y-component of the electric field was mapped (E_y).

3.6.1 Case I: Circular pixels

Though circular pixels are simpler to realize they are not the ideal candidates for large area devices. Simulations on circular pixels show that the field profile is non-uniform in between the pixels (Figure 3.8). As can be seen in Figure 3.8(a), the refractive index distribution is uniform in between the pixels. But a close look at the Figure 3.8(b) shows that the electric field profile is non-uniform. The field strength is maximum at the point at which the pixels are closest to each other and then drops as the distance increases. This result is obvious as the spacing between the pixels is not a constant in the case of circular pixels. As a consequence the current collection ability is expected to be non-uniform. This may lead to regions in the gaps that do not contribute to the current as efficiently as the regions that are closest to each other. Hence circular pixels are not the ideal candidates for a patterned structure.

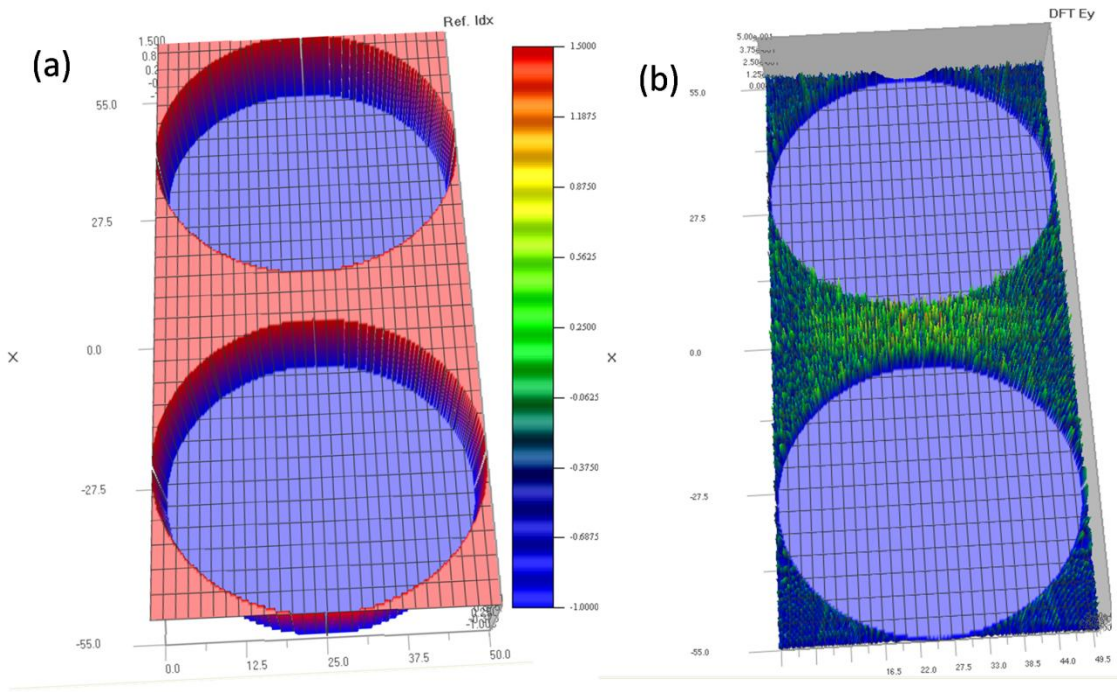

Figure 3.8: *FDTD simulations of circular pixels. (a) Refractive index profile. (b) Electric field profile in the x-y plane.*

3.6.2 Case II: Square pixels

Unlike circular pixels, square pixels (Figure 3.9(a)) exhibit uniform electric field profiles in the gaps as can be seen in Figure 3.9 (b). The field is uniform all around the pixel which will result in uniform current generation from these regions.

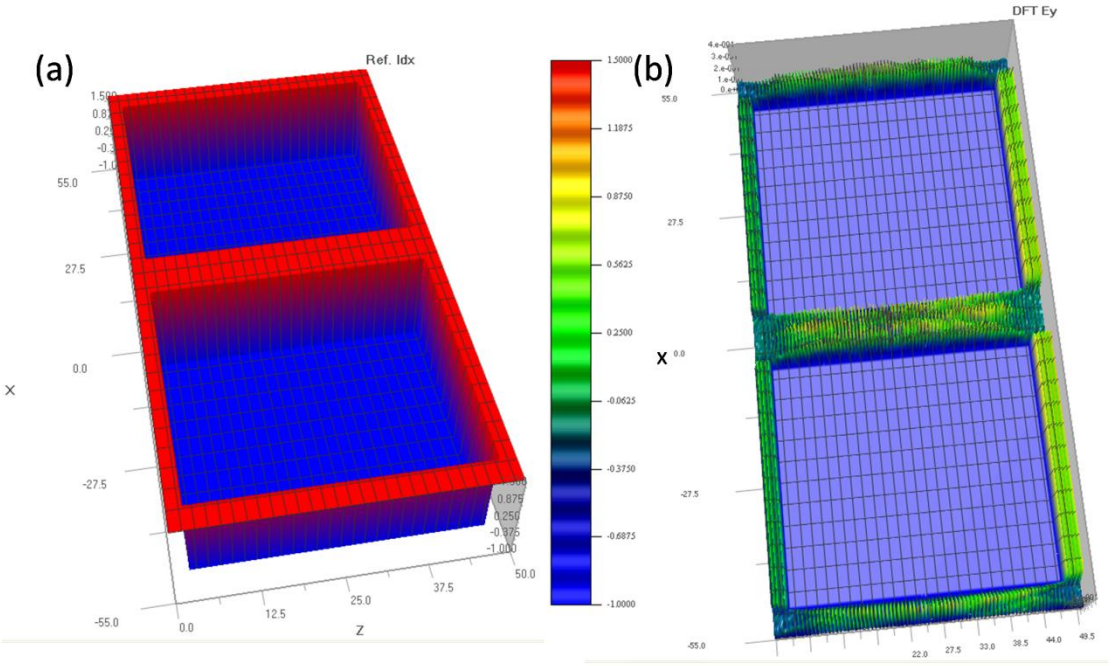

Figure 3.9: *FDTD simulations of square pixels. (a) Refractive index profile. (b) Electric field profile in the x-y plane.*

Even though the field is uniform along the edges, there seems to be a drop at the corners. Considering the fact the corners will have additional contributions from four electrodes, this drop may be compensated.

3.6.3 Case III: Triangular pixels

Triangular pixels (Figure 3.10(a)) behave similar to that of the square pixels. Since the inter pixel distance in constant, so is the electric field distribution. As can be seen in Figure 3.10 (b), the field is uniform all around the pixel, and will lead to uniform current in the gaps.

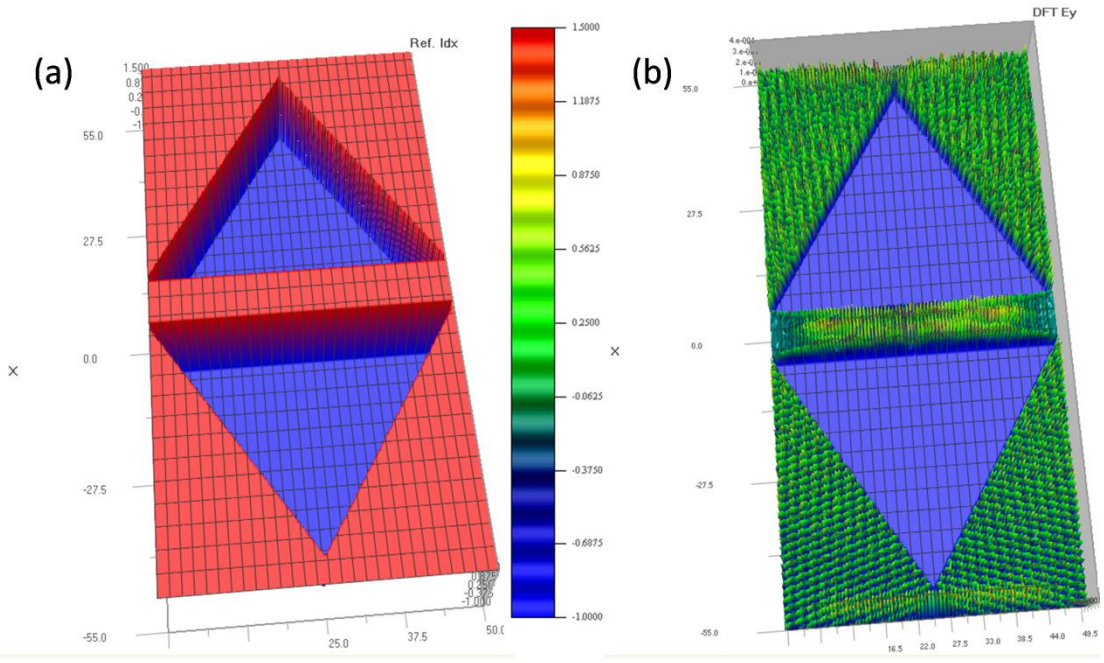

Figure 3.10: *FDTD simulations of triangular pixels. (a) Refractive index profile. (b) Electric field profile in the x-y plane.*

Hence, considering the electric field distribution along with perimeter to area ratio, it turns out that triangular pixels are the ideal candidates for large area devices.

3.7 Proposed module design

The proposed module design for large area devices that retain efficiency needs to incorporate patterned and thick electrodes. A single large area device is practically of no use as it is capable of delivering a large current but not sufficient voltage. From the S-Q limit and considering material parameters, the typical built-in potential observed is about 0.6-0.9 V. Hence, several devices need to be serially connected so that the photo-voltages from all the cells add up as shown in Figure 3.11. A strip like pattern that is serially connected can deliver several volts depending upon the number of strips. The width of the strips is limited by the sheet resistances and a favoured width is about 1 cm. The length of the strip decides the current that the module can source. e.g. if the efficiency of the strip is a modest 5% and the current density obtainable under 1 sun is 15 mA/cm^2, then the length of the strip needs to be 10 cm if the required current is 150 mA (since the width is 1 cm). The proposed design will need to incorporate electrode patterning such that the sheet resistance is lowered and an efficiency of 5% is preserved over 10 cm^2 area as shown in Figure 3.11.

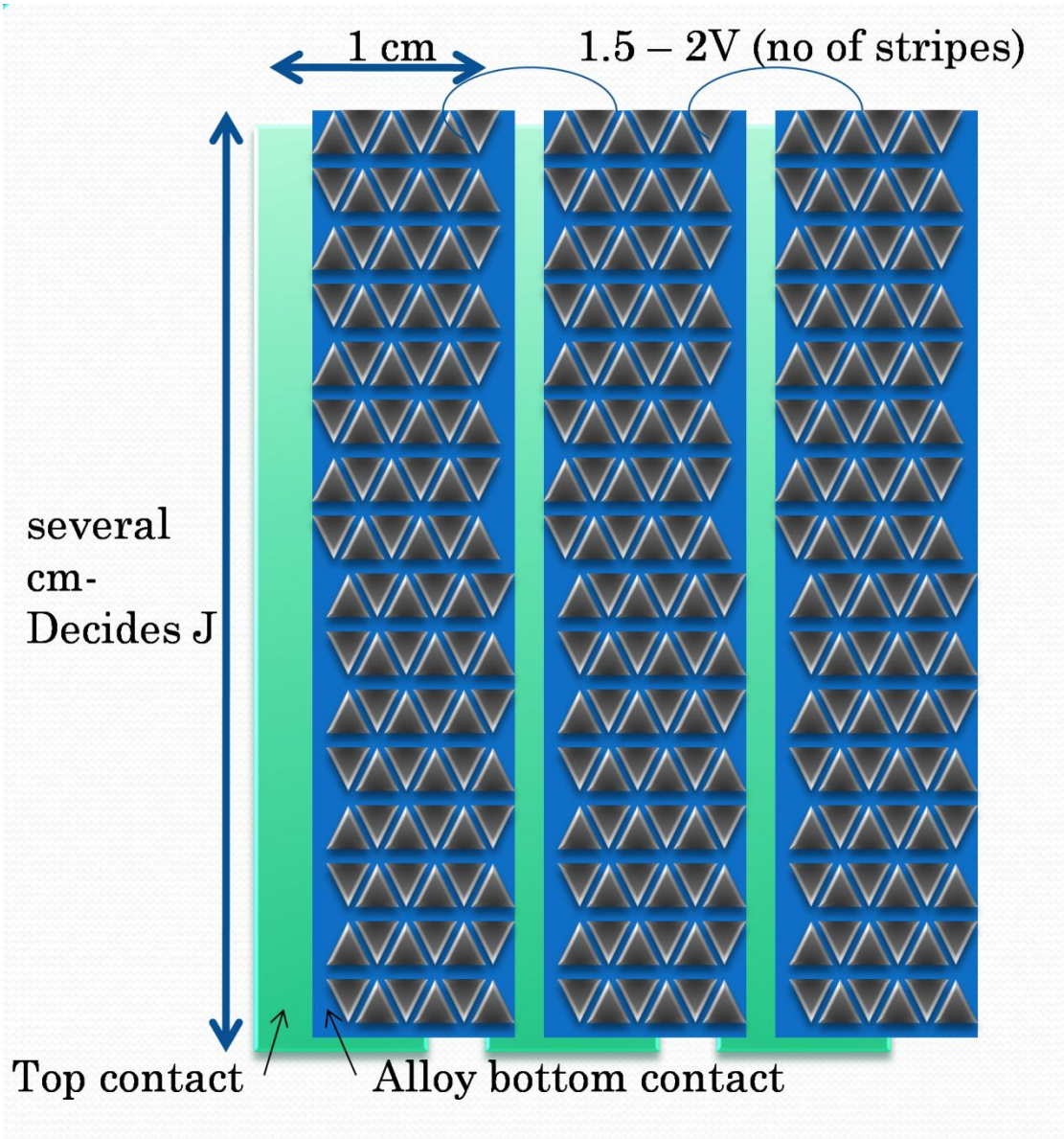

Figure 3.11: *Proposed design for large area organic solar cell based modules.*

3.8 Alloy as electrode for other BHJ systems

The alloy is also suitable for as an electrode material for a wide range of polymer blends like PCDTBT:PCBM, P3HT: N2200 (poly{[N,N'-bis(2-octyldodecyl)-naphthalene-1,4,5,8-bis(dicarboximide)-2,6-diyl]-alt-5,5'-(2,2'-bithiophene)}) and also non-fullerene acceptors like perylenes. Inverted devices of PCDTBT:PCBM were fabricated and the alloy was utilized as the hole collecting electrode.

(a)

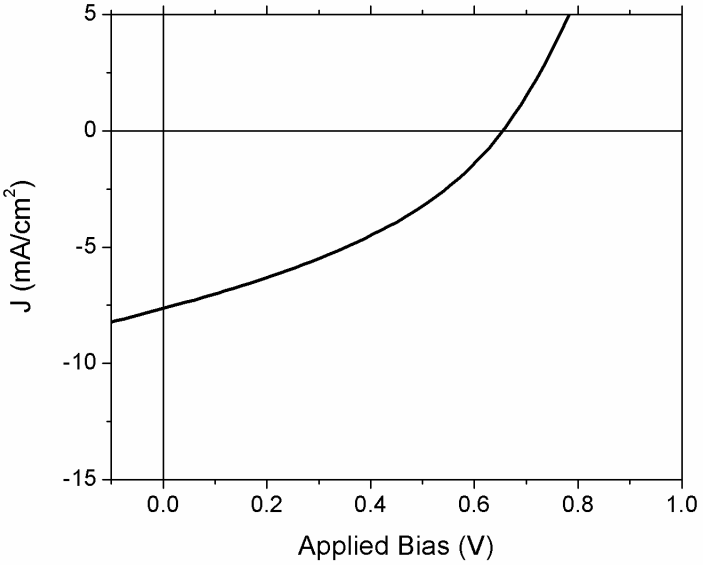

(b)

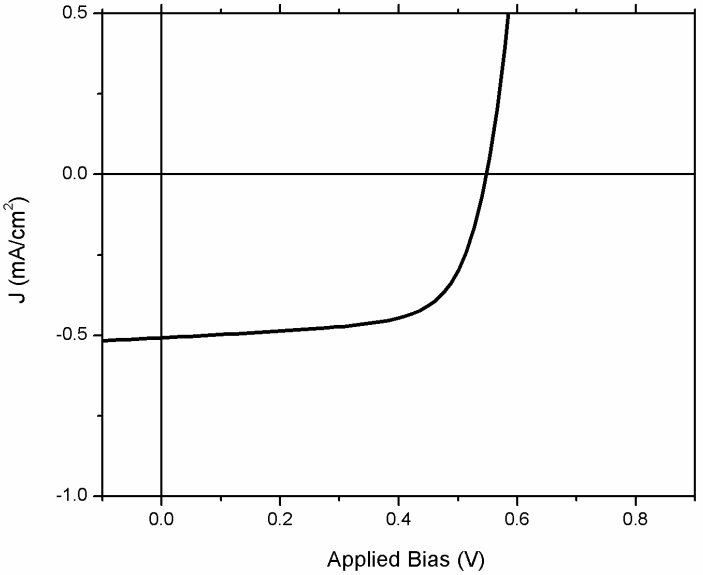

Figure 3.12: *(a) J-V for ITO/ZnO/PCDTBT:PCBM/MoO_3/Alloy device. (b) J-V for ITO/PEDOT:PSS/P3HT:N2200/Alloy device. (Reprinted with permission from A. J. Das, K. S. Narayan, Retention of Power Conversion Efficiency - from Small Area to Large Area Polymer Solar Cells. Advanced Materials* ***2013****, 25, 2193. © 2013 John Wiley and Sons)*

The devices consisted of ZnO as the electron buffer layer and MoO_3 as the hole buffer layer. Moderately high currents of about 8 mA/cm^2 were obtained even though the work-function of the alloy was not ideal for hole collection. In P3HT:N2200 devices, very high FF (66%) was achieved, which is indicative of very high charge extraction.

Summary

The area-scaling issue was addressed in this chapter. Large area designs based on collective and efficient small area devices were proposed and demonstrated. Low melting point alloys were utilized as an alternative to conventional thermal evaporation of metals. They could be deposited at low temperatures and manipulated to yield patterned devices. Excellent device performance was observed using these alloys indicating that they are indeed a viable alternative to aluminium and silver electrodes. The present technique can be further refined for the realization of commercially feasible OSCs in a cost-effective manner with high fill factors and low sheet resistances. The need for an elaborate glove-box and vacuum-coating arrangement can be eliminated to realize realistic low cost energy solutions.

References

[1] A. K. Pandey, J. M. Nunzi, B. Ratier, A. Moliton, Size effect on organic optoelectronics devices: Example of photovoltaic cell efficiency *Physics Letters A* **2008**, *372*, 1333.

[2] S. Choi, W. J. Potscavage, B. Kippelen, Area-scaling of organic solar cells *Journal of Applied Physics* **2009**, *106*.

[3] D. Gupta, M. Bag, K. S. Narayan, Area dependent efficiency of organic solar cells *Applied Physics Letters* **2008**, *93*.

[4] W.-I. Jeong, J. Lee, S.-Y. Park, J.-W. Kang, J.-J. Kim, Reduction of Collection Efficiency of Charge Carriers with Increasing Cell Size in Polymer Bulk Heterojunction Solar Cells *Advanced Functional Materials* **2011**, *21*, 343.

[5] D. Gao, D. S. Seferos, Size-dependent behavior of polymer solar cells measured under partial illumination *Solar Energy Materials and Solar Cells* **2011**, *95*, 3516.

[6] F. C. Krebs, S. A. Gevorgyan, J. Alstrup, A roll-to-roll process to flexible polymer solar cells: model studies, manufacture and operational stability studies *Journal of Materials Chemistry* **2009**, *19*, 5442.

[7] F. C. Krebs, T. Tromholt, M. Jorgensen, Upscaling of polymer solar cell fabrication using full roll-to-roll processing *Nanoscale* **2010**, *2*, 873.

[8] M. He, W. Han, J. Ge, Y. Yang, F. Qiu, Z. Lin, All-conjugated poly(3-alkylthiophene) diblock copolymer-based bulk heterojunction solar cells with controlled molecular organization and nanoscale morphology *Energy & Environmental Science* **2011**, *4*, 2894.

[9] M. He, F. Qiu, Z. Lin, Conjugated rod-coil and rod-rod block copolymers for photovoltaic applications *Journal of Materials Chemistry* **2011**, *21*, 17039.

[10] J.-F. Salinas, H.-L. Yip, C.-C. Chueh, C.-Z. Li, J.-L. Maldonado, A. K. Y. Jen, Optical Design of Transparent Thin Metal Electrodes to Enhance In-Coupling and Trapping of Light in Flexible Polymer Solar Cells *Advanced Materials* **2012**, n/a.

[11] M. Jørgensen, K. Norrman, S. A. Gevorgyan, T. Tromholt, B. Andreasen, F. C. Krebs, Stability of Polymer Solar Cells *Advanced Materials* **2012**, *24*, 580.

[12] J. Ajuria, I. Etxebarria, W. Cambarau, U. Munecas, R. Tena-Zaera, J. C. Jimeno, R. Pacios, Inverted ITO-free organic solar cells based on p and n semiconducting oxides. New designs for integration in tandem cells, top or bottom detecting devices, and photovoltaic windows *Energy & Environmental Science* **2011**, *4*, 453.

[13] D. Angmo, T. T. Larsen-Olsen, M. Jorgensen, R. R. Sondergaard, F. C. Krebs, Roll-to-Roll Inkjet Printing and Photonic Sintering of Electrodes for ITO Free Polymer Solar Cell Modules and Facile Product Integration *Advanced Energy Materials* **2013**, *3*, 172.

[14] D. Angmo, M. Hösel, F. C. Krebs, All solution processing of ITO-free organic solar cell modules directly on barrier foil *Solar Energy Materials and Solar Cells* **2012**, *107*, 329.

[15] J.-S. Yu, I. Kim, J.-S. Kim, J. Jo, T. T. Larsen-Olsen, R. R. Sondergaard, M. Hosel, D. Angmo, M. Jorgensen, F. C. Krebs, Silver front electrode grids for ITO-free all printed polymer solar cells with embedded and raised topographies, prepared by thermal imprint, flexographic and inkjet roll-to-roll processes *Nanoscale* **2012**, *4*, 6032.

[16] R. Søndergaard, M. Manceau, M. Jørgensen, F. C. Krebs, New Low-Bandgap Materials with Good Stabilities and Efficiencies Comparable to P3HT in R2R-Coated Solar Cells *Advanced Energy Materials* **2012**, *2*, 415.

[17] R. Søndergaard, M. Helgesen, M. Jørgensen, F. C. Krebs, Fabrication of Polymer Solar Cells Using Aqueous Processing for All Layers Including the Metal Back Electrode *Advanced Energy Materials* **2011**, *1*, 68.

[18] D. Gupta, M. Bag, K. S. Narayan, Correlating reduced fill factor in polymer solar cells to contact effects *Applied Physics Letters* **2008**, *92*.

[19] S. Mukhopadhyay, A. J. Das, K. S. Narayan, High-Resolution Photocurrent Imaging of Bulk Heterojunction Solar Cells *The Journal of Physical Chemistry Letters* **2012**, 161.

[20] S. Mukhopadhyay, K. S. Narayan, Rationalization of donor-acceptor ratio in bulk heterojunction solar cells using lateral photocurrent studies *Applied Physics Letters* **2012**, *100*, 163302.

[21] S. Mukhopadhyay, S. Ramachandra, K. S. Narayan, Direct Observation of Charge Generating Regions and Transport Pathways in Bulk Heterojunction Solar Cells with Asymmetric Electrodes Using near Field Photocurrent Microscopy *The Journal of Physical Chemistry C* **2011**, *115*, 17184.

[22] D. Kabra, K. S. Narayan, Direct estimate of transport length scales in semiconducting polymers *Advanced Materials* **2007**, *19*, 1465.

[23] D. Kabra, J. Verma, N. S. Vidhyadhiraja, K. S. Narayan, Model for Studies of Lateral Photovoltaic Effect in Polymeric Semiconductors *Ieee Sensors Journal* **2008**, *8*, 1663.

[24] M. J. Currie, J. K. Mapel, T. D. Heidel, S. Goffri, M. A. Baldo, High-efficiency organic solar concentrators for photovoltaics *Science* **2008**, *321*, 226.

[25] W. G. J. H. M. van Sark, K. W. J. Barnham, L. H. Slooff, A. J. Chatten, A. Buchtemann, A. Meyer, S. J. McCormack, R. Koole, D. J. Farrell, R. Bose, E. E. Bende, A. R. Burgers, T. Budel, J. Quilitz, M. Kennedy, T. Meyer, C. D. M. Donega, A. Meijerink, D. Vanmaekelbergh, Luminescent Solar Concentrators - A review of recent results *Optics Express* **2008**, *16*, 21773.

[26] S. Tsoi, D. J. Broer, C. W. M. Bastiaansen, M. G. Debije, Patterned dye structures limit reabsorption in luminescent solar concentrators *Optics Express* **2010**, *18*, A536.

[27] A. Polman, H. A. Atwater, Photonic design principles for ultrahigh-efficiency photovoltaics *Nature Materials* **2012**, *11*, 174.

[28] H. Jin, C. Tao, M. Velusamy, M. Aljada, Y. L. Zhang, M. Hambsch, P. L. Burn, P. Meredith, Efficient, Large Area ITO-and-PEDOT-free Organic Solar Cell Sub-modules *Advanced Materials* **2012**, *24*, 2572.

[29] H. J. Snaith, The perils of solar cell efficiency measurements *Nature Photonics* **2012**, *6*, 337.

[30] M. Bag, D. Gupta, N. Arun, K. S. Narayan, Deformation of metallic liquid drop by electric field for contacts in molecular-organic electronics *Proceedings of the Royal Society a-Mathematical Physical and Engineering Sciences* **2009**, *465*, 1799.

[31] J. F. Salinas, J. L. Maldonado, G. Ramos-Ortiz, M. Rodriguez, M. A. Meneses-Nava, O. Barbosa-Garcia, R. Santillan, N. Farfan, On the use of Woods metal for fabricating and testing polymeric organic solar cells: An easy and fast method *Solar Energy Materials and Solar Cells* **2011**, *95*, 595.

[32] B. Omrane, C. K. Landrock, Y. Chuo, D. Hohertz, J. Aristizabal, B. Kaminska, K. L. Kavanagh, Long-lasting flexible organic solar cells stored and tested entirely in air *Applied Physics Letters* **2011**, *99*, 263305.

[33] A. J. Das, K. S. Narayan, Retention of Power Conversion Efficiency - from Small Area to Large Area Polymer Solar Cells *Advanced Materials* **2013**, *25*, 2193.

[34] A. J. Das, K. S. Narayan, An organic solar cell and methods thereof, PCT/IB2012/056338

[35] M. Chakaroun, A. Moliton, J. M. Nunzi, B. Ratier, Electronic components with integrated encapsulation EP2308115 A1

Chapter4
Light Harvesting in Organic Solar Cells

In the right light, at the right time, everything is extraordinary. Aaron Rose

4.1 Introduction

Light harvesting in solar cells is has been an important component to enhance the efficiency of devices by trapping [1-4], concentrating [5-6] or reconverting light in to different wavelengths [7-8]. Implementation of light harvesting has been demonstrated using photonic crystals and plasmonics [9-11], luminescent solar concentrators or down-conversion using nano-structures [6-7, 12-20], surface texturing or dome or cone shaped structures [21-22]. In most cases light trapping results in an enhanced short circuit current density due to a larger number of photons being absorbed. Light management in organic solar cells is necessary due to the limitation of the thickness of the active absorbing film. The active layer thickness cannot exceed a certain limit, typically 100-150 nm, beyond which the charge extraction is reduced. Lower charge extraction decreases the fill factor even if the short circuit current increases [23]. This results in an optimum thickness at which the product of the fill factor and short circuit current is maximum. Due to the film thickness being about 150 nm, it is semi-transparent and a substantial amount of light is not retained in the device. Most polymer blends do not uniformly absorb light over the entire visible spectrum leaving low absorption regions in the spectrum. These regions not only have limited contribution to the device current, in addition, these wavelengths are easily transmitted.

In this regard, we implement light management strategies to circumvent the problem of low absorption regions in the visible spectrum. The first strategy, involves incorporating a fluorescent molecule which absorbs in the low absorption region of the blend and emits efficiently in the high absorption region of the blend. This process of down-conversion can enhance the device current due conversion of wasted light in to

useful light. These molecules can be introduced in to the spaces in between the patterns to improve the current generated in the gap regions.

The second strategy is the use of microlens arrays to concentrate solar light and improve the device performance. Microlens arrays have been utilized to improve light collection in solar cells and detectors [24-26]. Fabrication methods are generally complex and require specialized lithography equipment resulting in increased cost of such devices when manufactured over large areas. We demonstrate a facile, soft approach to fabricate microlens arrays with unusual focusing properties. The non-spherical (or aspherical) profile modifies the input beam resulting in large depth of focus and hence suitable for concentrating light with a large alignment tolerance.

4.2 Light harvesting strategy I: down conversion

A low band gap donor-acceptor (D-A) PCPDTBT was chosen in our experiments [21]. PCPDTBT exhibits absorption up to the infrared regime 1 μm and a spectral window of low-absorption is observed in the 500 - 600 nm range [22]. This makes it a model system to study light management by down-conversion. Regions in the dip zone can exhibit absorption lower by a factor of two as compared to the spectral regions where high external quantum efficiency (EQE) is achieved. However, this material limitation need not necessarily be a limiting factor in the present device architecture. If a suitable dye can be incorporated in to the dielectric matrix it can be a source of additional useful flux. It should be noted that the dielectric layer is not a part of the active device. e.g. the dye-dispersed layer in the inter-electrode gaps can absorb the 500-600 nm radiation and re-emit in the 600 – 800 nm range, which can be efficiently harvested back into the active layer. This could bridge the absorption dip and the material drawback need not be a constraint.

4.2.1 Scheme for light harvesting

The schematic in Figure 4.1(a) depicts the mechanism of light harvesting where the red region represents the dye-dispersed PC matrix (D-PC). Red (600- 800 nm) and blue (400 nm) components of the incident white-light are absorbed by the donor (PCPDTBT) and acceptor (PCBM), respectively. A substantial amount of green light (500 nm, green arrows) reaches the electrodes as well as inter-electrode gaps owing to the transparency of PCPDTBT in the 500-600 nm spectral range. A large fraction of the green light is normally reflected by the alloy electrode in to the BHJ region. The rest is absorbed by the D-PC and re-emitted in the red (700-900 nm) which is the dominant absorption band of PCPDTBT. This red emission is either reflected by the alloy (straight red arrows) via normal reflection which encompasses the entire structure or guided (curved red arrows) due to the isotropic emission of dye in the PC film (Figure 4.1(a)). The emitted radiation from the dye is trapped and efficiently absorbed by the D-A polymer and charges generated at distances within decay length (L_d) can diffuse to the electrode to give rise to an additional current.

For light harvesting experiments, LDS 759 dye (Exciton, Inc.) was selected as it fulfilled the absorption and emission requirements for PCPDTBT as shown in Figure 4.1(b). Polyvinylidene fluoride (PVDF) or polymethylmethacrylate (PMMA) films on PC with the dye (5 wt. %) were spin coated from dimethylacetamide (DMA) and dimethylformamide (DMF), respectively. Perforations were then made on to these sheets with varying sizes and spacing.

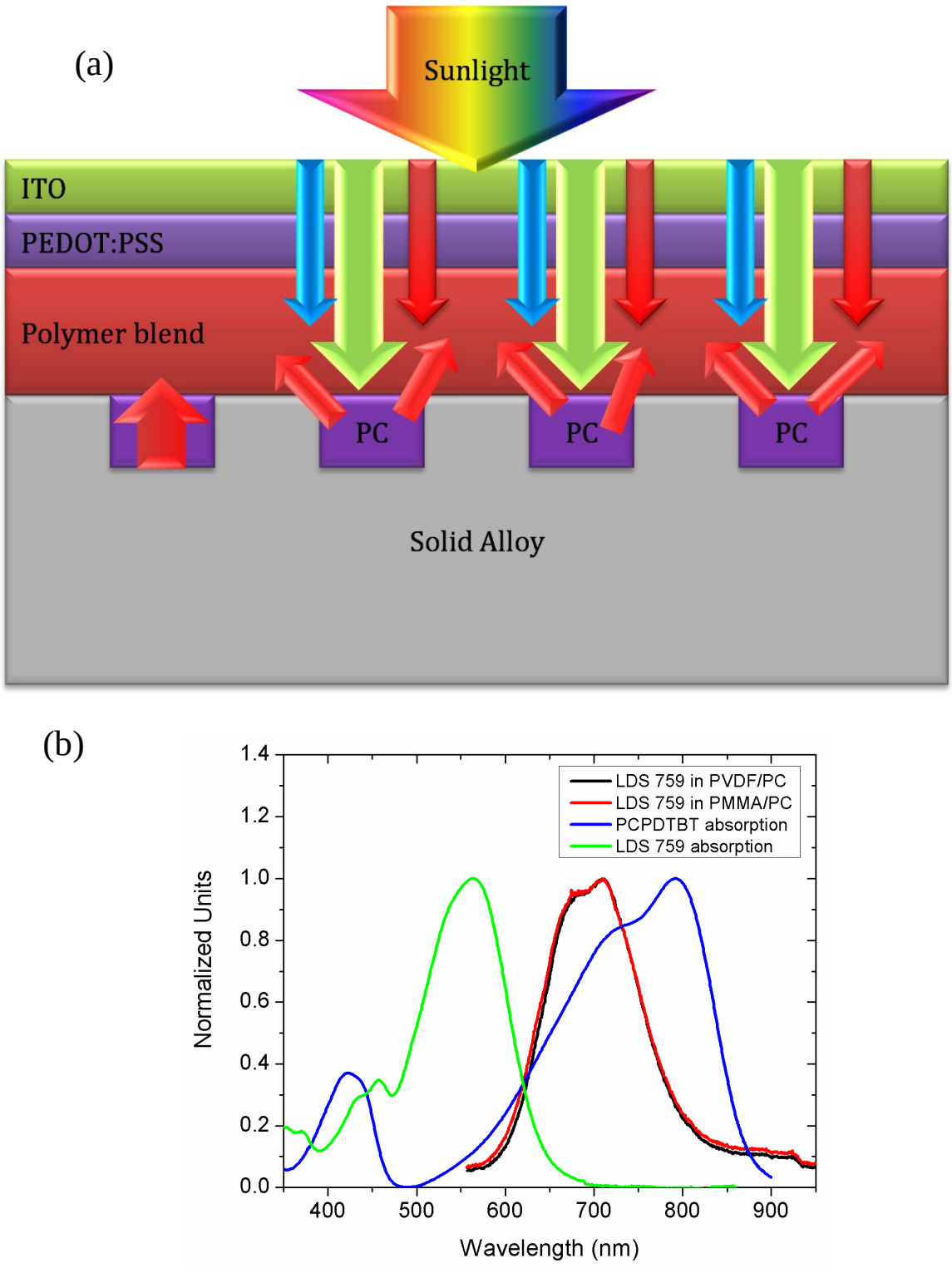

***Figure 4.1**: (a) Light harvesting scheme. (b) Absorption and emission spectra of LDS 759 and PCPDTBT.*

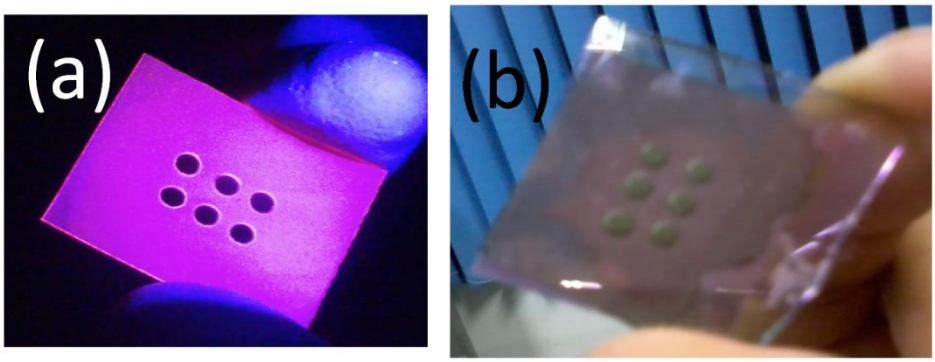

Figure 4.2: *(a) Perforated polycarbonate sheet with dye layer under U-V illumination. (b) A 3x2 solar cell with dye doped PC layer.*

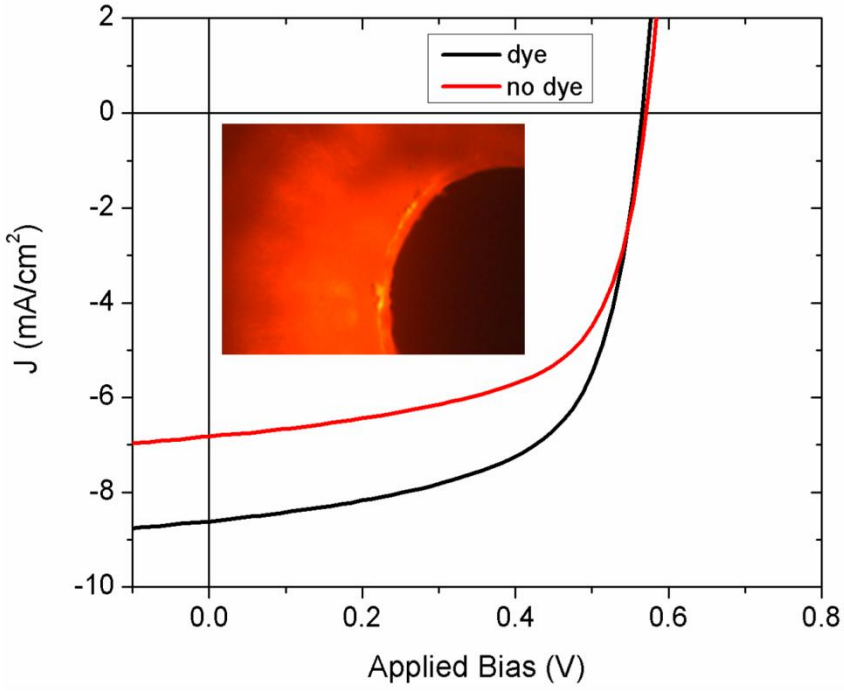

Figure 4.3: *J-V characteristics of a single pixel device with and without dye. (Inset, dye doped PC film under green illumination. (Reprinted with permission from A. J. Das, K. S. Narayan, Retention of Power Conversion Efficiency - from Small Area to Large Area Polymer Solar Cells. Advanced Materials 25, 2193, (2013). © 2013 John Wiley and Sons)*

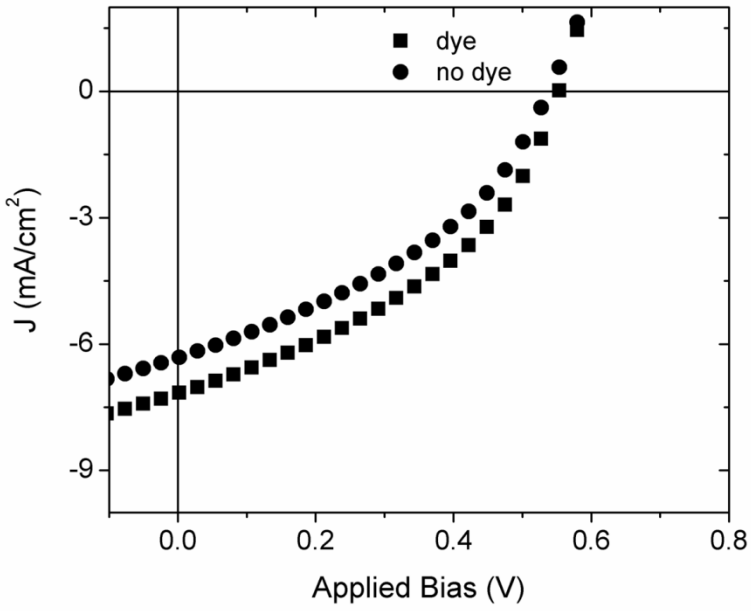

Figure 4.4: *J-V characteristics of 8 pixel device with and without dye. (Reprinted with permission from A. J. Das, K. S. Narayan, Retention of Power Conversion Efficiency - from Small Area to Large Area Polymer Solar Cells. Advanced Materials, 25, 2193, (2013). © 2013 John Wiley and Sons)*

Dye coated PC films showed a purple emission under UV/white light (Figure 4.2(a) and a bright red emission under 532 nm illumination as shown in Figure 4.3, inset. Devices with 0.01 cm^2 x 6-8 sub cells (Figure 4.2(b)) incorporating LDS 759 layer exhibited an increase in J_{sc} and η as shown in Figure 4.3. Several devices (about 12 in number) were tested from different batches of polymers and the improvement in J_{sc} was 12.1 ± 4.2% (maximum of up to 25% in some devices) indicating that emission from the dye was being absorbed by the D-A polymer (see Figure 4.3 and Table 4.1).

Table 4.1: Comparison of device performance with inclusion of dye layer

Device geometry	J_{sc} (mA/cm^2) Typical	Enhancement (%)		
		Typical	Average	Best
8 pixel	6.31	13.2	12.1 ± 4.2	26
8 pixel with dye	7.12			

(Reprinted with permission from A. J. Das, K. S. Narayan, Retention of Power Conversion Efficiency - from Small Area to Large Area Polymer Solar Cells. Advanced Materials 25, 2193, (2013). © 2013 John Wiley and Sons)

4.3 Bridging the EQE dip in BHJ blends

The EQE dip is generally present in most D-A polymer systems like PCPDTBT, PCDTBT amongst others. Even though high efficiencies have been observed in these systems, there is a scope for further improvement by incorporating light management strategies. An enhancement in J_{sc} needs to be validated by an EQE measurement in order to ascertain that the dye is contributing to the improvement.

The observed increase in J_{sc} has been validated by carrying EQE measurements on devices with and without the dye layers. The EQE shown in Figure 4.5 clearly indicates that an enhancement is observed at wavelengths corresponding to that of the dye absorption. An enhancement of 18-25% in EQE is observed validating the increase in J_{sc} from I-V measurements. Hence incorporating a dye dispersed dielectric matrix can bridge the minima present in the EQE due to low absorption of the polymer. This feature is analogous to enhancement in the NIR region of a resonant microcavity photodiode structure that was implemented using distributed Bragg reflector based substrates [27].

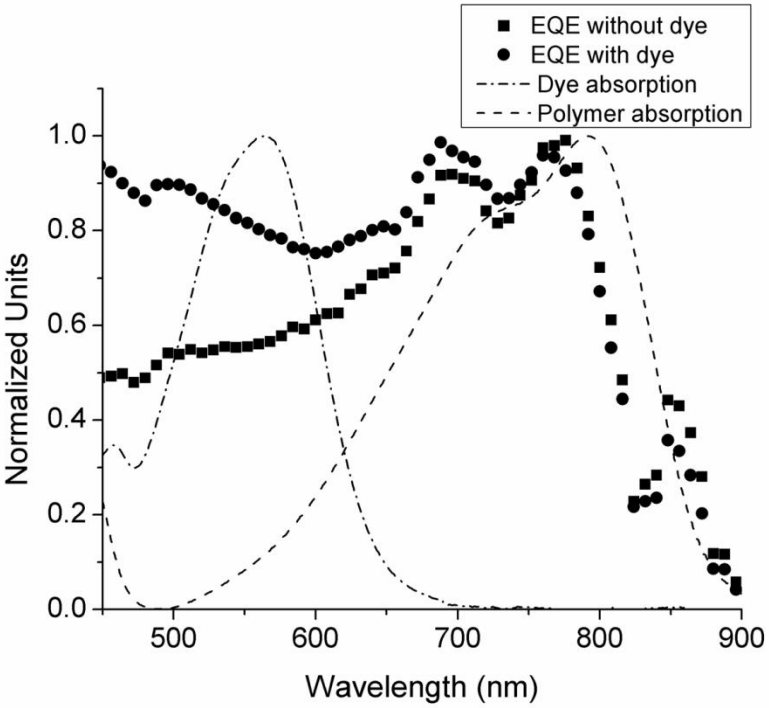

Figure 4.5: *EQE of a typical PCPDTBT:PCBM alloy-OSC without and with the dye. (Reprinted with permission from A. J. Das, K. S. Narayan, Retention of Power Conversion Efficiency - from Small Area to Large Area Polymer Solar Cells. Advanced Materials 25, 2193, (2013). © 2013 John Wiley and Sons)*

4.3.1 Enhanced decay length observed by photocurrent scanning

Devices were scanned under an upright microscope coupled to a pulsed laser. The laser through the microscope objective was focused on the sample and the stage was scanned in a raster like manner. Current from the device was monitored using a lock-in amplifier connected to the computer via LabView software. Figures 4.6(a) and (b) show the photocurrent maps of a device without and with a dye layer, respectively. By taking several line scans across these images and fitting an exponential function and subsequent averaging, a decay length was arrived at. As shown in Figure 4.6(c), the decay length for the device with the dye layer is larger than that of the device without the dye.

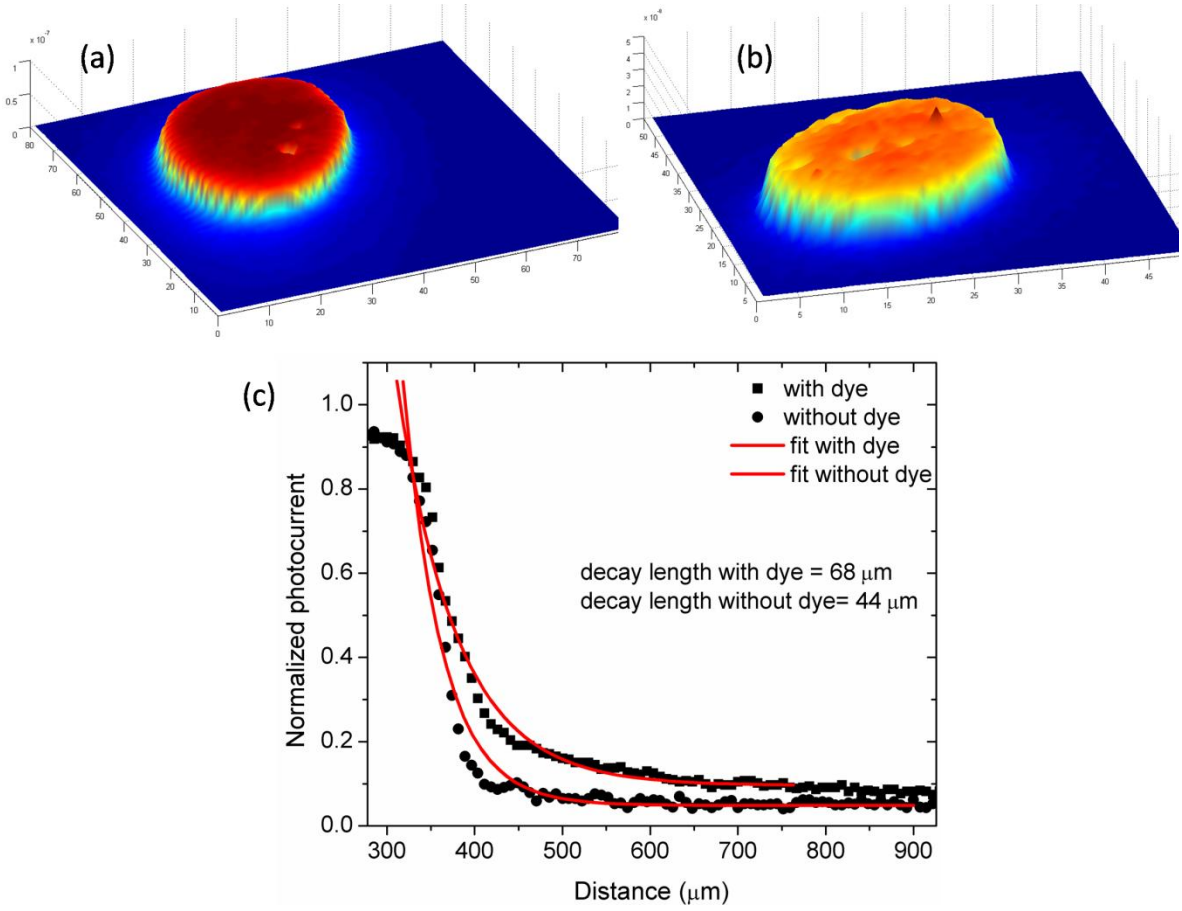

Figure 4.6: *2D photocurrent scan of alloy-OSC (a) without dye, (b) with dye. (c) photo-current decay profile for OSC with and without dye.*

The enhancement turns out to be about 35-50% which is an overestimate due to the large spot size of the laser. Microscope objectives of 10-20x were utilized which had a limited focusing capability and hence led to an overestimation of the decay length. Nevertheless, an enhancement is observed indicating that additional photons are generated in the spaces that contribute to the lateral photocurrent.

4.4 Optical simulations

These observations are also validated by finite difference time domain (FDTD) simulations of the Maxwell's equations with appropriate boundary conditions for the device geometry as shown in Figure 4.7. This geometry represents the gap in between the two patterned electrodes that incorporates a dye layer. Experimental absorption data of the dye was utilized to model the dye layer represented by a 2-term Lorentz model. The polymer blend was modelled using a 3-term Lorentz model where the ITO/PEDOT:PSS layers were treated as dielectrics as they do not exhibit appreciable dispersion in the wavelength range of simulation (please see Chapter 2, Section 2.5.3 and Appendix B more details). The absorption spectrum was calculated by subtracting the reflection spectrum from unity as the transmission in this geometry can be neglected due to a thick metal/alloy coating.

4.4.1 Absorption

Simulation results show an absorption improvement by 18% when a dye is included in the geometry as shown in Figure 4.8. This result is in reasonable accordance with the experimental observations which show a J_{sc} improvement of 12 ± 4.2 %. This device geometry can be implemented for various polymeric BHJ systems like Poly(3-hexylthiophene) (P3HT), Poly[[9-(1-octylnonyl)-9H-carbazole-2,7-diyl]-2,5-thiophenediyl-2,1,3-benzothiadiazole-4,7-diyl-2,5-thiophenediyl] (PCDTBT) as well as small molecule systems like copper phthalocyanine (CuPc). CuPc absorption profile is similar to that of PCPDTBT and hence LDS 759 itself can be utilized as the re-emission layer.

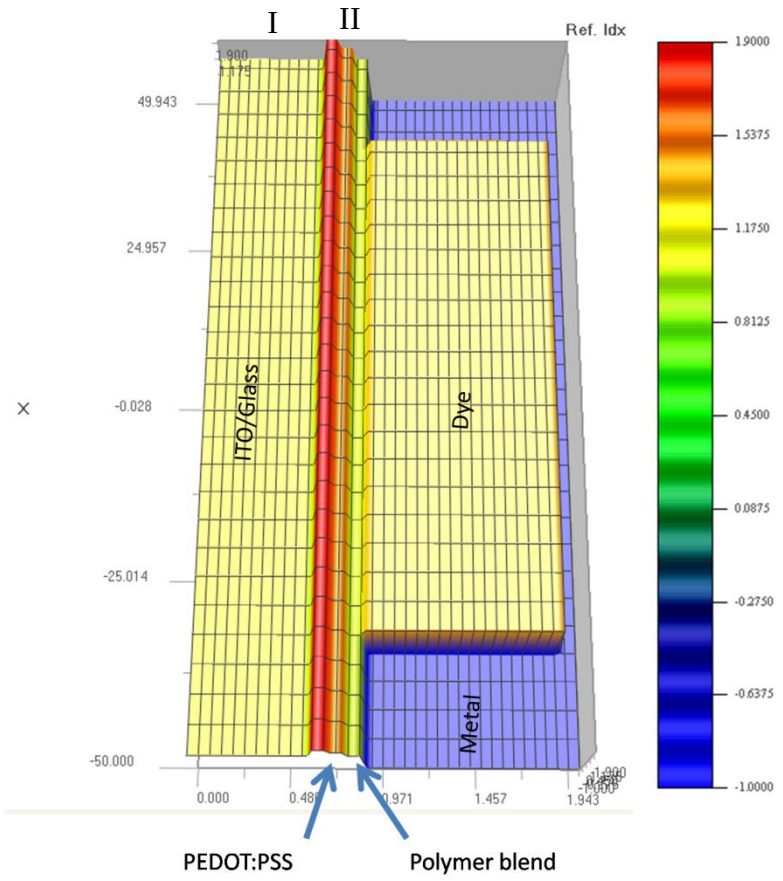

Figure 4.7: *Refractive index map of an organic solar cell with a dye layer sandwiched between two patterned electrodes.*

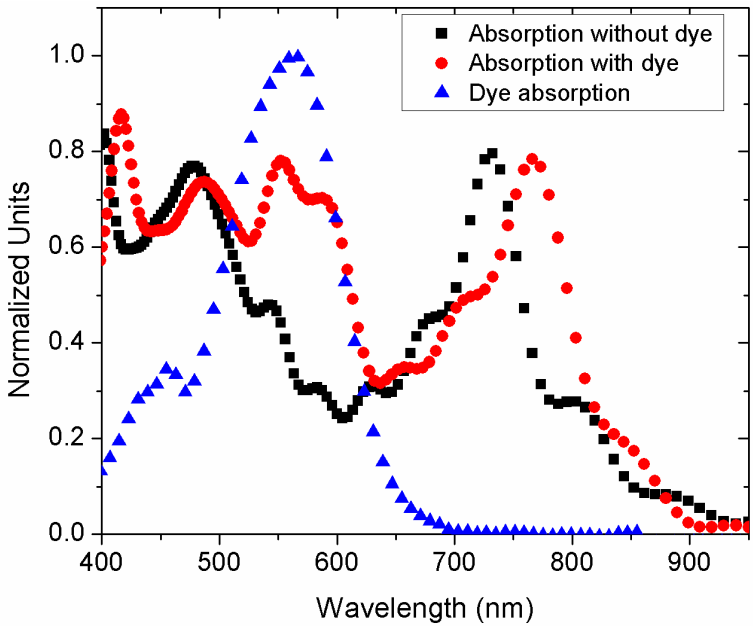

Figure 4.8: *Optical FDTD simulations of a PCPDTBT:PCBM alloy-OSC showing increased absorption due the inclusion of a suitable dye like LDS 759.*

4.4.2 Angle dependence simulations

Angle dependent simulations were carried out in order to arrive at the optimum angle of incidence. The angle of the light source was varied from 0^o to 90^o i.e. normal incidence to grazing incidence. Panels (a) in Figures 4.9-4.15 show the electric field (real part) distribution in the device. Panels (b) in the corresponding images show a line profile along the propagation direction. The procedure of analysis is based on analyzing the field strength in the Glass/ITO/PEDOT:PSS (shaded portion I) and polymer blend region (shaded region II) in the (b) panels of Figures 4.9-4.15 and comparing their relative strength. Large field strengths in region I indicate wave-guiding in the ITO/Glass layer which is undesirable. Field strength in region II must be lower than the neighbouring regions indicating that there is absorption of light in the active layer. Region III must

show a moderate field strength whose magnitude lies in between the fields at region I and region III.

Case 0°:

For the case of normal incidence, region II shows a low field strength indicating that light is absorbed in the polymer blend. Region I shows field strength of 1.6 units as compared to the 0.9 units in region II. The ratio (α= II/I) turns out to be 0.56. Region III shows that the absorption due to the dye. Due to the presence of alloy reflectors around the dye, region III shows higher field strength due to reflections.

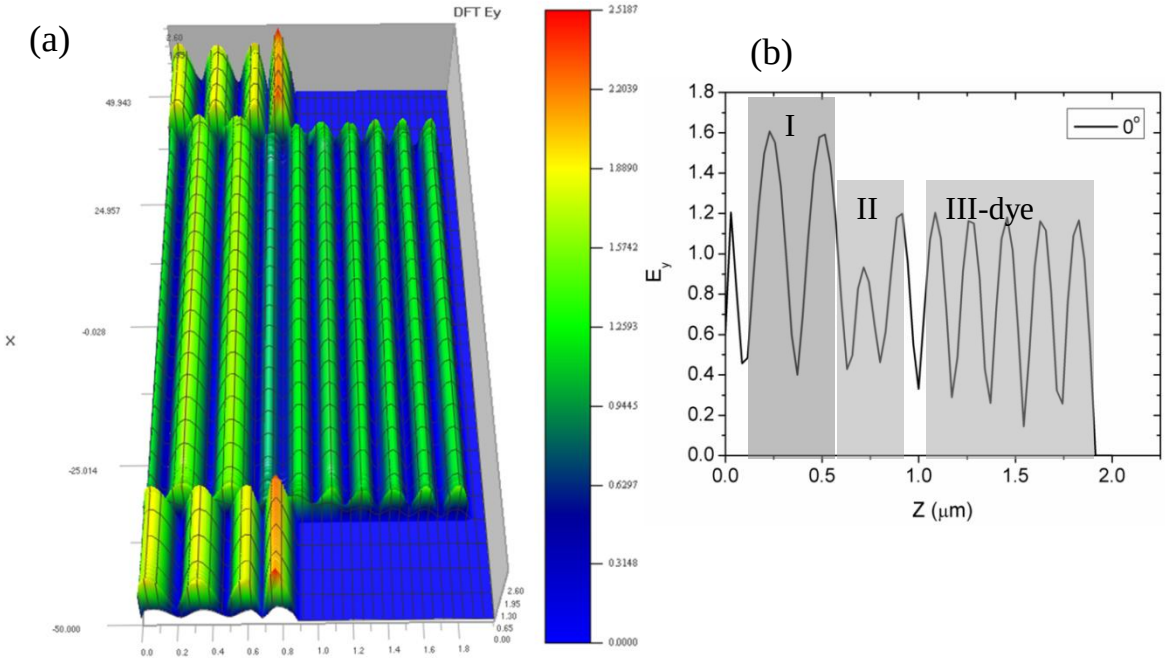

Figure 4.9: *FDTD simulations for a plane wave source incident at an angle of 0° w.r.t to the normal of the device (a) 2D electric field map. (b) Line profile of the electric field along the propagation direction.*

This implies that not only light is being absorbed in the polymer region, in addition there is minimal light guiding in the Glass/ITO/PEDOT:PSS region.

Case 15^o:

At an angle of incidence of 15^o, region I shows an intensity of 1.6 and region II shows an intensity of 0.75 as shown in Figure 4.10. α=0.46, which implies that the absorption in the polymer blend is even better at this angle. Since the field in region I is unchanged, this implies that the guiding in the Glass/ITO/PEDOT:PSS region is not very different at 15^o. Hence a slight tilt of the solar cell may yield better efficiency. Enhanced absorption at this angle is a result of increased path length of light in the active layer as shown in Figure 4.10 (c).

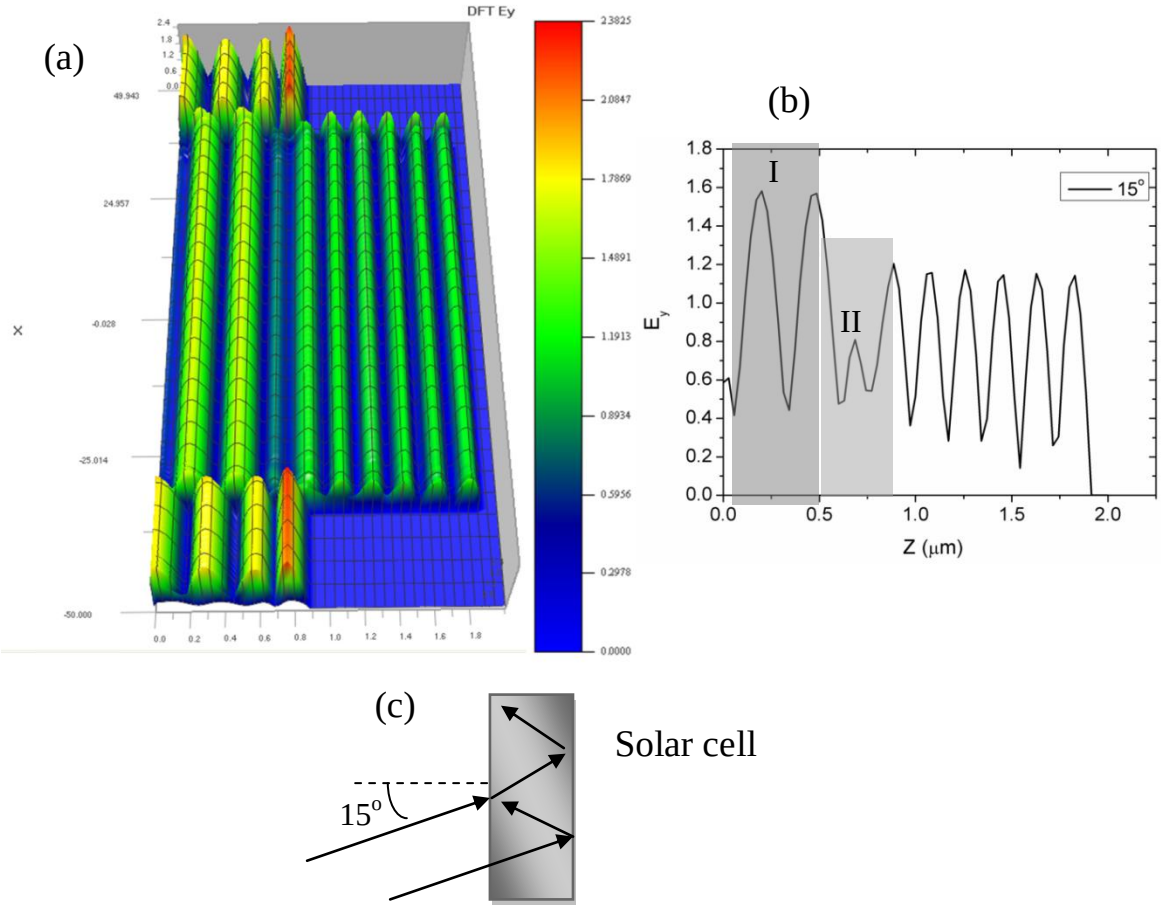

Figure 4.10: *FDTD simulations for a plane wave source incident at an angle of 15^o w.r.t to the normal of the device. (a) 2D electric field map. (b) Line profile of the electric field along the propagation direction. (c) Schematic depicting the path length of light in the solar cell.*

Case 30^{o}:

At an angle of incidence of 30^{o}, region I shows an intensity of 1.3 and region II shows an intensity of 1.6 as shown in Figure 4.11. α=1.23, which implies that the absorption in the polymer blend is low as compared to that of the Glass/ITO/PEDOT:PSS region at this angle. Lowering of the field in region I is desirable but the field region II remains high implying that the light in not absorbed efficiently at this angle. Hence a tilt angle greater than 30 ^{o} is not desirable for the solar cell.

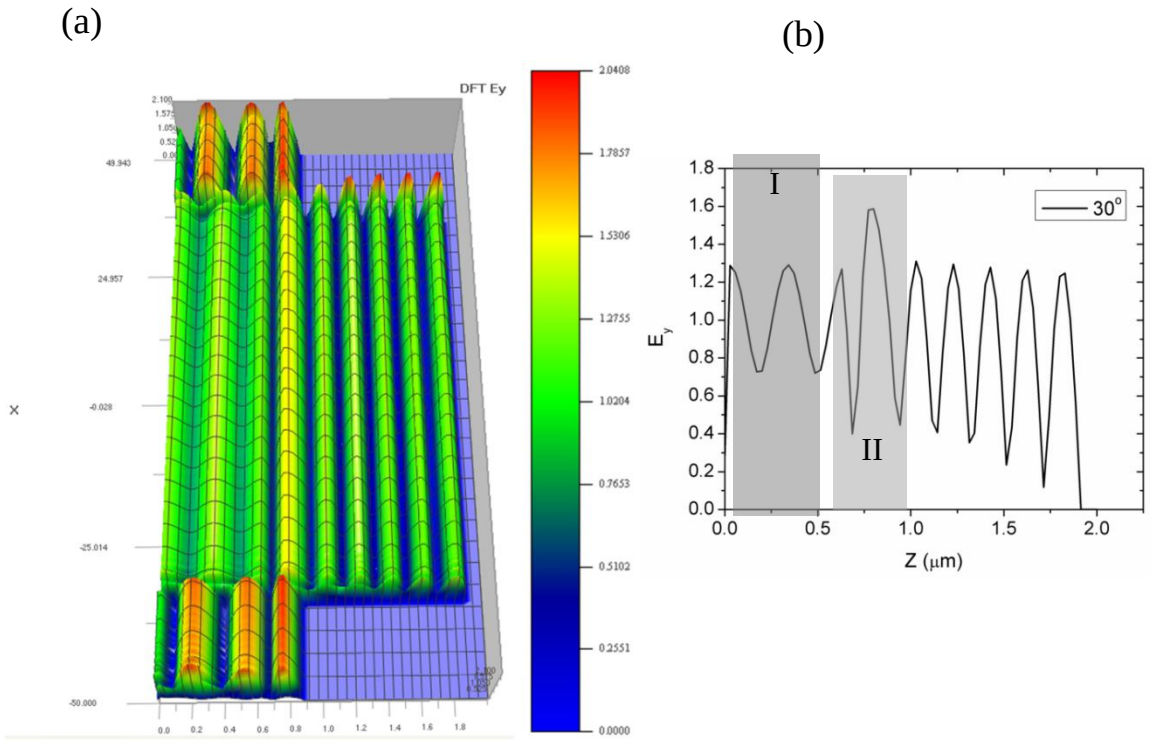

Figure 4.11: *FDTD simulations for a plane wave source incident at an angle of 30^{o} w.r.t to the normal of the device. (a) 2D electric field map. (b) Line profile of the electric field along the propagation direction.*

Case 45^{o}:

At an angle of incidence of 45^{o}, region I shows an intensity of 1.7 and region II shows an intensity of 1.0 as shown in Figure 4.12. α=1.7, which implies that much of the light is being trapped in region I this angle. Higher strength of electric field in region I is not desirable. Hence a tilt angle greater than 45 ^{o} is not advantageous for the solar cell.

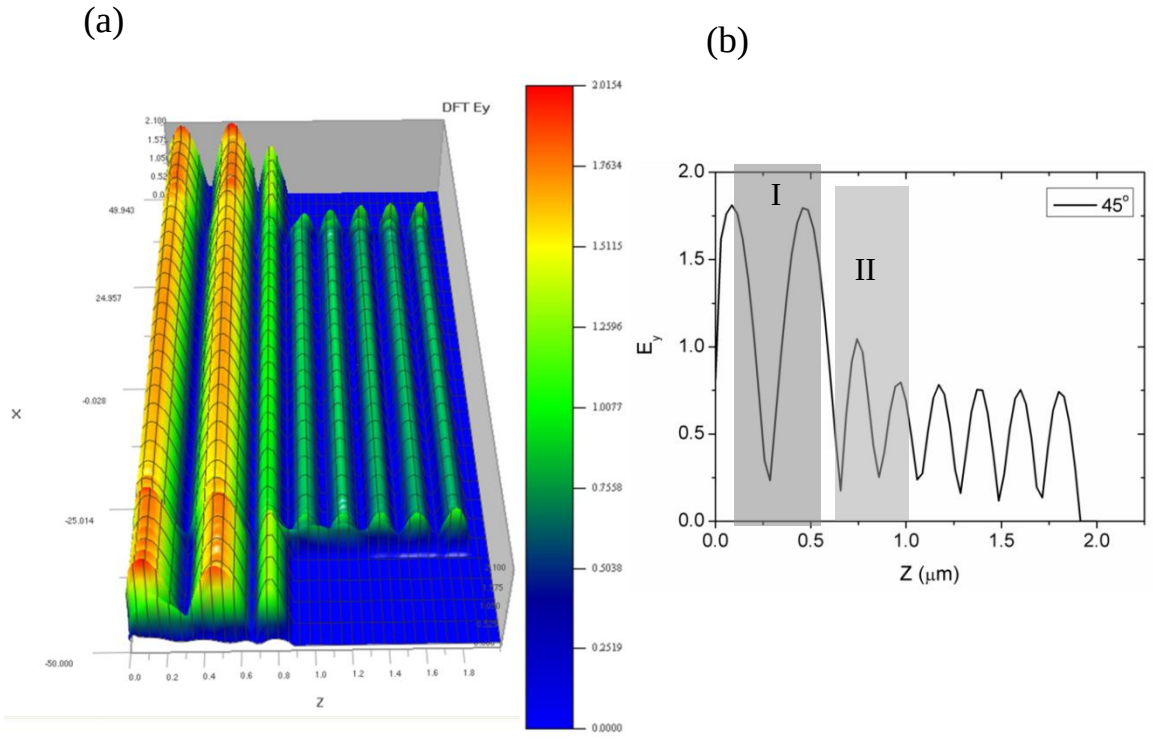

Figure 4.12: *FDTD simulations for a plane wave source incident at an angle of 45^{o} w.r.t to the normal of the device. (a) 2D electric field map. (b) Line profile of the electric field along the propagation direction.*

Case 60^o:

Larger angles of incidence were simulated in order to investigate the directionality of the emission from the dye in the presence of alloy reflectors. At an angle of incidence of 60^o, region I shows an intensity of 1.5 and region II shows an intensity of 0.9 as shown in Figure 4.13. α=0.6, which implies that the absorption in the polymer blend is better as compared to that angle of incidence at 45^o but not better than 15^o. There is also evidence that the field profile transforms from a two-lobed type to s single-lobed type indicating enhanced guiding.

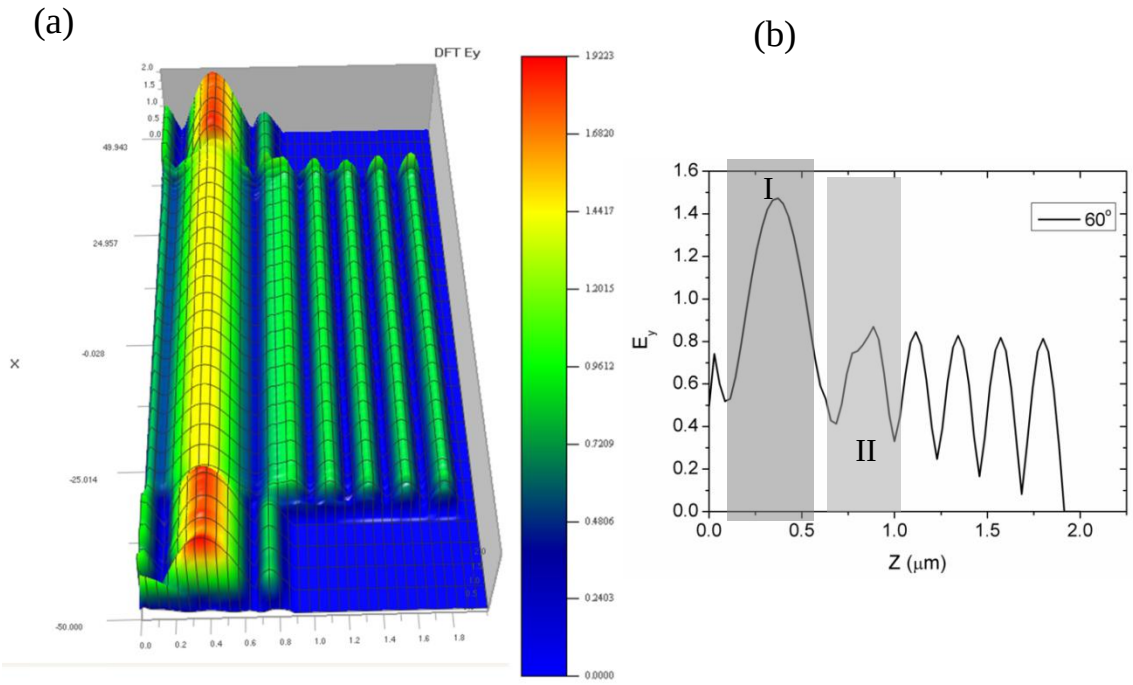

Figure 4.13: *FDTD simulations for a plane wave source incident at an angle of 60^o w.r.t to the normal of the device. (a) 2D electric field map. (b) Line profile of the electric field along the propagation direction.*

Case 75^o:

At an angle of incidence of 75^o, region I shows an intensity of 2.0 and region II shows an intensity of 0.5 as shown in Figure 4.14. α=0.25, which implies that the field in the polymer blend region is low but at the same time the field in region I is very high as compared to the lower angles on incidence. This indicates that the guiding in region I has enhanced and little light is reaching the polymer blend. In expected lines, large angles support guiding and hence a tilt angle of 75^o is not desirable for the solar cell.

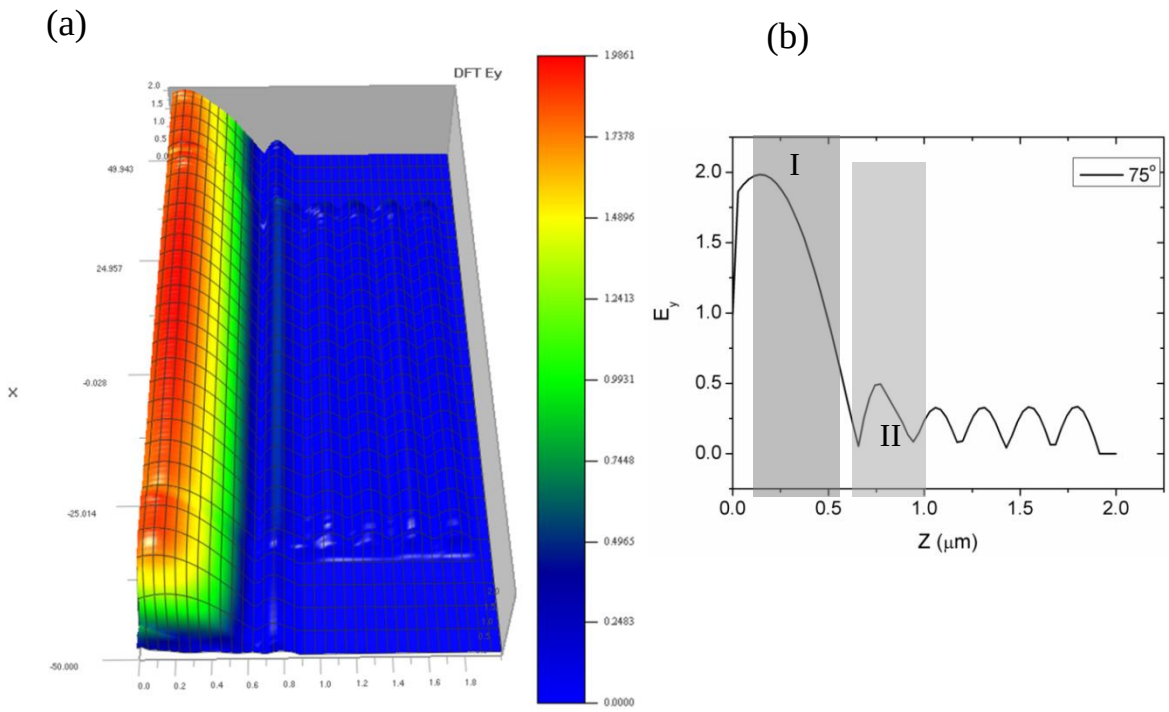

Figure 4.14: *FDTD simulations for a plane wave source incident at an angle of 75^o w.r.t to the normal of the device. (a) 2D electric field map. (b) Line profile of the electric field along the propagation direction.*

Case 90^o:

At an angle of incidence of 90^o, region I shows an intensity of 0.55 and region II shows an intensity of 0.05 as shown in Figure 4.15. α=0.1, which implies that the field in the polymer blend region is low but at the same time the field in region I is very high as compared to the lower angles on incidence similar to the 75^o case. This indicates that the guiding in region I has enhanced and little light is reaching the polymer blend. In expected lines, large angles support guiding and hence a tilt angle of 90^o or grazing incidence is not desirable for the solar cell.

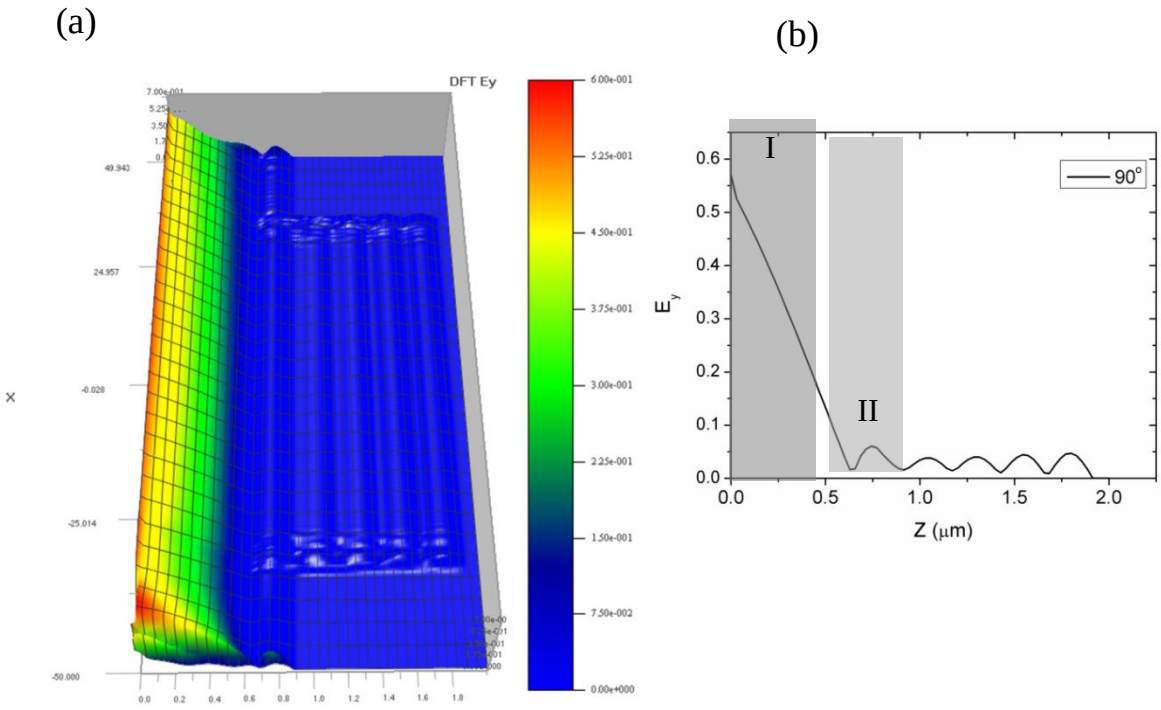

Figure 4.15: *FDTD simulations for a plane wave source incident at an angle of 90^o w.r.t to the normal of the device. (a) 2D electric field map. (b) Line profile of the electric field along the propagation direction.*

Hence, it can be concluded that a tolerance of 15^o may be permissible in the angle of incidence. Near normal incidence is beneficial as larger path lengths are traversed by the light beam as compared to the perfectly normal incidence, leading to enhanced

absorption. For very large angles of incidence (>45^{o}), guiding in the ITO/PEDOT:PSS layers dominates resulting in lower flux in the polymer or dye regions.

Summary: Down conversion

Light harvesting by down conversion was demonstrated in patterned OSC. By incorporating suitable dyes in the dielectric matrix, the efficiency of the solar cell could be enhanced by 12-25%. The dye matrix not only harvests and re-emits light in the useful part of the absorption spectrum, it also acts like an encapsulant to prevent moisture and oxygen contacting the active layer. This strategy can be applied to most thin film solar technologies as well.

4.5 Light harvesting strategy II: Polymer micro-lens arrays

Microlens arrays have been utilized as concentrators, anti-reflection coatings for solar cells and photodetectors [25-26]. Recently, it has been demonstrated that the efficiency of organic solar cells could be enhanced by 15-60% by incorporating microlens arrays [27-28]. Microlens arrays not only focus light into the active layer, they also prevent normally reflected light from exiting the cell. This leads to enhanced light trapping within the cell and a higher short circuit current. These arrays can be fabricated using soft lithography methods utilizing PDMS as the microlens material [28]. Conventional microlens arrays are typically made of small lenses with individual dimensions in the range of 5-500 μm. They possess spherical lens profiles which imposes the condition of point focus. In other words, they focus incoming light into a single point in the image plane, in this case the active layer. Hence the solar cell needs to be carefully aligned with the focal plane of the microlens in order to effectively utilize the concentrator. However, the above condition need not be true for lenses with aspherical or conical height profiles. These lenses have the ability to transform an incoming plane wave into a Bessel beam which exhibits limited diffraction and can possess a line focus. The second light management strategy in this chapter involves the fabrication of non-spherical microlens arrays and their applications in organic solar cells.

Bessel beams are a class of non-diffracting waves that can be manipulated to possess large focal lengths. They have a transverse field distribution defined by the zeroth-order Bessel function of the first kind. Due to their unusual properties like propagation invariance and self-reconstruction, these beam profiles have received a great deal of attention. Some of these properties are well suited for variety of applications like optical trapping [29-30], fabrication of polymer microfibres in solution [2], as virtual tips for near-field optics [31] and imaging [32]. Since early investigations on non-diffracting beams [33], several techniques have been demonstrated to generate Bessel beams; some examples include annular slits, axicons, and holographic gratings. Out of these methods, axicons [34] have shown to generate Bessel beams with high conversion efficiency. They can be realized from refractive, reflective, or diffractive elements. Thin film microaxicons have also been realized which offer several advantages over their bulk counterparts in terms of low loss, integration capability, and low weight. Several techniques have been demonstrated to fabricate thin film axicons including deposition of dielectric layers through shadow masks [35-36], transfer with reactive ion etching [37], electron beam lithography [38], or using a lens with spherical aberration [39]. Most of these methods are involved and require elaborate procedures along with specialized equipment to fabricate axicons with small wedge angles. In this regard, we demonstrate facile method to fabricate patterned, small wedge-angle axicons over large areas on flexible substrates.

4.5.1 Electrohydrodynamic instability

Electrohydrodynamic instabilities on viscous or visco-elastic polymer surfaces appear in the form of self-organized hexagonal ordered columnar patterns as shown in Figures 4.16 and 4.17 [40-48]. The pitch or spacing of these periodic patterns is determined by the thermodynamics of competition between the destabilizing electrostatic force and the stabilizing surface tension. The length scale of the patterns turns out to be a nonlinear function of the film thickness, strength of the electric field (EF), and surface tension of the film. The dynamics of the growth, evolution and modification of the columns are controlled by the rheological parameters like the viscosity and the field strength, while the aspect ratio is additionally dependent on the geometrical arrangement.

EF-induced pattern formation is brought about by placing a polymer film of thickness *h* on the substrate electrode in a capacitor-like geometry with the counter parallel electrode at a distance *d* from the bottom electrode.

4.5.2 Observation of non-cylindrical columns

A cross-sectional study on the columns revealed that beyond a certain aspect ratio, a gradient in the cross-sectional radius of the columns were observed which deviated from the cylindrical profiles (Figure 4.18). This observation was further investigated to fabricate non-spherical lens structures. Non-spherical contours of the column structure gave rise to beam characteristics that were similar to the ones reported for typical Bessel beams [49]. The method demonstrated a facile technique to fabricate microaxicons that combined the advantages of thin film and polymer technologies. Extremely low wedge angles 2° can be realized, along with reasonable control over the height, pitch, and width of the microaxicons [50].

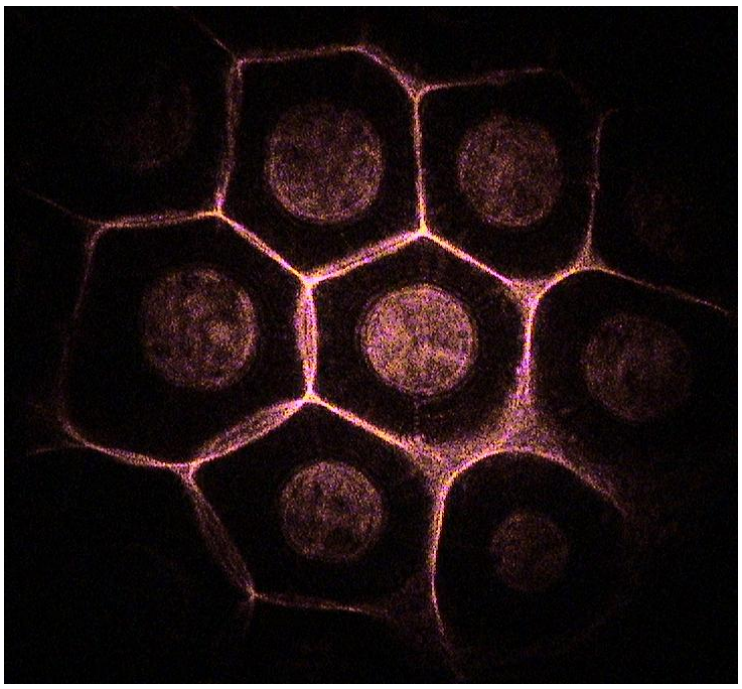

Figure 4.16: *Optical image of micro-pillar array under laser illumination.*

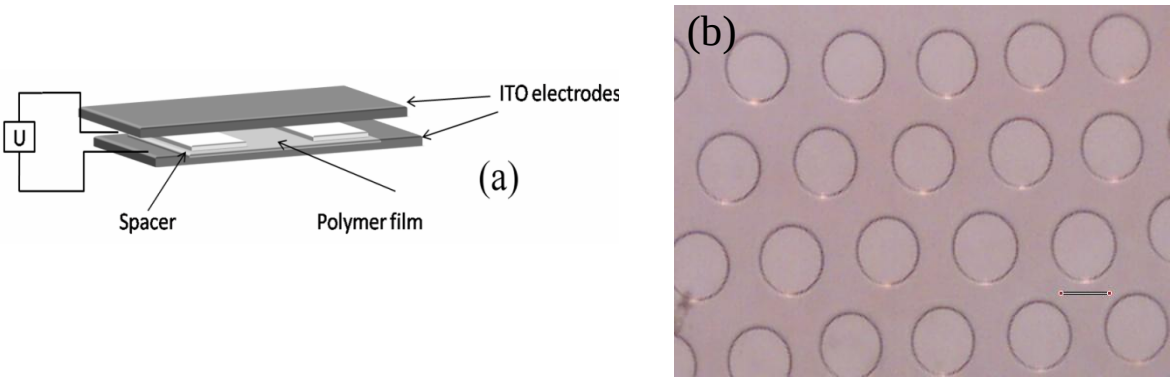

Figure 4.17: *(a) Experimental set-up to study electro-hydrodynamic instabilities in viscous polymer films. (b) Optical top-view microscope image of micro-pillar array. Scale bar: 300 μm. (Reprinted with permission from A. J. Das, K. S. Narayan, Observation of Bessel beams from electric-field-induced patterns on polymer surfaces. Optics Letters 2009, 34, 3391. © 2009 Optical Society of America)*

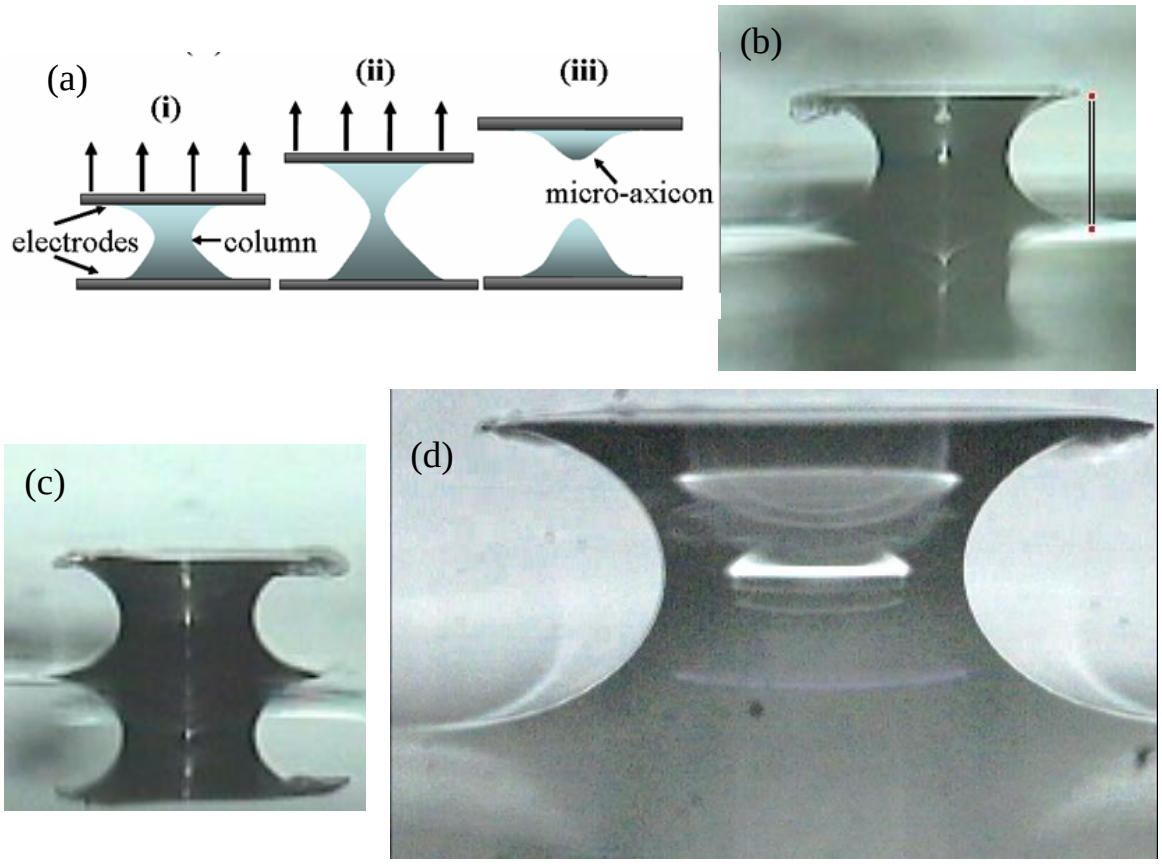

Figure 4.18: *Cross-sectional images of a single pillar under 10X and 50X magnification.*

4.5.3 Fabrication protocol

A schematic of the experimental setup for formation of polymer columns is shown in Figure 4.17(a). The polymer utilized in the experiments is polydimethylsiloxane (PDMS, Dow Corning) along with a crosslinker (Sylgard 184 curing agent). PDMS is optically transparent and hence an ideal material for lens arrays. Films with thickness *h* in the range of 28–30 μm were obtained by spin coating (40 s at 3600 rpm). A double layer of teflon tape 180 μm thick served as the spacer with a gap *d*−*h* between the film surface and the top contactor (ITO-coated cover slip glass). An external bias was introduced across the ITO electrodes. Application of an EF causes an electrohydrodynamic instability which is a destabilizing force. The surface tension on the other hand is a stabilizing force which competes with the electrostatic force. Eventually the EF is capable of deforming the film and amplifying any fluctuations on the surface leading to the formation of hexagonally ordered columns as shown in Figure 4.17(b). The characteristic wavelength of the periodic pattern is dependent on the surface tension of the film, the applied EF, and the thickness of the film. It can be expressed as,

$$\kappa = 2\pi E_p^{-2}\left[\frac{\gamma U}{\varepsilon_0 \varepsilon_p(\varepsilon_p-1)^2}\right]^{1/2} \quad \text{.....(4.1)}$$

where, U is the applied voltage, γ is the surface tension of the polymer film, ε_0 is free-space permittivity and ε_p is the dielectric constant of the polymer. E_p is the EF in the polymer film given by $E_p=U/(\varepsilon_p d-(\varepsilon_p-1)h)$. The periodicity of the pattern (κ) can be controlled by the EF and the film thickness, while the dynamics of the growth and evolution can be controlled by the viscosity and the EF [43].

A sustained growth of the pillar height maintaining a uniform circular cross-section, especially for large *d* (or aspect ratio), is not observed. The dumbbell nature of the cylinder observed can be attributed to additional adhesive or wetting interactions of the film with the electrified contact or electrode, which may promote an increase in contact area. These distortions in the symmetry akin to spheroid cone transformations or deformations of a spherical drop in an EF can be explained by a stability analysis [51].

Hence, the extent of tapering can be controlled by the electric field which in turn controls the contact area.

These contours, resembling pedestals are shown in Figure 4.18 (b-d). The cross-linker allows the sample to be treated thermally 90°C at this stage for about 1 hr.

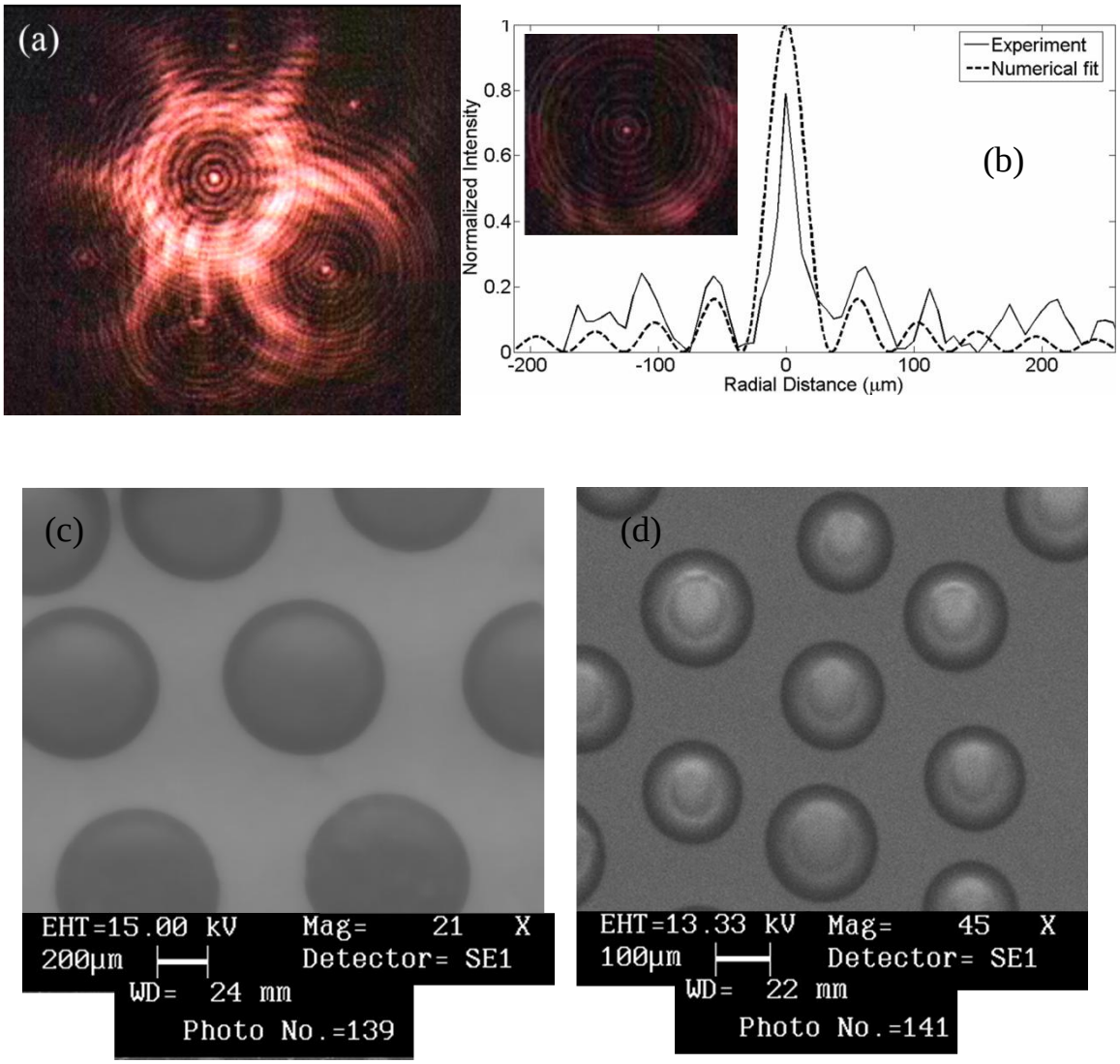

Figure 4.19: *(a)Array of Bessel beams. (b) Transverse profile of a Bessel beam. (c) and (d) SEM images of microlens array. (Reprinted with permission from A. J. Das, K. S. Narayan, Observation of Bessel beams from electric-field-induced patterns on polymer surfaces. Optics Letters 2009, 34, 3391. © 2009 Optical Society of America)*

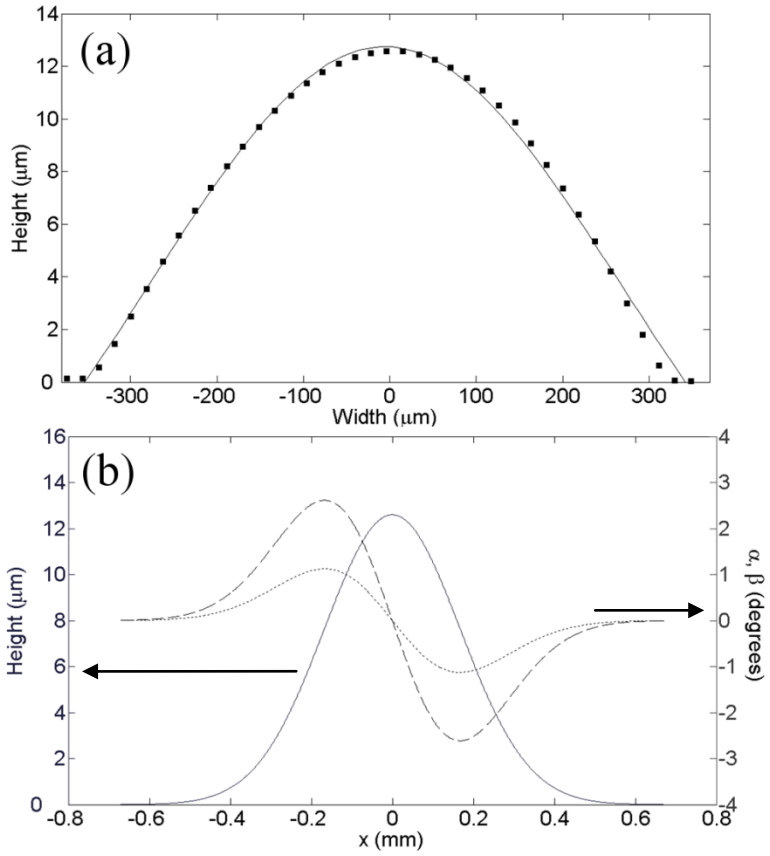

Figure 4.20: *(a) Profile of a single microlens as measured using a profilometer. (b) Angle of the beam with respect to the axicon angle and the height profile.*

Due to the viscous nature of PDMS the pattern features are maintained for a reasonable period (few hours) after removal of the field, as the polymer firmly adheres to the top electrode.

Fabrication of the microaxicon array involves peeling off the top electrode after the desired dimensions of the lens is achieved. During this process, the columns are gradually pulled apart mechanically due to the extension of the contactors, resulting in two non-spherical surfaces on both the electrodes. The individual pattern after the curing process assumes a shape of an axicon. A schematic depicting the various stages in the lens formation is shown in Figure 4.18(a). During the curing process there may be shrinkage in the height of the microaxicon due to stabilizing bulk interactions. This

results in lower wedge angles that are advantageous to obtain microlenses with large focal lengths.

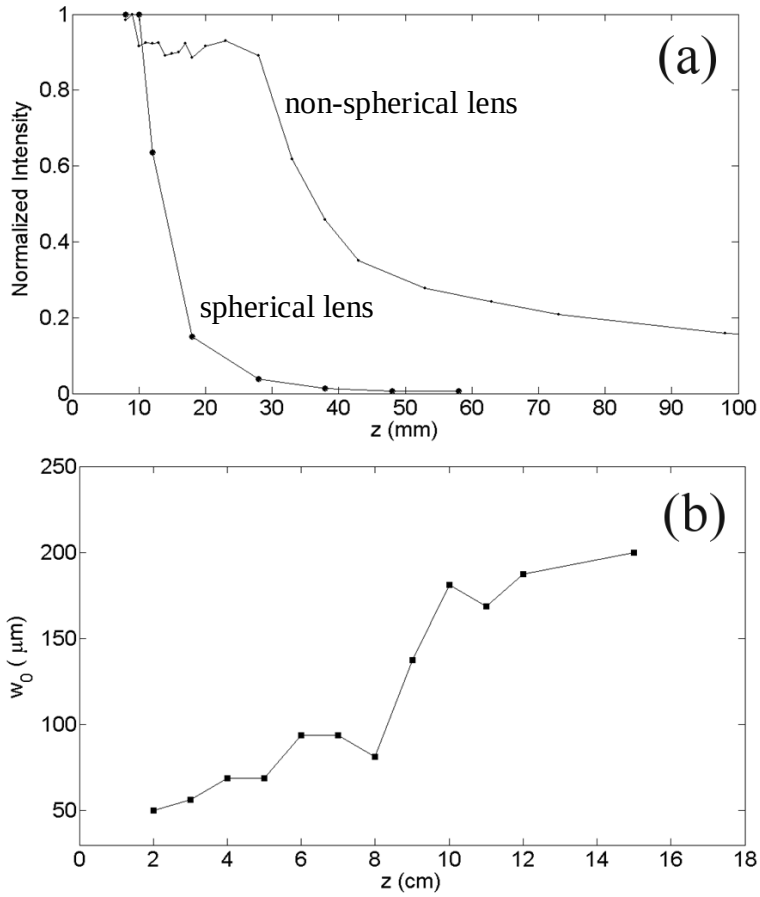

Figure 4.21: *(a) Comparison or focusing action of a spherical lens and Gaussian shaped microlens. (b) Variation of spot size as a function of axial distance for a Gaussian lens.*

4.5.4 Characterization of microlenses

Illuminating the microlens arrays with a Gaussian beam transformed the beam into a Bessel beam with the intensity profile described by Bessel function as shown in Figure 4.19 (a,b). Figure 4.19 (c,d) shows top-view scanning electron microscope (SEM) images of the microaxicon array fabricated with a 180 μm spacer at 800 V. The profiles were characterized by using a profilometer (Dektak, Veeco) and fitted excellently to a Gaussian function with coefficient of determination 0.99, as shown in Figure 20(a). The axicons had a height in the range of 12 to 18 μm. Considering a Gaussian-shaped axicon the angular distribution of the beam can be evaluated by the expression,

$$\beta(\rho) = \arcsin(n \sin \alpha) - \alpha(\rho) \quad \text{.....(4.2)}$$

where, α is the angle of the axicon, ρ is the radial coordinate, and n is the refractive index of the axicon material (PDMS). For a refractive index of n=1.43 (PDMS), a laser wavelength of 633 nm and a Gaussian thickness profile, the angles turn out to be < 2.61° and 1.12°, respectively (Figure 4.20(b)). The fringe spacing of the pattern was estimated to be about16.6 μm from the expression $\Delta r = (\lambda/2) \sin(\beta_{max})$ where, λ is the illumination wavelength and β_{max} is the maximum deflection of the Bessel beam (Figure 4.19(a,b)). The intensity distribution of the light–axicon interaction can be evaluated by the Fresnel diffraction integral,

$$A(r,z) = \frac{a_0 k}{iz} \int_0^{\infty} \exp\left[-\frac{\rho^2}{\omega^2} - i\beta\rho + \frac{ik(\rho^2+r^2)}{2z}\right] J_0(\rho)\rho d\rho \quad \text{.....(4.3)}$$

where, a_0 is the amplitude, k is the propagation constant, ω is the width of the input Gaussian beam, J_0 is the Bessel function of the zeroth order and first kind, and r and z are the radial and axial coordinates, respectively.

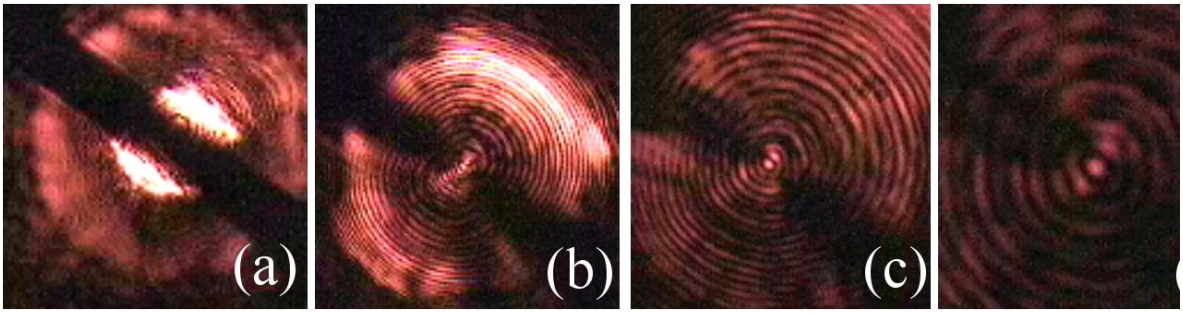

Figure 4.22: *Self-reconstruction of the Bessel beam around an obstacle of 150 μm at (a)2 mm (b)10 mm (c)30 mm (d)80 mm. (Reprinted with permission from A. J. Das, K. S. Narayan, Observation of Bessel beams from electric-field-induced patterns on polymer surfaces. Optics Letters 2009, 34, 3391. © 2009 Optical Society of America)*

In the present case, the cone takes on a Gaussian-shape profile,

$$\beta = \beta_0(\rho) \exp(-\rho^2/\omega_a^2) \quad \text{.....(4.4)}$$

where, the parameters β_0 and ω_a define realistic axicon features. Solving Eq. (4.3) numerically can lead to a solution that describes the modulation of axial intensity of the Bessel beam [52].

4.5.5 Characteristics of Bessel beams

In order to study the beam properties, the microaxicon array was illuminated with a He–Ne laser and observations were made from the vertex side by using a CCD camera. Transverse intensity profiles were recorded with a CCD camera with a 10x objective. The microaxicons typically had a focii at 1 cm from the vertex.

Features indicating that the beam had Bessel-like characteristics are the following. (i) The beam cross section had a uniform central region corresponding to the zeroth-order mode, which was verified with transverse intensity measurements. Figure 4.19(a,b) shows the CCD image of the Bessel beam at 4 cm from the array along with the corresponding transverse intensity profiles of the beam. A Bessel function of the zeroth order and first kind was fitted to the experimentally obtained intensity profile, and a satisfactory agreement was observed as shown in Figure 4.19(b). (ii) Axial variation of the on-axis intensity measured Bessel beam is compared with a Gaussian beam with a similar initial spot size in Figure 4.21(a). It was evident that the Bessel beam did not exhibit noticeable diffraction for about 40 mm, which indicates an order of magnitude enhancement in the depth of focus as compared to the Gaussian beam. Modulation of the axial intensity due to the rounded tip of the axicon was observed [52-53] on the CCD camera. It is not very prominent in Figure 4.21(a) since the aperture size was large in comparison with the central core diameter and there was a finite contribution from the neighbouring rings. Nevertheless it is noticeable is Figure 4.21(a). (iii) Beam core diameter measured for different axial positions as shown in Figure 4.21(b) and was found to be invariant 4 cm from the array, confirming the presence of a Bessel zone. (iv) Self-reconstruction of the transverse intensity profile of the beam was observed where the beam could heal in the presence of an obstacle (Figure 4.22).

4.5.6 Bessel beams from solar and white light sources

Since a degree of spatial coherence is necessary to observe Bessel beams, we investigated white light sources like the Hg lamp and sunlight for white light Bessel beams. It turns out that the coherence length of white light sources and the sunlight is about 100 μm [54]. This coherence length is sufficient to observe interference effects if the dimensions of the lenses is comparable. It turns out that the lateral dimensions of the individual microlenses are in the range of 100-400 μm, which is ideal for white light sources. Under white light illumination, Bessel beams were observed as shown in Figure 4.23(a,b). There was also a dispersion-like feature observed as different wavelengths interfere at slightly different angles. It was interesting to observe Bessel like beams from sunlight as well (Figure 4.22(b)).

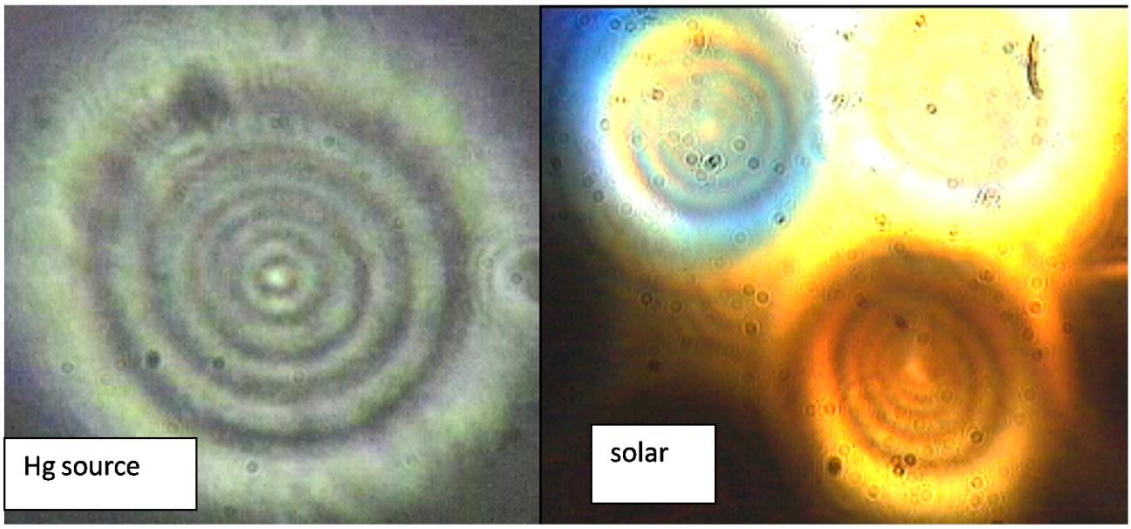

Figure 4.23: *White light Bessel beams from (a) Hg lamp, (b) Sunlight. A mirror was used to reflect sunlight under AM 1.0 conditions on to an optical setup comprising of the microlens arrays. A 20 μm pinhole was used to image the Bessel beams on a CCD camera.*

4.6 Implications in solar cells

Microlens arrays can be easily integrated into solar cells as light concentrators. Recently it has been demonstrated that microlens arrays improved the efficiency of P3HT and PCDTBT solar cells by 4-10% [55]. In this regard, the proposed design for light management is shown in Figure 4.24. Typically, microlens arrays need to be aligned axially such that the focus coincides with the active material. Since plane or Gaussian beams have a depth of focus several hundred micrometers, a small misalignment can cause the focus to shift away from the active layer. This is not a critical problem in silicon solar cells as the active material is several micrometers thick. But in the case of thin film solar cells like OSC, the active layer only a few hundred nanometers thick. Hence a small misalignment can cause the focus to shift away from the device itself. Microaxicon arrays can have a depth of focus several centimeters and can be tolerant to any misalignment making them suitable for thin film solar cells.

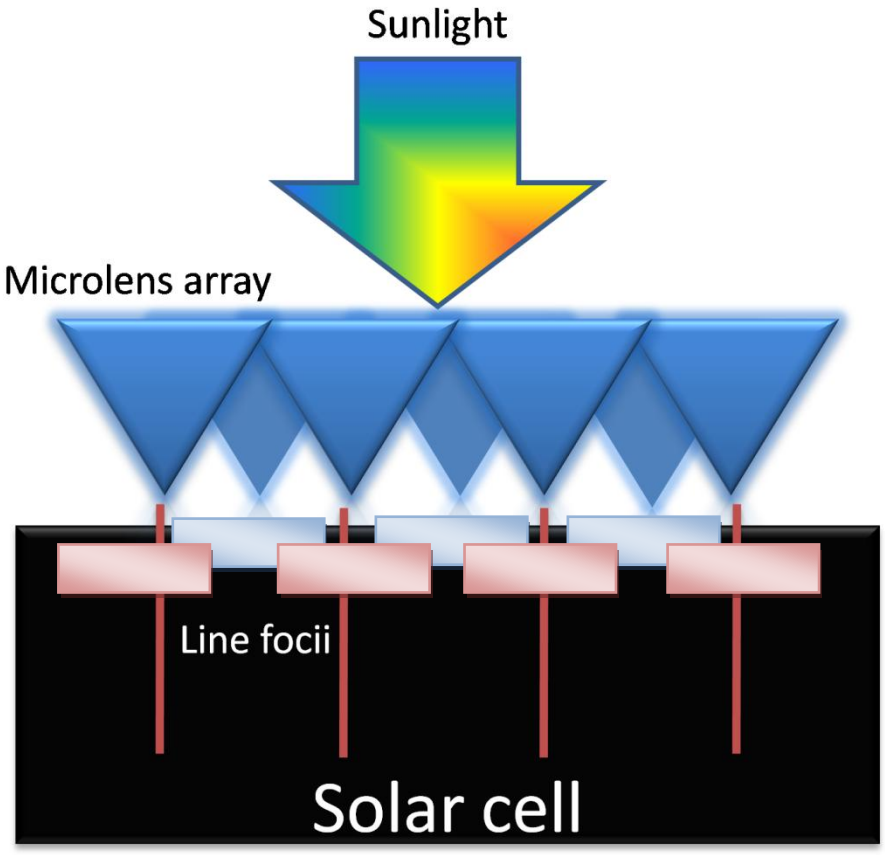

Figure 4.24: *Light management using non-spherical microlens arrays.*

Summary: Polymer microlens arrays

The results demonstrate an easy method to manipulate beam characteristics. It should be possible to optimize the method by controlling the dynamics of the growth process to obtain appropriate patterns for desired beam characteristics. The possibility of fabricating polymer microaxicon arrays by using a simple and reproducible lithography-free technique and using EF strength, film thickness, and rheological parameters as factors that control the height and pitch of the microaxicon array should have a wide range of applications. The beam from the EF-induced deformation exhibited all the basic features of a Bessel beam in terms of the non-diffracting distance and spot size variation with axial distances, including the self-reconstruction characteristics.

References

[1] H. S. Chang, H. C. Jung, H. T. Kim, Improved Light Trapping Structure for Monocrystalline Silicon Solar Cells *35th Ieee Photovoltaic Specialists Conference* **2010**, 3112.

[2] Y. R. Chen, Z. Q. Li, X. H. Chen, C. Liu, X. J. Ye, Z. B. Wang, Z. Sun, S. M. Huang, Improved performance of flexible amorphous silicon solar cells with silver nanowires *Journal of Applied Physics* **2012**, *112*.

[3] J. S. Cho, S. Baek, K. H. Yoon, Enhancement of light trapping by textured back electrodes in tandem micromorph n-i-p silicon thin film solar cells *Current Applied Physics* **2011**, *11*, S2.

[4] S. Colodrero, A. Mihi, J. A. Anta, M. Ocana, H. Miguez, Experimental Demonstration of the Mechanism of Light Harvesting Enhancement in Photonic-Crystal-Based Dye-Sensitized Solar Cells *Journal of Physical Chemistry C* **2009**, *113*, 1150.

[5] K. Barnham, J. L. Marques, J. Hassard, P. O'Brien, Quantum-dot concentrator and thermodynamic model for the global redshift *Applied Physics Letters* **2000**, *76*, 1197.

[6] R. Bose, D. J. Farrell, A. J. Chatten, M. Pravettoni, A. Buechtemann, J. Quilitz, A. Fiore, L. Manna, K. W. J. Barnham, Luminescent Solar Concentrators: Nanorods and Raytrace Modeling *Pvsc: 2008 33rd Ieee Photovoltaic Specialists Conference, Vols 1-4* **2008**, 24.

[7] R. Bose, M. Gonzalez, P. Jenkins, R. Walters, J. Morseman, M. Moss, C. McLain, P. Linsert, A. Buchtemann, A. J. Chatten, K. W. J. Barnham, Resonance Energy Transfer in Luminescent Solar Concentrators *35th Ieee Photovoltaic Specialists Conference* **2010**, 467.

[8] M. J. Currie, J. K. Mapel, T. D. Heidel, S. Goffri, M. A. Baldo, High-efficiency organic solar concentrators for photovoltaics *Science* **2008**, *321*, 226.

[9] R. Biswas, C. Xu, Photonic and plasmonic crystal based enhancement of solar cells - Theory of overcoming the Lambertian limit *Journal of Non-Crystalline Solids* **2012**, *358*, 2289.

[10] S. B. Mallick, M. Agrawal, P. Peumans, Optimal light trapping in ultra-thin photonic crystal crystalline silicon solar cells *Optics Express* **2010**, *18*, 5691.

[11] X. H. Li, W. C. H. Choy, L. J. Huo, F. X. Xie, W. E. I. Sha, B. F. Ding, X. Guo, Y. F. Li, J. H. Hou, J. B. You, Y. Yang, Dual Plasmonic Nanostructures for High Performance Inverted Organic Solar Cells *Advanced Materials* **2012**, *24*, 3046.

[12] J. Bomm, A. Buchtemann, A. J. Chatten, R. Bose, D. J. Farrell, N. L. A. Chan, Y. Xiao, L. H. Slooff, T. Meyer, A. Meyer, W. G. J. H. M. van Sark, R. Koole, Fabrication and full characterization of state-of-the-art quantum dot luminescent solar concentrators *Solar Energy Materials and Solar Cells* **2011**, *95*, 2087.

[13] D. K. G. de Boer, C. R. Ronda, W. Keur, A. Meijerink, New luminescent materials and filters for Luminescent Solar Concentrators *High and Low Concentrator Systems for Solar Electric Applications Vi* **2011**, *8108*.

[14] Y. R. Do, Cylindrical luminescent solar concentrators are more efficient if they're hollow *Laser Focus World* **2011**, *47*, 10.

[15] M. A. ElShahawy, A. F. Mansour, Optical properties of some luminescent solar concentrators *Journal of Materials Science-Materials in Electronics* **1996**, *7*, 171.

[16] J. Gutmann, M. Peters, B. Blasi, M. Hermle, H. Zappe, J. C. Goldschmidt, Towards photonic luminescent solar concentrators *Next Generation (Nano) Photonic and Cell Technologies for Solar Energy Conversion Ii* **2011**, *8111*.

[17] M. G. Hyldahl, S. T. Bailey, B. P. Wittmershaus, Photo-stability and performance of CdSe/ZnS quantum dots in luminescent solar concentrators *Solar Energy* **2009**, *83*, 566.

[18] S. McDowall, B. L. Johnson, D. L. Patrick, Simulations of luminescent solar concentrators: Effects of polarization and fluorophore alignment *Journal of Applied Physics* **2010**, *108*.

[19] C. L. Mulder, P. D. Reusswig, A. P. Beyler, H. Kim, C. Rotschild, M. A. Baldo, Dye alignment in luminescent solar concentrators: II. Horizontal alignment for energy harvesting in linear polarizers *Optics Express* **2010**, *18*, A91.

[20] C. L. Mulder, L. Theogarajan, M. Currie, J. K. Mapel, M. A. Baldo, M. Vaughn, P. Willard, B. D. Bruce, M. W. Moss, C. E. McLain, J. P. Morseman, Luminescent Solar Concentrators Employing Phycobilisomes *Advanced Materials* **2009**, *21*, 3181.

[21] S. Jeong, E. C. Garnett, S. Wang, Z. G. Yu, S. H. Fan, M. L. Brongersma, M. D. McGehee, Y. Cui, Hybrid Silicon Nanocone-Polymer Solar Cells *Nano Letters* **2012**, *12*, 2971.

[22] B. V. Andersson, U. Wuerfel, O. Inganas, Full day modelling of V-shaped organic solar cell *Solar Energy* **2011**, *85*, 1257.

[23] T. Kirchartz, T. Agostinelli, M. Campoy-Quiles, W. Gong, J. Nelson, Understanding the Thickness-Dependent Performance of Organic Bulk Heterojunction Solar Cells: The Influence of Mobility, Lifetime, and Space Charge *Journal of Physical Chemistry Letters* **2012**, *3*, 3470.

[24] E. Randone, G. Martini, M. Fathi, S. Donati, SPAD-Array Photoresponse is Increased by a Factor 35 by use of a Microlens Array Concentrator *2009 Ieee Leos Annual Meeting Conference Proceedings, Vols 1and 2* **2009**, 324.

[25] H. J. Nam, S. C. Jeong, D. Y. Jung, Y. K. Kim, K. M. Han, J. Yi, Fabrication of Textured Silicon Solar Cell using Microlens as Anti-Reflection Layer *Commad: 2008 Conference on Optoelectronic and Microelectronic Materials & Devices* **2008**, 246.

[26] M. Manevich, N. P. Eisenberg, Development of transparent microlens in negative photoresist for solar application *9th Meeting on Optical Engineering in Israel* **1995**, *2426*, 242.

[27] Y. Q. Chen, M. Elshobaki, Z. Ye, J. M. Park, M. A. Noack, K. M. Ho, S. Chaudhary, Microlens array induced light absorption enhancement in polymer solar cells *Physical Chemistry Chemical Physics* **2013**, *15*, 4297.

[28] J. D. Myers, W. R. Cao, V. Cassidy, S. H. Eom, R. J. Zhou, L. Q. Yang, W. You, J. G. Xue, A universal optical approach to enhancing efficiency of organic-based photovoltaic devices *Energy & Environmental Science* **2012**, *5*, 6900.

[29] D. McGloin, K. Dholakia, Bessel beams: diffraction in a new light *Contemporary Physics* **2005**, *46*, 15.
[30] T. Cizmar, V. Garcez-Chavez, K. Dholakia, P. Zemanek, Optical trapping in counter-propagating Bessel beams *Optical Trapping and Optical Micromanipulation* **2004**, *5514*, 643.
[31] T. Grosjean, D. Courjon, D. Van Labeke, Bessel beams as virtual tips for near-field optics *Journal of Microscopy-Oxford* **2003**, *210*, 319.
[32] R. Arimoto, C. Saloma, T. Tanaka, S. Kawata, Imaging Properties of Axicon in a Scanning Optical-System *Applied Optics* **1992**, *31*, 6653.
[33] J. Durnin, J. J. Miceli, J. H. Eberly, Comparison of Bessel and Gaussian Beams *Optics Letters* **1988**, *13*, 79.
[34] J. H. McLeod, The Axicon: A New Type of Optical Element *J. Opt. Soc. Am.* **1954**, *44*, 592.
[35] R. Grunwald, S. Woggon, R. Ehlert, W. Reinecke, Thin-film microlens arrays with non-spherical elements *Pure and Applied Optics* **1997**, *6*, 663.
[36] R. Grunwald, H. Mischke, W. Rehak, Microlens formation by thin-film deposition with mesh-shaped masks *Applied Optics* **1999**, *38*, 4117.
[37] R. Grunwald, U. Neumann, V. Kebbel, H. J. Kuhn, K. Mann, U. Leinhos, H. Mischke, D. Wulff-Molder, Vacuum-ultraviolet beam array generation by flat micro-optical structures *Optics Letters* **2004**, *29*, 977.
[38] W. C. Cheong, B. P. S. Ahluwalia, X. C. Yuan, L. S. Zhang, H. Wang, H. B. Niu, X. Peng, Fabrication of efficient microaxicon by direct electron-beam lithography for long nondiffracting distance of Bessel beams for optical manipulation *Applied Physics Letters* **2005**, *87*.
[39] A. Burvall, K. Kolacz, Z. Jaroszewicz, A. T. Friberg, Simple lens axicon *Applied Optics* **2004**, *43*, 4838.
[40] T. P. Russell, Z. Q. Lin, E. Schaffer, U. Steiner, Aspects of electrohydrodynamic instabilities at polymer interfaces *Fibers and Polymers* **2003**, *4*, 1.
[41] T. P. Russell, Z. Q. Lin, T. Kerle, K. A. Leach, Y. Lin, E. Shaeffer, U. Steiner, Directing self-assembly of polymers with electric fields. *Abstracts of Papers of the American Chemical Society* **2002**, *224*, U366.
[42] Z. Q. Lin, T. Kerle, T. P. Russell, E. Schaffer, U. Steiner, Electric field induced dewetting at polymer/polymer interfaces *Macromolecules* **2002**, *35*, 6255.
[43] E. Schaffer, T. Thurn-Albrecht, T. P. Russell, U. Steiner, Electrohydrodynamic instabilities in polymer films *Europhysics Letters* **2001**, *53*, 518.
[44] N. Arun, A. Sharma, P. S. G. Pattader, I. Banerjee, H. M. Dixit, K. S. Narayan, Electric-Field-Induced Patterns in Soft Viscoelastic Films: From Long Waves of Viscous Liquids to Short Waves of Elastic Solids *Physical Review Letters* **2009**, *102*.
[45] Z. Q. Lin, T. Kerle, T. P. Russell, E. Schaffer, U. Steiner, Structure formation at the interface of liquid liquid bilayer in electric field *Macromolecules* **2002**, *35*, 3971.
[46] K. A. Leach, Z. Q. Lin, T. P. Russell, Early stages in the growth of electric field-induced surface fluctuations *Macromolecules* **2005**, *38*, 4868.

[47] M. D. Morariu, N. E. Voicu, E. Schaffer, Z. Q. Lin, T. P. Russell, U. Steiner, Hierarchical structure formation and pattern replication induced by an electric field *Nature Materials* **2003**, *2*, 48.

[48] Z. Q. Lin, T. Kerle, S. M. Baker, D. A. Hoagland, E. Schaffer, U. Steiner, T. P. Russell, Electric field induced instabilities at liquid/liquid interfaces *Journal of Chemical Physics* **2001**, *114*, 2377.

[49] R. Grunwald, U. Griebner, F. Tschirschwitz, E. T. J. Nibbering, T. Elsaesser, V. Kebbel, H. J. Hartmann, W. Juptner, Generation of femtosecond Bessel beams with microaxicon arrays *Optics Letters* **2000**, *25*, 981.

[50] A. J. Das, K. S. Narayan, Observation of Bessel beams from electric-field-induced patterns on polymer surfaces *Optics Letters* **2009**, *34*, 3391.

[51] L. Oddershede, S. R. Nagel, Singularity during the onset of an electrohydrodynamic spout *Physical Review Letters* **2000**, *85*, 1234.

[52] O. Brzobohaty, T. Cizmar, P. Zemanek, High quality quasi-Bessel beam generated by round-tip axicon *Optics Express* **2008**, *16*, 12688.

[53] O. Brzobohaty, T. Cizmar, P. Zemanek, Quasi-Bessel beam generated by oblate-tip axicon *16th Polish-Slovak-Czech Optical Conference on Wave and Quantum Aspects of Contemporary Optics* **2008**, *7141*.

[54] H. Mashaal, A. Goldstein, D. Feuermann, J. M. Gordon, First direct measurement of the spatial coherence of sunlight *Optics Letters* 2012, 37, 3516.

[55] Y. Chen, M. Elshobaki, Z. Ye, J.-M. Park, M. A. Noack, K.-M. Ho, S. Chaudhary, Microlens array induced light absorption enhancement in polymer solar cells Physical Chemistry Chemical Physics 2013, 15, 4297.

Chapter 5
Study of Degradation in Organic Solar Cells

"The sun is new each day." –Heraclitus

5.1 Introduction

OSCs have exhibited compelling efficiencies which may make them feasible for realistic applications that are market compatible [1]. This implies that the excellent semiconducting organic materials have been synthesized leading to high efficiencies. But OSCs comprises of several components like transparent electrodes, electron or hole transport layers and buffer layers. It turns out that some of these layers are unstable in the presence of oxygen and moisture, thereby reducing the lifetime of these devices. Hence it is very essential to address the stability issue if OSC will have to function effectively over extended periods of time under ambient conditions. A typical OSC comprises of transparent electrodes like ITO on a substrate like glass or plastic, hole extraction layers like PEDOT:PSS or certain metal oxides, the polymer blend and a metal electrode; (i) Low work-function metals like calcium and aluminium which have been routinely used as the electron collecting electrodes are very reactive leading to unwanted reactions at the metal-polymer interface [2-4]. This limits the lifetime of the devices from several hours to a few days. (ii) Acidic nature of PEDOT:PSS corrodes the ITO surface leading to lower conductivity and charge extraction [5-6]. (iii) Photo-stability of the polymer blend has been studied under various conditions like UV exposure and continuous irradiation. Detrimental effects of such exposures have been reported due to photo-oxidation of the materials [7-8]. Towards this end, several improvements in lifetime have been suggested; encapsulation [9-12], inverted geometries [13-18], oxide coatings [19-20], purification of polymers [21-22] amongst several others.

A few fundamental questions can be posed in this regard. Is the degradation primarily due to the bulk or interface? Is the degradation predominantly physical or chemical in nature? If there are significant contributions from both bulk and interfacial factors, do they occur at different time scales? Systematic studies would then need to be carried out to single out factors that have a larger contribution to degradation at smaller time scales. This chapter attempts to address the above questions that would assist in designing better devices with larger lifetimes. The possibility of low-melting alloys electrodes is explored as encapsulants. Studies reveal that better contacting of metal alloys with the polymer blend in addition to thicker electrodes improves device lifetime dramatically. Device stability is studied by carrying out current-voltage (I-V), Capacitance-Voltage (C-V) and photocurrent noise measurements as a function of time. The effect of blend morphology on the device lifetime is also studied by utilizing processing additives.

5.2 Stability of alloy organic solar cells without additive

In order to ascertain the most reactive/unstable layer in the solar cell several measurements were carried out. It turns out that the polymer-bulk degradation is a slower process as compared to the interfacial process of cathode-oxidation. Deposition of a fresh alloy electrode on the active BHJ layer in the vicinity of a sufficiently-degraded Al device reveals a high performance. The efficiency is comparable to the magnitude exhibited by a pristine Al device as shown in Figure 5.1. Hence the stability of the polymer-cathode interface is of vital importance for the device performance. Several devices have been stored at ambient conditions and deposition of a fresh electrode almost always yields efficiencies comparable to the pristine device. It is to be noted that all stability measurements have been performed in accordance with the ISOS-L-1 protocol [23] under ambient humidity and room temperature.

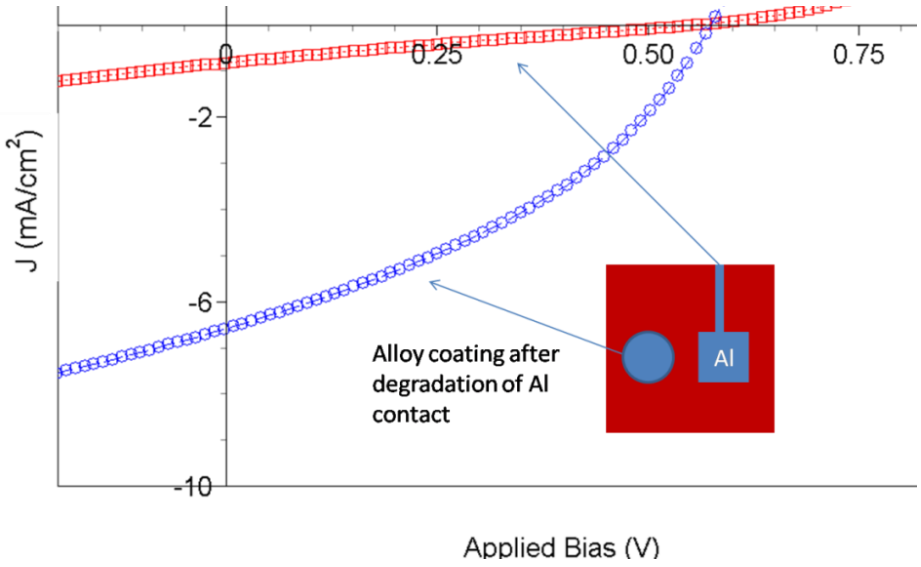

Figure 5.1: *J-V curve indicating the stability of the polymer blend as compared to the polymer blend-metal interface. Depositing fresh electrodes in the vicinity of already degraded devices yields high efficiency.*

Solvent additive have shown to control and improve the morphology of bulk heterojunction solar cells [24]. In order to study the effect of the additive on device stability, the first set of devices were fabricated without the solvent additive. Time dependent efficiency of an alloy-OSC was compared with a control device which was coated with 40nm thick Al film using a vacuum evaporation unit. Figure 5.2 shows the comparison of PCPDTBT:PCBM[70] device performance with alloy and Al cathodes spanning three different time scales. As can be seen in Figure 5.2(a), the Al device encapsulated with an epoxy sealed glass cover-slip degrades with time and the efficiency drops by 90% of its original efficiency after about 400 hr storage and illumination at 300 K and 70% humidity [23]. In contrast the efficiency of alloy-OSC drops by 18% from the original efficiency after 500 hr without any additional encapsulation. Figure 5.2(c) shows that the Al-OSC without encapsulation degrades rapidly and retains only 10% of its efficiency after 2 hr. In contrast, the alloy-OSCs exhibit an increase in efficiency with the time in the initial stages as shown in Figure 5.2(b) [25]. An increased V_{oc} leads to increased η, consistent with the fact that oxidation of metal cathode (Indium, Tin) leads

to modification of energy levels at the interface. Formation of an insulating or semi-conducting oxide may promote better charge build up leading to increased V_{oc}.

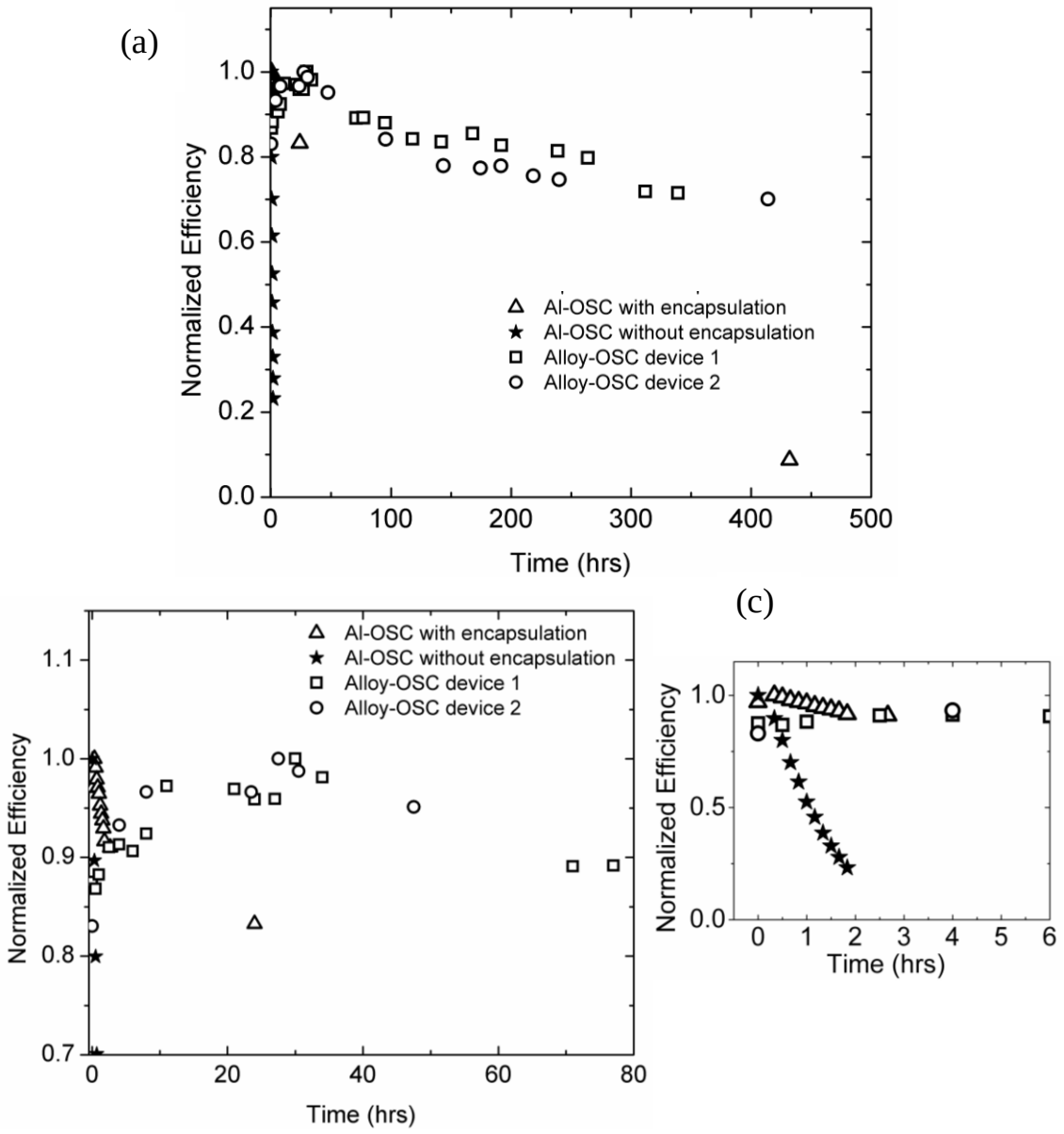

Figure 5.2: *Stability of alloy-OSC without solvent additives over (a) 500 hrs, (b) 80 hrs and (c) 6 hrs. (Reprinted with permission from A. J. Das, K. S. Narayan, Retention of Power Conversion Efficiency - from Small Area to Large Area Polymer Solar Cells. Advanced Materials* ***2013****, Early View. © 2013 John Wiley and Sons)*

There is evidence from X-ray reflectivity studies that a macroscopic rough oxide forms on liquid metal surfaces of Indium on exposure to oxygen [26]. Since the deposition is done at room temperature, the presence of an oxide cannot be neglected. The actual mechanism that leads to this improvement is still a matter of debate though [19-20]. XPS spectra of the exposed alloy were obtained, compared with reports from literature and a resemblance was observed confirming the presence of oxides of In and Sn (Figure 5.3) [27].

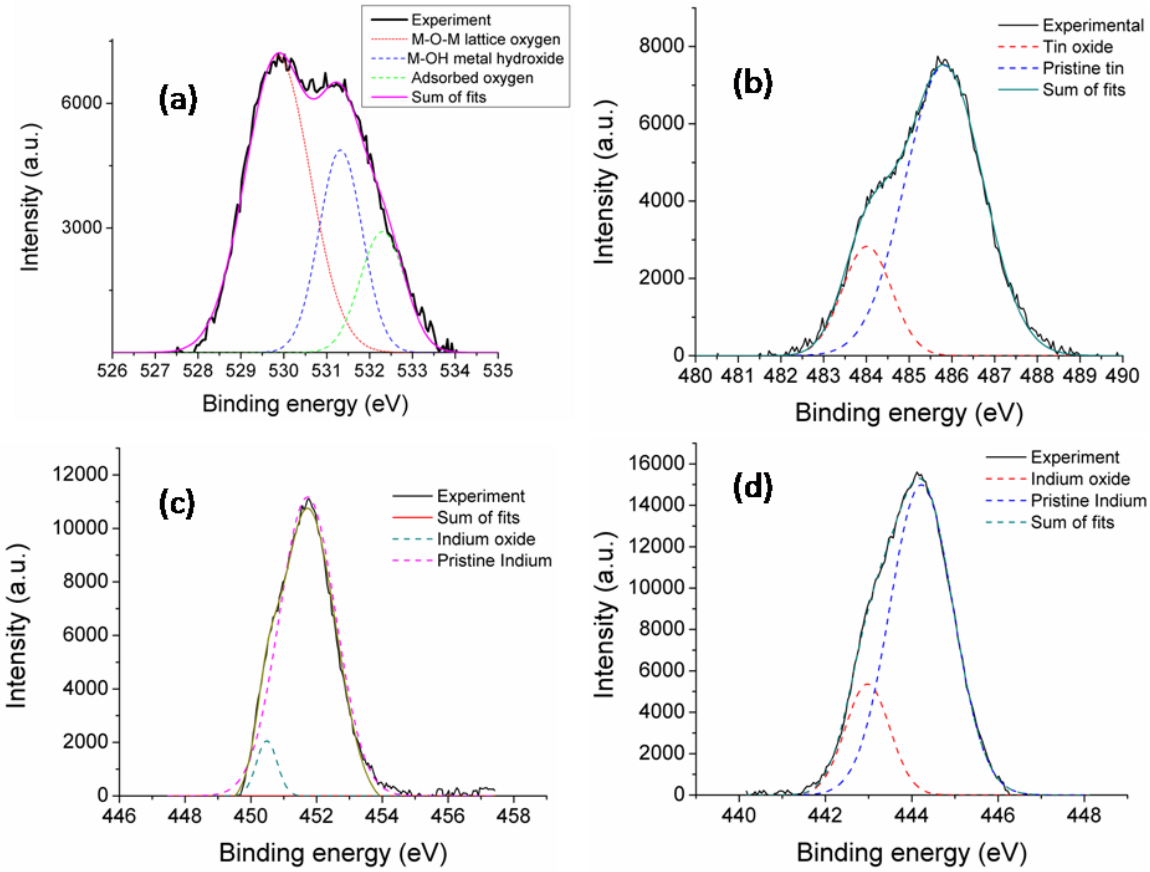

Figure 5.3: *XPS Spectra of an exposed alloy surface indicating the presence of various oxides (a) O1s (b) Sn 3d5/2, (c) In 3d3/2 and (d) In 3d5/2. (Reprinted with permission from A. J. Das, K. S. Narayan, Retention of Power Conversion Efficiency - from Small Area to Large Area Polymer Solar Cells. Advanced Materials* ***2013****, Early View. © 2013 John Wiley and Sons)*

O1s spectra in Figure 5.3(a) can be de-convoluted into 3 Gaussians with peaks centered at 529.9 eV due to M–O–M lattice oxygen, at 531.3 eV corresponding to M–OH

metal hydroxide oxygen, and at 532.3 eV corresponding to adsorbed oxygen. Similarly, in the case of Sn 3d5/2, the presence of two Gaussians in the envelope is an indication of oxide formation. The peak at 484.6 eV is the native Sn and the peak at 485.82 eV corresponds to an oxide of Sn (Figure 5.3(b)). In the case of Indium, the 3d is split into a doublet 3d5/2 and 3d3/2. The native Indium in 3d5/2 level occurs at 443.34 eV whereas the corresponding In_2O_3 oxide occurs at 444.4 as shown in Figure 5.3(c). In the case of 3d3/2, the native Indium occurs at 450 eV and the oxide occurs at 451.95 eV. The positions of the peaks have been verified across several reports in order to confirm the presence of oxides.

Hence alloy-OSC showed an extended lifetime without any encapsulation as compared to Al solar cells with sufficient encapsulation. The role of additive is needs to be ascertained in stability of the devices as additives can improve the performance of solar cells. The next section deals with the stability of solar cells with solvent additives.

5.3 Stability of alloy organic solar cells with additive

Devices processed with additives exhibit high initial efficiencies due to better control of morphology [24, 28-29]. Hence recent developments across various research groups have shown that additives enhance device performance for a variety of donor acceptor combinations. Stability of alloy-OSC devices with additive processing was monitored as shown in Figure 5.4. Up to 9 devices were tested and there was a steep fall in the efficiency in the 24-48 hr period due to a drop in the fill factor followed by a saturation-like behavior at longer times as shown in Figure 5.4. The alloy coating was several mm thick and any moisture or oxygen diffusion through the alloy could be ruled out.

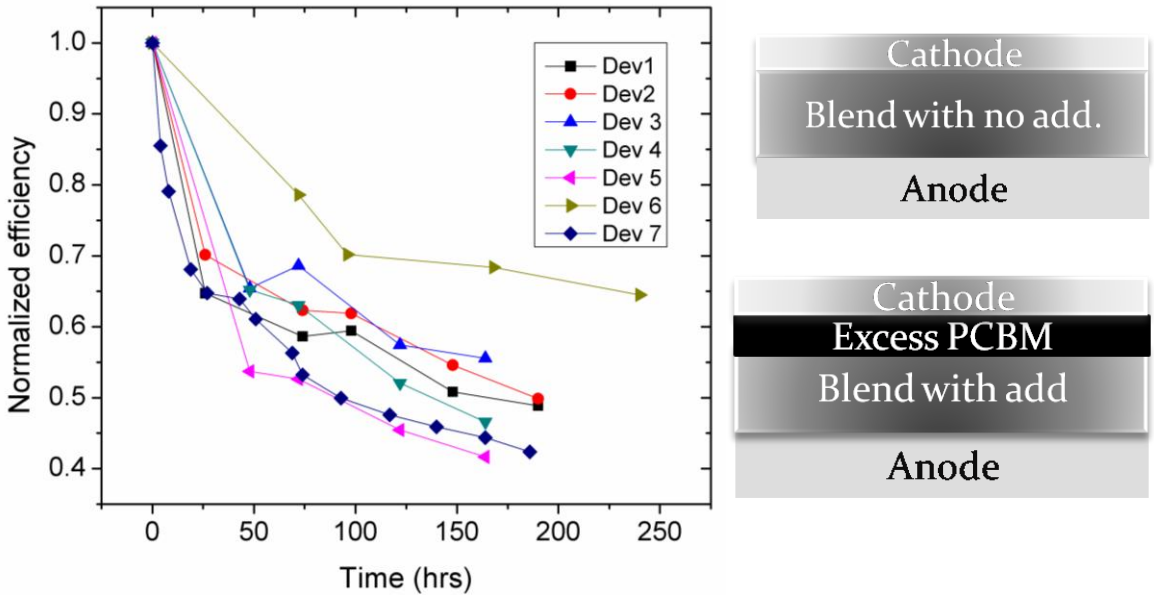

Figure 5.4: *Stability of several alloy-OSC devices with processing additives. Initial degradation is very rapid followed by a saturation-like behaviour after about 100 hrs. The panel on the right depicts vertical section of a device without and with processing additives. Higher concentration of the reactive fullerene is a cause for the initial rapid degradation in the case of additive processed devices.*

5.3.1 Possible causes of low device stability processed with additives

The additive is generally a high boiling point solvent like DIO that selectively dissolves the acceptor PCBM. During the removal of the additive in a vacuum chamber, PCBM is brought to the surface of the film (Figure 5.4). This process improves electron collection because PCBM, the electron acceptor is in contact with the electron collecting electrode. In the case of alloy-OSC the deposition of alloy is done at ambient conditions.

As a result, the more reactive PCBM is exposed to oxygen and moisture. When the PCBM comes in contact with the alloy in air, there is a possibility of a reaction that hinders electron collection. Further, it has been observed that device degradation begins at the edges and permeates inward [30]. Since, monitoring I-V data alone is not conclusive to prove the above hypothesis; C-V measurements were carried out as a function of time. C-V measurements are sensitive to interfacial changes and can provide

valuable information about injection at electrodes. By comparing the efficiency obtained by I-V with that of C-V it could be possible to extract additional information that could explain the drop in the efficiency.

5.4 C-V Measurements- negative capacitance as a tool to study interfacial degradation

Capacitance measurements are generally very sensitive to the device geometry as $C = \varepsilon A/d$, ε being the permittivity, A is the area and d the spacing between two electrodes. Under the assumption of a uniform field across the device, capacitance measurements are often a useful tool to determine interfacial changes. In this regard, the phenomenon of negative capacitance (NC) has been widely studied in organic and inorganic semiconductor devices like diodes, transistors and solar cells [31-41]. The occurrence of negative capacitance was explained by Shulman et. al. using a generalized approach [42]. They showed that NC is observed when a DC voltage is superimposed with AC signal on a device which undergoes relaxation processes with nonlinear J–V relationship. The combined effect of nonlinearity and DC bias results in an additional ac current. This current can, under certain conditions, lag behind the voltage giving rise to an inductive or NC-like effect. It is to be noted that a negative capacitance does not imply a negative dielectric constant but a pseudo-inductive response of the device at a particular frequency and voltage. Ershov et al. attributed the origin of NC phenomenon to sources such as charge carrier recombination, traps, impurities, interface effects, and charge generation mechanisms [43].

NC is commonly observed in organic light emitting diodes and is indicative of the e–h pair recombination under bipolar injection regime [32]. NC has also been reported in organic solar cells like P3HT:PCBM [44] where the effect of illumination could be studied [45]. The model proposed by Bisquert et al. describes NC in organic devices based on the cascade like hopping of electrons from metal to the interfacial states to bulk states of the semiconductor in sequential manner under non-equilibrium conditions [46-48]. The device is driven to a non-equilibrium condition when the rate of electrons

populating interfacial states different from the rate depopulation of the bulk states. Due to such a mismatch, the observation of NC in organic devices occurs because of injection process. This fact is utilized to study the stability of OSC and probe the role of degradation of electrode-polymer interface.

5.4.1 Typical NC behavior in OSC

A typical C-V behavior of an organic solar cell with PBDTTT-C-T:PCBM blend and alloy electrodes is shown in Figure 5.5(a). Depending on the applied voltage, the capacitance behavior can be classified into three distinct regions as shown in Figure 5.5 (a). About 16 devices were tested with repeatable observations.

5.4.1.1 Regime I: Low voltage

At low applied voltages $0 < V < V_{oc}$ or V_{bi}, the capacitance of the device does not vary with the voltage (region I in Figure 5.5(a)). Depending on the dark currents in the device, the capacitance is in the range of 1.5-2 nF. As the device degrades the magnitude of the dark current increases leading to lowering of the capacitance to under 1 nF. Though capacitance in this regime varies as the device ages, it is not very sensitive to small changes in the device performance.

5.4.1.2 Regime II: At open circuit

For the condition $V \sim V_{oc}$, the capacitance is maximum due to the absence of any current in the device. The capacitance increases from the 1.5 nF to over 4 nF as shown in region II in Figure 5.5(a). Capacitance at V_{oc} is again not sensitive to small changes in the device performance. Since the V_{oc} is generally invariant in the time scales of our measurements, this capacitance is not affected by degradation of the device.

5.4.1.3 Regime III: Beyond the open circuit

For the condition $V > V_{oc}$, the capacitance begins to fall in magnitude until it reaches a zero value. If the voltage is further increased, the capacitance takes up negative values indicating and inductive type behavior (region III in Figure 5.5(b)). This behavior can be explained using the band diagram shown in Figure 5.5(b). Electrons are injected into interfacial states present at the alloy-semiconductor interface. This is followed by hopping transport to the conduction bands of the semiconductor (bulk). Since the

measurement is done with an ac signal ~ 10 kHz frequency, the injection into the interfacial states does not occur when the polarity is reversed. The charges in the conduction band of the semiconductor must now relax or depopulate the levels so that they are available for transport in the next cycle of the injection. If the lifetimes of these levels are higher than the injection rate, then further injection is limited. This leads to a drop in the capacitance of the device as it is already charged.

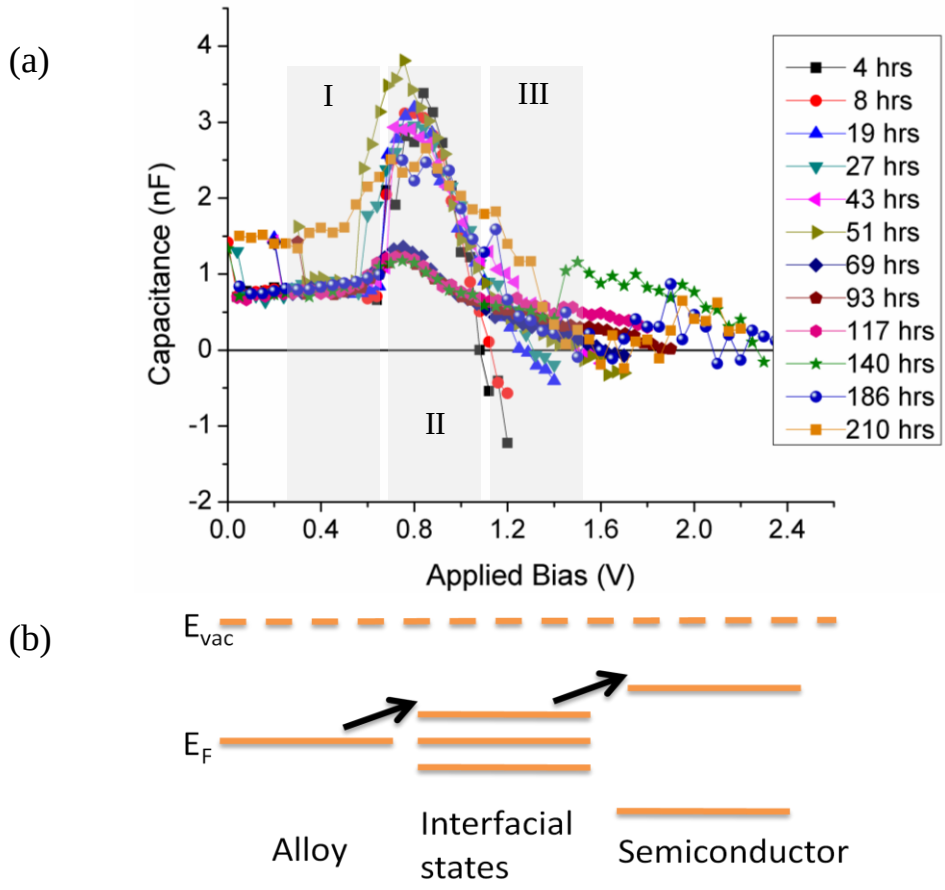

Figure 5.5: *(a) Typical C-V behavior of alloy-OSC as a function of time. Region II very sensitive to degradation as compared to region I or II. (b) Band diagram depicting the sequential injection of electrons from the alloy to the bulk of the semiconductor.*

At a certain ac frequency and voltage, the capacitance of the device is minimal (~0). Instead an ac current that lags the voltage is generated giving rise to negative capacitance or a pseudo-inductive effect. As can be seen in Figure 5.5(a) region III, the onset of NC is

very sensitive to device degradation and hence can be used as a tool to study device stability.

5.4.2 Disappearance of negative capacitance with device degradation

As discussed earlier the onset of NC is sensitive to the injection properties of the electrode which in turn is related to the device degradation. In other words, the onset of NC is directly related to the efficiency of charge injection at the both the hole and electron injecting electrodes. Since, the ITO/PEDOT:PSS electrode is not in contact with oxygen or moisture, hole injection is not significantly altered at this electrode. Considering that the bulk of polymer blend is stable in the time frame of measurements, the primary cause of degradation can be attributed to the alloy-polymer blend interface.

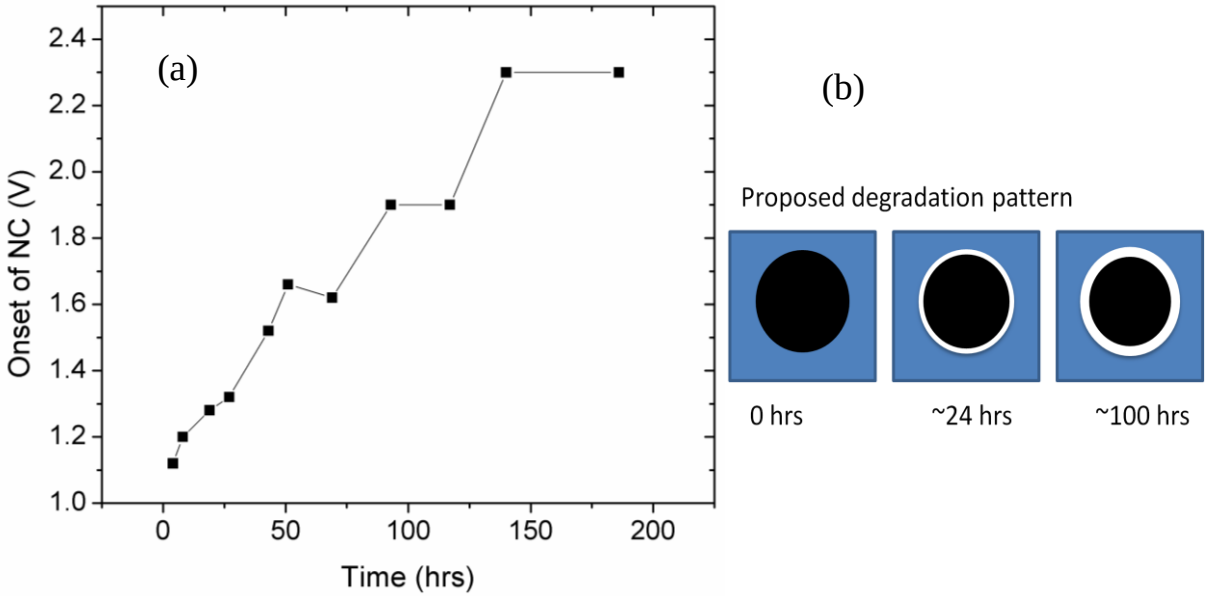

Figure 5.6: *(a) Onset of NC as a function of time. (b) Proposed degradation pattern of the alloy-polymer interface. Degradation sets in from the exposed edges and permeates inward. After about 100 hrs the edge itself acts like a barrier preventing further reaction.*

Figure 5.6(a) shows that a monotonic increase is observed in the onset of NC as the device degradation occurs. This is followed by a saturation and disappearance of the NC effect as shown in Figure 5.5(a). The disappearance of NC occurs at 100-150 hrs after the device has been fabricated. It turns out that this time frame is similar to one at which the slope change occurs in the efficiency-time plot in Figure 5.4. A possible explanation for such an observation

is the edge degradation of the alloy-polymer interface as shown in Figure 5.6(b).

As the device degrades, a reaction occurs at the edge and permeates inwards from the electrode edge. This results in the formation of a barrier for injection at the alloy-polymer blend interface as shown in Figure 5.7. Hence a larger voltage would be necessary to injection charges in to the interfacial states leading to the shifting of onset of NC towards larger voltages (Figure 5.6(a)). After sufficient degradation, the barrier becomes too large for injection into the interfacial states leading to the disappearance of the NC effect. At the same time the reaction at the alloy-polymer blend interface ceases leading to a saturation-like effect as shown in Figure 5.4.

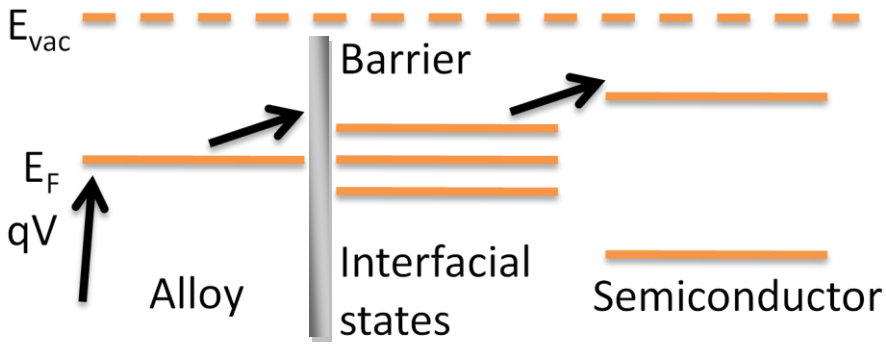

Figure 5.7: *Band diagram depicting the formation of a barrier as a result of device degradation. Formation of a barrier increases the potential required to inject electrons into the interfacial states resulting in a higher onset voltage for NC.*

5.4.3 Implications in organic solar cells

From the above measurements it is very evident that edge-sealing must be carried out in OSC due to the reaction of alloy with the PCBM that is present on the surface. Most n-type organic materials are unstable due to the LUMO level or the conduction level being closer to the vacuum. Since additives are irreplaceable in OSC as they control the morphology and the evolution of PCBM being desirable for charge extraction, it is vital that the edges of the device be sealed in order to preserve the efficiency over extended periods of time.

5. 5Noise measurements in organic solar cells

Noise in electrical or electronic systems, is a random disturbance as it interferes with or masks the signal. However, understanding the sources of noise, whether intrinsic or extrinsic, can provide useful information about the system. In the past, noise has been utilized to study hot carriers in semiconductors [49-52], generation-recombination [53-56] and traps [57-59]. Out of the various types of noise present in electronic systems, the 1/f type noise has been a very useful tool in studying various processes [55, 60-66]. Noise in organic solar cells has been utilized to study the degradation and carrier dynamics [62, 67]. By systematically studying of noise in these systems, it was possible to observe noise signatures in the Ohmic, trap-filling transition and space charge limited regimes of the I-V curve. If extrinsic sources of noise are eliminated in solar cells, low frequency intrinsic noise turns out to be an important indicator of device stability [62].

In this chapter the variation of noise in OSC is studied as a function of time. Fluctuations of the noise parameters in different frequency regimes are analyzed in order to correlate the efficiency drop and results from C-V measurements to arrive at a comprehensive picture of the device degradation in alloy-OSC.

5.5.1 Low-frequency: 1/f noise feature

Noise from PBDTTT-C-T:PCBM solar cells was captured and analyzed as mentioned in Chapter 2.7. Subsequent to amplification by a factor of 10^7-10^9, a noise patterned was observed in the oscilloscope as shown in Figure 5.8(a). Several experiments were carried out to rule out or filter other noise sources. Enclosing the device in a Faraday cage illuminated by DC powered bulb eliminated any line noise. The device area was kept minimal (~1 mm^2) to minimize thermal noise due to large currents. The device was also replaced with resistors of similar resistance and no distinct features were observed in such cases. Hence, it could be ascertained that the source of noise was due to photogenerated charge carriers.

The noise spectrum of OSC under illumination was observed to have two distinct features; i) a low-frequency 1/f $^{\delta}$ like feature and ii) a high-frequency log-normal like feature. 1/f feature is commonly observed in many electronic systems and can be empirically described by the Hooge's formula [68-73];

$$S(f) = \frac{AI_0^2}{f^{\delta}} \quad \text{.....(5.1)}$$

where *S(f)* is the power spectral density, *A* is the noise magnitude coefficient, *I* is the current, *f* is the frequency, δ is the Hooge's parameter.

The low-frequency feature appears in the range of 1-10 kHz. The noise spectral density could be fit to a straight line in the log-log scale as shown in Figure 5.8(b). The exponent δ turns out to be about2 for PBDTTT-C-T:PCBM solar cells (for about 16 tested devices).

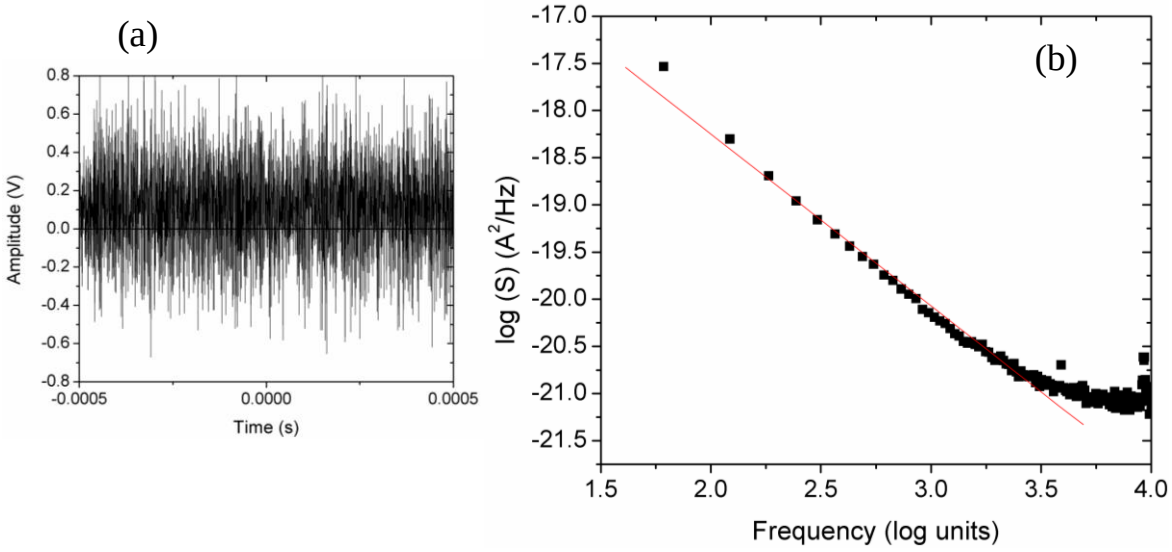

Figure 5.8: (a) *A time varying photocurrent noise signal. (b) 1/f noise spectrum of organic solar cell with PBDTTT-C-T:PCBM blend.*

5.5.2 High-frequency: lognormal-like noise feature

The high-frequency feature appears beyond 100 kHz, centered about 250 kHz as shown in Figure 5.9(a,b). This feature unlike in severely degraded devices [62], did not

show appreciable change in the position or width with device degradation. This feature was attributed earlier to the formation of traps in the bulk of the polymer blend.

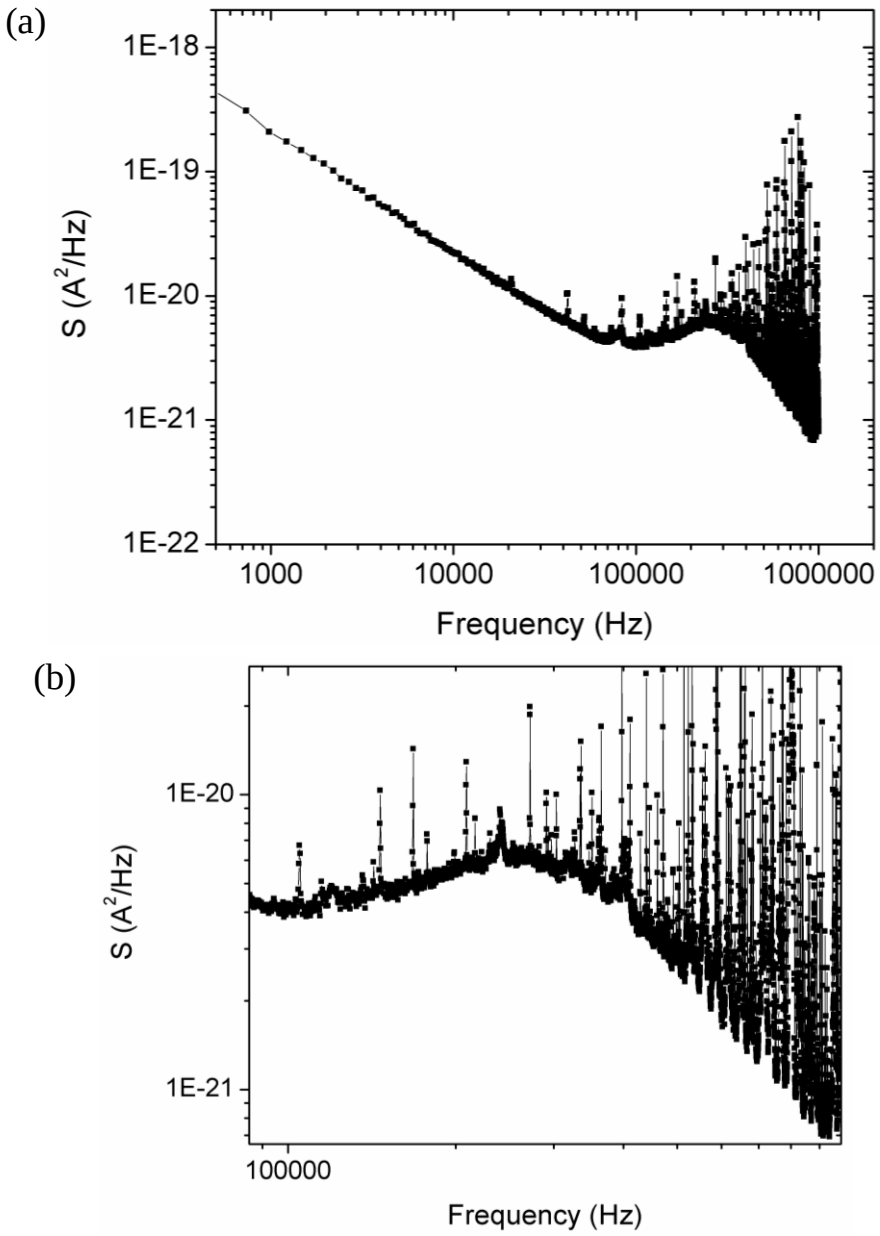

Figure 5.9: *(a) High-frequency noise feature in OSC. (b) A zoomed in plot of (a).*

A red shift of this feature with time indicated the formation of deep traps as reported by Bag et. al. [62]. In the time frame of the current measurements, the formation

of traps is limited by the superior encapsulation by the alloy electrode. Hence the absence of any variation of the high-frequency feature is an indication of good encapsulation.

5.5.3 1/f noise as a tool to study device degradation

Unlike the high-frequency feature, the 1/f feature was sensitive to device degradation and the slope of the curve was observed to oscillate with a time period of about40 hrs, with $1.7 < \delta < 2.8$ and followed by saturation to a value of 1.9 after about 100-120 hrs as shown in Figure 5.10 (a,b). The saturation like behavior in the efficiency hence is reflected in the 1/f slope as well as C-V measurements. It can be concluded that the 1/f noise is more sensitive to changes in the injection at electrodes rather than the bulk in efficient devices. It is possible that noise related to generation-recombination or traps is masked due to the noise generated at the interfaces. Thermal expansion of the alloys can be one of the factors contributing to an oscillatory behaviour. Most alloys have a shrinkage of 0.02%-0.1% after casting and this process may take several days to stabilize (please see APPENDIX D for more details). Further studies are necessary to study the degradation properties of efficient solar cells and correlate the observations made from I-V and C-V measurements.

Comparison with noise from Al electrodes

Earlier reports of noise studies on Al electrodes have indicated that the Hooge's parameter increased from 1.2 to 1.9 in the case of PCPDTBT:PCBM devices [62]. Al electrodes degrade very rapidly under ambient conditions and hence the variation of the Hooge's parameter is very different. If noise measurements are carried out after a substantial amount of degradation, then the electrodes itself have a lower contribution to the noise. Hence, noise due to the formation of deep traps could be observed in the case of PCPDTBT:PCBM devices [62]. However, in the case of alloy electrodes the degradation is much slower as compared to that of Al electrodes. Hence, the device does not attain a substantially degraded state even after several 1000 hrs. The dominant contribution to the fluctuations in the Hooge's parameter comes from the interface of the alloy and polymer and not the bulk of the polymer. The role of electrode seems to be a critical factor in determining the nature of fluctuations in these devices.

Summary

Stability of alloy-OSC was studied in detail by varying processing conditions like the usage of additives. OSC without additives are less efficient but stable over long time periods (>500 hrs). OSC with the additive have better morphology leading to higher

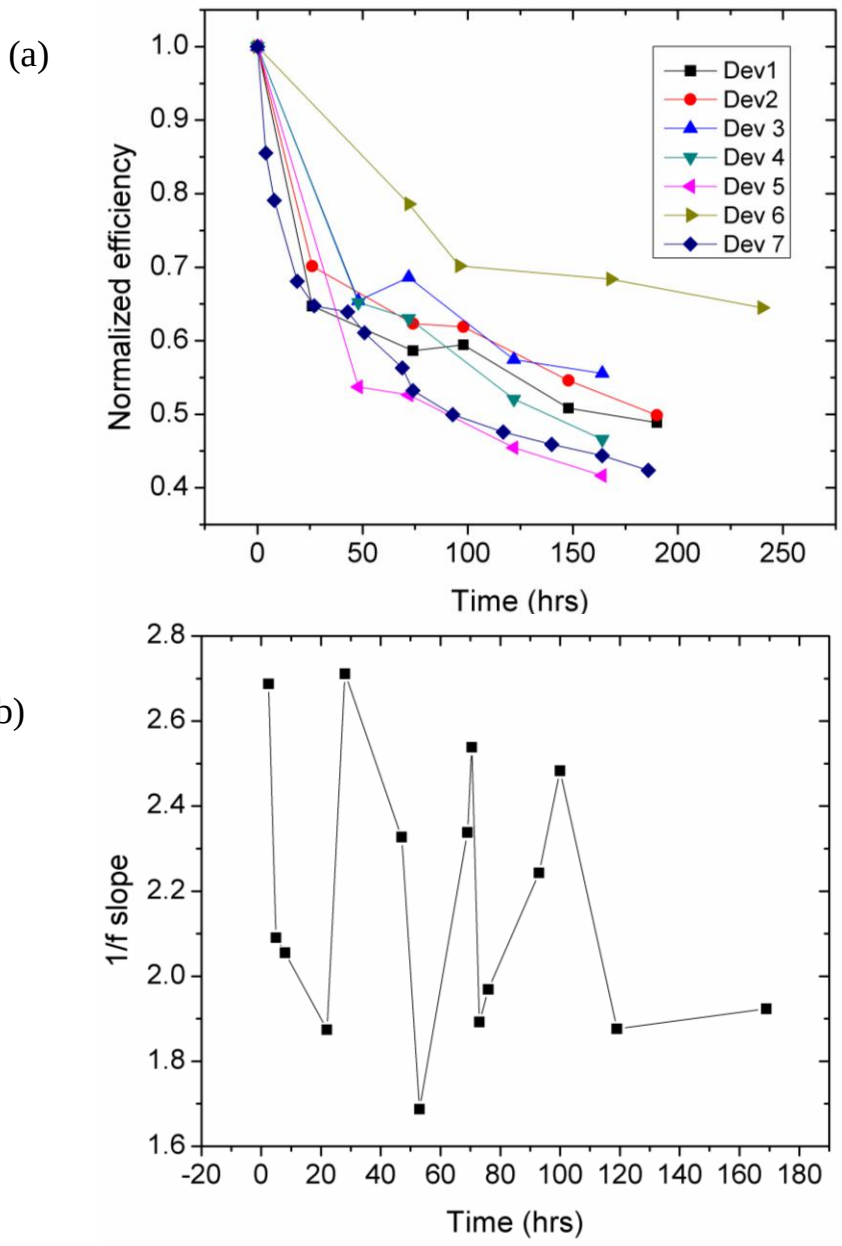

Figure 5.10: *(a) Variation of efficiency of alloy-OSCs with time. (b) Variation of 1/f slope as a function of time.*

initial efficiency. However, they lose 20-30% of the initial efficiency rapidly within 50-100 hrs of fabrication. This was attributed to the PCBM migration to the surface and subsequent edge reactions that lowered the efficiency. C-V measurements as a function of time showed that NC is a measure of device efficiency. The onset voltage at which NC occurred increased monotonically and reached saturation around 100 hrs. In this time frame the NC disappeared and no further change was observed in the C-V behaviour. This reason for such an observation could be attributed to the reduction of injection of electrons at the alloy-polymer blend interface due to reaction of the edges with the oxygen or moisture. Noise measurements were also carried out on OSC at the short circuit condition. A 1/f like noise feature which was sensitive to changes in the injection was observed. Noise related to the degradation of the semiconductor itself could not be extracted due to the fluctuations present at the alloy-OSC interface. Nevertheless, noise studies proved to be an important tool along with C-V measurements to study device degradation.

References

[1] Z. C. He, C. M. Zhong, S. J. Su, M. Xu, H. B. Wu, Y. Cao, Enhanced power-conversion efficiency in polymer solar cells using an inverted device structure. *Nature Photonics* **2012**, *6*, 591.

[2] S. A. Gevorgyan, M. Jorgensen, F. C. Krebs, A setup for studying stability and degradation of polymer solar cells. *Solar Energy Materials and Solar Cells* **2008**, *92*, 736.

[3] M. Jorgensen, K. Norrman, F. C. Krebs, Stability/degradation of polymer solar cells. *Solar Energy Materials and Solar Cells* **2008**, *92*, 686.

[4] F. C. Krebs, Degradation and stability of polymer and organic solar cells. *Solar Energy Materials and Solar Cells* **2008**, *92*, 685.

[5] M. P. de Jong, L. J. van IJzendoorn, M. J. A. de Voigt, Stability of the interface between indium-tin-oxide and poly(3,4-ethylenedioxythiophene)/poly(styrenesulfonate) in polymer light-emitting diodes. *Applied Physics Letters* **2000**, *77*, 2255.

[6] T. Yamanari, T. Taima, J. Sakai, J. Tsukamoto, Y. Yoshida, Effect of Buffer Layers on Stability of Polymer-Based Organic Solar Cells. *Japanese Journal of Applied Physics* **2010**, *49*.

[7] C. H. Peters, I. T. Sachs-Quintana, W. R. Mateker, T. Heumueller, J. Rivnay, R. Noriega, Z. M. Beiley, E. T. Hoke, A. Salleo, M. D. McGehee, The Mechanism of

Burn-in Loss in a High Efficiency Polymer Solar Cell. *Advanced Materials* **2012**, *24*, 663.

[8] E. Voroshazi, B. Verreet, T. Aernouts, P. Heremans, Long-term operational lifetime and degradation analysis of P3HT: PCBM photovoltaic cells. *Solar Energy Materials and Solar Cells* **2011**, *95*, 1303.

[9] R. Schroeder, G. Feistritzer, W. Graupner, G. Meinhardt, D. Berman, P. Preishuber-Pfluegl, F. Stelzer, D. Faiman, G. Leising, Organic solar cells - Stabilization by plastic encapsulation. *Antec '99: Plastics Bridging the Millennia, Conference Proceedings, Vols I-Iii* **1999**, 3844.

[10] G. Dennler, C. Lungenschmied, H. Neugebauer, N. S. Sariciftci, M. Latreche, G. Czeremuszkin, M. R. Wertheimer, A new encapsulation solution for flexible organic solar cells. *Thin Solid Films* **2006**, *511*, 349.

[11] C. Lungenschmied, G. Dennler, G. Czeremuszkin, M. Latreche, H. Neugebauer, N. S. Sariciftci, Flexible encapsulation for organic solar cells - art. no. 617912. *Photonics for Solar Energy Systems* **2006**, *6197*, 17912.

[12] Z. X. Wu, L. D. Wang, C. Chang, Y. Qiu, A hybrid encapsulation of organic light-emitting devices. *Journal of Physics D-Applied Physics* **2005**, *38*, 981.

[13] B. Gholamkhass, N. M. Kiasari, P. Servati, An efficient inverted organic solar cell with improved ZnO and gold contact layers. *Organic Electronics* **2012**, *13*, 945.

[14] S. K. Hau, H. L. Yip, N. S. Baek, J. Y. Zou, K. O'Malley, A. K. Y. Jen, Air-stable inverted flexible polymer solar cells using zinc oxide nanoparticles as an electron selective layer. *Applied Physics Letters* **2008**, *92*.

[15] C. H. Hsieh, Y. J. Cheng, P. J. Li, C. H. Chen, M. Dubosc, R. M. Liang, C. S. Hsu, Highly Efficient and Stable Inverted Polymer Solar Cells Integrated with a Cross-Linked Fullerene Material as an Interlayer. *Journal of the American Chemical Society* **2010**, *132*, 4887.

[16] T. Oida, T. Naito, Y. Miyagawa, M. Sasaki, K. Harafuji, Air-Stable Inverted Organic Solar Cells with Pentacene Anode Buffer Layer. *Japanese Journal of Applied Physics* **2011**, *50*.

[17] Y. Sahin, S. Alem, R. de Bettignies, J. M. Nunzi, Development of air stable polymer solar cells using an inverted gold on top anode structure. *Thin Solid Films* **2005**, *476*, 340.

[18] H. Schmidt, H. Flugge, T. Winkler, T. Bulow, T. Riedl, W. Kowalsky, Efficient semitransparent inverted organic solar cells with indium tin oxide top electrode. *Applied Physics Letters* **2009**, *94*.

[19] M. D. Wang, F. Y. Xie, W. G. Xie, S. Z. Zheng, N. Ke, J. Chen, N. Zhao, J. B. Xu, Device lifetime improvement of polymer-based bulk heterojunction solar cells by incorporating copper oxide layer at Al cathode. *Applied Physics Letters* **2011**, *98*.

[20] M. D. Wang, Q. Tang, J. An, F. Y. Xie, J. A. Chen, S. Z. Zheng, K. Y. Wong, Q. A. Miao, J. B. Xu, Performance and Stability Improvement of P3HT:PCBM-Based Solar Cells by Thermally Evaporated Chromium Oxide (CrOx) Interfacial Layer. *Acs Applied Materials & Interfaces* **2010**, *2*, 2699.

[21] R. F. Salzman, J. G. Xue, B. P. Rand, A. Alexander, M. E. Thompson, S. R. Forrest, The effects of copper phthalocyanine purity on organic solar cell performance. *Organic Electronics* **2005**, *6*, 242.

[22] S. R. Cowan, W. L. Leong, N. Banerji, G. Dennler, A. J. Heeger, Identifying a Threshold Impurity Level for Organic Solar Cells: Enhanced First-Order Recombination Via Well-Defined PC84BM Traps in Organic Bulk Heterojunction Solar Cells. *Advanced Functional Materials* **2011**, *21*, 3083.

[23] M. O. Reese, S. A. Gevorgyan, M. Jorgensen, E. Bundgaard, S. R. Kurtz, D. S. Ginley, D. C. Olson, M. T. Lloyd, P. Moryillo, E. A. Katz, A. Elschner, O. Haillant, T. R. Currier, V. Shrotriya, M. Hermenau, M. Riede, K. R. Kirov, G. Trimmel, T. Rath, O. Inganas, F. L. Zhang, M. Andersson, K. Tvingstedt, M. Lira-Cantu, D. Laird, C. McGuiness, S. Gowrisanker, M. Pannone, M. Xiao, J. Hauch, R. Steim, D. M. DeLongchamp, R. Rosch, H. Hoppe, N. Espinosa, A. Urbina, G. Yaman-Uzunoglu, J. B. Bonekamp, A. J. J. M. van Breemen, C. Girotto, E. Voroshazi, F. C. Krebs, Consensus stability testing protocols for organic photovoltaic materials and devices. *Solar Energy Materials and Solar Cells* **2011**, *95*, 1253.

[24] J. K. Lee, W. L. Ma, C. J. Brabec, J. Yuen, J. S. Moon, J. Y. Kim, K. Lee, G. C. Bazan, A. J. Heeger, Processing additives for improved efficiency from bulk heterojunction solar cells. *Journal of the American Chemical Society* **2008**, *130*, 3619.

[25] A. J. Das, K. S. Narayan, Retention of Power Conversion Efficiency - from Small Area to Large Area Polymer Solar Cells. *Advanced Materials* **2013**, n/a.

[26] H. Tostmann, E. DiMasi, P. S. Pershan, B. M. Ocko, O. G. Shpyrko, M. Deutsch, Surface structure of liquid metals and the effect of capillary waves: X-ray studies on liquid indium. *Physical Review B* **1999**, *59*, 783.

[27] M. G. Kim, M. G. Kanatzidis, A. Facchetti, T. J. Marks, Low-temperature fabrication of high-performance metal oxide thin-film electronics via combustion processing. *Nature Materials* **2011**, *10*, 382.

[28] S. J. Lou, J. M. Szarko, T. Xu, L. P. Yu, T. J. Marks, L. X. Chen, Effects of Additives on the Morphology of Solution Phase Aggregates Formed by Active Layer Components of High-Efficiency Organic Solar Cells. *Journal of the American Chemical Society* **2011**, *133*, 20661.

[29] S. Mukhopadhyay, A. J. Das, K. S. Narayan, High-Resolution Photocurrent Imaging of Bulk Heterojunction Solar Cells. *The Journal of Physical Chemistry Letters* **2012**, 161.

[30] D. M. Tanenbaum, H. F. Dam, R. Rosch, M. Jorgensen, H. Hoppe, F. C. Krebs, Edge sealing for low cost stability enhancement of roll-to-roll processed flexible polymer solar cell modules. *Solar Energy Materials and Solar Cells* **2012**, *97*, 157.

[31] Y. Li, C. D. Wang, L. F. Feng, C. Y. Zhu, H. X. Cong, D. Li, G. Y. Zhang, Elucidating negative capacitance in light-emitting diodes using an advanced semiconductor device theory. *Journal of Applied Physics* **2011**, *109*.

[32] E. Ehrenfreund, C. Lungenschmied, G. Dennler, H. Neugebauer, N. S. Sariciftci, Negative capacitance in organic semiconductor devices: Bipolar injection and charge recombination mechanism. *Applied Physics Letters* **2007**, *91*.

[33] M. Matsumura, Y. Hirose, Negative-capacitance effect in forward-biased metal oxide semiconductor tunnel diodes (MOSTD). *Japanese Journal of Applied Physics Part 2-Letters* **2000**, *39*, L123.

[34] B. K. Jones, J. Santana, M. McPherson, Negative capacitance effects in semiconductor diodes. *Solid State Communications* **1998**, *107*, 47.

[35] N. A. Penin, Negative capacitance in semiconductor structures. *Semiconductors* **1996**, *30*, 340.

[36] X. Wu, E. S. Yang, H. L. Evans, Negative Capacitance at Metal-Semiconductor Interfaces. *Journal of Applied Physics* **1990**, *68*, 2845.

[37] A. I. Khan, D. Bhowmik, P. Yu, S. J. Kim, X. Q. Pan, R. Ramesh, S. Salahuddin, Experimental evidence of ferroelectric negative capacitance in nanoscale heterostructures (vol 99, 113501, 2011). *Applied Physics Letters* **2012**, *100*.

[38] S. Salahuddin, Negative Capacitance In A Ferroelectric-Dielectric Heterostructure For Ultra Low-Power Computing. *Spintronics V* **2012**, *8461*.

[39] A. I. Khan, D. Bhowmik, P. Yu, S. J. Kim, X. Q. Pan, R. Ramesh, S. Salahuddin, Experimental evidence of ferroelectric negative capacitance in nanoscale heterostructures. *Applied Physics Letters* **2011**, *99*.

[40] A. I. Khan, C. W. Yeung, C. M. Hu, S. Salahuddin, Ferroelectric Negative Capacitance MOSFET: Capacitance Tuning & Antiferroelectric Operation. *2011 Ieee International Electron Devices Meeting (Iedm)* **2011**.

[41] S. Salahuddin, S. Dattat, Use of negative capacitance to provide voltage amplification for low power nanoscale devices. *Nano Letters* **2008**, *8*, 405.

[42] J. Shulman, Y. Y. Xue, S. Tsui, F. Chen, C. W. Chu, General mechanism for negative capacitance phenomena. *Physical Review B* **2009**, *80*.

[43] M. Ershov, H. C. Liu, L. Li, M. Buchanan, Z. R. Wasilewski, A. K. Jonscher, Negative capacitance effect in semiconductor devices. *Ieee Transactions on Electron Devices* **1998**, *45*, 2196.

[44] A. T. Mallajosyula, S. S. K. Iyer, B. Mazhari, Capacitance-voltage characteristics of P3HT:PCBM bulk heterojunction solar cells with ohmic contacts and the impact of single walled carbon nanotubes on them. *Organic Electronics* **2012**, *13*, 1158.

[45] C. Lungenschmied, E. Ehrenfreund, N. S. Sariciftci, Negative capacitance and its photo-inhibition in organic bulk heterojunction devices. *Organic Electronics* **2009**, *10*, 115.

[46] J. Bisquert, A variable series resistance mechanism to explain the negative capacitance observed in impedance spectroscopy measurements of nanostructured solar cells. *Physical Chemistry Chemical Physics* **2011**, *13*, 4679.

[47] J. Bisquert, G. Garcia-Belmonte, A. Pitarch, H. J. Bolink, Negative capacitance caused by electron injection through interfacial states in organic light-emitting diodes. *Chemical Physics Letters* **2006**, *422*, 184.

[48] I. Mora-Sero, J. Bisquert, F. Fabregat-Santiago, G. Garcia-Belmonte, G. Zoppi, K. Durose, Y. Proskuryakov, I. Oja, A. Belaidi, T. Dittrich, R. Tena-Zaera, A. Katty, C. Levy-Clement, V. Barrioz, S. J. C. Irvine, Implications of the negative capacitance observed at forward bias in nanocomposite and polycrystalline solar cells. *Nano Letters* **2006**, *6*, 640.

[49] T. Kuhn, L. Reggiani, L. Varani, A Model Current Spectral Density for Hot-Carrier Noise in Semiconductors. *Journal of Applied Physics* **1991**, *69*, 7097.

[50] V. B. Orlov, A. V. Yakimov, Fluctuations in Hot Charge-Carriers Mobility and 1/F Noise in Semiconductors. *Physica B-Condensed Matter* **1989**, *154*, 175.

[51] P. Hu, C. S. Ting, Noise-Power Temperature for Steady-State Hot-Electron Systems in Semiconductors. *Physical Review B* **1987**, *35*, 4162.
[52] V. B. Orlov, A. V. Yakimov, 1/F Noise in Semiconductors with Hot Carriers. *Izvestiya Vysshikh Uchebnykh Zavedenii Radiofizika* **1987**, *30*, 1255.
[53] F. E. Zocchi, Current and voltage noise spectrum due to generation and recombination fluctuations in semiconductors. *Physical Review B* **2006**, *73*.
[54] Y. Sato, H. Miyagi, H. Takano, S. Taguchi, T. Matsumoto, K. Sato, Transit-time-limited shot noise due to carrier generation in semiconductors: A new approach. *Solid-State Electronics* **1998**, *42*, 664.
[55] N. B. Lukyanchikova, M. V. Petrichuk, N. P. Garbar, A. P. Sasciuk, D. I. Kropman, 1/F Noise and Generation Recombination Processes at Discrete Levels in Semiconductors. *Physica B-Condensed Matter* **1990**, *167*, 201.
[56] L. Reggiani, P. Lugli, V. Mitin, Generation-Recombination Noise of Hot Carriers in Semiconductors. *Solid-State Electronics* **1988**, *31*, 543.
[57] K. Amberiadis, R. W. Grimes, M. R. Kump, G-R Noise Spectra of Semiconductors and Insulators with Various Trap Distributions. *Solid-State Electronics* **1990**, *33*, 975.
[58] S. Kugler, Evaluation of the Trap Concentration in Highly Doped Semiconductors from Low-Frequency Noise Spectra. *Journal of Applied Physics* **1989**, *66*, 219.
[59] S. Kugler, K. Heime, W. Schlapp, G. Weimann, Determination of Trap Parameters in Highly Doped Semiconductors from Low-Frequency Noise Spectra. *Noise in Physical Systems : Including I/F Noise, Biological Systems and Membranes* **1990**, 201.
[60] H. V. Asriyan, F. V. Gasparyan, 1/f noise component conditioned by built-in electric field in semiconductors. *Modern Physics Letters B* **2004**, *18*, 427.
[61] H. V. Asriyan, F. V. Gasparyan, V. M. Aroutiounian, Built-in electric field as an additional source of 1/f noise in semiconductors. *Noise and Information in Nanoelectronics, Sensors and Standards* **2003**, *5115*, 401.
[62] M. Bag, N. S. Vidhyadhiraja, K. S. Narayan, Fluctuations in photocurrent of bulk heterojunction polymer solar cells-A valuable tool to understand microscopic and degradation processes. *Applied Physics Letters* **2012**, *101*.
[63] E. Borovitskaya, M. S. Shur, On theory of 1/f noise in semiconductors. *Solid-State Electronics* **2001**, *45*, 1067.
[64] Z. Celikbutler, T. Y. Hsiang, Spatial Correlation-Measurements of 1/F Noise in Semiconductors. *Solid-State Electronics* **1988**, *31*, 241.
[65] N. V. Dyakonova, M. E. Levinshtein, Model of Bulk 1/F Noise in Semiconductors. *Soviet Physics Semiconductors-Ussr* **1989**, *23*, 175.
[66] B. I. Fuks, Low-Frequency Noise in Doped Semiconductors. *Soviet Physics Semiconductors-Ussr* **1990**, *24*, 1265.
[67] H. Katsu, Y. Kawasugi, R. Yamada, H. Tada, Low frequency noise in organic solar cells. *2011 21st International Conference on Noise and Fluctuations (Icnf)* **2011**, 77.
[68] F. Gruneis, 1/f noise due to atomic diffusion of impurity centers in semiconductors. *Fluctuation and Noise Letters* **2001**, *1*, L197.
[69] M. Tacano, A New Approach to the Hooge Noise Parameter for 1/F Noise in Semiconductors. *Solid-State Electronics* **1991**, *34*, 917.

[70] Y. Zhu, M. J. Deen, A Study on Hooge Empirical 1/F Noise Relation in Semiconductors. *Quantum 1/F Noise & Other Low Frequency Fluctuations in Electronic Devices* **1993**, *282*, 76.

[71] F. N. Hooge, 1/F Noise Sources. *Ieee Transactions on Electron Devices* **1994**, *41*, 1926.

[72] F. N. Hooge, The Relation between 1/F Noise and Number of Electrons. *Physica B-Condensed Matter* **1990**, *162*, 344.

[73] F. N. Hooge, Is There a Simple Empirical Relation for 1/F Noise. *Noise in Physical Systems : Including I/F Noise, Biological Systems and Membranes* **1990**, 375.

Chapter 6
Three-dimensional Microlasers Based on Polymer Fibres

"Do not look into laser with remaining eye."~Anonymus

6.1 Introduction

Optical microresonators and microlasers are vital components in optical communication, integrated optics and sensors [1-2] among many other applications. Resonators can be fabricated in a variety of shapes and geometries such as one-dimensional (1D) wires, two-dimensional (2D) disks [3-4], spirals [5], rings [6], squares [7-8], and other exotic shapes like toroids [9], stadiums [10-11] and bubbles [6]. These lasers are either based on a 1D- Fabry-Perot type or a 2D whispering gallery-like mode (WGM) feedback. Some of the above mentioned 2D resonators like stadiums, serve as model platforms to study phenomena like wave chaos. In some of these 2-D cavities, ray contours can be tailored to prevent the stabilization of closed orbits leading to chaotic modes [12]. Additionally, 3D resonators have often been utilized as waveguides to channel light in luminescent solar concentrators [13-15]. Solar light incident at any angle is guided in these resonators and delivered to a photovoltaic module thereby eliminating the need for solar trackers.

Even though extensive studies have been carried out on 1-D and 2-D microcavities, 3-D microcavities are relatively less explored probably due to fabrication challenges posed by lithographic techniques. Bottle-like microcavities have been explored for three-dimensional (3D) mode structures with coexisting WGM and "bouncing ball" modes (BB) [16]. The BB modes are axial modes and the WGM modes are azimuthal in nature. Such resonators exhibit high Q-factors along with a large dynamic tuning range than that of conventional resonators and have found applications as optical switches and add-drop filters [17-26]. In these cases, a basic requirement is that the resonator should possess a fibre-like geometry in order to

sustain axial modes. Even though bottle resonators have been demonstrated using optical fibres, the control of modes is ensured through tapering and not via cross-sectional shape [25].

In this chapter, we explore lasing in 3-D microcavities that have been fabricated by relatively simple but controlled methods. The approach adopted by us is electrospinning. Electrospinning has proven to be a versatile method to produce fibres and nano-particles of a variety of materials. We exploit this method to spin dye-doped polymer fibres with various dimensions and geometries including coaxial structures [27]. Fibres with non-circular cross-sections have been spun from certain polymer solutions like PS/THF (tetrahydrofuran) [28-31]. It was shown that, at a critical compressive stress, non-circular cross-sections can be energetically favoured over a circular cross-section [28]. Surface modes can be stabilized or frozen into a variety of cross-sectional shapes like rounded-rectangles, squares and other higher order modes depending on the Young's modulus of the polymer. Control over the cross-sectional shape can lead to interesting optical mode patterns.

There have been earlier reports of lasing in electro-spun nano-fibres but our observations and interpretations are very different as the lasing in those fibres resembled features of a 1D resonator [32]. In our case, the transverse dimensions are large ($>>\lambda$, where λ is the central lasing wavelength) with the ability to support 3D optical modes [33]. The process of electrospinning is inherently large scale with low input volume of the polymer solution. Further, reproducible fibres of consistent size and shape can be fabricated. We present results and interpretation that point to realization of 3D mode structures in the laser spectrum. We also observe the feedback trajectories that are essentially dictated by the fibre geometry. Even though the lasing is mirror-less, relatively low lasing thresholds (200 nJ) have been observed along with moderate Q factors (7×10^3).

Though a direct relevance to organic solar cells is not brought about in this chapter, several implications can be derived that may assist in designing efficient devices. e.g. the effect of poling the polymer film could result in a better alignment of the chromophores or dipoles and may assist in charge transport or separation [34]. Additionally these fibres can be used for light harvesting applications in solar cells owing to their fluorescent properties. However, this chapter presents the lasing

characteristics of 3D resonators and any further inference to solar cells is beyond the scope of this chapter.

6.2 Fabrication of lasing fibres

Fabrication of fibres was carried out using the electrospinning technique. A solution mixture consisting of the polymer with dye (DCM) was loaded into a syringe with a metallic tip/ needle in order to take electrical contacts. A collection metal substrate was positioned under the syringe at a distance of a few centimeters. A voltage of 6 kV was then applied to the tip. As the motorized stage was powered, the piston moved at the rate of a few mm/min and a spherical drop of the solution emerged from the tip. The motor speed was controlled till the spherical drop deformed into a cone i.e. the Taylor cone, due to electro-static charging. This cone gradually extended to form fibres on the collection plate. The diameter of the fibre could be controlled by adjusting the concentration of the polymer in the solution or viscosity. Fibre diameters were in the range of 10-50 μm and the cross-sectional shape observed was elliptical or oblate. Though a circular cross-section is generally favoured in these fibres, several cross-sectional other shapes can be achieved by adjusting the polymer concentration in the solvent and also the choice of the solvent. Cylindrical fibres have been widely studied and the WGM modes are well established. In contrast, fibres with elliptical or stadium shaped cross-sections may possess complex WGM modes along with the possibility of axial resonances. Hence, ribbon-like fibres with dissimilar x-y dimensions provide interesting platforms to study optical modes and resonance patterns.

6.2.1 SEM and Optical characterization of fibres

SEM characterization of the fibres was carried out in order to arrive at cross-sectional information. The samples were sputtered with gold and the substrate was tilted to obtain cross-sectional images. The cross-sectional dimensions dictate the

length of the trajectories and would be essential in the lasing mode analysis. SEM images of fibres investigated for lasing are shown in Figure 6.2(a,b). As can be seen from these images the cross-sections are non-circular as expected due to the concentration of the polymer solution. Fluorescence microscopy was also carried out on the fibres and the emission intensity and the spectrum was recorded at each point (Figure 6.3). Fluorescence line profile of a typical fibre in Figure 6.1(a) is shown in Figure 6.2(b) and the fibre dimensions are in accordance with the SEM images. In order to ascertain that the active material was uniformly doped in the fibre, z-stack confocal microscopy was carried out. The cross-sectional SEM and the reconstructed confocal image as shown in Figure 6.1(c) are in reasonable agreement.

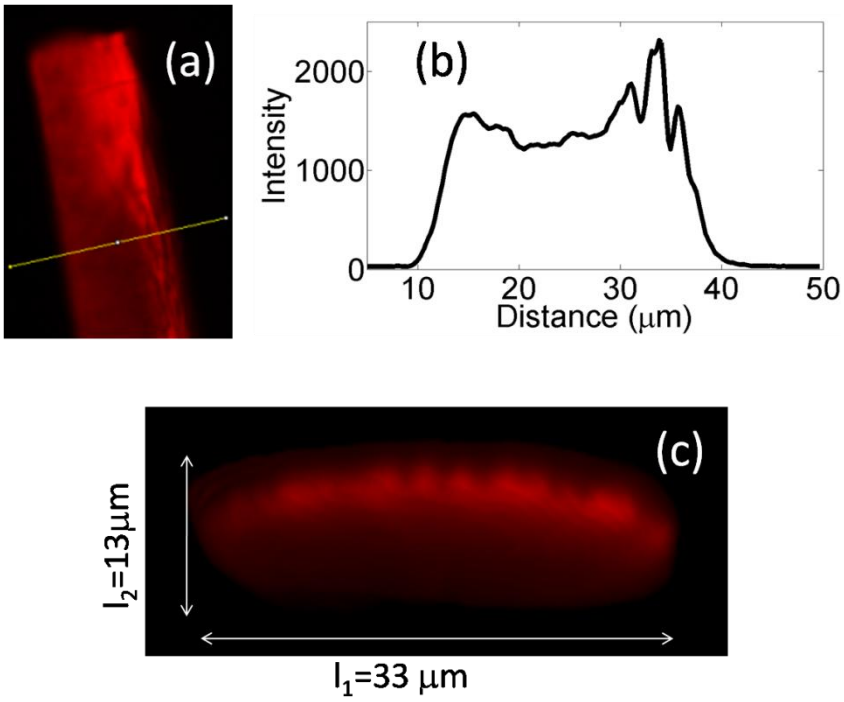

Figure 6.1: *(a) Top view confocal image of the fibre. (b) Fluorescence intensity along the profile selected in (a). (c) Cross-sectional shape reconstructed from the z-stack confocal microscopy with a resolution of 1μm. (Reprinted with permission from A. J. Das, C. Lafargue, M. Lebental, J. Zyss, K. S. Narayan, Three-dimensional microlasers based on polymer fibres fabricated by electrospinning. Applied Physics Letters 2011, 99. © 2011, American Institute of Physics)*

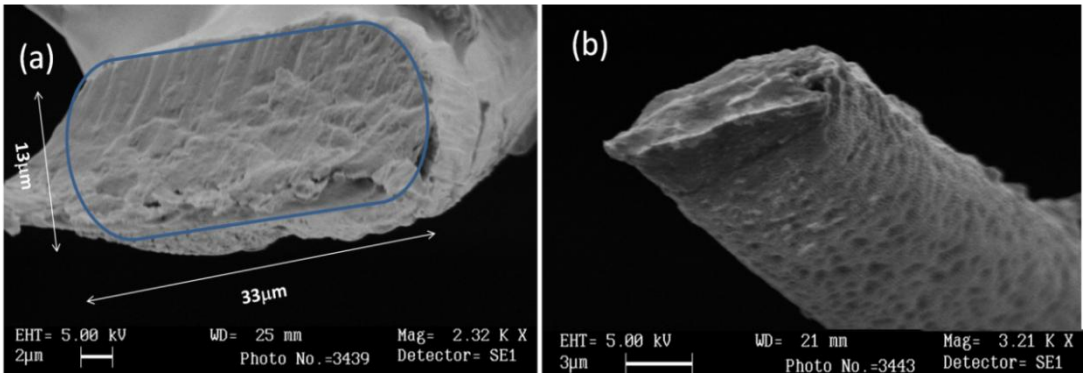

Figure 6.2: *(a) Cross-sectional SEM image of typical fibres outlined to show non-cylindrical contour. (b) SEM image of a fibre showing the cross-section as well as a portion along the fibre axis. (Reprinted with permission from A. J. Das, C. Lafargue, M. Lebental, J. Zyss, K. S. Narayan, Three-dimensional microlasers based on polymer fibres fabricated by electrospinning. Applied Physics Letters 2011, 99. © 2011, American Institute of Physics)*

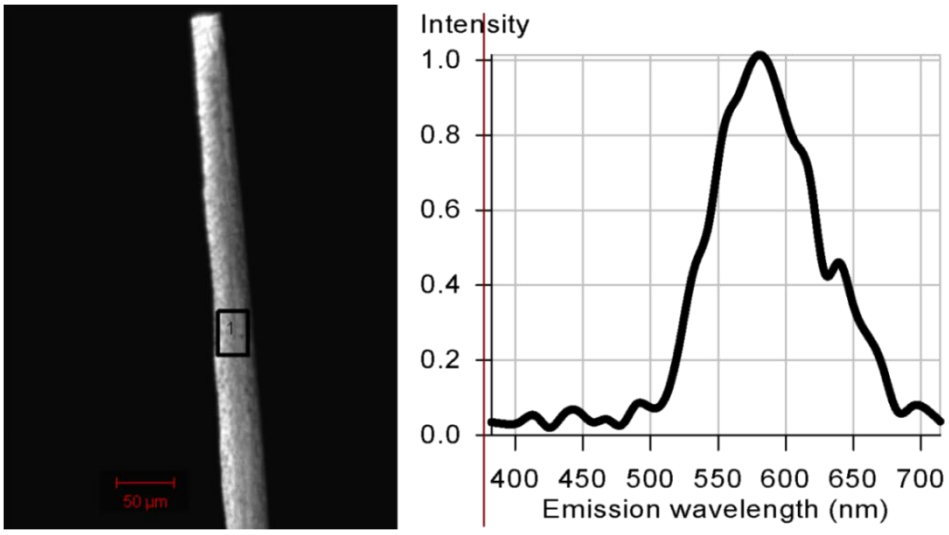

Figure 6.3: *Confocal image of a typical fibre with the fluorescence spectrum from the spot labeled as 1. Excitation λ= 543 nm. (Reprinted with permission from A. J. Das, C. Lafargue, M. Lebental, J. Zyss, K. S. Narayan, Three-dimensional microlasers based on polymer fibres fabricated by electrospinning. Applied Physics Letters 2011, 99. © 2011, American Institute of Physics)*

6.3 Lasing characteristics

The pumping scheme is shown in Figure 6.4(a) where the fibre was mounted on a calibrated rotational stage. The fibre was optically pumped with a frequency doubled Nd:YAG laser (λ = 532 nm, 10 ns pulses) with a beam size about 200 µm in diameter. It was ensured that the beam size was much larger than the fibre section, and smaller than the fibre length. Lasing is generally recognized by a set of signatures. a) Presence of a threshold, b) collapse of the linewidth at threshold, c) mode structure related to the cavity dimensions. A clear threshold was observed at which the spectrally broad fluorescence emission collapsed to a very narrow emission. This was accompanied by a dramatic increase in the emission intensity and a change of slope in the input-output power relationship as shown in Figure 6.5(a) and Figure 6.6.

Figure 6.5(b) shows a typical laser spectrum resembling a comb-like structure, which is a clear evidence of quantization due to a cavity effect. The geometrical length (L) of dominant periodic orbits that are sustained in the cavity laser modes can be inferred from the free spectral range (FSR) as shown in Figure 6.4(c). The FSR can be derived from the resonance condition, $q\lambda = 2nL$, where q is an integer, n is the refractive index, L is the geometric length in a Fabry-Perot cavity. In terms of frequency, $\upsilon = cq/2L$, considering $c=\upsilon\lambda$. The frequency separation between two resonances is then given by $\Delta\upsilon = [(q+1)\ c/2L - qc/2L]$, or $\Delta\upsilon = c/2L$. Taking the derivative of $\lambda=c/\upsilon$ results in $\Delta\lambda = (c/\upsilon^2)\Delta\upsilon$. Substituting for $\Delta\upsilon$ as $c/2L$, we get $\Delta\lambda = \lambda^2/n_{full}L$ [10], where n_{full} is the net refractive index. In this expression, the refractive index n_{full} should be approximated as the sum of the bulk index and a group velocity correction due to finite dispersion of the bulk material [10].

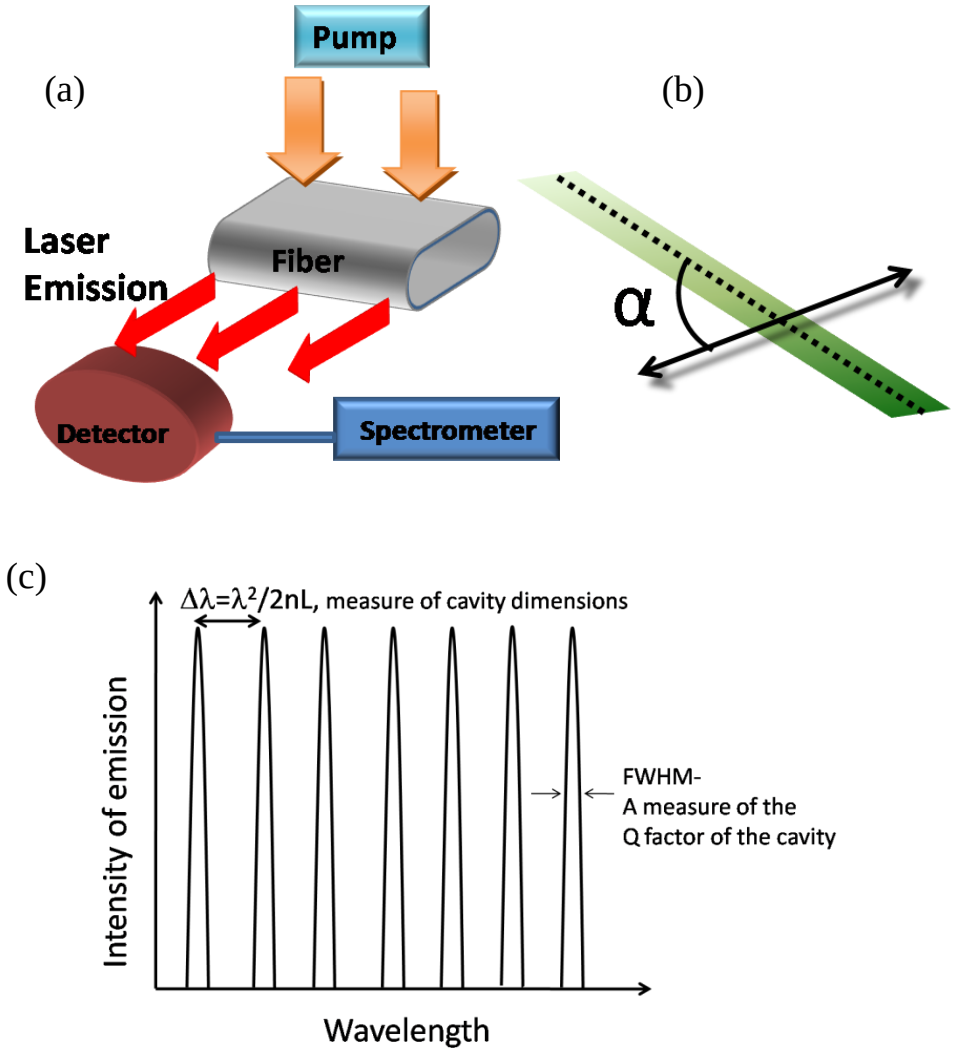

Figure 6.4: *(a) Pumping and detection scheme. (b) Orientation of the pump polarization according to the fibre axis. (c) Typical lasing spectrum. (Reprinted with permission from A. J. Das, C. Lafargue, M. Lebental, J. Zyss, K. S. Narayan, Three-dimensional microlasers based on polymer fibres fabricated by electrospinning. Applied Physics Letters 2011, 99. © 2011, American Institute of Physics)*

Ellipsometry measurements were carried out in order to arrive at the refractive index at the lasing frequencies. It turns out that the bulk refractive index was obtained as n= 1.65 ± 0.04 and a corresponding dispersion contribution leading to n_{full} = 1.75 ± 0.06. The FSR analysis usually is not complex and can be conveniently inferred from

a Fourier transform of the emission spectrum. But in these samples the spectra are strongly modulated and such data processing can lead to inaccurate interpretation.

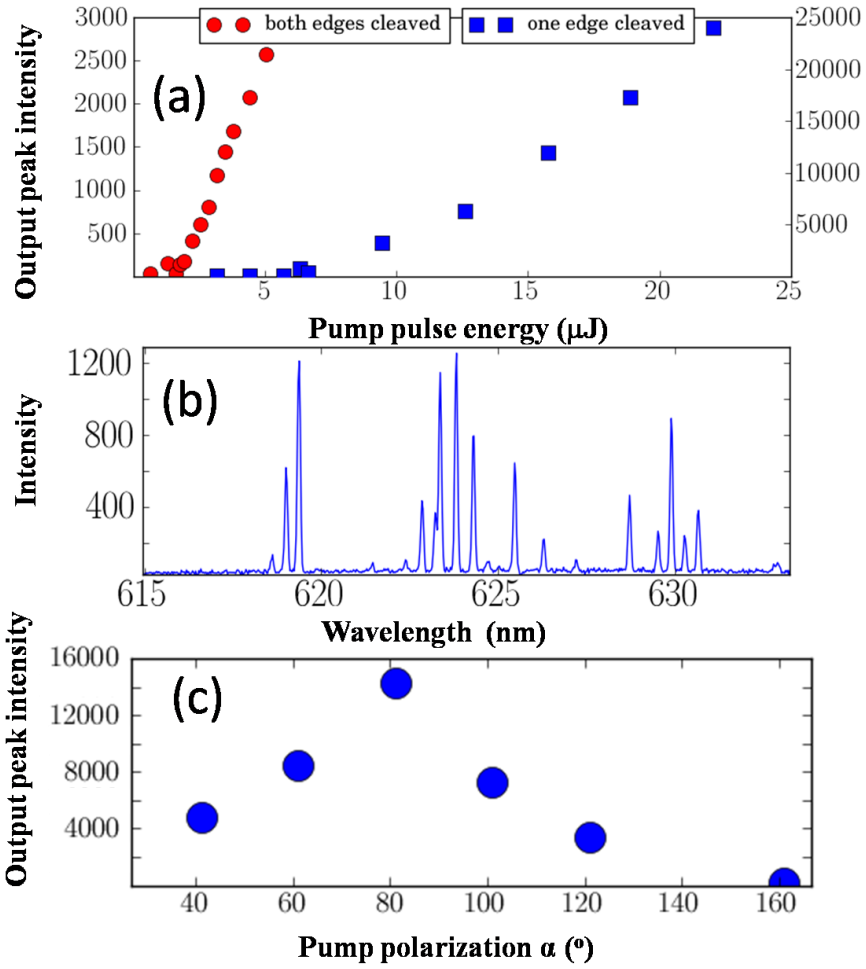

Figure 6.5: *(a) Detected intensity versus pump energy for fibres with one or two cleaved edges. (b) Typical lasing spectrum from the fibre shown in Figure 6.2(b), with a single cleaved edge. The pump area was located a few 100s of μm away from the cleaved edge. (c) Typical dependence of lasing on the angle of the pump polarization α (see Figure 6.4(b) for notation). (Reprinted with permission from A. J. Das, C. Lafargue, M. Lebental, J. Zyss, K. S. Narayan, Three-dimensional microlasers based on polymer fibres fabricated by electrospinning. Applied Physics Letters 2011, 99. © 2011, American Institute of Physics)*

e.g. modulated spectra could originate from laser dynamics or the specific resonator contour or even coupled cavities. FSR derived from the spectrum in Figure 6.5(b) varies from 1.0 to 1.3 nm, which leads to an experimental geometrical length L

= 660 ± 110 µm (for the refractive index obtained from ellipsometry measurements). The perimeter length can be estimated at about 30 µm for the fibre shown in the SEM image in Figure 6.2(b), which obviously is much lower than L, by a factor of 20.

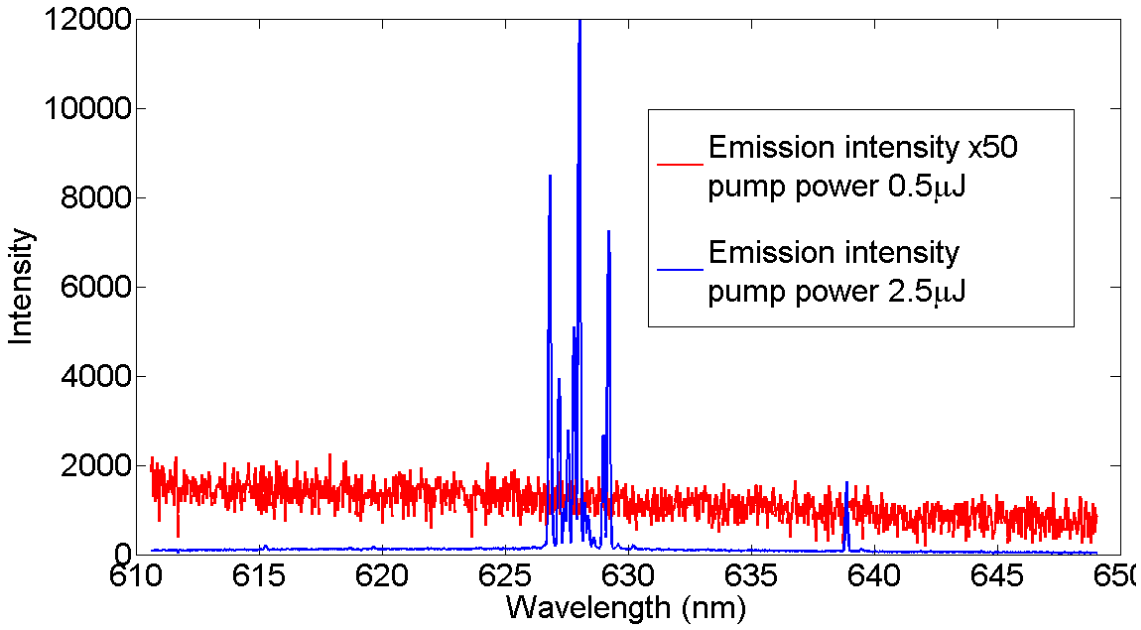

Figure 6.6: *Intensity of emission for two different pump powers-one below threshold (red curve) and above threshold (blue curve). The emission intensity increases rapidly at threshold and a simultaneous narrowing of the spectrum can be observed.*

It is possible to interpret this periodic orbit as a 2D trajectory, lying in the cross-section of the fibre. But it should then be-folded or repeated about 20 times. Hence it is much more likely that corresponding orbits explore the longitudinal or axial path of the fibre. The origin of the quantized modes along the axis can then be attributed to cleaved edges, defects/discontinuities in the fibre, or modulations of the fibre cross-section which provide a reflection.

6.3.1 Evidence of 3D-lasing

In order to ascertain that the lasing explores axial paths further investigation was carried out. We arrived at two specific observations that strongly support the existence of a 3D path. Firstly, inverted optical microscope images of the fluorescence were recorded under pumping and the filtered images are shown in Figure 6.7(a). Enhanced guiding of fluorescence is observed as the input power was increased. Even though the excitation spot was several hundred micrometers away, the fluorescence was guided efficiently. This fact accounts reasonably well for the spectra shown in Figures 6.7 (b-d) where new modes emerged as the pumping energy was increased. These additional peaks occurred at shorter spacings or larger path lengths and hence could be assigned to axial modes [20, 35].

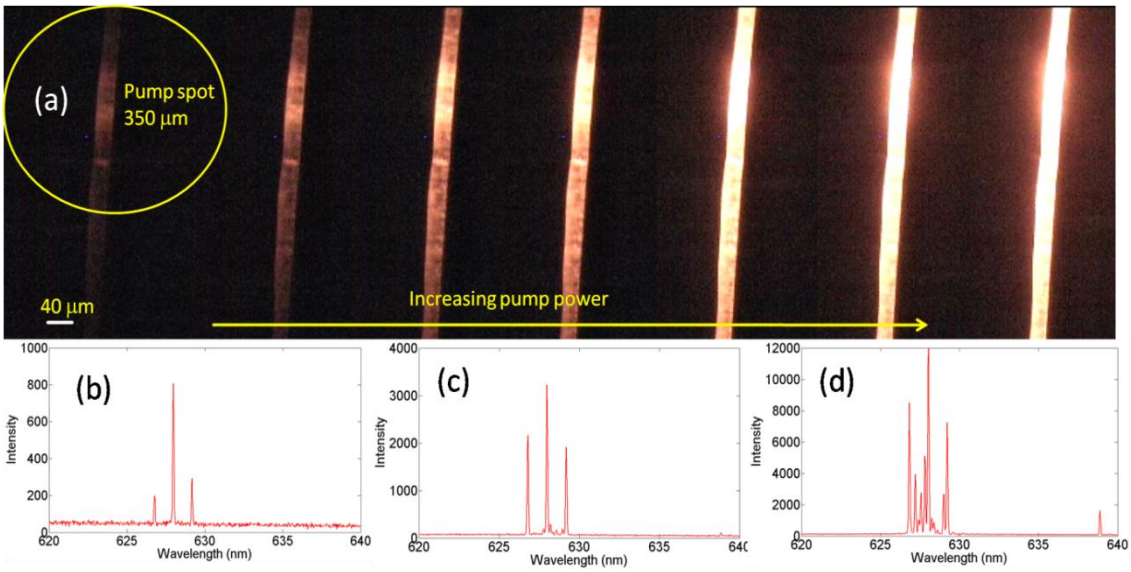

Figure 6.7: *(a) Series of fluorescence images evidencing light guiding. As pump power was increased from left to right, the length of the emitting part was seen to increase. (b-d) Spectra collected on the same fibre in the same configuration save the pump energy P, evidencing the emergence of new modes: (b) P = 1 a.u., (c) P = 1.5 a.u., and (d) P = 2 a.u.. (Reprinted with permission from A. J. Das, C. Lafargue, M. Lebental, J. Zyss, K. S. Narayan, Three-dimensional microlasers based on polymer fibres fabricated by electrospinning. Applied Physics Letters 2011, 99. © 2011, American Institute of Physics)*

Secondly, there was a strong dependence of lasing on the pump polarization. As shown in Figure 6.5(c), the collected emission was maximum for when the pump polarization was oriented at about 80° with respect to the fibre axis (see scheme in Figure 6.4(b)). This angle seems to be a robust quantity for the system, since it appeared with ±10° for each measured fibre, irrespective of the size or geometry of the section. In general for solid-state organic lasers, there is an intimate connection between the pump polarization and the structure of lasing modes. There is also a dependence on the molecular structure of the laser dye [36]. In the case of the laser dye (DCM) used here, which can be approximated to a linear dipole, the laser action is more probable and is maximized when the pump polarization is perpendicular to the path of light amplification. Lasing was observed to occur for pump polarizations around $\alpha \sim 80°$ and but not for $\alpha \sim 0°$ (i.e. aligned with the fibre axis) in spite of very large pump powers. This evidence points to the fact that lasing modes are not lying in the fibre cross-section like conventional WGMs but exploring a more complex 3D path. These modes resemble coupled cavities where one cavity modulates the mode pattern. Only modes that are common to both cavities are sustained. A closer look at the laser spectra reveals that there are two sets of mode spacings. We speculate that axial and azimuthal resonances are coupled leading to two sets of spacings. The smaller paths are in accordance with the fibre cross-sections and the larger paths are in reasonable agreement with the axial dimensions.

Furthermore, it was observed that the lasing threshold reduced by an order of magnitude when both ends of the fibre were cleaved. The fibre investigated in Figure 6.2(a) had a threshold of 1 μJ whereas another one with both edges cleaved had a threshold as low as 200 nJ (see Figure 6.5(a)). This is interpreted as a more efficient axial feedback occurring due to the presence of reflection from the both edges.

6.3.2 Ruling out random lasing

Experiments were also carried out to rule out random lasing which has been observed in polymer/dye based films like poly (phenylene vinelynes) or PPV [37-40]. Random lasing occurs in disordered media when cavities are unintentionally created due to scattering centers. Due to the porosity of the fibres and the presence of defects, it is essential to rule out random lasing in these 3D resonators. Ruling out random lasing in turn will assist in assignment of transverse and longitudinal modes as well. Random lasers are characterized by a) non-linear input-output power relationships, b) time varying emission spectra and c) absence of periodic quantized modes in the laser spectra [41]. We observed a clear threshold and the input-output relationship was linear and not a higher order polynomial as shown in Figure 6.5(a). This is an indication that there is one single cavity and not randomly distributed cavities. Lasing spectra from random lasers fluctuates with time as different cavities emit at different time intervals. The present case several consecutive emission profiles were captured and there was no frequency shift observed as shown in Figure 6.8.

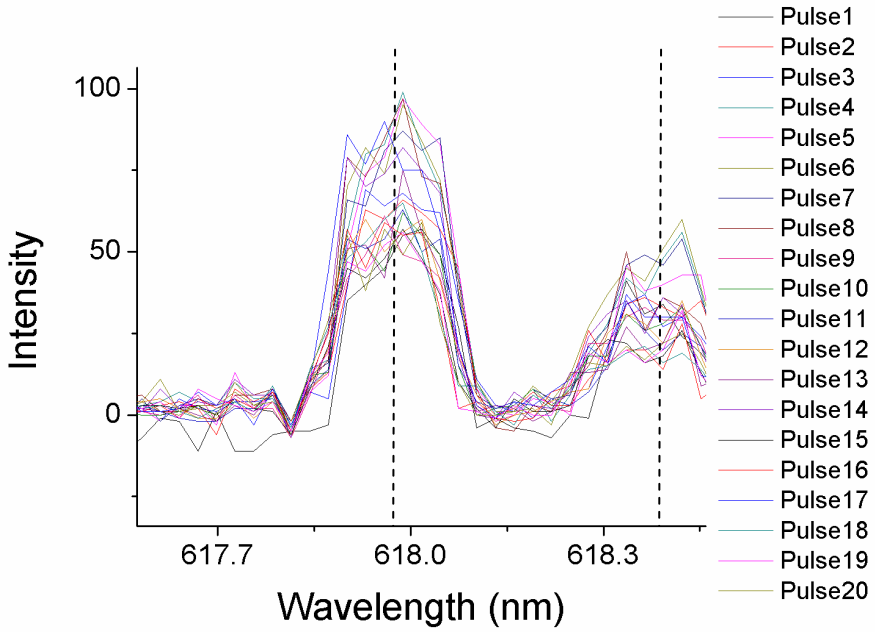

Figure 6.8: *Single-shot continuous spectra of the polymer fibre laser showing that the spectral position does not vary with time.*

Random lasers do not exhibit a clear FSR or comb like modes separated by a fixed frequency. Additionally, they have lower Q factors due to incomplete light confinement. In the present case, equi-spaced modes are observed confirming the presence of a single cavity and quantization of optical paths as shown in Figure 6.5(b). Moderately high Q factors ~ 10^3-10^4 have been achieved indicating that there is better light confinement. Hence, the lasing in these 3D microresonators is a result of well-defined optical paths due to total-internal-reflections at the facets and a coupling of Fresnel reflections from the edges.

Summary

Electrospun dye-doped polymer fibres offer interesting cavity structures which can support unconventional optical mode patterns. An appropriate choice of the polymer matrix, dye concentration and the solvent can lead to fibres with non-cylindrical cross-section. Lasing was demonstrated in these fibres with a non-planar geometry. Mode analysis suggests that 3D optical modes are supported in these cavities with azimuthal and axial feedback. The resonators had moderately high Q-factors in spite of the absence of mirrors giving rise to low lasing thresholds. These microlasers not only are suitable for studying higher dimensional modes, they can be envisaged in applications ranging from multi-directional sources, active sensors and integrated optical components.

References

[1] K. J. Vahala, Optical microcavities *Nature* **2003**, *424*, 839.
[2] A. M. Armani, R. P. Kulkarni, S. E. Fraser, R. C. Flagan, K. J. Vahala, Label-free, single-molecule detection with optical microcavities *Science* **2007**, *317*, 783.
[3] T. J. Kippenberg, S. M. Spillane, D. K. Armani, K. J. Vahala, Fabrication and coupling to planar high-Q silica disk microcavities *Applied Physics Letters* **2003**, *83*, 797.
[4] X. S. Jiang, Q. Lin, J. Rosenberg, K. Vahala, O. Painter, High-Q double-disk microcavities for cavity optomechanics *Optics Express* **2009**, *17*, 20911.

[5] T. Ben-Messaoud, J. Zyss, Unidirectional laser emission from polymer-based spiral microdisks *Applied Physics Letters* **2005**, *86*.

[6] T. Ben-Messaoud, S. X. Dou, E. Toussaere, A. Potter, D. Josse, G. Kranzelbinder, J. Zyss, Longitudinal pumping of polymer microring lasers *Synthetic Metals* **2002**, *127*, 159.

[7] N. Djellali, M. Lebental, R. Dubertrand, C. Schmit, E. Bogomolny, J. Zyss, Spectra and periodic orbits in a square shaped organic micro-lasers *Icton 2008: Proceedings of 2008 10th Anniversary International Conference on Transparent Optical Networks, Vol 4* **2008**, 61.

[8] G. D. Chern, A. W. Poon, R. K. Chang, T. Ben-Messaoud, O. Alloschery, E. Toussaere, J. Zyss, S. Y. Kuo, Direct evidence of open ray orbits in a square two-dimensional resonator of dye-doped polymers *Optics Letters* **2004**, *29*, 1674.

[9] T. J. Kippenberg, S. M. Spillane, K. J. Vahala, Demonstration of ultra-high-Q small mode volume toroid microcavities on a chip *Applied Physics Letters* **2004**, *85*, 6113.

[10] M. Lebental, J. S. Lauret, J. Zyss, C. Schmit, E. Bogomolny, Directional emission of stadium-shaped microlasers *Physical Review A* **2007**, *75*.

[11] M. Lebental, J. S. Lauret, R. Hierle, J. Zyss, Highly directional stadium-shaped polymer microlasers *Applied Physics Letters* **2006**, *88*.

[12] E. Bogomolny, N. Djellali, R. Dubertrand, I. Gozhyk, M. Lebental, C. Schmit, C. Ulysse, J. Zyss, Trace formula for dielectric cavities. II. Regular, pseudointegrable, and chaotic examples *Physical Review E* **2011**, *83*.

[13] R. Bose, M. Gonzalez, P. Jenkins, R. Walters, J. Morseman, M. Moss, C. McLain, P. Linsert, A. Buchtemann, A. J. Chatten, K. W. J. Barnham, Resonance Energy Transfer in Luminescent Solar Concentrators *35th Ieee Photovoltaic Specialists Conference* **2010**, 467.

[14] M. J. Kastelijn, C. W. M. Bastiaansen, M. G. Debije, Influence of waveguide material on light emission in luminescent solar concentrators *Optical Materials* **2009**, *31*, 1720.

[15] P. P. C. Verbunt, A. Kaiser, K. Hermans, C. W. M. Bastiaansen, D. J. Broer, M. G. Debije, Controlling Light Emission in Luminescent Solar Concentrators Through Use of Dye Molecules Aligned in a Planar Manner by Liquid Crystals *Advanced Functional Materials* **2009**, *19*, 2714.

[16] M. Sumetsky, Whispering-gallery-bottle microcavities: the three-dimensional etalon *Optics Letters* **2004**, *29*, 8.

[17] D. O'Shea, C. Junge, M. Pollinger, A. Vogler, A. Rauschenbeutel, All-optical switching and strong coupling using tunable whispering-gallery-mode microresonators *Applied Physics B-Lasers and Optics* **2011**, *105*, 129.

[18] D. O'Shea, C. Junge, S. Nickel, M. Pollinger, A. Rauschenbeutel, Ultra-high Q whispering-gallery-mode bottle microresonators: properties and applications *Laser Resonators and Beam Control Xiii* **2011**, *7913*.

[19] M. Pollinger, A. Rauschenbeutel, All-optical signal processing at ultra-low powers in bottle microresonators using the Kerr effect *Optics Express* **2010**, *18*, 17764.

[20] M. Pollinger, D. O'Shea, F. Warken, A. Rauschenbeutel, Ultrahigh-Q Tunable Whispering-Gallery-Mode Microresonator *Physical Review Letters* **2009**, *103*.

[21] P. Bianucci, X. Wang, J. G. C. Veinot, A. Meldrum, Silicon nanocrystals on bottle resonators: Mode structure, loss mechanisms and emission dynamics *Optics Express* **2010**, *18*, 8466.

[22] P. Bianucci, J. G. C. Veinot, A. Meldrum, Coupling Silicon Nanocrystal Fluorescence to Optical Bottle Resonators *Nanoscale Luminescent Materials* **2010**, *28*, 297.

[23] M. Ding, G. S. Murugan, G. Brambilla, J. S. Wilkinson, M. N. Zervas, Robust Mode-Selection in Optical Bottle Microresonators *2012 Conference on Lasers and Electro-Optics (Cleo)* **2012**.

[24] G. S. Murugan, M. N. Petrovich, Y. Jung, J. S. Wilkinson, M. N. Zervas, Hollow-bottle optical microresonators *Optics Express* **2011**, *19*, 20773.

[25] G. S. Murugan, J. S. Wilkinson, M. N. Zervas, Novel fiber bottle microresonator add-drop filters *Optical Components and Materials Vii* **2010**, *7598*.

[26] G. S. Murugan, J. S. Wilkinson, M. N. Zervas, Selective excitation of whispering gallery modes in a novel bottle microresonator *Optics Express* **2009**, *17*, 11916.

[27] W. E. Teo, S. Ramakrishna, A review on electrospinning design and nanofibre assemblies *Nanotechnology* **2006**, *17*, R89.

[28] L. F. Wang, C. L. Pai, M. C. Boyce, G. C. Rutledge, Wrinkled surface topographies of electrospun polymer fibers *Applied Physics Letters* **2009**, *94*.

[29] S. Megelski, J. S. Stephens, D. B. Chase, J. F. Rabolt, Micro- and nanostructured surface morphology on electrospun polymer fibers *Macromolecules* **2002**, *35*, 8456.

[30] C. L. Pai, M. C. Boyce, G. C. Rutledge, Morphology of porous and wrinkled fibers of polystyrene electrospun from dimethylformamide *Abstracts of Papers of the American Chemical Society* **2009**, *238*.

[31] C. L. Pai, M. C. Boyce, G. C. Rutledge, Morphology of Porous and Wrinkled Fibers of Polystyrene Electrospun from Dimethylformamide *Macromolecules* **2009**, *42*, 2102.

[32] A. Camposeo, F. Di Benedetto, R. Stabile, A. A. R. Neves, R. Cingolani, D. Pisignano, Laser Emission from Electrospun Polymer Nanofibers *Small* **2009**, *5*, 562.

[33] A. J. Das, C. Lafargue, M. Lebental, J. Zyss, K. S. Narayan, Three-dimensional microlasers based on polymer fibers fabricated by electrospinning *Applied Physics Letters* **2011**, *99*.

[34] B. B. Y. Hsu, J. Seifter, C. J. Takacs, C. Zhong, H.-R. Tseng, I. D. W. Samuel, E. B. Namdas, G. C. Bazan, F. Huang, Y. Cao, A. J. Heeger, Ordered Polymer Nanofibers Enhance Output Brightness in Bilayer Light-Emitting Field-Effect Transistors *Acs Nano* **2013**, *7*, 2344.

[35] G. S. Murugan, J. S. Wilkinson, M. N. Zervas, Optical Excitation and Probing of Bottle Microresonators *Emerging Trends and Novel Materials in Photonics* **2010**, *1288*, 22.

[36] I. Gozhyk, G. Clavier, R. Meallet-Renault, M. Dvorko, R. Pansu, J. F. Audibert, A. Brosseau, C. Lafargue, V. Tsvirkun, S. Lozenko, S. Forget, S. Chenais, C. Ulysse, J. Zyss, M. Lebental, Polarization properties of solid-state organic lasers *Physical Review A* **2012**, *86*.

[37] R. C. Polson, Z. V. Vardeny, Spatially mapping random lasing cavities *Optics Letters* **2010**, *35*, 2801.

[38] A. Tulek, R. C. Polson, Z. V. Vardeny, Naturally occurring resonators in random lasing of pi-conjugated polymer films *Nature Physics* **2010**, *6*, 303.
[39] R. C. Polson, A. Chipouline, Z. V. Vardeny, Random lasing in pi-conjugated films and infiltrated opals *Advanced Materials* **2001**, *13*, 760.
[40] R. C. Polson, Z. V. Vardeny, Random lasing in dye-TiO2 solutions and pi-conjugated polymer films *Physica B-Condensed Matter* **2003**, *338*, 219.
[41] A. Tulek, Z. V. Vardeny, Studies of random laser action in pi-conjugated polymers *Journal of Optics* **2010**, *12*.

Chapter 7
Summary and Future Directions

The thesis addressed the major drawbacks of organic solar cells namely, the 'area-issue' and the 'stability-issue'. Area dependence of the device efficiency was studied in detail and a device geometry was proposed that could retain the efficiency as the device area was scaled up. Low-melting metal alloys were utilized as electrode materials to yield highly efficient solar cells. These alloys could be modified in their molten state to fabricate patterned solar cells. The shape, size and the spacing of the patterns were optimized by electrical and optical considerations. It was concluded that triangular pixels of a few mm. sq. area, spaced by a characteristic decay length was a viable solution to the area-issue.

The next part explored the possibilities of integrating light management in to the patterned organic solar cells. Spaces in between the patterns were replaced by a suitable dye-doped dielectric matrix that could down-convert transmitted photons. This resulted in an enhanced efficiency due increased absorption of the device structure. The dielectric matrix could additionally serve as an encapsulation. In the next section, microlens arrays were fabricated by soft lithography methods that could focus solar light and improve light collection of the device structure. The lenses had non-spherical height profiles which could convert Gaussian beams to Bessel beams. These beams had unusual properties like self-reconstruction and extended focal lengths making them ideal for solar concentrators.

The stability-issue was addressed in the next section, where I-V, C-V and noise measurements were carried out to study the sources of device degradation. Processing conditions of the device were varied to study the effect of additives on device stability. It was observed that large concentrations of the acceptor in the device surface, though desirable due to better charge extraction, was the source of device degradation in the 100-200 hrs period. C-V measurements showed the disappearance of a negative capacitance feature as a function of time. This was related to the lowering of injection at the alloy electrode due to the formation of a barrier at the edge that permeated inward as a function of time.

Noise measurements also in agreement with the C-V measurements as the slope of the noise spectrum oscillated as a function of time.

Three-dimensional microlasers were studied in the final section of the thesis. Non-cylindrical dye-doped polymer fibers were fabricated by electrospinning. The facets of the fiber along with its edges had the ability to reflect light by total-internal-reflection. Lasing action was demonstrated in these micro-cavities with signatures of light confinement in three dimensions. Modes observed from spectral measurements showed two different characteristics corresponding to axial and azimuthal quantization. Polarization properties of the laser and the pump source were studied to infer the alignment of the dye molecules in the matrix. The lasers had low thresholds of lasing indicating moderately high Q-factors.

Future directions

The designs for large area solar cells can be implemented over larger areas, with better optimization and control over electrode parameters. It is also envisaged that the process can be roll-to-roll compatible incorporating flexible alloy electrodes. This would require the alloy to be made printable in the form of an ink or suspension.

Light management via down-conversion and microlenses can also be realized in a flexible manner and integrated with the devices maintaining print processing ability.

Stability of the devices needs to be studied in greater depth by considering the thermal properties of the alloy. A better understanding of the noise features over different frequency regimes should enable robust designs that improve device lifetimes. Edge sealed, efficient devices can be fabricated that can operate effectively over several years.

APPENDIX A

Additional area gained due to the decay region for a circular electrode

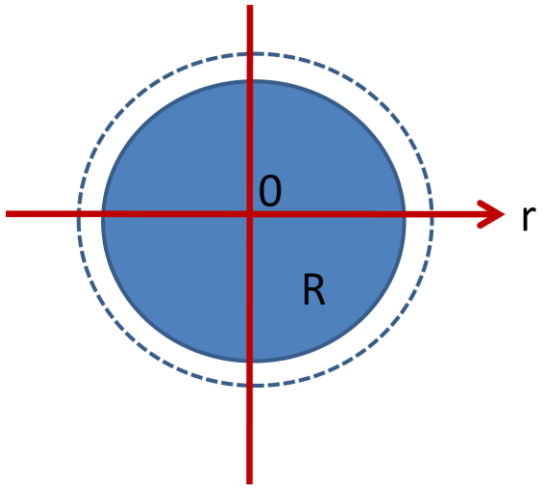

$$A_{decay} = 2\pi \int_{R}^{\infty} re^{-ar} dr = \frac{2\pi R}{a}$$

$$a = 1/L_d$$

R is the radius of the circular electrode and L_d is the decay length. Define gain factor G as the percentage increase in the area with respect to the actual device area,

G = 100 x Adecay/(A+Adecay); where A=πR^2.

=100 x (2π R/a)/(2π R/a + πR^2)

= 200/ (aR+2)

Taking L_d=80μm for PCPDTBT:PCBM blend, pixel radius= 0.1 cm, 0.15cm. G turns out to be 13.8% and 9.6% indicating that a large fraction of carriers diffuse through from the vicinity.

A circular pattern is not ideal for an actual large area device as it cannot fill up a 2-D space without leaving spaces. Triangular, square, hexagonal pixels are a better choice. In order to maximize peripheral area the perimeter must be maximized. Larger the perimeter larger is the charge collecting region in the vicinity. Simple calculations point to the fact that for the same area the geometric shape with the highest perimeter is a triangle.

Triangular patterns can fill up a 2-D space and have the largest perimeter; hence they are the best choice for pattern shapes.

Perimeter of triangle>square>hexagon>circle for the same area.

For an area of 1 cm^2,

Radius of the circle: r = sqrt (1/pi) = 0.564cm

Perimeter of the circle = 2 pi (0.564 cm) = 3.545 cm

Side of a square = 1cm and perimeter = 4 cm

Perimeter of a hexagon = 3.72 cm

Perimeter of a triangle = 4.6 cm

APPENDIX B

Lorentzians for PCPDTBT:PCBM[70] (1:3.5)

Lorentz model:

$$\varepsilon(\omega) = \varepsilon_{\infty} + \sum_{n=1}^{\infty} \left(\frac{\chi_0 \, G_n \, \omega_0^2}{\omega_{0n}^2 + i\Gamma_n \omega - \omega^2} \right)$$

where, ω_{0n} are the resonant frequencies

G_n are related to the oscillator strengths

Γ_n are the damping coefficient

ε_{∞} is the permittivity at $\omega=\infty$

χ_0 is the permittivity at $\omega=0$.

S.no	ω_o (cm^{-1})	ω_p (cm^{-1})	Γ (cm^{-1})	G
1	12456	3792	784	0.0927
2	13486	4097	1637	0.0923
3	26890	24398	20007	0.823

$\varepsilon_{inf} = 3.35$

Lorentzians for P3HT:PCBM[70] (1:1)

ε_{inf} = 2.35

S.no	ω_o (cm^{-1})	ω_p (cm^{-1})	Γ (cm^{-1})	G
1	20793	7373	2380	0.126
2	22997	7271	3809	0.100
3	19393	6632	1864	0.117
4	29496	13048	6923	0.196
5	36843	21294	4066	0.334
6	17969	5252	1666	0.085

Lorentzians for LDS 759

ε_{inf} = 2.25

S.no	ω_o (cm^{-1})	ω_p (cm^{-1})	Γ (cm^{-1})	G
1	29340	4372	5641	0.022
2	17173	6909	1437	0.162

APPENDIX C

MATLAB Code to evaluate noise spectrum

```
%%This function evaluates the frequency distribution of a thermal source

function freqdis
N=input('how many files '); % takes up to 100 files
Fs =2000000; t = -0.5:1/Fs:.5; %sampling rate depending on the noise frequency range
m=0;
f=(0:4096)*Fs/8192;              % 8192 point FFT
 p=input('enter name of file ','s');
e=zeros(99987,1); ;              % initialization
aver=zeros(8192,1);
k=1;
for i=1:N ;              % open and read data from files
fid = fopen(p, 'r');
c = dlmread(p,'\t',5);
d=c(:,2);
wordcount=size(p,2);
wordcount=wordcount-4;
for j=1:12
e=d(1+m:8192+m);

 %% compute FFT of time data
pxx=fft(e,8192);%%fft of time data
pxxz=log(abs(pxx(1:size(pxx))).^2);
```

```
freqm=find(pxxz>=max(pxxz));
freqmax(k)=freqm(1,1);
k=k+1;
m=m+8192;
aver=aver+pxxz;
hold on
end
m=0;
if i<10
   p(wordcount-1)=num2str(0);
   p(wordcount)=num2str(i);
else
    p(wordcount-1:wordcount)=num2str(i);
end
end
 aver=aver/(12*N);
plot(f,aver(1:4097)); % plot averaged power spectrum
%Option for plotting histograms
% hist((freqmax*30.5),f);
%counts = hist(freqmax*15.26,f);
% hold on
%plot(f,counts,'o');
% %  hist(freqmax,x); %histogram of frequencies
% % figure
%  plot(t,d)
fclose('all');
```

APPENDIX D

Thermal properties of low melting alloys

General Characteristics

In addition to having low melting temperatures CS Alloys are virtually non-shrinking, several expand or grow after they are solid. All are relatively soft and brittle. Some, like CS Alloys, work soften. All have high density, averaging about three cu. ins. per pound. The numbers in parenthesis refer to other CS Alloys literature giving more details on the specific end use. Write for your copy.

	2# Cakes	2# Slabs	3/16" U Bars	Special Shapes on Request	Wire	Typical End Uses	Melting Point - Degree F	Range (Degree F) (No definite melting point)	Melting Point - Degree C	Range (Degree C) (No definite melting point)	Growth or Shrinkage	After Casting	Weight Lbs./In.3	Tensile Strength Lbs./In.2	Brinell Hardness No.	Maximum Load 30 Seconds, Lbs./In.2	Safe Load Sustained Lbs./In.2	Electrical Conductivity Compared with pure cooper	Composition (%)
Low 117 Alloy	X	X	X	X	No	Use in jigging or fixturing delicate parts for machining (honeycomb), (B5 Supp. 3); dental models, prosthetic development work; proof casting (internal measurements), (E10); fusible element in safety devices (E3); radiopaque contrast medium in X-Ray; low temperature solder (E9)	117	-	47.2	-	Initial Expansion, Shrinks to .0000" in 30 minutes	Stable in 2 hours at -.0002" Per Inch	.32	5400	12	-	-	3.34%	Bismuth: 4 Lead: 22.6 Tin: 8.3 Cadmium: 5.3 Indium: 19
Low 136 Alloy	X	No	X	X	No	Anchor parts for machining (jet blades), testing, inspection (A1); block lenses in optical manufacturing; proof casting (E10); fusible element in safety devices (sprinkler heads (E3); fusible cores in compound cores; low melt solder (E9); sealing adjustment screws.	136	-	57.8	-	Initial Expansion, .0000" in one Hour	Stable in 5 hours at -.0002" Per Inch	.31	6300	14	-	-	2.43%	Bismuth: 4 Lead: 22.6 Tin: 12.0 Indium: 21

Table D1: Properties of low melting alloys. Thermal shrinkage specifications are highlighted.

GUIDE VALUES			
Density		8.58 $g.cm^{-3}$	
Brinell Hardness		23	BS 240:1986 (1991)
Melting Point		135^{0}C	(see figs. 1 & 2
Specific Heat	(solid, 25^{0}C)	0.167 $J.g^{-1}.{}^0C^{-1}$	
	(liquid, 160^{0}C)	0.155 $J.g^{-1}.{}^0C^{-1}$	
Latent heat of fusion		49. 1 $J.g^{-1}$	(at immediate re-fusion)
Thermal conductivity		0.185 $J.sec^{-1}.cm^{-1}.{}^0C^{-1}$	
Electrical Resistivity		59 μ Ω.cm	(0.029 x conductivity of Cu)
Viscosity			(see fig. 6)
Compressive Properties: proof stress at 2 days and 70 days			
	(0.2% set)	41.6 rising to 46.7 Mpa	
	(1.0% set)	49.4 rising to 58.3 Mpa	
Tensile properties: data at 2 days and 70 days			BS EN 10 020
	Modulus of elasticity		(see fig. 5)
	Proof stress 0.2% set	32.1 rising to 42.1 Mpa	
	Tensile strength	60.1 rising to 62.3 Mpa	
	Elongation	80 falling to 55	

Table D2: Thermal properties of alloys over a period of 70 days. Data adapted from Mining and Chemical Products Ltd.

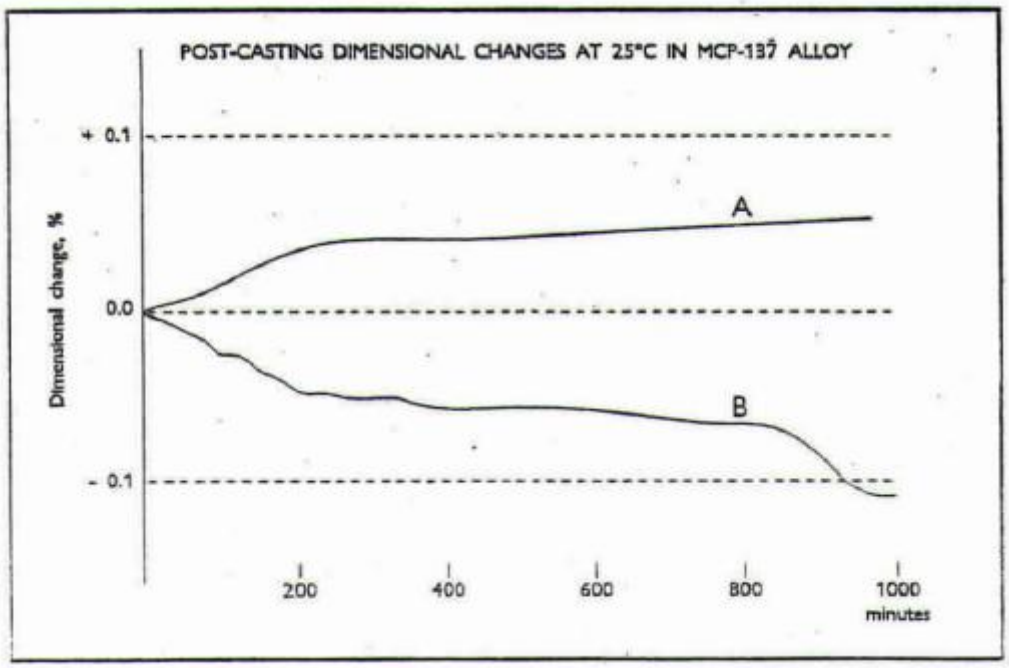

Figure D1: Graph depicting dimensional changes of alloy after being cast over a period of 1000 minutes. Data adapted from Mining and Chemical Products Ltd.